



Veröffentlichungen der DGK

Ausschuss Geodäsie der Bayerischen Akademie der Wissenschaften

Reihe C

Dissertationen

Heft Nr. 866

Felix Lucian Müller

**Improved polar geostrophic surface currents from satellite
altimetry**

München 2021

Verlag der Bayerischen Akademie der Wissenschaften

ISSN 0065-5325

ISBN 978-3-7696-5278-9

Diese Arbeit ist gleichzeitig veröffentlicht in:
MediaTUM <http://mediatum.ub.tum.de/?id=1574433>



Veröffentlichungen der DGK

Ausschuss Geodäsie der Bayerischen Akademie der Wissenschaften

Reihe C

Dissertationen

Heft Nr. 866

Improved polar geostrophic surface currents from satellite altimetry

Von der Fakultät für Luftfahrt, Raumfahrt und Geodäsie
der Technischen Universität München
zur Erlangung des Grades
Doktor-Ingenieur (Dr.-Ing.)
genehmigte Dissertation

Vorgelegt von

Felix Lucian Müller, M.Sc.

Geboren am 24.05.1990 in München, Bayern, Deutschland

München 2021

Verlag der Bayerischen Akademie der Wissenschaften

ISSN 0065-5325

ISBN 978-3-7696-5278-9

Diese Arbeit ist gleichzeitig veröffentlicht in:
MediaTUM <http://mediatum.ub.tum.de/?id=1574433>

Adresse der DGK:



Ausschuss Geodäsie der Bayerischen Akademie der Wissenschaften (DGK)

Alfons-Goppel-Straße 11 • D – 80 539 München
Telefon +49 – 331 – 288 1685 • Telefax +49 – 331 – 288 1759
E-Mail post@dgk.badw.de • <http://www.dgk.badw.de>

Prüfungskommission:

Vorsitzender: Prof. Dr.-Ing. habil. Thomas Wunderlich

Prüfer: Prof. Dr.-Ing. Florian Seitz
Prof. Dr.-Ing. Martin Horwath
Prof. Per Knudsen, Ph.D.

Die Dissertation wurde am 21.09.2020 bei der Technischen Universität München eingereicht und durch die Fakultät für Luftfahrt, Raumfahrt und Geodäsie am 04.01.2021 angenommen.

Diese Dissertation ist auf dem Server der Technischen Universität München unter <http://mediatum.ub.tum.de/?id=1574433> elektronisch veröffentlicht

© 2021 Bayerische Akademie der Wissenschaften, München

Alle Rechte vorbehalten. Ohne Genehmigung der Herausgeber ist es auch nicht gestattet, die Veröffentlichung oder Teile daraus auf photomechanischem Wege (Photokopie, Mikrokopie) zu vervielfältigen

Abstract

The north polar regions, in particular the northern Nordic Seas, are one of the most important gateways between the Arctic Ocean and the northern Atlantic. They are characterized by strong heat exchange to the atmosphere, freshwater inflow from the outlet glaciers, drifting sea ice and water masses flowing polewards and in equatorial direction. Particularly in this region, an increased heat exchange between the upper ocean layer and the atmosphere and the mixing of fresh polar with salty North Atlantic water has an effect on the density distribution of the water and thus on the thermohaline circulation. Changes in the northern Nordic Sea's circulation can cause changes to the global and local climate conditions. This motivates the continuous and homogeneous monitoring of geostrophic surface currents by satellite altimetry. However, in polar regions the observation of ocean currents, using for example satellite altimetry, is challenging and limited by difficult observation conditions for example caused, for example, by a rough sea state and sea ice conditions.

In order to overcome these challenges and provide a more comprehensive view on the sea surface circulation, this thesis focuses on developing a method for a homogeneous and gapless representation of geostrophic ocean surface currents by combining along-track satellite altimetry observations from 1995-2012 with simulated water heights referring to a geopotential surface provided by a high-resolution ocean model. The combination differs from conventional assimilating strategies, because it links simulated and observed data at the same processing level, sticking more to the observational part (i.e. altimetry data) and using only the model to bridge periods, where observations are missing or not available.

In order to use satellite altimetry observations in that area, sea ice-dedicated algorithms, such as an unsupervised classification for the reliable detection of open water observations within the sea ice domain and retracking of altimeter radar echoes during open ocean and sea ice conditions, are presented. Moreover, a validation procedure, based on external Synthetic Aperture Radar images and image processing methodologies has been successfully applied and indicates an overall good classification performance. The algorithms are developed for altimeters operating in different observation configurations and can be adapted to all existing satellite altimetry missions.

The combination of the conceptually different data sources is performed in terms of dynamic ocean topography (DOT) elevations. Therefore, a comparison of both quantities has been performed, revealing good agreement in terms of the dominant annual circulation and major variability patterns, and recommends a combination to benefit from

Abstract

the advantages of both datasets. However, limitations regarding the model setup, the profiled altimetry data, for example, in relation to the underlying geoid model have to be considered. Particularly, in the case of the geoid model, a comparison of several marine gravity fields reveals the need for improvement of existing geoid models including the use of an updated gravity database. Moreover, the comparison shows that all investigated marine gravity models suffer from different effects and a direct improvement is not noticeable.

The combination is based on a Principal Component Analysis, merging the 50 major spatial dynamic ocean topography (DOT) variability patterns with the temporal variability of the profiled altimetry-derived DOT heights. The result are daily homogeneous spatio-temporal consistent triangular meshes with a spatial resolution of up to 1 km covering a time span of 17 years.

A short data exploitation shows a slight decreasing velocity trend in northwards flowing warm Atlantic water and a negative correlation of circa 75% to warm and cool sea surface temperature periods, in contrast to the water masses flowing southwards experiencing a positive velocity trend. Furthermore, the combination method enables the detection of different flow branches of major, but also of smaller currents. In particular near the coast of East Greenland, the combination method enables the observation of current patterns, which are covered by sea ice most of the time.

Generally, the innovative combination of along-track altimeter DOT observation and simulated water heights, based on a Principal Component Analysis (PCA) can contribute to a deeper knowledge of the ocean surface circulation in a very climate significant region.

Zusammenfassung

Das nördliche Nordmeer, gelegen zwischen Grönland, Island und Norwegen, stellt eine der wichtigsten Verbindungsrouen zwischen dem Arktischen Ozean und dem Nordatlantik dar. Es ist gekennzeichnet durch starke Wärmeaustauschprozesse zwischen Ozean und Atmosphäre, Süßwassereintrag der anliegenden Gletscher, driftendes Meereis sowie pol- und äquatorwärts strömende Wassermassen. Gerade in dieser Region wirkt sich ein verstärkter Wärmeaustausch zwischen der oberen Ozeanschicht und der Atmosphäre sowie die Vermischung von frischem polarem mit salzigem Nordatlantikwasser auf die Dichteverteilung des Wassers und damit auf die thermohaline Zirkulation aus. Veränderungen in der Ozeanzirkulation des Nordmeeres können sich einerseits auf die lokalen klimatischen Bedingungen auswirken, aber andererseits auch auf die globale Ozeanströmung. Dieser Zusammenhang motiviert die kontinuierliche und lückenlose Beobachtung von geostrophischen Oberflächenströmungen mittels der Satellitenaltimetrie. Jedoch stellt dies in polaren Regionen durch schwierige Beobachtungsbedingungen, verursacht zum Beispiel durch Meereisbedeckung oder rauen Seegang, eine Herausforderung dar.

Um diese Schwierigkeiten zu überwinden und um einen umfassenden Blick auf die Meeresoberflächenzirkulation zu ermöglichen, zielt die Arbeit auf die Entwicklung einer Methode zur homogenen und lückenlosen Darstellung geostrophischer Meeresoberflächenströmungen ab. Dafür werden Beobachtungen der Satellitenaltimetrie zwischen 1995 und 2012 mit simulierten Wasserhöhen von einem hochaufgelösten Ozeanmodell kombiniert. Beide Datenquellen beziehen sich dabei auf eine geopotenzielle Referenzoberfläche. Die Kombination unterscheidet sich von herkömmlichen Assimilationsstrategien in der Hinsicht, dass sie simulierte und beobachtete Daten auf dem gleichen Prozessierungsniveau verbindet, wobei sie sich mehr auf die Beobachtungen der Altimetrie stützt und das Modell zur Füllung oder Überbrückung von Beobachtungslücken verwendet wird.

Um Altimeterbeobachtungen zuverlässig in polaren Gegenden nützen zu können, vor allem in Meereisregionen, werden spezielle Verfahren benötigt. Beispielsweise wird ein Klassifizierungsverfahren entwickelt, welches selbständig und ohne Vorwissen, basierend auf künstlicher Intelligenz, Altimeterbeobachtungen aus offenen Wasserstellen innerhalb des Meereises detektiert. Zusätzlich wird ein speziell entwickelter Ansatz zum Abtasten des Radarsignals und zur Bestimmung des Abstands zwischen Oberfläche und der Flughöhe des Satelliten genutzt. Das sogenannte Retracking-Verfahren ist in der Lage reflektierte Radarechos aus Meereisgebieten und dem offenen Ozean in einem Ansatz abzutasten um den Abstand zwischen Satellit und Erdoberfläche unabhängig von der Oberflächeneigenschaft zu bestimmen.

Zusammenfassung

Der Retracker- sowie Klassifizierungsalgorithmus werden innerhalb der Arbeit vorgestellt. Teil der Klassifizierung ist zusätzlich eine automatische quantitative Validierung, welche auf externen Radarbildern und Methodiken der Bildverarbeitung basiert und eine insgesamt gute Klassifizierungsleistung aufzeigt. Die entwickelten Ansätze sind auf verschiedene Altimeter Beobachtungskonzepte anwendbar und können an alle bestehenden Altimetriemissionen angepasst werden.

Die Kombination der konzeptionell völlig unterschiedlichen Daten erfolgt auf Basis der dynamischen Ozeantopographie (DOT). Dazu wird ein Vergleich beider Datensätze durchgeführt, der eine insgesamt gute Übereinstimmung in Bezug auf jährliche Schwingungen und deren wichtigsten Variabilitätsmuster aufzeigt. Der Vergleich empfiehlt die Kombination, um von den Vorteilen beider Datensätze profitieren zu können. Dennoch müssen Limitierungen bezüglich des Modells und dessen Aufbau sowie der auf den Bodenspuren vorhandenen Altimeterbeobachtungen, zum Beispiel in Bezug auf das verwendete Geoid Modell, berücksichtigt werden. Insbesondere im Falle des Geoidmodells zeigt ein Vergleich mehrerer mariner Schwerefelder die Notwendigkeit zur Verbesserung bestehender Geoidmodelle durch beispielsweise aktualisierte und erweiterte Schwerebeobachtungen. Darüber hinaus zeigt der Vergleich, dass alle untersuchten marinen Schwerefeldmodelle von unterschiedlichen Effekten betroffen sind und eine direkte Verbesserung nicht erkennbar ist.

Im Wesentlichen basiert die Kombination auf einer Hauptkomponentenanalyse, welche die 50 signifikantesten räumlichen Muster, abgeleitet aus dem Modell, mit der zeitlichen Variation der Altimeter abgeleiteten DOT Höhen verbindet. Das Ergebnis ist ein 17 Jahre umfassender, täglicher, räumlich-zeitlich konsistenter Datensatz auf Basis eines dreiecksvermaschten Gitters mit einer räumlichen Auflösung von bis zu 1 km.

Eine Datenauswertung zeigt einen leicht abnehmenden Geschwindigkeitstrend im polwärts fließenden warmen Atlantikwasser und eine negative Korrelation von ca. 75% zu warmen und kühlen Perioden der Ozeanoberflächentemperatur. Im Gegensatz zu den äquatorial strömenden Wassermassen, welche einen ansteigenden Geschwindigkeitstrend aufweisen. Darüber hinaus ermöglicht die Kombination die Erfassung verschiedener Strömungsäste größerer, aber auch kleinerer Strömungen. Insbesondere in der Nähe der ostgrönländischen Küste zeigen sich durch die Kombination Strömungsmuster, welche hauptsächlich von Meereis bedeckt sind.

Zusammenfassend kann die vorgestellte neuartige Kombination aus Altimeter Beobachtungen und simulierten Wasserhöhen, unter zentraler Verwendung der Hauptkomponentenanalyse zu einem tieferen Verständnis der Ozeanoberflächenzirkulation in einer für das regionale aber auch globale Klima relevanten Region beitragen.

Contents

Abstract	iii
Zusammenfassung	v
Contents	vii
1 Introduction	1
1.1 Background and Motivation	1
1.2 Research Goals	3
1.3 Ocean currents in the northern Nordic Seas	3
1.4 Thesis outline	5
2 Satellite altimetry in the northern Nordic Seas	9
2.1 Altimetry missions in the northern Nordic Seas	9
2.2 Radar altimetry - from the observed radar signal to geostrophic surface currents	11
2.2.1 From the observed radar signal to sea surface heights	11
2.2.2 From sea surface heights to geostrophic currents	14
2.3 Challenges of monitoring geostrophic surface currents by radar altimetry .	16
2.3.1 Retracking radar waveforms in the vicinity of rough sea states and sea ice conditions	16
2.3.2 Artificial intelligence for radar waveform classification	18
2.3.3 Validation of classification by SAR images and image processing techniques	20
2.3.4 Geoid models in the northern Nordic Seas	21

CONTENTS

3	Combination of altimetry observations with ocean modeling data	25
3.1	The Finite Element Sea Ice Ocean Model (FESOM)	25
3.2	Comparison of the dynamic ocean topography from altimetry and FESOM	27
3.3	Geostrophic currents from a combination of altimetry and FESOM	28
4	Scientific exploitation of the dataset	31
5	Conclusions and outlook	41
	Abbreviations	48
	List of Figures	49
	Bibliography	53
	Acknowledgements	63
	Scientific environment	65
A	Appendices	67
A.1	Publications	67
P-1.1	Monitoring the arctic seas: How satellite altimetry can be used to detect open water in sea-ice regions	68
P-1.2	Lead detection using cryosat-2 delay-doppler processing and sentinel- 1 sar images	90
P-2	Dynamic ocean topography of the northern nordic seas: a comparison between satellite altimetry and ocean modeling	108
P-3	Geostrophic currents in the northern nordic seas from a combination of multi-mission satellite altimetry and ocean modeling	126
	Co-authored publications	145
A.2	Supplementary material	146

1 Introduction

1.1 Background and Motivation

The West Spitsbergen Current (WSC) and East Greenland Current (EGC) are the most important transport routes of warm and saline water masses from the northern Atlantic Ocean in the Arctic Ocean and vice versa of cold and fresh polar water to the northern Atlantic Ocean. Both current systems cross the northern Nordic Seas are characterized by a total water volume transport of about 8 Sv - 10 Sv ($1 \text{ Sv} = 10^6 \frac{\text{m}^3}{\text{s}}$) in both directions at the Fram Strait region (Blindheim and Østerhus (2013), Rudels (2012)) and play a significant part of global circulation.

The ocean surface circulation in polar regions is affected by local winds, the sea ice drift causing drag effects and density differences as well as strong horizontal salinity gradients at the water surface due to inhomogeneous distribution of freshwater (Armitage et al. (2017)). In particular, strong differences in the horizontal pressure gradient cause accelerations in the geostrophic surface flow. Especially in the last decades, changes in the surface circulation, due to an increased inflow of warm Atlantic water to the Arctic Ocean, in connection with an enhanced mass loss of the Greenland ice sheet and a thinning of the sea ice coverage, can be observed (e.g. Kwok et al. (2009), Holliday et al. (2008), Church et al. (2004)).

Most of these studies are based on water flow simulations from dedicated ocean current models or observations from in situ systems measuring the velocity and flow direction at certain geographic locations. However, the latter are not able to provide spatially homogeneous distributed ocean current observations for a longer time period due to a sparse availability and irregular spatial distribution.

Ocean current models provide a large number of different spatio-temporal homogeneously distributed ocean current parameters. They enable detailed studies of individual components that contribute to the surface flow. However, they are limited to predefined mathematical equations and boundary conditions that only approximate the true state of the ocean circulation. Furthermore, ocean models are dependent on their forcing data, which significantly impact the level of detail and resolution of the simulation.

Even with the usage of space-based remote sensing techniques, a complete and direct observation of the geostrophic surface current components without applying further interpolation and transformation routines is not possible. Moreover, spaceborne observation techniques cannot provide direct measurements of geostrophic surface currents,

1 Introduction

since they can only observe physical and geometrical height differences, which, however, enable the determination of the dynamic ocean topography (DOT). The DOT is the difference between the sea surface height (SSH) and the geoid, which deviates up to 2 meters in amplitude, caused by hydrodynamic processes (e.g. water density and mass variations). The DOT provides information about the oceanic mass and heat transport. Geostrophic current components are derived by applying the geostrophic equations directly to the DOT heights. The DOT can be determined by using time-variable gravity field observations of the Gravity Recovery And Climate Experiment (GRACE) mission, for example. However, this only captures the variability of the water mass and neglects steric effects. In order to provide the full DOT information, steric height variations, for example observed by in situ buoys measuring temperature and salinity profiles from different ocean depths must be added. In contrast, satellite altimetry enables the geometrical determination of the full DOT by subtracting a geoid from observed SSHs.

Since the early 90s, satellite altimeters have provided profiled SSH elevations up to the high latitudes. However, satellite altimetry missions are placed on a fixed orbit configuration causing fixed revisit times and ground track patterns, thus limiting spatio-temporal comprehensive investigations of the surface circulation. In addition, altimetry SSH observations are usually limited to open ocean conditions, which lead to data gaps and irregular data sampling during sea ice conditions, since it is not possible to look through or under the ice layer. Nevertheless, the sea ice cover is not a uniform surface, but is interrupted by narrow elongated cracks (i.e. leads) and circular water openings (i.e. polynya) that allow a view of the sea level within the sea ice domain. Moreover, leads and polynyas have a significant contribution to ocean-atmosphere interaction, since they allow a barrier-free exchange of heat between the ocean and the atmosphere (e.g. Persson and Vihma (2016)). However, these small water openings within the ice are dynamically changing its shape, location and size due to ocean currents, rapidly changing air temperatures and local wind conditions. Their size can range from several meters to kilometers. Due to the shielding of the open ocean by the surrounding ice cover, the sea state conditions within these areas are calm, showing nearly no wave movements.

In connection with the global climate relevant importance of the northern Nordic Sea, the main motivation of the thesis has been to perform deep and comprehensive investigations of the geostrophic ocean surface currents in polar regions, strongly influenced by sea ice and harsh environmental conditions, through a combination of observational and simulated data, by benefiting from both data sources. The study aims at a combination more from an observational perspective, using model data, when observations are not available. It is not the object to improve existing ocean models by assimilating observational data. Instead the study focuses more on a linkage of datasets at the same data processing level. The combination is done based on the dynamic ocean topography and aims at the creation of a novel dataset providing a comprehensive description of the temporal evolution of geostrophic ocean surface currents in the northern Nordic Seas. The major output of the work consists of combined, time-variable geostrophic ocean current components and DOT maps featuring a high spatio-temporal resolution.

1.2 Research Goals

In connection with the given motivation, the thesis addresses four key questions:

- **How can altimetry sea surface height observations from open water bodies within the sea ice domain be identified and how can this be validated?**
- **How do simulated and observed dynamic ocean topography data differ and what should be considered when combining them?**
- **How does the combination work and how can it be validated?**
- **What can be learned from the combination dataset about the temporal variation of the surface currents in the northern Nordic Seas and what should be done in future studies to improve the results?**

The questions are answered below. The first three questions refer to the four publications this thesis is based on. The last question is addressed in a data exploitation (see Sec. 4). At first, an overview about the investigation area, in particular of the ocean circulation in the northern Nordic Seas, is given.

1.3 Ocean currents in the northern Nordic Seas

The northern Nordic Seas comprise the Greenland Sea in the center, the Barents Sea in the east, the Fram Strait in the north and is limited by the northeast coast of Greenland in the west. Southern parts adjoin the Norwegian Sea and the Denmark Strait. Transferred to geographic coordinates, the investigation area is defined by 72°N to 82°N and -30°W to 30°E (Figure 1.1) and belongs to the Arctic peripheral seas. The northern Nordic Seas are characterized by complex bathymetric structures, steep slopes, depths of up to 5600 m and shallow water as well as large shelf regions. The ocean bottom topography has a significant influence on the ocean currents in this region, which can be observed by the pathway of the WSC near the shelf edge of the Barents Sea (Koszalka et al. (2011), Orvik and Niiler (2002)).

The northern Nordic Seas depict the most important water mass exchange area between the Arctic Ocean and the North Atlantic (Blindheim and Østerhus (2013)). Warm Atlantic Water, coming from the Gulf Stream is carried by the Norwegian Atlantic Current and further northwards by the WSC through the Fram Strait via the Yermak and Svalbard branches into the Arctic Ocean (total transport circa 7 Sv, Rudels (2012)). Along the way, the warm Atlantic Water ($6-8^{\circ}\text{C}$) cools down and interacts with cold air masses, causing strong heat fluxes to the atmosphere (Brambilla et al. (2008)). This ocean-atmosphere interaction, stronger in the winter season (von Appen et al. (2016)), contributes significantly to the air temperature in northwestern Europe during winter

1 Introduction

(e.g. Rhines et al. (2008)). However, not all Atlantic Water enters the Arctic Ocean; nearly 45% (e.g. Teigen et al. (2011), de Steur et al. (2014)) recirculates and flows southwards mixing with the cold and less saline EGC.

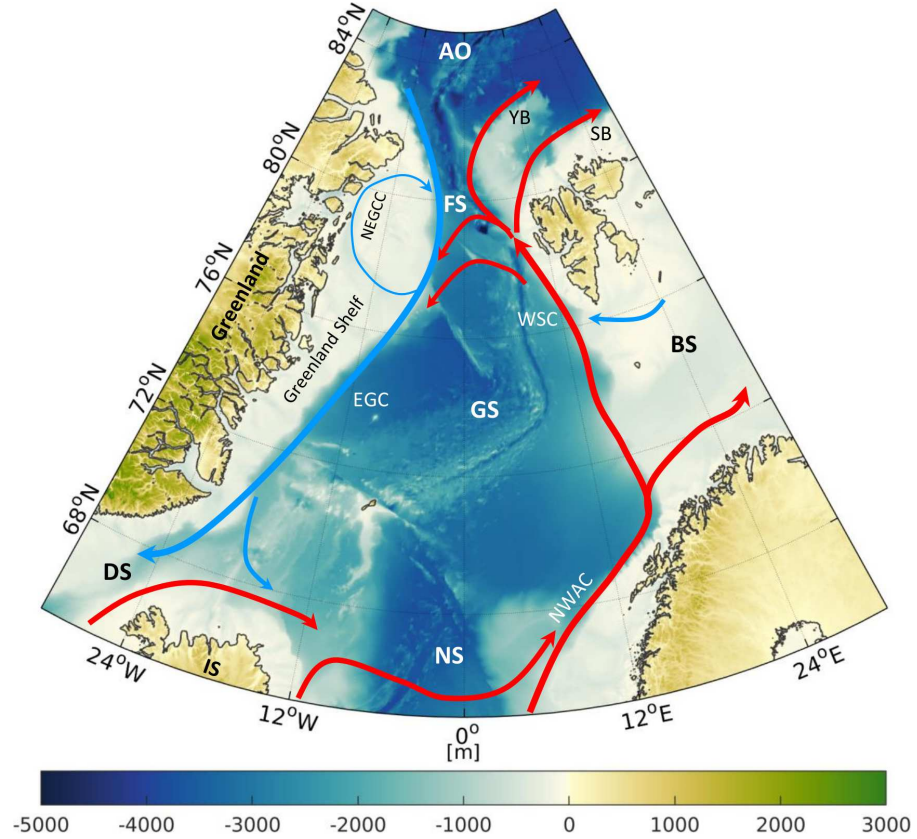


Figure 1.1: Topography based on Refined Topography-2 (RTopo2) model (Schaffer et al. (2016)) and major surface flow of the northern Nordic Seas including the Greenland Sea (GS), Barents Sea (BS), and Fram Strait (FS). The Arctic Ocean (AO), Denmark Strait (DS) and Norwegian Sea (NS) mark adjacent seas. Red arrows indicate inflowing Atlantic Water (West Spitsbergen Current, WSC; Yermak Branch, YB; Svalbard Branch, SB and Norwegian Atlantic Current, NWAC). Outflowing Polar Water is highlighted in blue (East Greenland Current, EGC; North-East Greenland Coastal Current, NEGCC). Thinner lines indicate subordinated currents.

Polar Water from the Arctic Ocean is transported southwards by the EGC along the eastern coast of Greenland through the western Fram Strait and Greenland Sea, where it merges with recirculating warm and saline Atlantic Water and inflowing freshwater from the outlet glaciers along the east coast of Greenland. The EGC shows different vertical layers with the less dense freshwater at the upper layer, the Atlantic Water in the intermediate depths and dense polar water in the deepest regions. This layer distribution does not remain stable along the EGC pathway (Håvik et al. (2017)). The

EGC represents the most important freshwater route, with a total transport volume of about 9 Sv, between the Arctic Ocean and the North Atlantic (e.g. de Steur et al. (2014), Woodgate et al. (1999)).

The exchange of warm saline Atlantic Water with fresh Polar Water in the northern Nordic Seas plays an important role in the Atlantic and the global thermohaline circulation (Talley (2008), Langehaug et al. (2016)). Furthermore, the Fram Strait is the main gate for the sea ice export from the Arctic Ocean. Nearly 90 % of the Arctic sea ice is exported via the EGC through the Fram Strait (Rudels et al. (1999)). The sea ice cover prevents the ocean from losing heat by forming a kind of insulation. However in recent years, the sea ice volume, thickness and coverage have been dramatically decreasing, leading to an enhanced ocean heat loss and changed circulation conditions (e.g. Selyuzhenok et al. (2020), Armitage et al. (2017), Kwok et al. (2009)).

1.4 Thesis outline

This thesis is based on four publications covering the three main research topics, (1) the reliable exploitation of along-track altimetry observations within the sea ice zone including a validation process based on image processing methods (i.e. P-1.1, P-1.2), (2) the determination of profiled DOT heights and a comprehensive comparison of them with simulated water heights (i.e. P-2), and (3) the generation of an improved representation of geostrophic ocean currents in the northern Nordic Seas (i.e. P-3):

P-1.1 Müller, F. L., Dettmering, D., Bosch, W., and Seitz, F. (2017). Monitoring the arctic seas: How satellite altimetry can be used to detect open water in sea-ice regions. *Remote Sensing*, 9(6), ISSN: 2072-4292, DOI: 10.3390/rs9060551

P-1.2 Passaro, M., Müller, F. L., and Dettmering, D. (2018b). Lead detection using cryosat-2 delay-doppler processing and sentinel-1 sar images. *Advances in Space Research*, 62(6):1610 – 1625, ISSN: 0273-1177, DOI: 10.1016/j.asr.2017.07.011

P-2 Müller, F. L., Wekerle, C., Dettmering, D., Passaro, M., Bosch, W., and Seitz, F. (2019b). Dynamic ocean topography of the northern nordic seas: a comparison between satellite altimetry and ocean modeling. *The Cryosphere*, 13(2):611–626, DOI: 10.5194/tc-13-611-2019

P-3 Müller, F. L., Dettmering, D., Wekerle, C., Schwatke, C., Passaro, M., Bosch, W., and Seitz, F. (2019a). Geostrophic currents in the northern nordic seas from a combination of multi-mission satellite altimetry and ocean modeling. *Earth System Science Data*, 11(4):1765–1781, DOI: 10.5194/essd-11-1765-2019

Figure 1.2 arranges the four publications and gives an overview of the logical order of the studies. All investigations and studies are conducted in the northern Nordic Seas. The thesis is divided into an observational part at the beginning (see Sec. 2) only referred to satellite altimetry and data processing, followed by an assessment section, evaluating

1 Introduction

the combination of simulated and observational data, completed by the combination approach (see Sec. 3). The thesis closes with an exploitation of the obtained results and final remarks.

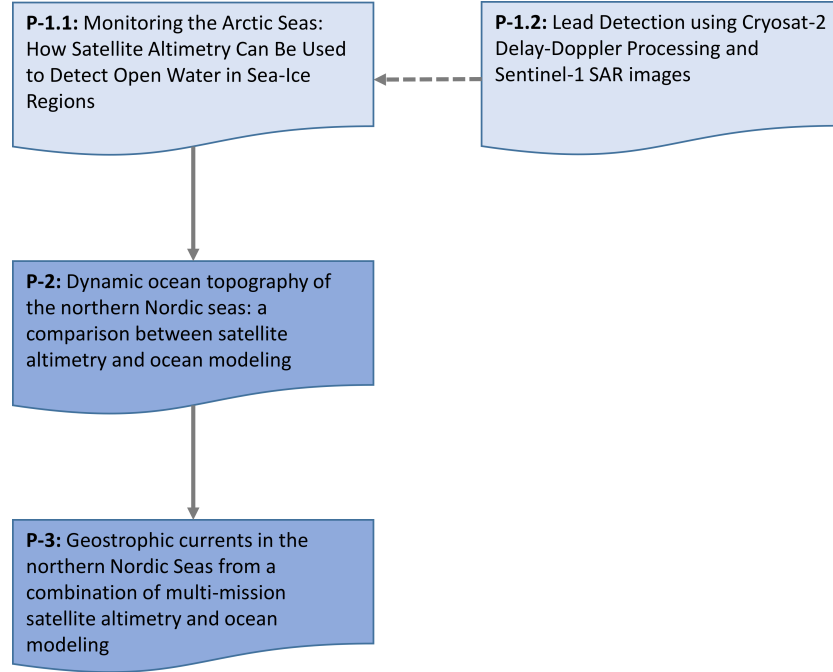


Figure 1.2: Connection of the four publications, which set the frame for this thesis. Light blue indicates investigations based on observational datasets only, blue the usage of both, simulations and observations. The arrows outline results and obtained knowledge that are transferred between the publications.

After introducing satellite altimetry missions observing north polar oceans in Section 2.1, the basic measurement principle of satellite altimetry and the concept of deriving geostrophic currents are explained in Section 2.2. Challenges related to the computation of geostrophic currents are described in Section 2.3. In particular, problem areas due to the complex observation environment, but also due to irregularities of the used gravity field data, are described. Section 2.3 starts with a comparison and assessment of different marine gravity fields followed by the description of a retracking algorithm developed for open ocean and sea ice conditions and an unsupervised classification method in order to assign altimeter radar echoes to open-water or sea ice conditions. The classification method developed in P-1.1 is applied to radar echoes (i.e. waveform) of the K_u -band operating European Space Agency (ESA) Environmental Satellite (Envisat) and Centre National d' Études Spatiales (CNES)/Indian Space Research Organisation (ISRO) satellite mission, Satellite with Argos and AltiKa (SARAL) working in K_a -band. Moreover, the developed classification strategy is applied to the ESA mission, European Remote Sensing Satellite-2 (ERS-2) and used in P-3.

The algorithm applied is based on the idea of an unsupervised waveform assignment requiring the application of artificial intelligence techniques such as partitional clustering (e.g. K-medoids). The classification approach is evaluated by an automatic and quantitative validation process comparing classified altimeter observations with Synthetic Aperture Radar (SAR) images of RADARSAT-2 (Japan Aerospace Exploration Agency (JAXA)/Mac Donald, Dettwiler and Associates Ltd. (MDA)), JAXA Advanced Land Observing Satellite (ALOS) and ESA/Copernicus mission Sentinel-1A by using image processing techniques. The validation approach is explained in P-1.2.

After cleaning up the altimeter database from measurements affected by sea ice, a transformation to DOT heights is performed, aiming at a comparison between the observational and model database. The comparison, examined in P-2, is based on Envisat observations and water heights of the Finite Element Sea Ice Ocean Model (FESOM). Therefore, Subsection 3.1 gives a brief introduction to the key aspects of ocean current model FESOM.

Finally, after analyzing both datasets, P-3 describes the combination and the generation of a combined DOT and geostrophic surface current dataset. The combination approach is mainly focused on a Principal Component Analysis (PCA), a method which is often applied to data reduction of multivariate timeseries data and commonly used for sea level reconstruction, mapping the sea level before spaceborne remote sensing techniques are launched (e.g. Church et al. (2004)).

The thesis closes with a brief data exploitation (Sec. 4) highlighting the potential of the combined surface currents and concluding remarks as well as an outlook pointing out to further future improvements in Section 5.

2 Satellite altimetry in the northern Nordic Seas

This chapter provides an introduction to the different radar satellite altimetry missions covering the northern Nordic Seas and gives an overview about the basic observation principle. The description of the satellite altimetry missions and observation principle is limited to the satellite altimetry missions, which are used in the investigation.

In addition, more detailed information on the derivation of geostrophic surface currents from sea surface height and connected challenges in the polar regions are presented. In particular, Chapter 2 addresses issues to derive reliable sea surface height observations in regions, which are affected by sea ice coverage and rapid changing environmental sea state conditions. A novel classification algorithm is introduced, which enables an unsupervised assignment (i.e. without the usage of pre-known training data) of radar echoes to open-water or sea ice conditions. Moreover, a quantitative and automatic validation process based on external SAR images is performed to evaluate the classification performance. Chapter 2 includes the results and investigations of P-1.1 and P-1.2.

2.1 Altimetry missions in the northern Nordic Seas

Satellite radar altimeters were designed primarily for the consistent monitoring of the global sea level, including the northern polar regions, which have been covered by various satellite altimetry missions since the early nineties. Between 1991 and 2012, radar altimeters mounted on ESA missions, European Remote Sensing Satellite-1 (ERS-1), ERS-2 and Envisat and from 2013 CNES/ISRO mission SARAL provide sea surface height information in polar regions until a latitudinal limit of 81.5°N .

One of the first altimeters was mounted on ERS-1, which observed the northern Nordic Seas between 1991 and early 2000. The successor mission ERS-2 was launched in 1995 and provided range measurements until 2003. Moreover, ERS-2 was placed on a repeat-orbit configuration, which means that the satellite is repeating its ground track after a certain time. In the case of ERS-2, this revisit time is set to 35 days. Unfortunately, after June 2003, a failure in the data storage management led to data gaps. ERS-2 was deorbited in 2011.

In 2002, Envisat was placed into the same orbit and continued data acquisition. In October 2010, Envisat left its nominal mission phase and was relocated on a drifting orbit

configuration, which means that the satellite is not able to retain its fix defined orbit and starts drifting. This may be due to instrument failures or the satellite has been deliberately placed in a drifting orbit for various reasons (e.g. changed observation strategy). In the case of Envisat, declining fuel reserves led to a change of orbit that allows an extended mission phase (i.e. Envisat-EM). Due to an unexpected communication loss, Envisat was decommissioned in May 2012.

10 months later, SARAL was brought at the same orbit of ERS-2 and Envisat, continuing sea surface monitoring until July 2016. Due to an issue in the steering wheels of SARAL, the satellite had to leave its nominal mission phase entering a drifting orbit. In contrast to the in K_u -band (13.6 GHz) working ESA missions, SARAL operates in K_a -band (35.75 GHz) showing a smaller footprint (i.e. by the radar altimeter illuminated area at the surface) up to 8 km (Bronner et al., 2016) versus 10 km of Envisat (Connor et al., 2009). Beside the footprint, further instrumental modifications led to an increased observation sampling rate of 40 Hz (175 m observation spacing on Earth) instead of 18 Hz (circa 400 m observation spacing on Earth) in the case of the ESA missions.

Figure 2.1 displays the temporal coverage of all satellite altimeter missions used in this thesis. All missions are on the same 35-day repeat-orbit configuration, except the extended mission phase of Envisat, which is characterized by drifting ground track patterns with revisit times of nearly 30 days. Further satellite altimetry missions, for example CNES/National Aeronautics and Space Administration (NASA) missions Jason-1, Jason-2 or Jason-3, are not used because they do not reach the northern Nordic Seas, due to different orbit characteristics. Other missions reaching the northern Nordic Seas such as the drifting phase of SARAL, ESA/Copernicus satellites Sentinel-3A and B, launched in 2016 and 2018 and Ice, Clouds, and Land Elevation Satellite (ICESat) as well as Ice, Clouds, and Land Elevation Satellite-2 (ICESat-2) operated by the NASA are not part of the investigation, since they do not cover the study period ranging from 1995 to 2012 and are characterized by a significantly changed observation as well as instrumental strategy (i.e. laser altimetry). ERS-1 and ESA Earth Explorer Opportunity Mission-2, CryoSat-2 are not part of the investigations, the first due to low quality of the radar echoes resulting in a reduced accuracy and the latter due to not yet adapted algorithms, considering the observation methodology of SAR altimetry. In Appendix, Figure A.1 provides an overview about the orbit configuration of the used ESA missions and SARAL and shows the limited spatial coverage of the CNES/NASA missions. Table A.1 summarizes key aspects of the used altimetry missions.

The thesis refers to K_u -band altimeters between 1995 and 2012 and includes additionally K_a -band observations between 2013 and 2016. Due to a different radar band, SARAL and Envisat radar observations are used to develop and test the unsupervised classification algorithm in publication P-1.1. However, SARAL as well as the drifting phase of SARAL are not part of P-3 due to a time gap between the end of Envisat and the launch of SARAL. Considering feasible measurements of Envisat and the temporal availability of the ocean current model (i.e. FESOM), the comparison of altimetry-derived dynamic ocean topography (DOT) heights and simulated differential water height (DWH) in P-2

2.2 Radar altimetry - from the observed radar signal to geostrophic surface currents

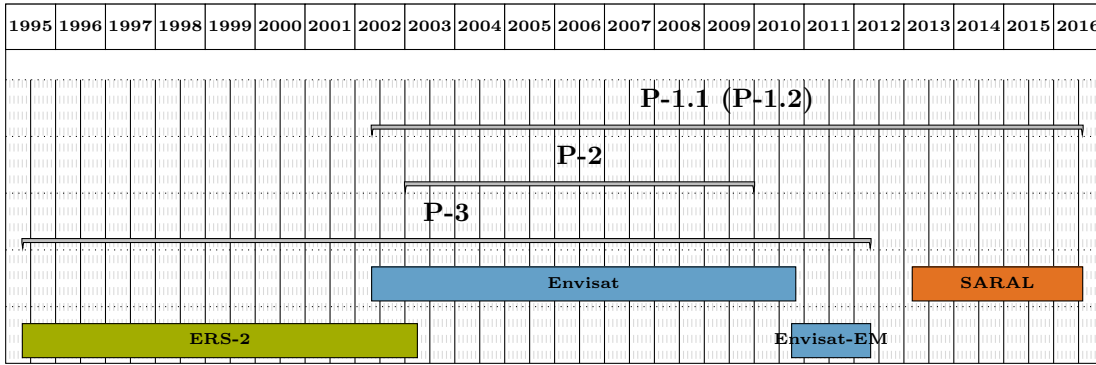


Figure 2.1: Timeline of radar altimetry missions included in the thesis and their application in each publication.

is limited to 2003-2009. On the other hand, ERS-2 and Envisat observations are included in the combination approach, described in P-3 enabling the generation of a combined DOT and geostrophic surface current dataset covering a time span of 17 years.

2.2 Radar altimetry - from the observed radar signal to geostrophic surface currents

2.2.1 From the observed radar signal to sea surface heights

Generally, all satellite altimeters orbiting the Earth measure the distance (i.e. range) between the satellite and the surface of Earth. Figure 2.2 shows on the left side the observing principle and on the right the geometrical linkage to different reference surfaces.

In order to observe the distance between the radar altimeter and the surface, the antenna emits short sequences of electromagnetic pulses in nadir direction to the ground level. The radar pulses hit the surface, illuminate a circular region (i.e footprint) and are reflected back to the satellite, where they are recorded by the on-board receiver. In the case of pulse-limited altimeters, the illuminated area during a measurement is set by the length of the emitted radar pulse, but can vary dependent on the roughness of the surface and instrumental adjustments (Vignudelli et al. (2019)).

Each registered radar echo is sampled and divided into pre-defined time windows (i.e. range bins), defining the altimeter waveform. For example, in the case of Envisat, each range bin corresponds to a time interval (t) of about 3.125 ns (Vignudelli et al. (2011)), which can be converted to a height of 46.84 cm by multiplying t by the speed of light and divide it by 2 considering a one-way measurement. The length of the waveform is dependent on instrumental characteristics and can vary between 64 and 128 bins, which refer in the case of Envisat to a window of circa 60 m. Due to changing surface

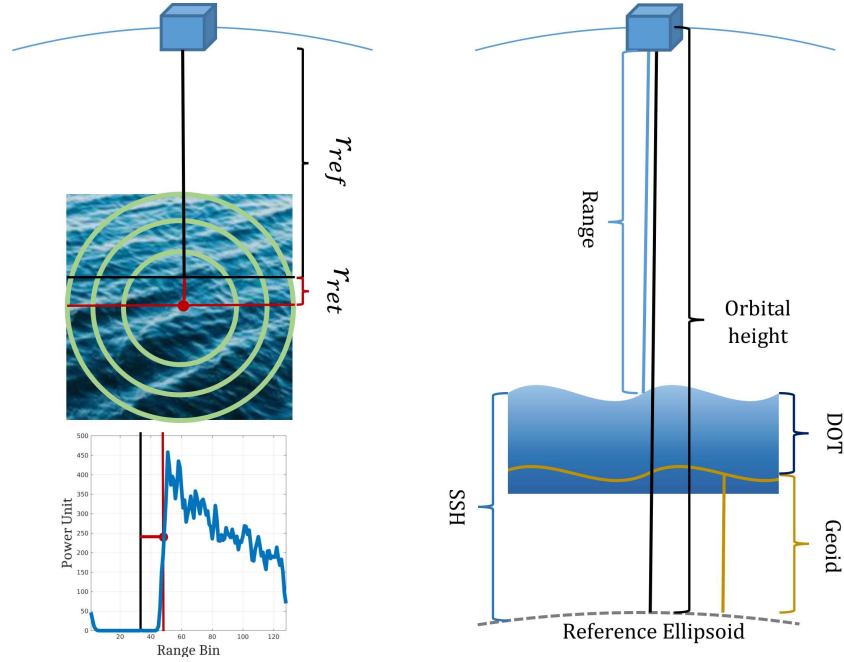


Figure 2.2: Observation (left) and geometric (right) principle of satellite altimetry. The left side shows in an exemplary way an Envisat waveform during normal open ocean conditions. The retracted range (r_{ret}) and the epoch are shown in red, the reference range (r_{ref}) in black. Circles indicate the propagation direction of the radar signals hitting the surface. The right side displays the relationship between range, orbital height, sea surface height, geoid and dynamic ocean topography.

conditions caused by various sea states, for example, the waveform shape can vary. Smooth surface conditions result in very narrow and peaky waveforms in contrast to open ocean conditions leading to broader waveform types. Each waveform provides information about the nature of the reflective surface and backscattered energy.

In order to obtain a high observation accuracy, so-called retracking algorithms such as the Adaptive Leading Edge Subwaveform+ (ALES+) retracker (Passaro et al. (2018a)) or threshold based approaches (e.g. Davis (1997)) are designed to find the most likely point at the surface level (i.e. epoch) by sampling waveforms using physical or mathematical, numerical models. The obtained range within this 60 m interval is labeled as retracking range (r_{ret}). The full range between the satellite and the Earth's topography is estimated by adding the reference range (r_{ref}) to r_{ret} . The reference range depends on the Earth's topography and is steadily adapted by the on-board processing system.

For many applications, the sea surface height, which means the distance between the water surface and the reference ellipsoid, is required. Therefore, the satellite's altitude above the reference ellipsoid (H_{sat}) is provided by precisely determined orbit parameters, based on space-geodetic observations such as Satellite Laser Ranging (SLR), Doppler Orbitography and Radiopositioning Integrated by Satellite (DORIS) and Global Navigation

2.2 Radar altimetry - from the observed radar signal to geostrophic surface currents

Satellite System (GNSS) observations. SSHs are then obtained by subtracting the range (R) from H_{sat} , referred to the center of mass of the satellite. Equation 2.1 shows this relationship:

$$SSH = H_{sat} - R \quad (2.1)$$

In order to provide meaningful SSHs, altimeter range observations need to be corrected for geophysical influences, path delays caused by the atmosphere and for effects of the illuminated surface, which expands Equation 2.1 to:

$$SSH = H_{sat} - (R + \sum R_{atm} + \sum R_{geo} + \sum R_{surf} + \sum R_{instr}) \quad (2.2)$$

The following paragraph lists all effects and magnitudes, described in Rosmorduc et al. (2018).

$\sum R_{atm}$ includes atmospheric path delays caused by the ionosphere and troposphere affecting the radar signal directly. The ionosphere causes an attenuation of the radar signal, due to the atmosphere's electronic content. In order to account for ionospheric path delays, a correction is applied to the altimeter range, gathered from models or two-frequency altimeters. The magnitude of the correction ranges between 0 m and 0.5 m.

Effects caused by the troposphere are divided into a dry proportion, accounting for dry gases (e.g. oxygen, nitrogen) and a wet part consisting of water vapor and liquid water in the atmosphere. The correction for the dry proportion is generally taken from models, in the case of the wet part, the correction is obtained from models, but can also directly be observed by a microwave radiometer. The magnitude of the correction varies between 0 m and 0.5 m for the wet part and is about 2.3 m for the dry troposphere.

$\sum R_{geo}$ indicates geophysical effects, which are not acting on the radar signal directly, but have to be reduced in order to observe the sea level properly. The biggest amount of the geophysical influences is induced by the attraction of the Sun and Moon. Ocean, solid earth, pole tides and tidal loading effects can cause sea level height variations up to 15-20 m, in total. Moreover, atmospheric loading and wind forcing effects are considered by the inverse barometric correction and high resolution barometric models. The combination of air pressure changes at a low frequency and impacts due to wind forcing at high frequencies is summarized as dynamic atmosphere correction, which features a magnitude of about 0.15 m.

$\sum R_{surf}$ is referred to the surface on which a radar signal is reflected. In this category, the biggest error budget (circa 50 cm) on range observations is caused by the electromagnetic bias or sea state bias. The sea state bias correction compensates amplification and damping effects in the backscattered power of the returning radar echo reflected by ocean wave troughs and crests. It is mainly estimated by empirical approaches modeling the relationship between wave height and wind speed (Tran et al. (2010)).

2 Satellite altimetry in the northern Nordic Seas

$\sum R_{instr}$ substitutes corrections, which are applied due to biases or drifts within the instrument and the radar signal processing chain. For example, biases (e.g. time tag) can occur due to drifting effects of the Ultra-Stable Oscillator (USO), which defines the exact time a radar pulse is emitted. The order of magnitude R_{instr} is about 0.01 m.

Besides, pulse-limited satellite altimetry missions, so-called SAR or Delay-Doppler (DD) altimeters (e.g. CryoSat-2), provide SSH information. The main difference to pulse-limited altimetry lies in the on-board processing of the incoming radar echoes because the Doppler bandwidth is fully exploited. DD altimeters record reflected radar signals of an illuminated area as long it is visible (e.g. Raney (1998)). This improves the signal-to-noise ratio and leads to higher range accuracy up to a factor of 2 (Phalippou and Enjolras (2007)). However, due to this changed observation strategy, the waveforms are characterized by a different shape and power properties resulting in an necessary adaption of the retracking algorithm, which is not part of the current study.

2.2.2 From sea surface heights to geostrophic currents

Satellite altimetry enables the study of the geostrophic component of the major ocean currents. In order to derive surface ocean currents from altimetry observations, the deviation of the sea surface with respect to a geoid, called the dynamic ocean topography, needs to be computed. The geoid is defined as an equipotential surface of the Earth's gravity field depending on the mass distribution and the angular velocity of the Earth. It approximates very closely the mean sea surface. However, hydrodynamic processes due to changes in salinity and temperature cause deflections of up to 2 m in amplitude, which define the DOT. According to ocean surface currents, the slopes of the DOT in connection with the Coriolis force are used to derive the velocity and direction of the geostrophic currents. In particular, DOT heights are estimated by subtracting geoid elevations (N) above the reference ellipsoid from SSHs. Equation 2.3 illustrates the functional relation:

$$DOT = H_{sat} - (R + \sum R_{atm} + \sum R_{geo} + \sum R_{surf} + \sum R_{instr}) - N \quad (2.3)$$

Geostrophic currents represent horizontal surface movements of water particles, which result from the balance between the horizontal pressure gradients and the Coriolis force. These horizontal pressure gradients are proportional to the sea level slope (e.g. Stewart (2009)). Elevation differences in the sea surface cause an acceleration to the water masses. The so-called geostrophic flow explains major ocean current patterns (e.g. Gulf Stream) on the rotating Earth, without the influences of wind- or wave-induced current motions (i.e. a-geostrophic currents).

In order to explain the geostrophic flow, the full momentum equation (Navier-Stokes Equation) of a liquid mass, in Cartesian coordinates (x,y,z) and with velocity vector $\mathbf{v}(u,v,w)$ is shown in Equation 2.4. The equation describes the change of momentum by

2.2 Radar altimetry - from the observed radar signal to geostrophic surface currents

applied forces (e.g. Coriolis force, gravity, friction), which act on liquids with constant mass.

$$\begin{aligned}
 \frac{\partial u}{\partial t} + u \frac{\partial u}{\partial x} + v \frac{\partial u}{\partial y} + w \frac{\partial u}{\partial z} &= -\frac{1}{\rho} \frac{\partial p}{\partial x} + 2\Omega v \sin \varphi + F_x \\
 \frac{\partial v}{\partial t} + u \frac{\partial v}{\partial x} + v \frac{\partial v}{\partial y} + w \frac{\partial v}{\partial z} &= -\frac{1}{\rho} \frac{\partial p}{\partial y} - 2\Omega u \sin \varphi + F_y \\
 \frac{\partial w}{\partial t} + u \frac{\partial w}{\partial x} + v \frac{\partial w}{\partial y} + w \frac{\partial w}{\partial z} &= -\frac{1}{\rho} \frac{\partial p}{\partial z} + 2\Omega u \cos \varphi - g + F_z
 \end{aligned} \tag{2.4}$$

where, $\frac{1}{\rho} \nabla p$ is the pressure gradient, related to the density ρ , the friction $F_{x,y,z}$ and the Coriolis term $2\Omega \times \mathbf{v}$ with the Earth angular velocity Ω . The gravity acceleration is substituted by g and the time by t .

Assuming a stationary ocean ($u = v = w = 0$) with no change of momentum and no friction of the water particles, the horizontal momentum equations are 0, while the vertical component is dependent on g at a certain latitude (ϕ) and depth level (Stewart (2009)):

$$\frac{1}{\rho} \frac{\partial p}{\partial x} = 0; \quad \frac{1}{\rho} \frac{\partial p}{\partial y} = 0; \quad \frac{1}{\rho} \frac{\partial p}{\partial z} = -g(\phi, z) \tag{2.5}$$

where $\frac{\partial p}{\partial x}, \frac{\partial p}{\partial y}$ represent the horizontal and $\frac{\partial p}{\partial z}$ the vertical pressure gradients. Equation 2.5 represents the hydrostatic equilibrium. Adding the Earth's rotation, the water particles, which are flowing from high to low pressure, are deflected by the Coriolis force. The water particles are deflected to the right on the Northern Hemisphere and to the left on the Southern Hemisphere. This phenomenon describes the geostrophic balance, which is the balance of the Coriolis force and the pressure gradients. By assuming that the horizontal velocities are much larger than the vertical (i.e. $w \ll u, v$) ones and g is only an external force, the momentum equations are transformed to (Stewart (2009)) :

$$\frac{1}{f\rho} \frac{\partial p}{\partial x} = v; \quad -\frac{1}{f\rho} \frac{\partial p}{\partial y} = u; \quad \frac{1}{\rho} \frac{\partial p}{\partial z} = -g \tag{2.6}$$

The Coriolis force, dependent on ϕ and Ω , is substituted by $f = 2\Omega \sin(\phi)$. v and u are the geostrophic velocity components in meridional and zonal flow direction. Please note, $z = 0$ in order to compute the geostrophic motion at the sea surface.

Applying the relationship between SSH differences and the horizontal pressure gradients (see Stewart (2009)) and only referring to the horizontal movements, Equation 2.6 can be transferred to:

$$\frac{g}{f} \frac{\partial h}{\partial x} = v \quad - \frac{g}{f} \frac{\partial h}{\partial y} = u \quad (2.7)$$

where, $\frac{\partial h}{\partial x}, \frac{\partial h}{\partial y}$ are now describing the slope of the DOT in x and y direction. u, v are substituting the geostrophic velocity components at the surface, which can be derived from satellite altimetry-derived DOT observations.

2.3 Challenges of monitoring geostrophic surface currents by radar altimetry

The derivation of meaningful altimetry-based geostrophic surface currents is strongly related to the reliability of the observed SSH and the quality of the used geoid model. The following chapter provides an overview about the most significant challenges that arise when computing geostrophic velocity components in polar oceans. The first part is related to the description of necessary steps in the altimeter processing enabling a reliable exploitation of the radar waveforms followed by uncertainties of the geoid model.

2.3.1 Retracking radar waveforms in the vicinity of rough sea states and sea ice conditions

The northern Nordic Seas are characterized by ocean surface conditions that are difficult to monitor in particular the presence of sea ice or rough sea states (Serreze and Barry (2014)), which directly affect the shape and backscatter characteristics of the reflected altimetry radar signal (Figure 2.3). Moreover, the complexity of the surface properties and the transition between leads, sea ice and open ocean, which is not necessarily characterized by a clear delimitation of the areas, makes it challenging to apply only one retracking algorithm. Moreover, the application and combination of different surface type-dedicated retracking algorithms can lead to systematic height offsets (i.e. retracker bias), which require further processing steps (Bulczak et al. (2015), Peacock and Laxon (2004)). In order to avoid this issue, the retracking approach must be able to handle single-peak waveforms (Fig. 2.3, right), and open ocean (i.e. Brown-like waveform shape, Brown (1977)) conditions, within one retracking algorithm.

Related to this requirement, Passaro et al. (2018a) developed a novel retracking strategy (i.e. ALES+), which is essentially based on the Adaptive Leading Edge Subwaveform (ALES) retracker (Passaro et al. (2014)), but includes an additional component for an improved fitting of single-peak waveforms. Furthermore, ALES+ is able to provide homogeneous range estimations for any kind of water surfaces (Passaro et al. (2018a)). However, ALES+ is not adapted to DD waveforms, which restricts the application to pulse-limited altimetry missions.

2.3 Challenges of monitoring geostrophic surface currents by radar altimetry

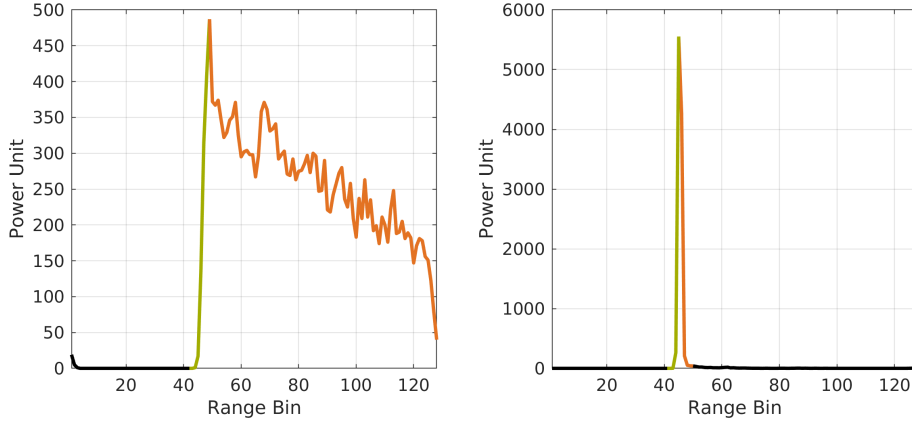


Figure 2.3: Examples of Envisat open ocean (Brown-like, left) and calm water (single-peak; right) waveforms. Green indicates the leading edge; orange highlights the trailing edge.

ALES+ follows mainly the steps of ALES, described in more detail in Passaro et al. (2014). ALES is primarily developed for the precise determination of the correct leading edge (Fig. 2.3, green waveform parts) and trailing edge slope (i.e. the angle between green and orange waveform parts) of coastal and open ocean waveforms by selecting and investigating the right subwaveform. ALES+ is an extension of the conventional ALES approach to identify the correct leading edge for all kind of waveform types. Before running the standard processing steps of ALES, ALES+ includes an additional fitting of waveforms with a steep trailing edge by first estimating the waveform parameter c_ξ , provided in the Brown-Hayne model, which is the standard functional form that describes received altimeter waveforms (Brown (1977), Hayne (1980)). In particular, c_ξ substitutes all influences on the waveform that can affect the slope of the trailing edge, such as the antenna beam width or the mispointing angle (Vignudelli et al. (2011)).

At first, a threshold (see Passaro et al. (2018a)), based on the Pulse-Peakiness (PP) of a waveform, decides for the standard ocean leading edge detection (i.e. ALES) or non-standard leading edge detection (i.e. ALES+). The PP is introduced by Peacock and Laxon (2004) and provides information about the shape of the backscattered power distribution of the radar echo and indirectly about the reflectivity of the surface. Further, it describes the ratio of the maximum power to the mean power of the waveform. Waveforms, reflected by calm water areas, are characterized by a dominant peak and less noise featuring steep leading- and trailing edges show high PP values in contrast to open ocean waveforms, which display mainly lower PP values (see Appendix Fig. A.2). The standard leading edge detection, applied to open ocean waveforms, follows the routines of ALES and is explained more in detail in Passaro et al. (2014). The non-standard leading edge detection, applied for single-peak waveforms, is described in Passaro et al. (2018a). The following description refers to the ALES+ starting with the detection of the leading edge, followed by the decision for an external or standard estimation of c_ξ .

Leading-edge detection based on ALES+

After deciding for a non-standard leading edge detection, the first part of ALES+ refers to the determination of the leading edge. Therefore, the waveforms are normalized by applying a normalization factor of $1.3 \cdot \text{median}(\text{waveform})$ indicating the closest position of the maximum power of the leading edge. The normalization factor results from empirical tests conducted in Passaro et al. (2018a). In the next steps the start and the stop bin of the leading edge are determined. The leading edge starts if a change of 0.01 units in comparison to the previous bin is detected and holds for at least the next 4 bins without a 10% decrease of the normalized power. The leading edge stops at the first bin, the sign of the derivative of the rising part of the waveform changes and is kept for the following 3 bins.

Decision of trailing edge slope computation based on ALES+

In the next processing step, the computation of the trailing edge slope parameter, c_ξ , is conducted. The computation of c_ξ is again dependent on the PP, which decides for an external estimation of c_ξ or a direct application of the conventional Brown-Hayne model. In contrast to the first PP, the choice of c_ξ is related to the PP of normalized waveforms in order to avoid inaccuracies due to the presence of other peaks in the trailing edge. If the threshold is not exceeded, c_ξ is directly estimated following the conventional application of the Brown-Hayne model. The waveform is forwarded to the standard ALES processing. However, if the threshold is exceeded, a preliminary estimation just based on the determination of c_ξ is performed. In a next step, the a-priori estimated c_ξ is introduced as a pre-known parameter to the Brown-Hayne model before continuing with the normal ALES processing procedure.

In the end, the application of ALES+ results in homogeneous estimated altimeter ranges, which need no further processing dependent on the reflective surface. However, since ALES+ can retrack all kinds of relevant surface types in the polar regions, as long as a clear leading edge can be found (Passaro et al. (2018a)), further processing steps are required to distinguish between radar echoes reflected from water areas, such as ocean or leads, and waveforms originating from sea ice surfaces. Due to the complexity of changing surface characteristics, a simple threshold based for example on PP, is not enough for a reliable surface discrimination. Therefore, a classification approach based on artificial intelligence is developed, which finds autonomously similar patterns among the waveform dataset.

2.3.2 Artificial intelligence for radar waveform classification

The northern Nordic Seas are characterized by a seasonally occurring sea ice coverage with a maximum in March. The melting period starts in April and accelerates until the minimum is reached in September (Kvingedal (2013)). The sea ice conditions are

2.3 Challenges of monitoring geostrophic surface currents by radar altimetry

dependent on the sea ice import through the Fram Strait and on local ice growth. Beside drifting sea ice floes with variable size, the sea ice layer is interrupted by closed or semi-closed open water areas, called leads and polynyas. The first are narrow and elongated cracks and can vary from several meters to kilometers and a few meters to hundreds of meters in width. The latter are mainly entirely closed and nearly constant areas of open water with a more circular shape. In the northern Nordic Seas, they mainly develop close to the coast and in the vicinity of landfast ice (i.e. stable ice anchored to the coast). These open water areas can provide insights into the sea level within the sea ice zone by using altimetry if dedicated detection algorithms are introduced to the altimetry data processing chain. Beside mission-dependent fixed defined threshold strategies (e.g. Connor et al. (2009), Peacock and Laxon (2004)), one of these detection strategies is an innovative unsupervised classification approach, which is independent of the radar frequency as well as mission-specific characteristics and is applied for the first time to K_u -band radar echoes of Envisat and K_a -band waveforms of SARAL (Müller et al. (2017)).

The unsupervised classification belongs to the so-called artificial intelligence algorithms, which enables the detection of similar, hidden patterns within a given dataset, without the use of pre-known information or training data (Xu and Wunsch (2008)). In the present context, unsupervised classification methods are transferred to altimetry waveforms to find similarities within a given sample of various waveforms collected from open ocean, sea ice and lead/polynya conditions. The idea is to find single-peak waveforms, originating from calm water areas (i.e. leads and polynyas), and Brown-like (open ocean) waveforms automatically (Fig. 2.3) without the use of pre-defined fixed thresholds in order to exploit all possible usable radar data for deriving SSH observations independent of the surface conditions and observation season. For this purpose, K-medoids, belonging to the partitional clustering algorithms (Celebi (2014)) are applied, only using as input the waveform itself and the backscattered power, for splitting the waveform sample.

The following publication describes the unsupervised classification process for waveform samples of Envisat and SARAL and provides information about the classification performance, resulting in a consistency rate of 70.7% for Envisat and 76.9% in case for SARAL. The validation is based on circa 15000 Envisat and 20000 SARAL classification results, which are compared to image processed and binarized SAR images, indicating open water and sea ice areas. The automatic and quantitative validation approach is described in the next subsection. Moreover, the unsupervised classification is transferred unchanged and applied to waveforms of ERS-2 (not part of P-1.1).

P-1.1 Müller, F. L., Dettmering, D., Bosch, W., and Seitz, F. (2017). Monitoring the arctic seas: How satellite altimetry can be used to detect open water in sea-ice regions. *Remote Sensing*, 9(6), ISSN: 2072-4292, DOI: 10.3390/rs9060551

The unsupervised classification was also applied to CryoSat-2 SAR waveforms yielding an overall classification performance of 97% (Dettmering et al. (2018)). Moreover, the

classification concept is part of Göttl et al. (2016) to assign and label waveforms in the inland area resulting in an overall improvement of about 25% in the estimation of lake water level time series compared to conventional approaches.

2.3.3 Validation of classification by SAR images and image processing techniques

In order to assess the performance of the unsupervised classification a method is developed, which enables an automated, quantitative comparison with backscatter images from side-looking imaging SAR instruments during sea ice conditions. The radar images are spatially and temporally collocated, considering the altimetry overflight locations and times. Compared to other spaceborne sensors working in the visible spectrum, SAR instruments are not affected by the illumination conditions caused by the sun and the cloud cover. This is particularly beneficial in the northern Nordic Seas, during the polar night in winter and a cloud cover of up to 80-90% in summer (Hurdle (1986)). Moreover, the provided pixel resolution ranging from 40 m in the case of Sentinel-1 to 100 m for ALOS enable the detection of leads ranging from a few meters up to hundred of meters in width. In order to account for sea ice movements between the observation times of altimetry and the image data, the acquisition time gap should be as small as possible. However, the possibility for simultaneous comparisons is limited by the orbit characteristics of the satellite missions, for example due to fixed revisit times, caused by the repeat orbit configuration. Therefore, the images are shifted to compensate for the sea ice motion by using daily sea ice velocity fields from a combination of passive and active microwave sensors as well as in situ information from buoys, which are frozen into the ice or mounted on top of sea ice floes. In order to enable an automatic and quantitative comparison, the radar images are converted to binary images, indicating only water and sea ice surfaces, by applying morphological gray scale operations and adaptive thresholding techniques. In the last step, the altimetry classification results are interpolated to the SAR pixel coordinates by using a nearest-neighbor interpolation, enabling a direct point-wise comparison of both datasets.

The automated validation technique based on SAR images was mainly developed within the framework of another threshold-based classification approach (i.e. supervised classification) based on CryoSat-2 stack data, but can be used independently. The method is described in:

P-1.2 Passaro, M., Müller, F. L., and Dettmering, D. (2018b). Lead detection using cryosat-2 delay-doppler processing and sentinel-1 sar images. *Advances in Space Research*, 62(6):1610 – 1625, ISSN: 0273-1177, DOI: 10.1016/j.asr.2017.07.011

The identical method, but adding two more imaging SAR missions (i.e. RADARSAT-2 and ALOS), is applied for the validation of the unsupervised classification of Envisat and SARAL data, described in Müller et al. (2017).

The classification process, starting with the application of the unsupervised assignment of waveforms, followed by an validation process based on external imaging data is also included in a review publication by Quartly et al. (2019).

2.3.4 Geoid models in the northern Nordic Seas

For determining the DOT, it is crucial to know about geoid uncertainties which can have a direct influence on the along-track DOT computation (Skourup et al. (2017)). Since the launch of the gravity satellite missions Gravity field and steady-state Ocean Circulation Explorer (GOCE) and Gravity Recovery And Climate Experiment (GRACE), global geoid models have been significantly improved in the lower spherical harmonic degrees, providing an accuracy of up to 2-3 mm (Forsberg and Skourup (2005)). Shorter wavelengths between 10 km to 30 km are mainly based on gravity observations from regional in situ campaigns or various satellite altimetry missions. But in the case of spaceborne sensors, only altimeters can contribute to wavelength between 5 km and 100 km spatial resolution (Sansò and Sideris (2013)). One approach to use satellite altimetry-derived gravity data for the geoid determination is based on a remove-restore approach by reducing a long wavelength geoid model and a mean dynamic topography from SSH observations obtaining residual geoid elevations. These residuals are converted to gravity anomalies, filtered and added back to the long wavelength geoid to provide the total gravity signal (Sansò and Sideris (2013)).

At higher latitudes, however, the available gravity measurements, contributing to the shorter wavelengths, are very sparse and based only on selective gravity surveys (e.g. submarine expeditions) or few altimetry missions that reach polar areas. Particularly, in polar ocean regions, gravity fields include gravity data from altimetry without a sufficient sea ice flagging or dedicated retracking algorithms (see previous sections), cause artifacts or unrealistic geoid elevations. Moreover, errors in the higher harmonic degrees (>719) significantly affect the computation of altimetry-derived along-track DOT heights such as those described in Skourup et al. (2017). Referring to McAdoo et al. (2013) and Kwok and Morison (2015), these artifacts can cause deflections of up to several decimeters. Related to this issue, Skourup et al. (2017), McAdoo et al. (2013) and Kwok and Morison (2015) explain that the geoid accounts for a significant portion of the error budget for a reliable DOT determination, which must be particularly considered in polar regions.

In the present investigation for N (Eq. 2.3), the Optimal Geoid Model for Modeling Ocean Circulation (OGMOC) is used, which is one of the the newest high-resolution gravity fields, developed up to a spherical harmonic degree of 2190 corresponding to a global spatial resolution of 9.13 km (Gruber and Willberg (2019)). In harmonic degrees, ≤ 719 OGMOC consists of a combination of the gravity fields, European Improved Gravity model of the Earth by New techniques 6-C4 (EIGEN6-C4) (Förste et al. (2014)) and the Experimental gravity field model 2016 (XGM2016) (Pail et al. (2018)). Following Gruber and Willberg (2019), higher degrees are fully represented by EIGEN6-C4, which includes DTU10 gravity anomalies (DTU10GRA), gathered from ERS-1 in the higher

2 Satellite altimetry in the northern Nordic Seas

latitudes (Andersen (2010)). Moreover, to account for old altimeter data, parts of the marine gravity field DTU13GRA (Andersen et al. (2014)) and three years of CryoSat-2 observations are partly blended.

OGMOC, dedicated and developed for ocean currents, is identified as the best choice for this study. But lack of information of the ground truth makes it difficult to quantify errors in one specific geoid solution and complicates a clear separation of geoid-caused artifacts or oceanographic phenomena (Kwok and Morison (2015)). However, permanent artificial height deviations, which cannot be explained physically, indicate geoid errors. In order to better assess these effects, Figure 2.4 shows in an exemplary way for January (sea ice conditions) and September (no sea ice) monthly averaged and arranged into bins, the along-track DOT heights of Envisat between 2003-2009 (the bin structure follows the description of Müller et al. (2019b)). Underlining the investigations of Skourup et al. (2017), seasonally independent, stationary differences of up to 60 cm, caused by geoid inaccuracies are clearly visible in the northern Fram Strait area (e.g. at $2^{\circ}\text{E}/80.8^{\circ}\text{N}$).

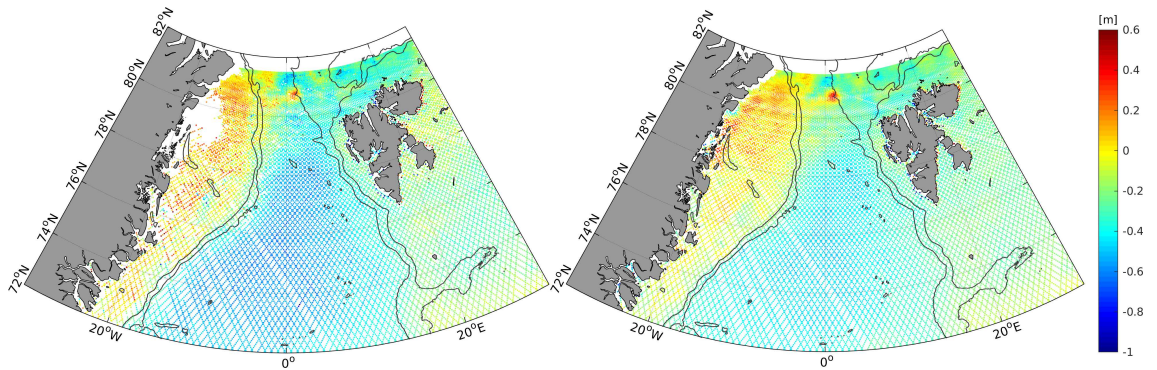


Figure 2.4: Examples of Envisat-derived along-track DOT elevations averaged for January (left) and September (right) and arranged into bins of 7.5 km length between 2003-2009. RTopo2 bathymetric lines (Schaffer et al. (2016)) indicate the Greenland Sea Basin (-1500 m) and the Greenland Shelf (-450 m).

In order to evaluate the need for regularly updated marine gravity field data, Figure 2.4 motivates for a short comparison of different marine gravity fields of the Danish Technical University, which is a leader in the creation of marine gravity fields based on altimeter data that covers the high latitudes. The comparison is based on the latest altimetry-based gravity data (i.e. DTU15GRA, Andersen et al. (2017) and DTU17GRA, Andersen and Knudsen (2020)).

Figure 2.5 shows the differences among the various marine gravity fields, illustrating the problem of inaccuracies in the marine geoid determination. As a reminder, OGMOC includes gravity anomalies of DTU10GRA and partly of DTU13GRA. It appears that updated altimetry data and refined computation methods can compensate for some artificial deflections, especially in coastal and sea ice regions (DTU15GRA, DTU17GRA). Nevertheless, no complete improvement can be surprisingly seen between the release of DTU10GRA and DTU17GRA. For example, artifacts - eliminated in DTU15GRA -

2.3 Challenges of monitoring geostrophic surface currents by radar altimetry

are present once again in DTU17GRA. Especially, the height artifact (15 mGal) at $2^{\circ}\text{E}/80.8^{\circ}\text{N}$ is spotted well in Fig. 2.5a, proving that DTU10GRA passes this artifact directly to the altimetry-derived along-track DOT (Fig. 2.4). Furthermore, the artifact is also seen in DTU15GRA versus the latest gravity model, DTU17GRA (Fig. 2.5d), which is not directly explainable, but indirectly by the application of filter algorithms and background models included in the computation (pers. communication Ole B. Andersen). In addition, an issue is detected in the computation of DTU15GRA gravity anomalies in relation to the zero meridian, showing interrupted and strongly smoothed structures of the gravity anomalies.

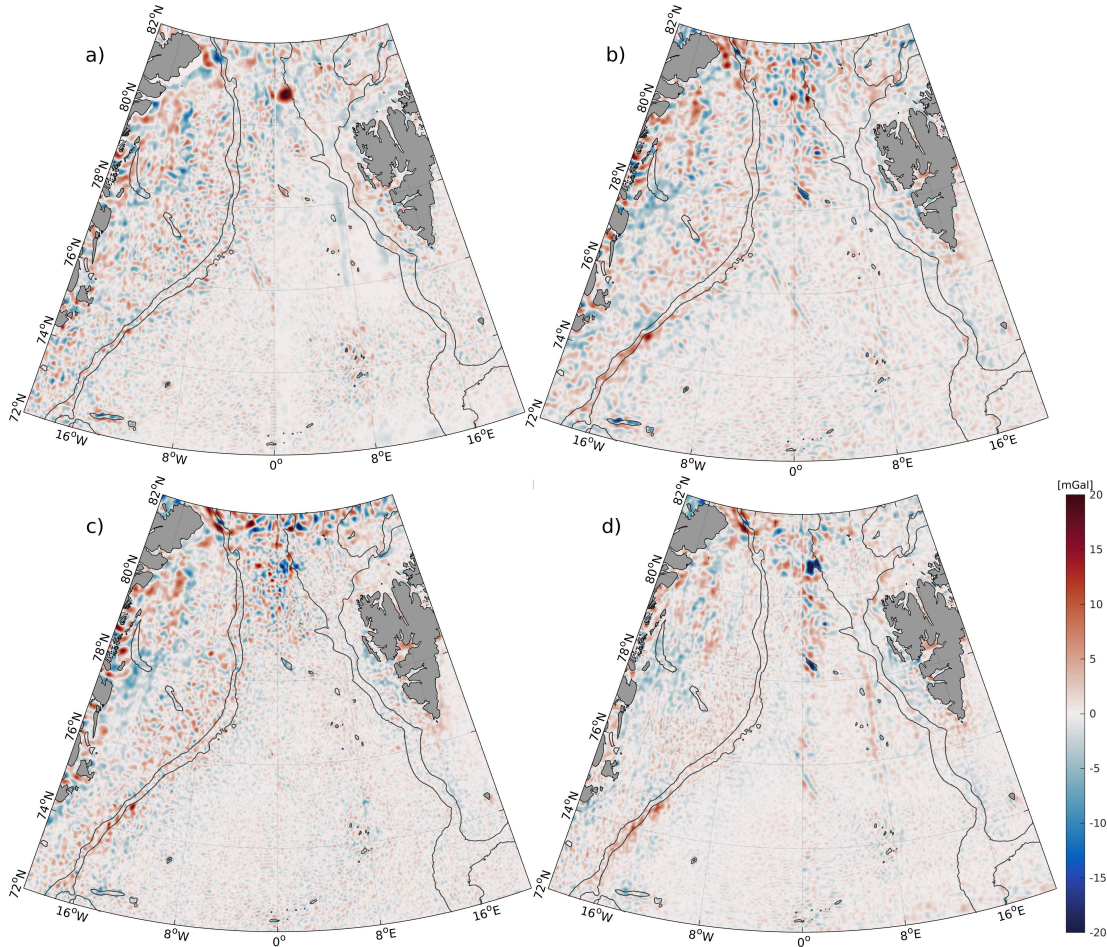


Figure 2.5: Comparison between (a) DTU10GRA - DTU15GRA, (b) DTU10GRA - DTU17GRA (c) DTU13GRA - DTU15GRA and (d) DTU15GRA - DTU17GRA gravity fields in terms of gravity anomalies in mGal. Contour lines indicate depths of -450 m and -1500 m, taken from RTopo2 (Schaffer et al. (2016)).

To summarize, a brief comparison of currently available marine gravity fields demonstrate the challenges of the geoid determination at polar latitudes and underlines the need for updated in situ and altimetry-derived gravity observations. Moreover, the com-

2 Satellite altimetry in the northern Nordic Seas

parison shows that currently no perfect geoid is available for this region. Furthermore, the comparison shows that all marine gravity solutions are affected by different effects, which does not indicate a continuous improvement.

3 Combination of altimetry observations with ocean modeling data

The thesis presents an innovative methodology to combine observed with modeled water heights at the same processing stage in order to benefit from the advantages of both datasets. It aims to provide sea surface currents from equally combined, but conceptually totally different, data sources. The modeled water heights are used to fill in or bridge observation gaps in the altimeter data.

In polar regions, altimetry observations are characterized by an irregular data cover caused by the seasonal sea ice coverage. Moreover, it must be dealt with a poor data coverage due to a fixed observation geometry, since only one repeat orbit configuration of 35 days is available. The idea is to fill in simulated water heights, where no altimetry data exists and to enable a homogeneous representation of the DOT and derived geostrophic currents, without additional smoothing effects by interpolating altimetry observations in space and time, for example. The ocean model FESOM (Wang et al. (2014)) provides daily differential water heights (DWH) by a spatial resolution of up to 1 km. The observational dataset consists of ERS-2 and Envisat-derived along-track DOT observations. Both data sources refer to a geopotential surface. In the case of altimetry, it is provided by the geoid and in case of FESOM by the ocean bottom topography.

In order to check both quantities for consistency, a comparison by analyzing constant offsets, annual variability and regional seasonal patterns based on DOT, as well as DWH elevations is necessary. The following chapter provides a brief introduction about FESOM, followed by the comparison of the observational and modeled data and closes with the combination.

3.1 The Finite Element Sea Ice Ocean Model (FESOM)

The Finite Element Sea Ice Ocean Model (FESOM) is a global hydrostatic ocean circulation model solving for a standard set of primitive hydrostatic equations (Danilov et al. (2004)), which are an approximation of the Navier-Stokes equation (e.g. Marshall et al. (1997)). The standard set of primitive hydrostatic equations generally includes, the conservation of momentum equation, the continuity equation, the thermodynamics equation, the equation of state and the equation of diffusion for the salinity (e.g. Temam

3 Combination of altimetry observations with ocean modeling data

and Ziane (2005)). Since ocean modeling is not the focus of this thesis, more additional information focusing on the general background of ocean circulation modeling is provided in Griffies (2004).

FESOM is defined on unstructured, triangular meshes, which allow for flexible spatial refinements and the resolution of jagged coastlines as well as small straits and passages (e.g. Fram Strait). The model equations are discretized by the application of the finite-element method (Danilov et al. (2004)). FESOM exists in different versions and development stages. The investigations in the thesis are based on a modified model configuration of FESOM Version 1.4 (see Wang et al. (2014)), described by Wekerle et al. (2017). In order to account for sea ice, FESOM includes a sea ice component mapping the major sea ice drift pathways. Moreover, relative sea surface elevations (i.e. DWH) with respect to the ocean bottom topography (i.e. RTopo2 model; Schaffer et al. (2016)) projected on a sphere are given. Following Androsov et al. (2018), the DWH is referenced to an own model coordinate system (z) being very close at $z = 0$ to the geoid. However, secular changes, such as effects due to the glacial isostatic adjustment or the self-gravitation are not visible to the ocean model, causing a constant offset of 47 cm (Androsov et al. (2018)).

The model configuration used provides daily ocean parameters for the northern Nordic Seas with regional mesh densifications in the central Fram Strait and Greenland Sea ranging from 4.5 km up to less than 1 km, enabling an eddy-resolving resolution at different vertical layers. However, in the present work, only model results at the surface (i.e. $z = 0$) are considered. Furthermore, FESOM conserves volume, but no mass, since a global steric height correction is missing in order to ensure the full conservation of mass. Furthermore, it does not model the atmospheric loading. Following the explanations of Androsov et al. (2018), a mass conservation would require detailed, regional information about inflow and outflow of fresh water through the ocean boundaries (e.g. glacial melting water, river discharge, precipitation-evaporation ratio, etc.), which is not included in the model setup being used.

FESOM is driven by daily and 2° degree spatially resolved CORE2 (Large and Yeager (2008)) atmospheric reanalysis data, monthly river runoff (Dai et al. (2009)) and sea surface salinity fields (Steele et al. (2001)). In comparison with observational data, Wekerle et al. (2017) indicate good accordance of FESOM in terms of circulation patterns, hydrography and eddy activity. However, Richter et al. (2018) refer to a bias towards a higher assumed salinity in the Atlantic Water layer due to model uncertainties in simulating the correct pathway of the North Atlantic water, which can lead to displacements in the representation of the annual oscillation.

More information regarding the used FESOM configuration can be found in Wekerle et al. (2017). In the following sections, only modeled sea surface elevations are used, which are available in a daily resolution from 2002 - 2009. After 2009, no model output is delivered, since the forcing datasets were not available.

3.2 Comparison of the dynamic ocean topography from altimetry and FESOM

Before the combination, the datasets are compared in terms of the DOT and DWH. Following the explanation of Androsov et al. (2018), the volume conservation implies that DWH is not modeled correctly in an absolute sense (missing global mean steric height correction), but in relative height differences leading to correctly simulated horizontal pressure gradients. In conjunction with the DOT, it follows that:

$$\nabla DOT = \nabla DWH \quad (3.1)$$

Therefore, DOT and DWH are considered as equivalent and are summarized as DOT elevations in the next sections.

Similarities and discrepancies are evaluated based on profiled observed and modeled DOT heights within the 2003 - 2009 Envisat investigation period. Therefore, the model data are interpolated on the altimeter along-track coordinates. The assessment analysis focuses on constant offsets and seasonal DOT variabilities in regional parts (i.e. shelf, deep basin) and in the northern Nordic Seas as a whole. In general, the comparison reveals good agreement and depicts the annual oscillation as the most dominant signal captured by both datasets. The comparison showed a constant offset of about 47 cm between both datasets, which is consistent with the description of Androsov et al. (2018). The assessment shows up to 2-3 times stronger amplitudes of the observational dataset, in contrast to the phase, which indicates good agreement (Müller et al. (2019b)). A regional reduction by constant offsets and the annual signal of both datasets, results in a good accordance and high correlations of the DOT time series. The best consistency can be found in ice-free areas and in regions affected by ocean currents.

Inconsistencies are divided into three categories concerning issues of the model, altimetry observations and the geoid model (i.e. OGMOC, Subsec. 2.3.4). In contrast to open ice-free ocean regions, satellite altimetry observations suffer from a stronger scattering in sea ice regions. Even applying sea ice-dedicated algorithms, such as a sophisticated retracker sampling single-peak, but also Brown-like waveforms within one approach and an unsupervised classification for detecting waveforms reflected by open water areas within the sea ice domain, the noise level is increased compared to the open ocean. Moreover, in sea ice regions, the applied altimetry range corrections are characterized by an enhanced error budget, causing uncertainties in the range estimation and the reliable determination of the annual signal.

In the case of the model, differences in the representation of the annual signal in terms of amplitude and phase might occur due to a stronger smoothing of the model output, caused by a too strongly adjusted sea ice friction and the added numerical diffusion coefficient stabilizing the model computations. Moreover, as mentioned above, the model preserves only the volume and neglects a global steric height correction for a complete

preservation of mass. In the global model, the freshwater inflow is integrally 0, transferred to the regional domain it is likely that this affects the annual cycle, so that the amplitude is reduced and phase shifts are caused. Another reason in a smaller modeled annual amplitude can be found in the forcing models, which are characterized by an excessively coarse spatial resolution. Furthermore, following the explanations of Richter et al. (2018), FESOM uses inter-annual runoff data of Dai et al. (2009), neglecting a subglacial and submarine melting of the Greenland ice sheet, which leads to errors in the simulation of the EGC water mass transport along of the shelf edge. This may also influence the correct location of the modeled Atlantic Water flow crossing the northern Nordic Seas.

The comparison states that even with an improvement of the known problems, limitations such as the difference of the absolute height level and an enhanced observation noise in regions affected by sea ice will persist. However, a combination of both quantities is useful because of a general good agreement, showing no significant differences between both datasets. The comparison suggests a combination in order to benefit from both datasets enabling the computation of a homogeneous DOT and geostrophic ocean surface circulation. The combination shall be performed in the sense that the temporal DOT variability and the absolute height reference are provided by altimetry. FESOM data are used to bridge regions influenced by sea ice, geoid artifacts and incomplete observation coverage. The detailed comparison of the observational and simulated database in terms of DOT heights can be found in:

P-2 Müller, F. L., Wekerle, C., Dettmering, D., Passaro, M., Bosch, W., and Seitz, F. (2019b). Dynamic ocean topography of the northern nordic seas: a comparison between satellite altimetry and ocean modeling. *The Cryosphere*, 13(2):611–626, DOI: 10.5194/tc-13-611-2019

3.3 Geostrophic currents from a combination of altimetry and FESOM

The combination is based on a Principal Component Analysis or empirical orthogonal function analysis (e.g. Preisendorfer (1988)). The concept of historic sea level reconstruction described, for example by Church et al. (2004) or Ray and Douglas (2011) is transferred for a combination of profiled altimetry-derived DOT heights with simulated spatio-temporally homogeneous DOT elevations in the investigation area. Similar approaches are used for signal decomposition described, for example by Schmeer et al. (2012) or for filling in data gaps in oceanographic datasets (e.g. Beckers and Rixen (2003)).

In this thesis the PCA is used to link the most dominant spatial patterns of the simulated DOT with profiled altimetry-derived DOT observations representing the temporal variability. In a first step, a constant mean and the annual signal are removed from the

3.3 Geostrophic currents from a combination of altimetry and FESOM

DOT elevations of both datasets. Furthermore, the 50 most dominant spatial patterns (i.e. empirical orthogonal functions), describing more than 99% of the total variance of the signal, are extracted from FESOM and linked to the along-track DOT observations to estimate the principal components describing the temporal evolution of each of the 50 most dominant spatial patterns. The estimation of the combined principal components is performed by applying a least-squares approach (Koch (1999)) as described in more detail in Müller et al. (2019a). In the next step, the derived principal components are multiplied by the spatial patterns (synthesis). The product of a principal component with the corresponding spatial signal defines a Mode. In the last step, the 50 Modes are summed up. Since the absolute height reference of the model is not clearly defined, the combined dataset is referenced to the altimetry height level by readding the offset and annual signal from the observed database.

The combination is described in detail by:

P-3 Müller, F. L., Dettmering, D., Wekerle, C., Schwatke, C., Passaro, M., Bosch, W., and Seitz, F. (2019a). Geostrophic currents in the northern nordic seas from a combination of multi-mission satellite altimetry and ocean modeling. *Earth System Science Data*, 11(4):1765–1781, DOI: 10.5194/essd-11-1765-2019

The main results are daily combined, unstructured DOT triangular meshes, which are transformed to geostrophic surface current components (i.e. meridional and zonal velocity components) by applying the geostrophic equations (Eq. 2.7). The spatial resolution is equal to the FESOM mesh. However, there are a few data gaps in the dataset, which are caused by a complete lack of altimetry observations preventing a reliable estimation of the principal components.

The combined dataset is validated by an external observation-based DOT product resulting in a positive correlation of about 80%. Moreover, the combined geostrophic currents are compared to independent drifter data measurements showing good agreement in spatial patterns, magnitude and flow direction. A direct pointwise evaluation reveals that 94% of the residuals are smaller than 0.15 m/s.

The final data product can be obtained from to PANGAEA (<https://doi.pangaea.de/10.1594/PANGAEA.900691>, Müller et al. (2019)), a freely accessible data repository for earth system and science data.

4 Scientific exploitation of the dataset

The thesis mainly focuses on the development and generation of the combination methodology and product. In the following chapter, a scientific data exploitation demonstrates the potential of the combined datasets. The analyses relate to the ocean current datasets and study the changing ocean surface current state between May 1995 and March 2012.

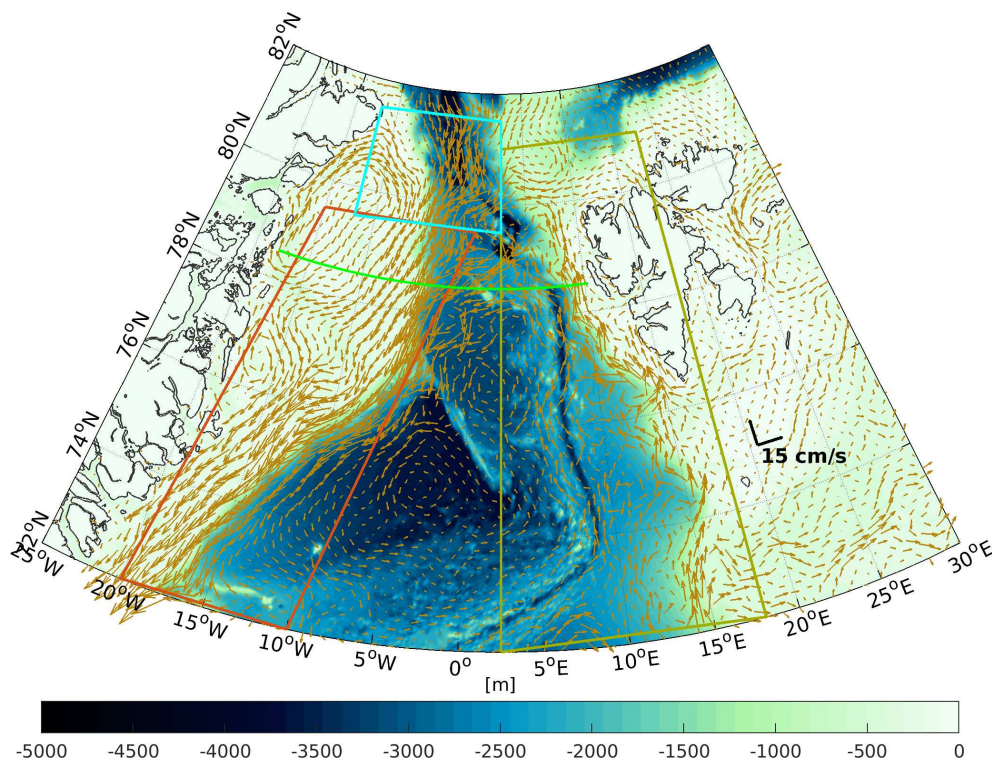


Figure 4.1: Mean surface current flow in the northern Nordic Seas derived from combined geostrophic datasets with RTopo2 bathymetry (Schaffer et al. (2016)) in the background between 1995 - 2012. Study areas for extended investigation are highlighted (polygons, line).

Figure 4.1 gives an overview of the mean velocity and direction of the major current systems in the northern Nordic Seas. Therefore, the velocity components are interpolated to a coarser regular grid with a spacing of 1° in longitude and 0.75° in latitude in order to keep the readability of Figure 4.1. The interpolation is performed by averaging the

4 Scientific exploitation of the dataset

velocity components within a cap-size of a 20 km radius around a grid node of the regular grid.

The currents follow very precisely the shelf edges of the Greenland Shelf (i.e. EGC) and the Barents Shelf (i.e. WSC). Both currents show strong interactions with the bathymetry. Further, recirculating Atlantic Water masses can be detected around 79°N. The WSC is characterized by a strong eddy activity and meandering of the main stream in contrast to the EGC, which is characterized by a clearer and wider flow pattern. In contrast to the current areas, the Greenland Sea center appears very weak with almost no significant current activity. However, parts of the Greenland Sea gyre between 72°N and 76°N are visible. Furthermore, Figure 4.1 displays clearly the current pattern of the North-East Greenland Coastal Current (NEGCC), which flows northwards, mainly under the sea ice layer, very close to the east Greenland coastline, before merging with the EGC in the Fram Strait region.

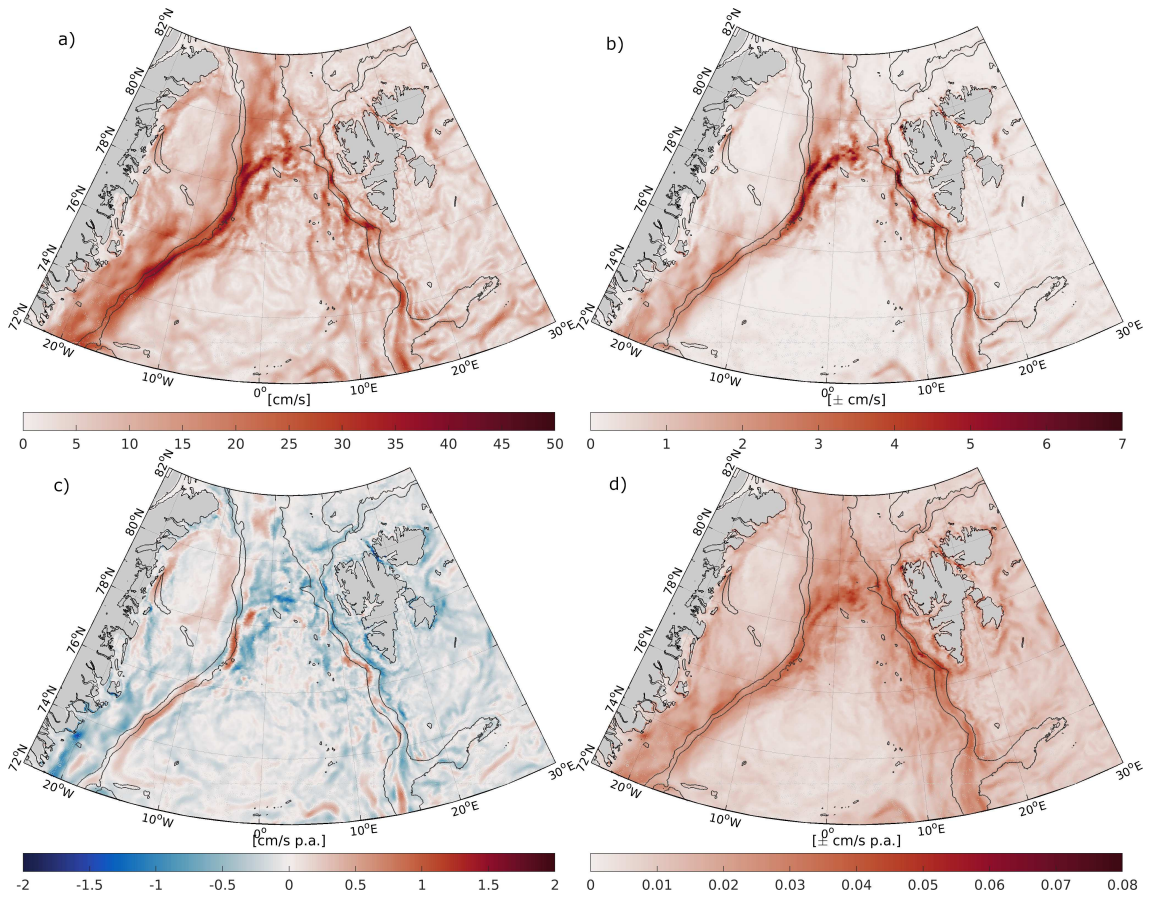


Figure 4.2: At the top: Mean absolute geostrophic surface velocity (a) and standard deviation (b). At the bottom: Surface velocity trend (c) and estimated uncertainty (d). Bathymetric contours indicate depths of -1500 m and -450 m, taken from RTopo2 (Schaffer et al. (2016)).

The mean absolute geostrophic surface velocities and corresponding trends per year, including uncertainty information, are shown in Figure 4.2. The major current systems are clearly detectable, which are characterized by mean velocities of about 45 cm/s in the EGC and 30 cm/s in the WSC. The flow variability is strongest in the current center, whereas the WSC is characterized by more eddies and flow activity alongside the main flow. Moreover, very low or nearly no surface flow velocities are observed in the northernmost part of the WSC.

The absolute velocity trends (Fig. 4.2) are generally small. The trend map indicates a multipath structure of the EGC mainly consisting of three branches, at the Greenland Shelf, along the shelf-break and more offshore, instead of one major flow area, which is also observed by in situ investigations conducted, for example, by Håvik et al. (2017). Håvik et al. (2017) found out that the Greenland Shelf branch mainly contributes to the freshwater transport from calving glaciers, whereas the branch at the Greenland shelf-break carries a large amount of Atlantic-origin Water. Furthermore, Håvik et al. (2017) argue that the offshore branch transports directly recirculating water masses of the WSC.

Figure 4.2c reveals a velocity increase of the surface flow in the core area of the EGC, strongest along the Greenland shelf-break (circa 1.08 cm/s p.a. ± 0.04 cm/s p.a.) and weaker at the northern Greenland Shelf as well as in the western Fram Strait region. On the other side, decreasing surface velocities, up to -1.27 cm/s p.a. (± 0.04 cm/s p.a.) are observed in the southeast Fram Strait, where the EGC mixes with recirculating Atlantic water, in the Spitsbergen coastal regions and in southern Greenland Shelf regions. Moreover, a positive trend is indicated in the NEGCC close to the northeast Greenland coast. Similar to the EGC, Figure 4.2c indicates a multipath structure of the WSC, separating the current into a west and east component. However, the WSC is primarily characterized by a weakening of the surface flow up to about -1.26 cm/s p.a. (± 0.04 cm/s p.a.) near the Spitsbergen coast.

The spatial monthly variability and annual oscillations of the geostrophic surface velocity are presented in Figure 4.3. An increased inflow of Atlantic Water masses and enhanced Arctic Ocean outflow through the Fram Strait indicate overall strong flow activities during the winter months. In the case of WSC, strongest velocities are displayed during January, February and March, which can be confirmed by mooring observation that indicate largest volume transports during winter (von Appen et al. (2016)). During the winter season, the EGC is characterized by a broader flow pattern.

In late spring and early summer (i.e. April, May, June) and in autumn (i.e. Sept., Oct., Nov.) the WSC appears weaker. According to observations of Beszczynska-Möller et al. (2012), the Atlantic Water inflow is lowest in June, which is indicated in Figure 4.3 by a weaker main flow of the WSC. However, a slightly increased meandering is observed in July, which is not fully explainable (Crews et al. (2018)). Possibly, this behavior can be attributed to baroclinically unstable currents during the time of maximum sea surface temperature (Crews et al. (2018)). During July/August, the EGC appears more narrow, following very precisely the shelf-break by displaying current velocities of up to 40 cm/s.

4 Scientific exploitation of the dataset

This is related to strong differences of the horizontal pressure gradient, due to warm recirculating water masses mixing with cold and less saline freshwater from the Arctic Ocean.

Detailed analyses are performed in three subregions, Fram Strait, EGC and WSC (see Fig. 4.1, cyan, red and dark yellow polygons). In order to evaluate most dominant patterns, a moving average of 30 days per grid node is applied to the velocity components to cut out short-periodic noise. Figure 4.4 shows the absolute velocities, the annual signal and an estimated trend within the investigation period. The results indicate a positive trend (i.e. $0.9 \text{ mm/s} \pm 0.05 \text{ mm/s p.a.}$) of the obtained absolute velocities in the Fram Strait region and a seasonal cycle, which peaks in the winter (January) showing maximum mean velocities of about $12 \text{ cm/s} - 15 \text{ cm/s}$ and is weakest in the summer (July) with minimum velocities of about 2.5 cm/s . These observations fit well to previous studies for example by Armitage et al. (2017). The same velocity pattern, but with a reduced positive trend of about $0.3 \text{ mm/s} \pm 0.05 \text{ mm/s p.a.}$, can be seen in the EGC. However, a 4 cm/s stronger mean current velocity can be observed, which is likely related to recirculating Atlantic water masses, driving the thermohaline circulation in the Greenland Sea. Maximum velocity peaks can be found during the winter months 1996/1997, 2001/2002 and 2006/2007, whereas significantly slower speeds can be observed in the summer of 1998 and 2003. These peaks are mainly caused by variations in the thermohaline circulation influenced by variations in water density due to changes in salinity and sea surface temperature. For example, in the winter of 1996/1997, an extensive ice formation was observed in the Greenland Sea area (Rudels et al. (2012)). During the ice formation, salt is released to the surrounding areas leading to an increase in water density and consequently to stronger horizontal pressure gradients, resulting in higher current velocities.

In the case of the WSC, Figure 4.4 indicates an overall decreasing trend of (i.e. $-0.4 \text{ mm/s} \pm 0.03 \text{ mm/s p.a.}$) in the surface current velocity. Contrary to the EGC, the WSC is characterized by a weaker mean velocity of 5 cm/s and an annual amplitude of 1.3 cm/s , showing its maximum in February and minimum in August. Significant velocity maxima occur in winter 1997/1998 and 2003/2004, a clear minimum is detected in summer 1999. These peaks can be explained not only by density differences but also by variations of the sea level pressure and the influence of the northern Atlantic (e.g. Chafik et al. (2019), Holliday et al. (2008)).

Most of the water traveling through the northern Nordic Seas comes from the Gulf Stream and the Norwegian Atlantic current before entering the Greenland Sea. Warm saline surface water flows northwards, cools down, becomes denser and sinks, while warm water from southern regions can follow. This process is strongest in the winter due to a cooler atmosphere and faster cooling of the Atlantic water (e.g. von Appen et al. (2016)). However, a heating up of the atmosphere influences the heat exchange between ocean and atmosphere, which can be observed in an increase of the sea surface temperature (SST) and a decrease of the mean current velocity (e.g. Figure 4.4c).

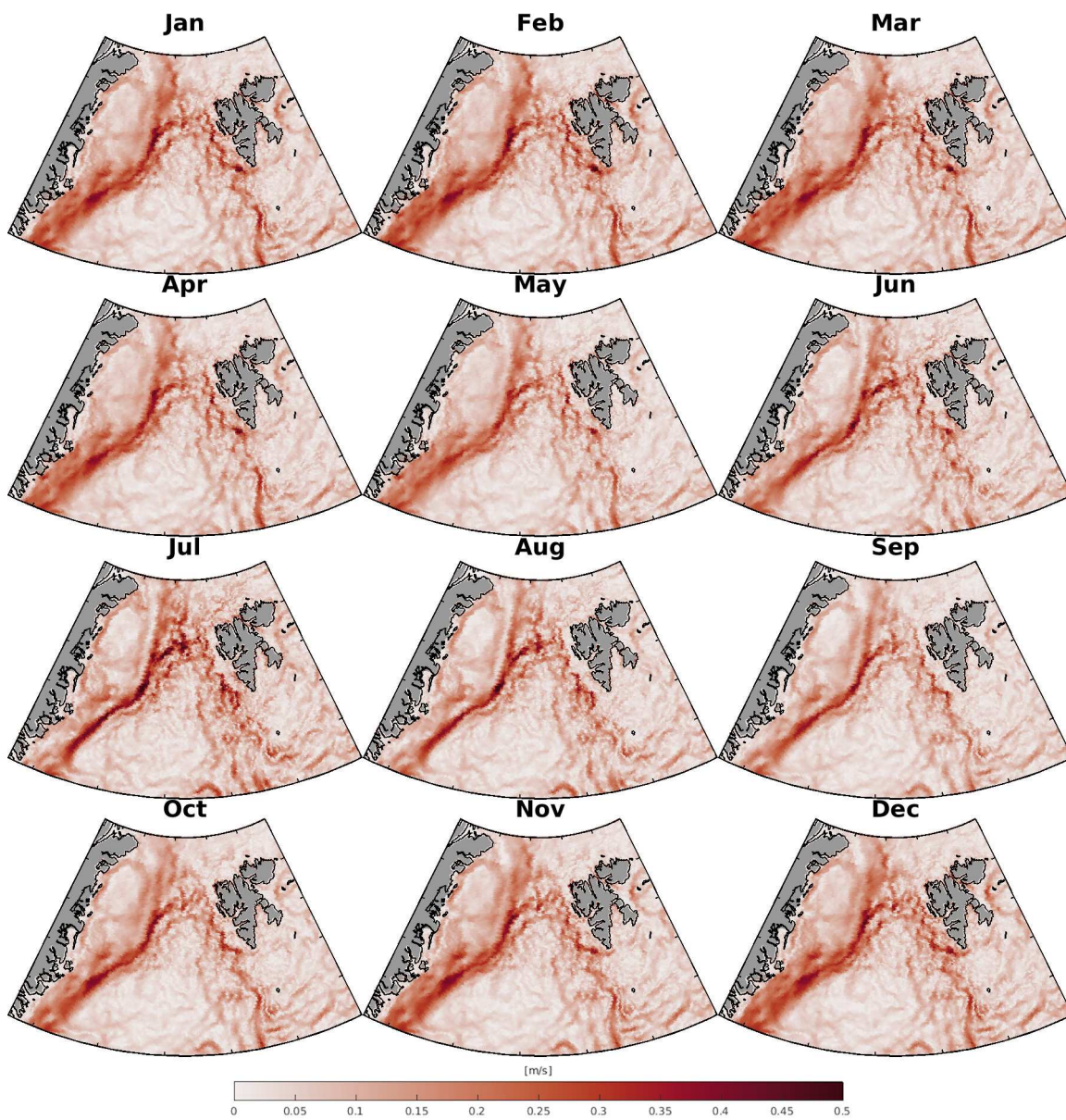


Figure 4.3: Monthly averaged ocean surface velocities within the investigation period, 1995-2012.

4 Scientific exploitation of the dataset

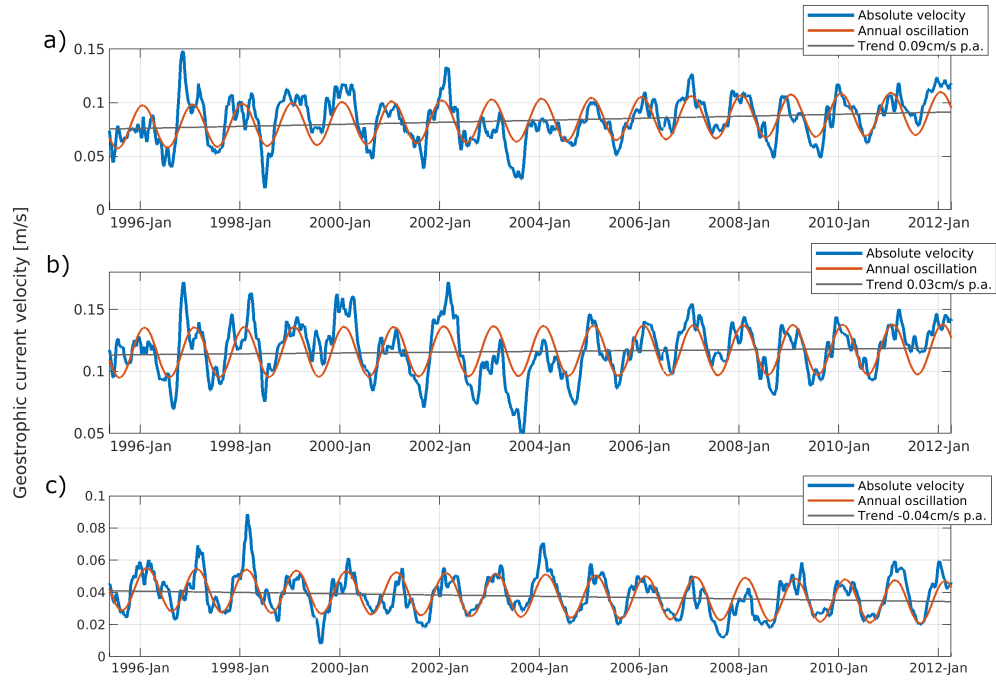


Figure 4.4: Time series of absolute geostrophic surface velocities, trend and annual signal for (a) Fram Strait, (b) EGC and (c) WSC area. Please note a changed scaling of the y-axis.

In order to investigate the connection between the SST and ocean surface velocity, a global daily SST dataset (Canada Meteorological Center (2012), Brasnett (2008)) is used for comparison. The SST grids are a combination of satellite and in situ observations collected for example by ships or an autonomous array of temperature measuring floats (e.g. Argo), provided on a 0.2° resolved, regular grid. In sea ice regions, the grid values are undefined. A conducted frequency analysis (see Appendix, Figure A.4) of the SST limited to the WSC area reveals a clear annual as well as semi-annual signal.

Figure 4.5 shows the temporal evolution of the absolute SST signal and SST anomalies (local offset, trend, annual and semi-annual oscillation are removed) and a comparison with standardized absolute geostrophic current velocity and SST in the WSC area. In order to be consistent with the velocity data, the daily SST are filtered with a 30-day moving average. The standardization is done by removing the mean from the daily values and dividing them by the standard deviation. The comparison of both time series shows a negative correlation of -0.75 , which underlines the relationship between increasing SST and a decreasing absolute geostrophic velocity in the WSC (e.g. Caesar et al. (2018), Praetorius (2018), Dong et al. (2019)).

A positive trend of 0.06°C p.a. indicates a continuous warming of the upper ocean layer (Beszczynska-Möller et al. (2012)). However, short-periodic anomalies underly this trend, revealing cool periods between 1996 - 1998 and slightly weaker ones between 2008 -

2012. A warm phase is identified between 2002 and 2007. Furthermore, a short warming period is identified between 1999-2000. A temperature maximum can be found in 2002 and 2006/2007, whereas the minimum occurs in 1997/1998. Especially in the years 2005 - 2007, permanently positive SST anomalies can be seen.

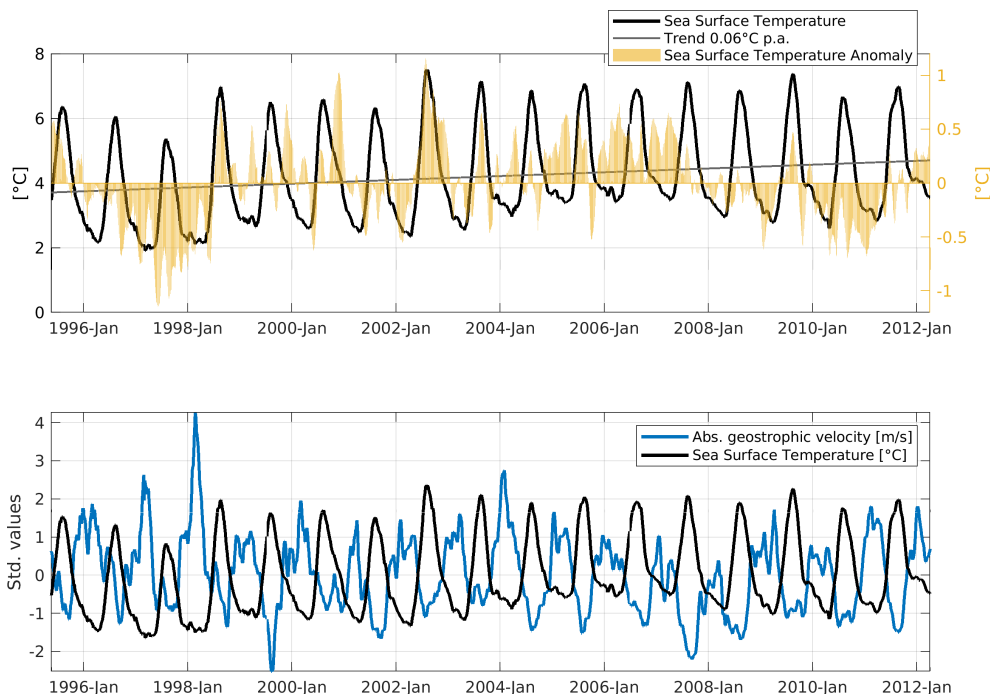


Figure 4.5: The upper plot shows the temporal evolution of the daily SST and reduced by the mean, trend, annual and semi-annual signal. The bottom plot shows a comparison between SST and absolute geostrophic velocities, reduced by their mean and standardized by their standard deviation. Both plots are limited to the WSC area (see dark green box in Fig. 4.1). Both datasets are filtered with a 30-day moving average.

The combined mean absolute geostrophic velocity anomalies of the cool phases (1996-1998, 2008-2012) and warm period (2002-2007) are displayed in Figure 4.6. Therefore, the mean absolute velocities are reduced by the mean speed covering 1995-2012 (Fig. 4.2). The mean absolute velocities are provided in the supplement (see Fig. A.3). Compared to the other periods, Figure 4.6a displays stronger residuals, especially at the continental slopes of the Barents Shelf (i.e. WSC) and the Greenland Shelf (i.e. EGC). Furthermore, Figure 4.6a shows a contrasting flow behavior, compared to Fig. 4.6 b,c in nearly all regions. In particular, the southern parts of the EGC show an opposite sign. During the cold period from 1996-1998, the main flow activity is at the Greenland Shelf, however, between 2002-2007, but also in the following period, there was a weakening in the southern path of the EGC. The NEGCC also shows a contrary behavior. During the cool period, a lower current circulation can be seen, but between 2008-2012 a significant

4 Scientific exploitation of the dataset

increase is visible. Between 1996-1998, the WSC shows stronger velocities close to the Spitsbergen west coast and weaker speeds more away from the coast. During the years, 2002-2012, the situation was completely reversed.

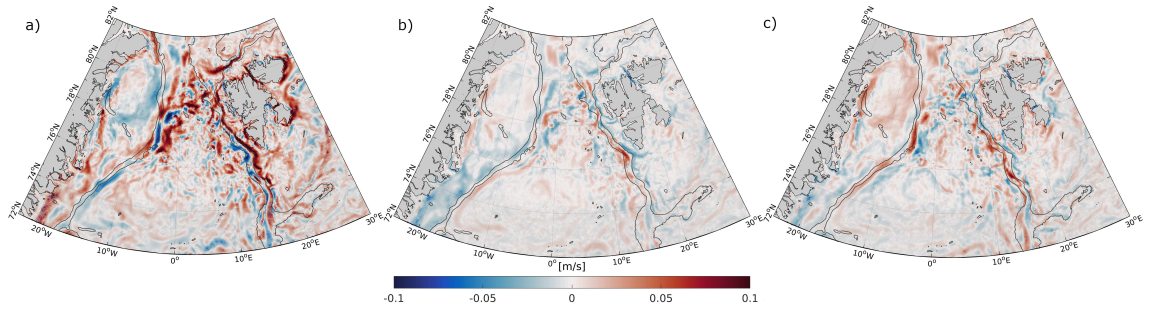


Figure 4.6: Anomalies of averaged absolute geostrophic surface velocity for cool periods, 1996-1998 (a), 2008-2012 (c) and a warm period between 2002-2007 (b) with respect to absolute surface velocity between 1995-2012. Bathymetric contours indicate depths of -1500 m and -450 m, taken from RTopo2 (Schaffer et al. (2016)).

Figure 4.6 provides an overview of different SST anomaly periods. More detailed, Figure 4.7 shows averaged surface currents and SST fields as background data for the winter months (i.e. December to March) 1997/1998 (Fig. 4.7a) and 2006/2007 (Fig. 4.7b). During the SST minimum, the WSC is characterized by strong and straight current patterns following the warm-cold water gradient close to the coast of Spitsbergen displaying a mean velocity of 6.5 cm/s and an averaged SST of 1.5°C. Moreover, an enhanced flow activity is shown in the region of recirculating Atlantic water masses merging with the EGC. In the winter of 2006/2007 the situation has changed. The mean seawater temperature has almost doubled to 3.2°C, while the WSC current velocity has decreased to 4.0 cm/s.

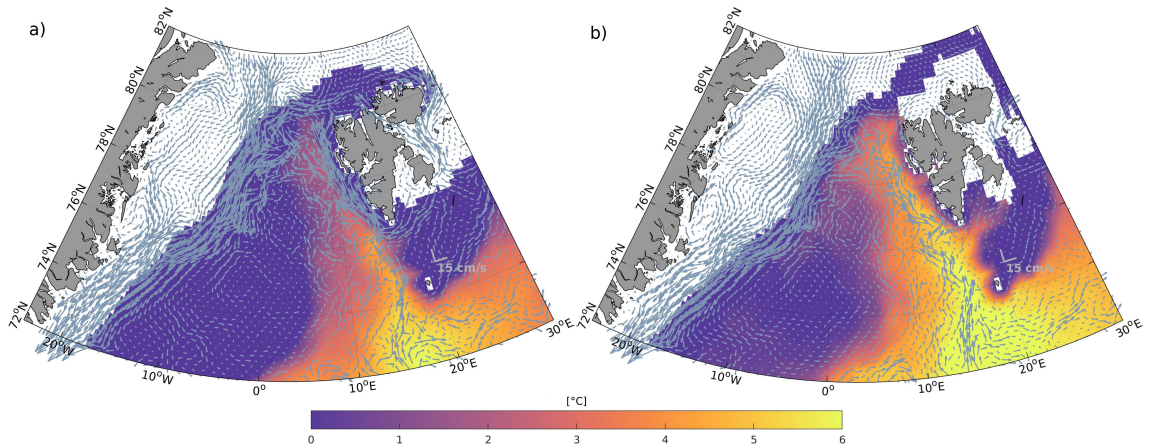


Figure 4.7: Mean surface currents and SST fields for the months of December to March, (a) 1997/1998 and (b) 2006/2007. For readability, the velocity data are interpolated to a regular grid.

A sectional view of the temporal change of the circulation with respect to a certain latitude is provided by Hovmöller diagrams (Fig. 4.8). The daily geostrophic zonal and meridional velocity components are low-pass filtered with a 30-day running mean and plotted versus time and longitude along a fixed latitudinal height of 78.5°N . Moreover, they are interpolated to virtual stations that spanning a chain of points with a regular point distance of 0.1° by computing the mean of the velocity components within a cap-size of 20 km radius around each virtual location. The selected section at the southern part of the Fram Strait (see Figure 4.1) is characterized from east to west, by the northward flowing WSC, recirculating water masses, the southwards flowing EGC, the Greenland Shelf, with very weak current velocities and the NEGCC close to the northeast Greenland coast. The diagrams provide an insight of the different branches of the currents. By analyzing the meridional current component, it turns out that the WSC consists of two branches. The eastern branch flows between 8°E and 10°E straight northwards, whereas the western branch appears broader mainly feeding the recirculation region between 2.5°W and 5°E , which is confirmed by studies based on velocity, salinity and temperature measurements of moored instruments (e.g. Beszczynska-Möller et al. (2012)). The recirculation of the Atlantic water masses is characterized by strong westward velocities in the zonal component around 2°W . A reduced recirculation is apparent in 1999, which also influences the EGC showing a lower flow velocity.

At around 4°W , indicated by dark blue colors in the vertical velocity component, the strongly southwards flowing, shelf-break following part of the EGC is clearly visible. Slightly farther west, weaker flow patterns southwards show parts of the EGC moving on the Greenland shelf. Going farther west, the Greenland Shelf displays weak velocities with no significant temporal changes. However, close to the Greenland coastline, an increasingly stronger and wider current flowing predominantly northwards is observed. This flow section between 17.75°W and 16.5°W belongs to the NEGCC and is mainly fed by incoming recirculated warm Atlantic water masses (e.g. Sneed and Hamilton (2016)), showing its velocity maximum during the summer months with an absolute mean velocity trend of $3.2 \text{ mm/s} \pm 0.1 \text{ mm/s}$ per year (according to Fig. 4.2c,d). Stronger (15-20 cm/s) and longer summer maxima as well as a higher velocity variability between summer and winter can be seen from 2002, which could possibly be related to the start of the warm water period in 2002 (Fig. 4.5 and Fig. 4.6). Close to the coast, the warmer saline water hits the calving northeast glaciers and leads to an intensified melting resulting in an enhanced freshwater input (e.g. Khan et al. (2014), Mayer et al. (2018)). It can be speculated that a warming of the recirculated Atlantic water, combined with an increased input of fresh water, could lead to an acceleration of the general flow velocity of the NEGCC due to increased density differences resulting in stronger horizontal pressure gradients. However, this cannot be fully confirmed due to a lack of long periodic in situ observations. Fig. 4.8 provides a sectional view of the geostrophic velocity currents at 78.5°N . The different branches of the major, but also of subordinated currents (e.g. NEGCC) are clearly visible. However, the trends of EGC and WSC as displayed in Figure 4.4 cannot be identified. Moreover, no significant shifts of the EGC's and WSC's

4 Scientific exploitation of the dataset

current center are detected at this latitude. After 2002, there is a stronger increase which could possibly be related to the start of the warm period around 2002.

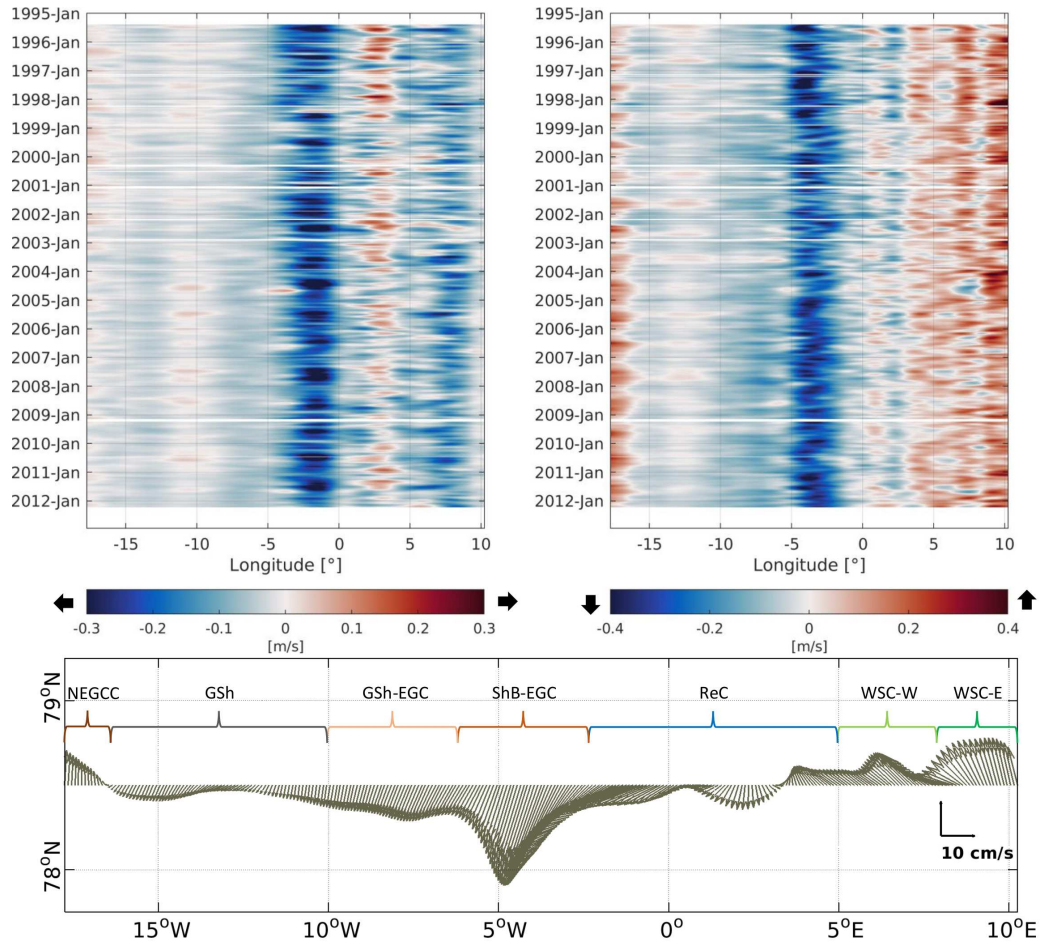


Figure 4.8: Top: Hovmoeller diagrams of daily zonal (left) and meridional (right) surface velocity components at 78.5°N. Black arrows indicate the flow direction. For readability, velocity components are interpolated on a regular grid. Bottom: Long-term mean (1995-2012) of geostrophic surface velocities at 78.5°N indicating different flow areas from west to east (North-East Greenland Coastal Current (NEGCC); Greenland-Shelf (GSh); Greenland Shelf East Greenland Current (GSh-EGC); Shelf-Break East Greenland Current (ShB-EGC); Recirculation (ReC); West Spitsbergen Current West (WSC-W); West Spitsbergen Current East (WSC-E)

5 Conclusions and outlook

The thesis presents a novel method that combines two conceptually different data sources (ocean current model and satellite altimetry) in order to benefit from the advantages of both datasets to perform comprehensive, homogeneous and spatio-temporal high resolution studies of surface circulation in a region of particular importance for the global climate. In addition, the developed method allows studies which are not limited to regional scales, but allows the comprehensive investigation of the surface circulation between the Arctic and Atlantic Ocean.

The thesis describes the development, validation and exploitation of a homogeneous combined ocean current dataset from simulated water level heights by an ocean current model and observed SSHs from satellite altimetry in a region characterized by challenging observation and rapid changing environmental conditions (e.g. due to sea ice coverage). Furthermore, the combination focuses more on the observational part and uses model data to fill and bridge data gaps of satellite altimetry. Moreover, the novel strategy proposed results a dataset covering nearly 17 years with a consistently high spatial and temporal resolution, which contributes to deeper and more comprehensive analyses of the polar ocean surface circulation. The method allows one to study temporal current variations in terms of intensity, velocity trend, annual oscillations and provides information about the location of the major current systems, even if the ocean current is mostly covered by sea ice.

In particular, the processing steps from the detection of open water radar waveforms within the sea ice area by an unsupervised classification, the computation of SSHs by applying a retracker algorithm, working in sea ice and open ocean areas and the derivation of along-track DOT heights by subtracting a high-resolution geoid are described. The thesis continues with a comparison between observed and simulated DOT representations and the combination of both quantities based on a PCA. A short dataset exploitation underlines possible application fields of the combined ocean current dataset.

Based on the presented research topics of this work, the questions formulated in Section 1.2 will be briefly revisited again.

How can altimetry sea surface height observations from open water bodies within the sea ice domain be identified and how can this be validated?

Subsection 2.3.2 presents an unsupervised classification approach, which enables the detection of waveforms reflected by open water bodies within the sea ice domain. More

5 Conclusions and outlook

in detail, the unsupervised classification assigns waveforms to open ocean, sea ice or lead/polynya conditions independent of the altimeter mission and without the use of training or specific knowledge about the surface conditions. The basic principle is an unsupervised search (i.e. clustering) of similar patterns among a set of waveforms using a pre-defined feature set and performing an assignment of the identified clusters to different surface conditions based on physical background knowledge about the waveform shape and reflection behavior. The classification approach can be easily transferred to all available altimetry missions, supporting a reliable detection of usable radar echoes within in regions characterized by challenging surface conditions.

The approach is validated by an automatic and quantitative comparison (Subsection 2.3.3) using image processing techniques applied to SAR images of imaging Earth observation satellites flying simultaneously with the altimetry missions. In order to account for drifting sea ice, the images are shifted with respect to the sea ice drift direction and velocity. The algorithm is not only usable as a validation method but also allows an independent detection of leads/polynyas based on radar images.

More in detail, the question is answered concerning the classification approach in publication P-1.1 and in the case of the quantitative validation in P-1.2.

How do simulated and observed dynamic ocean topography data differ and what should be considered when combining them?

Before the combination, the model and observation data are compared for consistency. Therefore, profiled FESOM- and altimetry-derived DOT are analyzed regarding dominant oscillations and variability patterns. Section 3.2 shows good agreement of both datasets in terms of the annual signal and high correlations in most of the northern Nordic Seas region, but particularly in ice-free areas and current regions with clear flow movements. Differences are shown in terms of the magnitude of the annual signal, showing up to 3 times higher values in the observations, which is explained by an enhanced smoothing of the model due to internal limitations and coarse resolved forcing data. Furthermore, inconsistencies are detected in the sea ice areas, mainly addressed to a higher error budget of the altimetry observations. To summarize, the comparison reveals that a combination of both data sets is useful for taking advantage of both variables in order to best represent ocean currents in this region.

Room for improvement is given by taking care of inconsistencies of the observed and simulated database. In the case of the observations, a large amount of the error budget can be attributed to the underlying geoid. Uncertainties in the higher spherical harmonic degrees and a lack of gravity information cause small-scale deflections of up to several decimeters. However, the following Section 2.3.4 reveals that even with the introduction of newer gravity fields, height deflections will persist and must be considered. In this connection, an improvement for the future can be seen in a comprehensive update of the marine in situ and altimetry gravity database. Furthermore, attention must be

paid to the observed altimeter ranges within the sea ice domain, which suffer from higher uncertainties and scattering. Even after applying sea ice-dedicated algorithms, an enhanced error budget remains.

From the model perspective, the occurring inaccuracies are seen in the strong smoothing and damping effects of the simulated DOT heights, due to coarse and not updated forcing models, in a too strongly adjusted sea ice fraction and numerical diffusion coefficient. Furthermore, inaccuracies in the representation of the annual oscillation are likely caused by a global computation of the model neglecting regional variations, since the freshwater input/output is set by default always integrally 0. In particular, the model only preserves volume by ignoring a steric correction for the complete simulation of mass. Moreover, the model disregards subglacial and submarine melting from the Greenland ice sheet, leading to uncertainties in the correct representation of the recirculating and southwards flowing water masses. Improvements in the model configuration due for example to the application of spatio-temporally high resolved forcing models and a consideration of local freshwater inflow, would lead to a more realistic representation of the most dominant spatial ocean circulation patterns.

The full comparison and assessment are described in P-2.

How does the combination work and how can it be validated?

The comparison method is explained in Section 3.3. Central element of the combination approach is the application of a Principal Component Analysis. However, before the combination is performed, both data sets are reduced by their mean and the annual signal. Afterwards, the 50 most dominant spatial pattern, indicating 99% of the total variance, of the simulated DOT are extracted and linked with the altimetry-derived along-track DOT elevations representing the temporal DOT variations. The result are a time series of principal components, which are multiplied by the corresponding spatial signal of the model. A summation of the multiplication pairs results in a combined dataset. The final dataset is provided by re-adding the altimetry-observed annual signal and offset to reference the combined dataset to the altimetry height level. In order to transform the combined DOT heights to geostrophic velocities, the geostrophic equations (see Section 2.2) are applied to the unstructured triangle mesh.

The combination is validated by independent surface drifter observations, reduced to geostrophic velocities and external multi-satellite datasets. The combination and its validation are described in P-3.

What can be learned from the combination dataset about the temporal variation of the surface currents in the northern Nordic Seas and what should be done in future studies to improve the results?

In order to answer this question, a data exploitation (Section 4) focuses on investigating the major geostrophic surface circulation systems in the northern Nordic Seas.

The data exploitation shows a slight decrease of the mean surface velocity in the WSC, which can be linked to a decrease of flow velocity of the Gulf Stream in the North Atlantic (e.g. Caesar et al. (2018), Praetorius (2018), Dong et al. (2019)) and to an increase of SST in that area. In addition, the surface circulation interacts with warm and cool periods by changing the mean current velocity and the position of the core stream, resulting in a negative correlation of about -0.75 between the temporal evolution of the SST and the mean absolute velocity in the WSC. On the other side, an increasing mean surface current velocity in the EGC area and the Fram Strait is observed. The strongest intensification up to 1.08 cm/s p.a. is shown at the Greenland Shelf edge. An assessment of the annual signal of the EGC circulation velocity reveals a maximum during the winter months. Furthermore, an intensified current circulation at the north Greenland Shelf is detected. These general current velocity behaviors were already observed by regional investigations, for example based on data from in situ buoys (e.g. Walczowski (2014)), but it had not been possible to determine them in high resolution for the whole area for a time period of about 17 years. For example, in contrast to the general trend of increasing velocity in the EGC, regionally decreasing flow velocities are shown in southern regions at the Greenland Shelf.

The western currents are poorly observed, due to challenging monitoring conditions mainly caused by sea ice and irregularly distributed in situ buoys, but this also reveals a big potential for the combined dataset. Furthermore, due to the high spatial resolution of the triangular mesh, the analyses show that it is possible to detect and study current variations in different branches of the major currents. Moreover, it is possible to investigate the flow variability along the east Greenland coast, even if major parts of the flow are beneath the sea ice (i.e. NEGCC). This is highly relevant because warm recirculating Atlantic water flows directly to the outlet glaciers on the coast of Greenland and thus influences their melting (Straneo and Heimbach (2013), Khan et al. (2014), Mayer et al. (2018)). However, it is not yet clear if an enhanced melting and warming of the Atlantic water accelerates the NEGCC. For future investigations, the dataset offers big potential in studying possible couplings between the current velocity and the enhanced freshwater inflow by the adjacent glaciers.

Moreover, the presented data exploitation offers room for further and deeper investigations, since the geostrophic ocean circulation is not only affected by SST variations, but also by changes in salinity, sea ice coverage and a changed freshwater budget. Furthermore, the influence of atmospheric drag, for example caused by wind stress or the sea surface air pressure, extends the study fields. In order to estimate and understand the total ocean circulation, these effects must be included.

The combined dataset covers a period of nearly 17 years (1995/05 - 2012/04) and provides geostrophic surface ocean current information of an area responsible for a worth living climate in Europe. The northern Nordic Seas are the most important factor for mild and mainly stable temperatures in northern Europe, since they are the northern extension of the Gulf Stream and the Norwegian Atlantic Current. Furthermore, the northern Nordic Seas represent the most important gateway between the Arctic and the Atlantic Ocean and have a significant influence on the global thermohaline circulation. Of course, 17 years are not enough to make climate relevant conclusions, manifested by the appearance of short periodically warm and cool phases within the investigation period. However, the combined dataset helps to detect and understand short spatio-temporal circulation patterns in the open ocean and within sea ice areas and it enables correlations with other ocean variables (e.g. SST). Moreover, the proposed combination method can be easily extended to all currently available altimetry data resulting in a combined dataset of more than 25 years.

It can be highly recommended to minimize detected issues by introducing an updated and more realistic simulation database for future processing or extension of the dataset. Moreover, it makes sense to extend the classification and retracking algorithms, developed within the framework of this thesis, to the entire satellite altimetry database to enable statements and predictions in the context of global and local climate changes. The work finally proves a successful combination of observed and simulated data on the same processing level and can contribute to a deeper understanding of ocean surface circulation in polar regions. Furthermore, this work extends existing products to a higher spatio-temporal resolved representation of the ocean surface circulation based on observations and simulations. Finally, the developed methodology can easily be extended and transferred to other polar ocean regions on Earth.

Abbreviations

Abbreviation	Description	Page Number
ALES	Adaptive Leading Edge Subwaveform	16–18
ALES+	Adaptive Leading Edge Subwaveform+	12, 16–18, 106
ALOS	Advanced Land Observing Satellite	7, 20
CNES	Centre National d' Études Spatiales	6, 9, 10, 144
DD	Delay-Doppler	14, 16, 88
DORIS	Doppler Orbitography and Radiopositioning Integrated by Satellite	12
DOT	dynamic ocean topography	iii, iv, vi, 2, 3, 5, 7, 10–12, 14, 16, 21–23, 25, 27–29, 41–43, 47, 106, 124, 125
DTU10GRA	DTU10 gravity anomalies	21–23, 48
DWH	differential water height	10, 25–27, 106
EGC	East Greenland Current	1, 4, 5, 28, 32–34, 36–39, 44, 48
EIGEN6-C4	European Improved Gravity model of the Earth by New techniques 6-C4	21
Envisat	Environmental Satellite	6, 7, 9–12, 17, 19, 20, 22, 25, 27, 47, 49, 67, 88, 106, 124, 144, 145
Envisat-EM	Environmental Satellite - Extended Mission	10, 11, 49, 144
ERS-1	European Remote Sensing Satellite-1	9, 10, 21
ERS-2	European Remote Sensing Satellite-2	6, 9–11, 19, 25, 49, 124, 144
ESA	European Space Agency	6, 7, 9, 10, 63, 124, 144
FESOM	Finite Element Sea Ice Ocean Model	7, 10, 25, 26, 28, 29, 42, 106, 124
GNSS	Global Navigation Satellite System	12
GOCE	Gravity field and steady-state Ocean Circu- lation Explorer	21
GRACE	Gravity Recovery And Climate Experiment	2, 21

Abbreviations

Abbreviation	Description	Page Number
ICESat	Ice, Clouds, and Land Elevation Satellite	10
ICESat-2	Ice, Clouds, and Land Elevation Satellite-2	10
ISRO	Indian Space Research Organisation	6, 9, 144
JAXA	Japan Aerospace Exploration Agency	7
MDA	Mac Donald, Dettwiler and Associates Ltd.	7
NASA	National Aeronautics and Space Administration	10
NEGCC	North-East Greenland Coastal Current	32, 33, 37, 39, 44
OGMOC	Optimal Geoid Model for Modeling Ocean Circulation	21, 22, 27, 106
PCA	Principal Component Analysis	iv, 7, 28, 41, 43, 124
PP	Pulse-Peakiness	17, 18, 49, 88, 145
RIP	Range Integrated Power	88
RTopo2	Refined Topography-2	4, 22, 23, 26, 31, 32, 38, 47–49, 145
SAR	Synthetic Aperture Radar	iii, 7, 9, 10, 14, 19, 20, 42, 67, 88, 89
SARAL	Satellite with Argos and AltiKa	6, 9–11, 19, 20, 49, 67, 144
SLR	Satellite Laser Ranging	12
SSH	sea surface height	2, 3, 9, 12–16, 19, 21, 41, 47, 67, 106
SST	sea surface temperature	iv, 34, 36–38, 44, 45, 48, 49, 145
USO	Ultra-Stable Oscillator	14
WSC	West Spitsbergen Current	1, 3, 32–34, 36–39, 44, 48, 49, 145
XGM2016	Experimental gravity field model 2016	21

List of Figures

1.1	Topography based on RTopo2 model (Schaffer et al. (2016)) and major surface flow of the northern Nordic Seas including the Greenland Sea (GS), Barents Sea (BS), and Fram Strait (FS). The Arctic Ocean (AO), Denmark Strait (DS) and Norwegian Sea (NS) mark adjacent seas. Red arrows indicate inflowing Atlantic Water (West Spitsbergen Current, WSC; Yermak Branch, YB; Svalbard Branch, SB and Norwegian Atlantic Current, NWAC). Outflowing Polar Water is highlighted in blue (East Greenland Current, EGC; North-East Greenland Coastal Current, NEGCC). Thinner lines indicate subordinated currents.	4
1.2	Connection of the four publications, which set the frame for this thesis. Light blue indicates investigations based on observational datasets only, blue the usage of both, simulations and observations. The arrows outline results and obtained knowledge that are transferred between the publications.	6
2.1	Timeline of radar altimetry missions included in the thesis and their application in each publication.	11
2.2	Observation (left) and geometric (right) principle of satellite altimetry. The left side shows in an exemplary way an Envisat waveform during normal open ocean conditions. The retracked range (r_{ret}) and the epoch are shown in red, the reference range (r_{ref}) in black. Circles indicate the propagation direction of the radar signals hitting the surface. The right side displays the relationship between range, orbital height, sea surface height, geoid and dynamic ocean topography.	12
2.3	Examples of Envisat open ocean (Brown-like, left) and calm water (single-peak; right) waveforms. Green indicates the leading edge; orange highlights the trailing edge.	17
2.4	Examples of Envisat-derived along-track DOT elevations averaged for January (left) and September (right) and arranged into bins of 7.5 km length between 2003-2009. RTopo2 bathymetric lines (Schaffer et al. (2016)) indicate the Greenland Sea Basin (-1500 m) and the Greenland Shelf (-450 m).	22

LIST OF FIGURES

2.5 Comparison between (a) DTU10GRA - DTU15GRA, (b) DTU10GRA - DTU17GRA (c) DTU13GRA - DTU15GRA and (d) DTU15GRA - DTU17GRA gravity fields in terms of gravity anomalies in mGal. Contour lines indicate depths of -450 m and -1500 m, taken from RTopo2 (Schaffer et al. (2016)). 23

4.1 Mean surface current flow in the northern Nordic Seas derived from combined geostrophic datasets with RTopo2 bathymetry (Schaffer et al. (2016)) in the background between 1995 - 2012. Study areas for extended investigation are highlighted (polygons, line). 31

4.2 At the top: Mean absolute geostrophic surface velocity (a) and standard deviation (b). At the bottom: Surface velocity trend (c) and estimated uncertainty (d). Bathymetric contours indicate depths of -1500 m and -450 m, taken from RTopo2 (Schaffer et al. (2016)). 32

4.3 Monthly averaged ocean surface velocities within the investigation period, 1995-2012. 35

4.4 Time series of absolute geostrophic surface velocities, trend and annual signal for (a) Fram Strait, (b) EGC and (c) WSC area. Please note a changed scaling of the y-axis. 36

4.5 The upper plot shows the temporal evolution of the daily SST and reduced by the mean, trend, annual and semi-annual signal. The bottom plot shows a comparison between SST and absolute geostrophic velocities, reduced by their mean and standardized by their standard deviation. Both plots are limited to the WSC area (see dark green box in Fig. 4.1). Both datasets are filtered with a 30-day moving average. 37

4.6 Anomalies of averaged absolute geostrophic surface velocity for cool periods, 1996-1998 (a), 2008-2012 (c) and a warm period between 2002-2007 (b) with respect to absolute surface velocity between 1995-2012. Bathymetric contours indicate depths of -1500 m and -450 m, taken from RTopo2 (Schaffer et al. (2016)). 38

4.7 Mean surface currents and SST fields for the months of December to March, (a) 1997/1998 and (b) 2006/2007. For readability, the velocity data are interpolated to a regular grid. 38

LIST OF FIGURES

4.8 Top: Hovmoeller diagrams of daily zonal (left) and meridional (right) surface velocity components at 78.5°N. Black arrows indicate the flow direction. For readability, velocity components are interpolated on a regular grid. Bottom: Long-term mean (1995-2012) of geostrophic surface velocities at 78.5°N indicating different flow areas from west to east (North-East Greenland Coastal Current (NEGCC); Greenland-Shelf (GSh); Greenland Shelf East Greenland Current (GSh-EGC); Shelf-Break East Greenland Current (ShB-EGC); Recirculation (ReC); West Spitsbergen Current West (WSC-W); West Spitsbergen Current East (WSC-E) 40

A.1 Ground track patterns of ERS-2, Envisat and SARAL in dark red; the drifting orbit phase of Environmental Satellite - Extended Mission (Envisat-EM) in green and Jason-1,2,3 in orange. The investigation area is defined by 72°N to 82°N and -30°W to 30°E (Figure 1.1) 146

A.2 Examples of Envisat waveforms for open ocean (left), sea ice (middle) and lead / polynya (right) conditions with Pulse-Peakiness (PP) values. 147

A.3 Averaged geostrophic surface velocity for cool periods, 1996-1998 (a), 2008-2012 (c) and a warm period between 2002-2007 (b). Bathymetric contours indicate depths of -1500 m and -450 m, taken from RTopo2 (Schaffer et al. (2016)). 147

A.4 Fourier analysis amplitude spectrum of the sea surface temperature within the WSC area between 1995-2012. 147

Bibliography

- Andersen, O., Knudsen, P., Kenyon, S., Factor, J., and Holmes, S. (2017). Global gravity field from recent satellites (dtu15) - arctic improvements. *First Break*, 35(12):37–40, ISSN: 0263-5046, DOI: 10.3997/1365-2397.2017022.
- Andersen, O. B. (2010). The dtu10 gravity field and mean sea surface. Second international symposium of the gravity field of the Earth (IGFS2), Fairbanks, Alaska.
- Andersen, O. B. and Knudsen, P. (2020). The dtu17 global marine gravity field: First validation results. In Mertikas, S. P. and Pail, R., editors, *Fiducial Reference Measurements for Altimetry*, pages 83–87. Springer International Publishing, ISBN: 978-3-030-39438-7, DOI: 10.1007/978-3-030-39438-7.
- Andersen, O. B., Knudsen, P., Kenyon, S., and Holmes, S. (2014). Global and arctic marine gravity field from recent satellite altimetry (dtu13). 2014(1):1–5, ISSN: 2214-4609, DOI: 10.3997/2214-4609.20140897.
- Androsov, A., Nerger, L., Schnur, R., Schröter, J., Albertella, A., Rummel, R., Savcenko, R., Bosch, W., Skachko, S., and Danilov, S. (2018). On the assimilation of absolute geodetic dynamic topography in a global ocean model: impact on the deep ocean state. *Journal of Geodesy*, ISSN: 1432-1394, DOI: 10.1007/s00190-018-1151-1.
- Armitage, T. W. K., Bacon, S., Ridout, A. L., Petty, A. A., Wolbach, S., and Tsamados, M. (2017). Arctic ocean surface geostrophic circulation 2003–2014. *The Cryosphere*, 11(4):1767–1780, DOI: 10.5194/tc-11-1767-2017.
- Beckers, J. M. and Rixen, M. (2003). Eof calculations and data filling from incomplete oceanographic datasets. *Journal of Atmospheric and Oceanic Technology*, 20(12):1839–1856, DOI: 10.1175/1520-0426(2003)020<1839:ECADFF>2.0.CO;2.
- Beszczyńska-Möller, A., Fahrbach, E., Schauer, U., and Hansen, E. (2012). Variability in Atlantic water temperature and transport at the entrance to the Arctic Ocean, 1997–2010. *ICES J. Mar. Sci.*, 69:852–863, DOI: 10.1093/icesjms/fss056.
- Blindheim, J. and Østerhus, S. (2013). *The Nordic Seas, Main Oceanographic Features*, pages 11–37. American Geophysical Union (AGU), ISBN: 9781118666296, DOI: 10.1029/158GM03.
- Brambilla, E., Talley, L. D., and Robbins, P. E. (2008). Subpolar mode water in the northeastern atlantic: 2. origin and transformation. *Journal of Geophysical Research: Oceans*, 113(C4), DOI: 10.1029/2006JC004063.

BIBLIOGRAPHY

- Brasnett, B. (2008). The impact of satellite retrievals in a global sea-surface-temperature analysis. *Quarterly Journal of the Royal Meteorological Society*, 134(636):1745–1760, DOI: 10.1002/qj.319.
- Bronner, E., Guillot, A., Picot, N., and Noubel, J. (2016). SARAL/AltiKa Products Handbook, P-MU-M-OP-15984-CN, Issue: 2 rev 5.
- Brown, G. (1977). The average impulse response of a rough surface and its applications. *IEEE Transactions on Antennas and Propagation*, 25(1):67–74, ISSN: 0018-926X, DOI: 10.1109/TAP.1977.1141536.
- Bulczak, A. I., Bacon, S., Naveira Garabato, A. C., Ridout, A., Sonnewald, M. J. P., and Laxon, S. W. (2015). Seasonal variability of sea surface height in the coastal waters and deep basins of the nordic seas. *Geophysical Research Letters*, 42(1):113–120, ISSN: 1944-8007, DOI: 10.1002/2014GL061796. 2014GL061796.
- Caesar, L., Rahmstorf, S., Robinson, A., Feulner, G., and Saba, V. (2018). Observed fingerprint of a weakening atlantic ocean overturning circulation. *Nature*, 556(7700):191–196, DOI: 10.1038/s41586-018-0006-5.
- Canada Meteorological Center (2012). Ghrrsst level 4 cmc0.2deg global foundation sea surface temperature analysis (gds version 2). DOI: 10.5067/GHCMC-4FM02, <http://podaac.jpl.nasa.gov/dataset/CMC0.2deg-CMC-L4-GLOB-v2.0>. [subset: Greenland Sea, Date accessed: 01.04.2020].
- Celebi, M. (2014). *Partitional Clustering Algorithms*. EBL-Schweitzer. Springer International Publishing, ISBN: 9783319092591.
- Chafik, L., Nilsen, J. E. Ø., Dangendorf, S., Reverdin, G., and Frederikse, T. (2019). North atlantic ocean circulation and decadal sea level change during the altimetry era. *Scientific Reports*, 9(1):1041, ISSN: 2045-2322, DOI: 10.1038/s41598-018-37603-6.
- Church, J. A., White, N. J., Coleman, R., Lambeck, K., and Mitrovica, J. X. (2004). Estimates of the regional distribution of sea level rise over the 1950–2000 period. *Journal of Climate*, 17(13):2609–2625, DOI: 10.1175/1520-0442(2004)017<2609:EOTRDO>2.0.CO;2.
- Connor, L. N., Laxon, S. W., Ridout, A. L., Krabill, W. B., and McAdoo, D. C. (2009). Comparison of Envisat radar and airborne laser altimeter measurements over Arctic sea ice. *Remote Sensing of Environment*, 113(3):563–570, ISBN: 0034-4257, ISSN: 00344257, DOI: 10.1016/j.rse.2008.10.015.
- Crews, L., Sundfjord, A., Albretsen, J., and Hattermann, T. (2018). Mesoscale eddy activity and transport in the atlantic water inflow region north of svalbard. *Journal of Geophysical Research: Oceans*, 123(1):201–215, DOI: 10.1002/2017JC013198.
- Dai, A., Qian, T., Trenberth, K. E., and Milliman, J. D. (2009). Changes in Continental Freshwater Discharge from 1948 to 2004. *J. Climate*, 22:2773–2792, DOI: 10.1175/2008JCLI2592.1.

- Danilov, S., Kivman, G., and Schröter, J. (2004). A finite-element ocean model: principles and evaluation. *Ocean Modelling*, 6(2):125 – 150, ISSN: 1463-5003, DOI: 10.1016/S1463-5003(02)00063-X.
- Davis, C. H. (1997). A robust threshold retracking algorithm for measuring ice-sheet surface elevation change from satellite radar altimeters. *IEEE Transactions on Geoscience and Remote Sensing*, 35(4):974–979, ISSN: 1558-0644, DOI: 10.1109/36.602540.
- de Steur, L., Hansen, E., Mauritzen, C., Beszczynska-Möller, A., and Fahrback, E. (2014). Impact of recirculation on the east greenland current in fram strait: Results from moored current meter measurements between 1997 and 2009. *Deep Sea Research Part I: Oceanographic Research Papers*, 92:26 – 40, ISSN: 0967-0637, DOI: 10.1016/j.dsr.2014.05.018.
- Dettmering, D., Wynne, A., Müller, F. L., Passaro, M., and Seitz, F. (2018). Lead detection in polar oceans—a comparison of different classification methods for cryosat-2 sar data. *Remote Sensing*, 10(8), ISSN: 2072-4292, DOI: 10.3390/rs10081190.
- Dong, S., Baringer, M. O., and Goni, G. J. (2019). Slow down of the gulf stream during 1993–2016. *Scientific Reports*, 9(1), DOI: 10.1038/s41598-019-42820-8.
- Forsberg, R. and Skourup, H. (2005). Arctic ocean gravity, geoid and sea-ice freeboard heights from icesat and grace. *Geophysical Research Letters*, 32(21), DOI: 10.1029/2005GL023711.
- Förste, C., Bruinsma, S., Abrikosov, O., Lemoine, J.-M., Marty, J. C., Flechtner, F., Balmino, G., Barthelmes, F., and Biancale, R. (2014). Eigen-6c4 the latest combined global gravity field model including goce data up to degree and order 2190 of gfz potsdam and grgs toulouse. GFZ Data Services, DOI: 10.5880/icgem.2015.1.
- Griffies, S. M. (2004). *Fundamentals of Ocean Climate Models*. Princeton University Press, ISBN: 978-0-691-11892-5.
- Gruber, T. and Willberg, M. (2019). Signal and error assessment of GOCE-based high resolution gravity field models. *Journal of Geodetic Science*, 9(1):71–86, DOI: 10.1515/jogs-2019-0008.
- Göttl, F., Dettmering, D., Müller, F. L., and Schwatke, C. (2016). Lake level estimation based on cryosat-2 sar altimetry and multi-looked waveform classification. *Remote Sensing*, 8(11), ISSN: 2072-4292, DOI: 10.3390/rs8110885.
- Hayne, G. (1980). Radar altimeter mean return waveforms from near-normal-incidence ocean surface scattering. *IEEE Transactions on Antennas and Propagation*, 28(5):687–692, ISSN: 0018-926X, DOI: 10.1109/TAP.1980.1142398.
- Holliday, N. P., Hughes, S. L., Bacon, S., Beszczynska-Möller, A., Hansen, B., Lavín, A., Loeng, H., Mork, K. A., Østerhus, S., Sherwin, T., and Walczowski, W. (2008). Reversal of the 1960s to 1990s freshening trend in the northeast north atlantic and nordic seas. *Geophysical Research Letters*, 35(3), DOI: 10.1029/2007GL032675.

BIBLIOGRAPHY

- Hurdle, B. G., editor (1986). *The Nordic Seas*. Springer New York, DOI: 10.1007/978-1-4615-8035-5.
- Håvik, L., Pickart, R. S., Våge, K., Torres, D., Thurnherr, A. M., Beszczynska-Möller, A., Walczowski, W., and von Appen, W.-J. (2017). Evolution of the east greenland current from fram strait to denmark strait: Synoptic measurements from summer 2012. *Journal of Geophysical Research: Oceans*, 122(3):1974–1994, DOI: 10.1002/2016JC012228.
- Khan, S. A., Bevis, M., Bamber, J. L., Wahr, J., Kjeldsen, K. K., Korsgaard, N. J., Stearns, L. A., Liu, L., Larsen, N. K., and S., M. I. (2014). Sustained mass loss of the northeast Greenland ice sheet triggered by regional warming. (March), DOI: 10.1038/NCLIMATE2161.
- Koch, K.-R. (1999). *Parameter Estimation and Hypothesis Testing in Linear Models*. Springer Berlin Heidelberg, DOI: 10.1007/978-3-662-03976-2.
- Koszalka, I., LaCasce, J., Andersson, M., Orvik, K., and Mauritzen, C. (2011). Surface circulation in the nordic seas from clustered drifters. *Deep Sea Research Part I: Oceanographic Research Papers*, 58(4):468 – 485, ISSN: 0967-0637, DOI: 10.1016/j.dsr.2011.01.007.
- Kvingedal, B. (2013). *Sea-Ice Extent and Variability in the Nordic Seas, 1967–2002*, pages 39–49. American Geophysical Union, ISBN: 9781118666296, DOI: 10.1029/158GM04.
- Kwok, R., Cunningham, G. F., Wensnahan, M., Rigor, I., Zwally, H. J., and Yi, D. (2009). Thinning and volume loss of the arctic ocean sea ice cover: 2003–2008. *Journal of Geophysical Research: Oceans*, 114(C7), DOI: 10.1029/2009JC005312.
- Kwok, R. and Morison, J. (2015). Sea surface height and dynamic topography of the ice-covered oceans from cryosat-2: 2011–2014. *Journal of Geophysical Research: Oceans*, 121(1):674–692, DOI: 10.1002/2015JC011357.
- Langehaug, H. R., Mjell, T. L., Otterå, O. H., Eldevik, T., Ninnemann, U. S., and Kleiven, H. F. (2016). On the reconstruction of ocean circulation and climate based on the “gardar drift”. *Paleoceanography*, 31(3):399–415, DOI: 10.1002/2015PA002920.
- Large, W. G. and Yeager, S. G. (2008). The global climatology of an interannually varying air–sea flux data set. *Climate Dynamics*, 33(2-3):341–364, DOI: 10.1007/s00382-008-0441-3.
- Marshall, J., Hill, C., Perelman, L., and Adcroft, A. (1997). Hydrostatic, quasi-hydrostatic, and nonhydrostatic ocean modeling. *Journal of Geophysical Research: Oceans*, 102(C3):5733–5752, DOI: 10.1029/96JC02776.
- Mayer, C., Schaffer, J., Hattermann, T., Floricioiu, D., Krieger, L., Dodd, P. A., Kanzow, T., Licciulli, C., and Schannwell, C. (2018). Large ice loss variability

- at nioghalvfjærdsfjorden glacier, northeast-greenland. *Nature Communications*, 9(1), DOI: 10.1038/s41467-018-05180-x.
- McAdoo, D. C., Farrell, S. L., Laxon, S., Ridout, A., Zwally, H. J., and Yi, D. (2013). Gravity of the arctic ocean from satellite data with validations using airborne gravimetry: Oceanographic implications. *Journal of Geophysical Research: Oceans*, 118(2):917–930, DOI: 10.1002/jgrc.20080.
- Müller, F. L., Dettmering, D., Bosch, W., and Seitz, F. (2017). Monitoring the arctic seas: How satellite altimetry can be used to detect open water in sea-ice regions. *Remote Sensing*, 9(6), ISSN: 2072-4292, DOI: 10.3390/rs9060551.
- Müller, F. L., Dettmering, D., Wekerle, C., Schwatke, C., Bosch, W., and Seitz, F. (2019). Geostrophic Currents in the northern Nordic Seas - A Combined Dataset of Multi-Mission Satellite Altimetry and Ocean Modeling (data). DOI: 10.1594/PANGAEA.900691.
- Müller, F. L., Dettmering, D., Wekerle, C., Schwatke, C., Passaro, M., Bosch, W., and Seitz, F. (2019a). Geostrophic currents in the northern nordic seas from a combination of multi-mission satellite altimetry and ocean modeling. *Earth System Science Data*, 11(4):1765–1781, DOI: 10.5194/essd-11-1765-2019.
- Müller, F. L., Wekerle, C., Dettmering, D., Passaro, M., Bosch, W., and Seitz, F. (2019b). Dynamic ocean topography of the northern nordic seas: a comparison between satellite altimetry and ocean modeling. *The Cryosphere*, 13(2):611–626, DOI: 10.5194/tc-13-611-2019.
- Orvik, K. A. and Niiler, P. (2002). Major pathways of Atlantic water in the northern North Atlantic and Nordic Seas toward Arctic. *Geophysical Research Letters*, 29(19), DOI: 10.1029/2002GL015002.
- Pail, R., Fecher, T., Barnes, D., Factor, J. F., Holmes, S. A., Gruber, T., and Zingerle, P. (2018). Short note: the experimental geopotential model xgm2016. *Journal of Geodesy*, 92(4):443–451, ISSN: 1432-1394, DOI: 10.1007/s00190-017-1070-6.
- Passaro, M., Cipollini, P., Vignudelli, S., Quartly, G. D., and Snaith, H. M. (2014). Ales: A multi-mission adaptive subwaveform retracker for coastal and open ocean altimetry. *Remote Sensing of Environment*, 145:173 – 189, ISSN: 0034-4257, DOI: 10.1016/j.rse.2014.02.008.
- Passaro, M., Kildegaard, S. R., Andersen, O. B., Boergens, E., Calafat, F. M., Dettmering, D., and Benveniste, J. (2018a). Ales+: Adapting a homogenous ocean retracker for satellite altimetry to sea ice leads, coastal and inland waters. *Remote Sensing of Environment*, ISSN: 0034-4257, DOI: 10.1016/j.rse.2018.02.074.
- Passaro, M., Müller, F. L., and Dettmering, D. (2018b). Lead detection using cryosat-2 delay-doppler processing and sentinel-1 sar images. *Advances in Space Research*, 62(6):1610 – 1625, ISSN: 0273-1177, DOI: 10.1016/j.asr.2017.07.011.

BIBLIOGRAPHY

- Peacock, N. R. and Laxon, S. W. (2004). Sea surface height determination in the arctic ocean from ers altimetry. *Journal of Geophysical Research: Oceans*, 109(C7), DOI: 10.1029/2001JC001026.
- Persson, O. and Vihma, T. (2016). *The atmosphere over sea ice*, chapter 6, pages 160–196. John Wiley & Sons, Ltd, ISBN: 9781118778371, DOI: 10.1002/9781118778371.ch6.
- Phalippou, L. and Enjolras, V. (2007). Re-tracking of sar altimeter ocean power-waveforms and related accuracies of the retrieved sea surface height, significant wave height and wind speed. In *2007 IEEE International Geoscience and Remote Sensing Symposium*, pages 3533–3536. ISSN: 2153-7003, DOI: 10.1109/IGARSS.2007.4423608.
- Praetorius, S. K. (2018). North atlantic circulation slows down. *Nature*, 556(7700):180–181, DOI: 10.1038/d41586-018-04086-4.
- Preisendorfer, R. W. (1988). *Principal component analysis in meteorology and oceanography*. Amsterdam ; New York : Elsevier ; New York, NY, U.S.A. : Distributors for the U.S. and Canada, Elsevier Science Pub. Co., ISBN: 9780444430144.
- Quartly, G. D., Rinne, E., Passaro, M., Andersen, O. B., Dinardo, S., Fleury, S., Guillot, A., Hendricks, S., Kurekin, A. A., Müller, F. L., Ricker, R., Skourup, H., and Tsamados, M. (2019). Retrieving sea level and freeboard in the arctic: A review of current radar altimetry methodologies and future perspectives. *Remote Sensing*, 11(7), ISSN: 2072-4292, DOI: 10.3390/rs11070881.
- Raney, R. K. (1998). The delay/doppler radar altimeter. *IEEE Transactions on Geoscience and Remote Sensing*, 36(5):1578–1588, ISSN: 1558-0644, DOI: 10.1109/36.718861.
- Ray, R. D. and Douglas, B. C. (2011). Experiments in reconstructing twentieth-century sea levels. *Progress in Oceanography*, 91(4):496 – 515, ISSN: 0079-6611, DOI: 10.1016/j.pocean.2011.07.021.
- Rhines, P., Häkkinen, S., and Josey, S. A. (2008). *Is Oceanic Heat Transport Significant in the Climate System?*, pages 87–109. Springer Netherlands, Dordrecht, ISBN: 978-1-4020-6774-7, DOI: 10.1007/978-1-4020-6774-7_5.
- Richter, M. E., von Appen, W.-J., and Wekerle, C. (2018). Does the east greenland current exist in the northern fram strait? *Ocean Science*, 14(5):1147–1165, DOI: 10.5194/os-14-1147-2018.
- Rosmorduc, V., Benveniste, J., Bronner, E., Dinardo, S., Lauret, O., Maheu, C., Milagro, M., Picot, N., Ambrozio, A., Escolà, R., Garcia-Mondejar, A., Schrama, E., Restano, M., and Terra-Homem, M. (2018). Radar altimetry tutorial. http://www.altimetry.info/filestorage/Radar_Altimetry_Tutorial.pdf.

- Rudels, B. (2012). Arctic ocean circulation and variability - advection and external forcing encounter constraints and local processes. *Ocean Science*, 8(2):261–286, DOI: 10.5194/os-8-261-2012.
- Rudels, B., J. Friedrich, H., and Quadfasel, D. (1999). The arctic circumpolar boundary current. *Deep Sea Research Part II: Topical Studies in Oceanography*, 46(6):1023 – 1062, ISSN: 0967-0645, DOI: 10.1016/S0967-0645(99)00015-6.
- Rudels, B., Korhonen, M., Budéus, G., Beszczynska-Möller, A., Schauer, U., Nummelin, A., Quadfasel, D., and Valdimarsson, H. (2012). The East Greenland Current and its impacts on the Nordic Seas: observed trends in the past decade. *ICES Journal of Marine Science*, 69(5):841–851, ISSN: 1054-3139, DOI: 10.1093/icesjms/fss079.
- Sansò, F. and Sideris, M. G., editors (2013). *Geoid Determination*. Springer Berlin Heidelberg, DOI: 10.1007/978-3-540-74700-0.
- Schaffer, J., Timmermann, R., Arndt, J. E., Kristensen, S. S., Mayer, C., Morlighem, M., and Steinhage, D. (2016). A global high-resolution data set of ice sheet topography, cavity geometry and ocean bathymetry. *Earth System Science Data Discussions*, 2016:1–21, DOI: 10.5194/essd-2016-3.
- Schmeer, M., Schmidt, M., Bosch, W., and Seitz, F. (2012). Separation of mass signals within grace monthly gravity field models by means of empirical orthogonal functions. *Journal of Geodynamics*, 59-60:124 – 132, ISSN: 0264-3707. Mass Transport and Mass Distribution in the System Earth.
- Selyuzhenok, V., Bashmachnikov, I., Ricker, R., Vesman, A., and Bobylev, L. (2020). Sea ice volume variability and water temperature in the greenland sea. *The Cryosphere*, 14(2):477–495, DOI: 10.5194/tc-14-477-2020.
- Serreze, M. and Barry, R. (2014). *The Arctic Climate System*. Cambridge Atmospheric and Space Science Series. Cambridge University Press, ISBN: 9781139952484.
- Skourup, H., Farrell, S. L., Hendricks, S., Ricker, R., Armitage, T. W. K., Ridout, A., Andersen, O. B., Haas, C., and Baker, S. (2017). An assessment of state-of-the-art mean sea surface and geoid models of the arctic ocean: Implications for sea ice freeboard retrieval. *Journal of Geophysical Research: Oceans*, 122(11):8593–8613, DOI: 10.1002/2017JC013176.
- Sneed, W. A. and Hamilton, G. S. (2016). Recent changes in the norske Øer ice barrier, coastal northeast greenland. *Annals of Glaciology*, 57(73):47–55, DOI: 10.1017/aog.2016.21.
- Steele, M., Morley, R., and Ermold, W. (2001). PHC: a global ocean hydrography with a high-quality Arctic Ocean. *J. Climate*, 14:2079–2087, DOI: 10.1175/1520-0442(2001)014<2079:PAGOHW>2.0.CO;2.

BIBLIOGRAPHY

- Stewart, R. H. (2009). *Introduction to physical oceanography*. University Press of Florida, ISBN: 978-1616100452.
- Straneo, F. and Heimbach, P. (2013). North atlantic warming and the retreat of greenlands outlet glaciers. *Nature*, 504(7478):36–43, DOI: 10.1038/nature12854.
- Talley, L. D. (2008). Freshwater transport estimates and the global overturning circulation: Shallow, deep and throughflow components. *Progress in Oceanography*, 78(4):257 – 303, ISSN: 0079-6611, DOI: 10.1016/j.pocean.2008.05.001.
- Teigen, S. H., Nilsen, F., Skogseth, R., Gjevik, B., and Beszczynska-Möller, A. (2011). Baroclinic instability in the west spitsbergen current. *Journal of Geophysical Research: Oceans*, 116(C7), DOI: 10.1029/2011JC006974.
- Temam, R. and Ziane, M. (2005). Chapter 6 - some mathematical problems in geophysical fluid dynamics. volume 3 of *Handbook of Mathematical Fluid Dynamics*, pages 535 – 658. North-Holland, ISSN: 1874-5792, DOI: 10.1016/S1874-5792(05)80009-6.
- Tran, N., Vandemark, D., Labroue, S., Feng, H., Chapron, B., Tolman, H. L., Lambin, J., and Picot, N. (2010). Sea state bias in altimeter sea level estimates determined by combining wave model and satellite data. *Journal of Geophysical Research: Oceans*, 115(C3), DOI: 10.1029/2009JC005534.
- Vignudelli, S., Kostianoy, A. G., Cipollini, P., and Benveniste, J., editors (2011). *Coastal Altimetry*. Springer Berlin Heidelberg, DOI: 10.1007/978-3-642-12796-0.
- Vignudelli, S., Scozzari, A., Abileah, R., Gómez-Enri, J., Benveniste, J., and Cipollini, P. (2019). Chapter four - water surface elevation in coastal and inland waters using satellite radar altimetry. In Maggioni, V. and Massari, C., editors, *Extreme Hydroclimatic Events and Multivariate Hazards in a Changing Environment*, pages 87 – 127. Elsevier, ISBN: 978-0-12-814899-0, DOI: 10.1016/B978-0-12-814899-0.00004-3.
- von Appen, W.-J., Schauer, U., Hattermann, T., and Beszczynska-Möller, A. (2016). Seasonal Cycle of Mesoscale Instability of the West Spitsbergen Current. *J. Phys. Oceanogr.*, 46:1231–1254, DOI: 10.1175/JPO-D-15-0184.1.
- Walczowski, W. (2014). *Atlantic Water in the Nordic Seas*. Springer International Publishing, DOI: 10.1007/978-3-319-01279-7.
- Wang, Q., Danilov, S., Sidorenko, D., Timmermann, R., Wekerle, C., Wang, X., Jung, T., and Schröter, J. (2014). The Finite Element Sea Ice-Ocean Model (FESOM) v.1.4: formulation of an ocean general circulation model. *Geosci. Model Dev.*, 7:663–693, DOI: 10.5194/gmd-7-663-2014.
- Wekerle, C., Wang, Q., von Appen, W.-J., Danilov, S., Schourup-Kristensen, V., and Jung, T. (2017). Eddy-Resolving Simulation of the Atlantic Water Circulation in the Fram Strait With Focus on the Seasonal Cycle. *J. Geophys. Res. Oceans*, DOI: 10.1002/2017JC012974.

BIBLIOGRAPHY

- Woodgate, R. A., Fahrbach, E., and Rohardt, G. (1999). Structure and transports of the east greenland current at 75n from moored current meters. *Journal of Geophysical Research: Oceans*, 104(C8):18059–18072, ISSN: 2156–2202, DOI: 10.1029/1999JC900146.
- Xu, R. and Wunsch, D. C. (2008). *Clustering*. John Wiley & Sons, Inc., DOI: 10.1002/9780470382776.

Acknowledgments

First of all I would like to thank my doctoral supervisor professor Dr. Florian Seitz for giving me the opportunity and confidence to do this work. Furthermore, I want to thank for his suggestions and inspired discussions because without his profound questions, this work would lack significant scientific quality. I would particularly like to thank my mentor Dr. Denise Dettmering. She was always there for discussions and questions. She supported me from the first to the last publications and introduced me to the skill of scientific working. This work would not have been possible without her focus on the essentials and for keeping me on the right path. I would also like to thank Dr. Wolfgang Bosch, who brought me to satellite altimetry many years ago, supervised my Bachelor's and Master's thesis, encouraged me to start a doctorate in satellite altimetry and helped me a lot with his scientific experience and creativity.

My special thanks go to Christian Schwatke, Alexander Kehm and Dr. Marcello Passaro, who became more than just colleagues in the last years. They always have an open ear for questions, discussions and helped me to keep motivated for finishing this thesis. Moreover, I wish to express my gratitude to all colleagues at DGFI-TUM, who always provided a good working atmosphere and an invaluable geodetic knowledge and expertise. I always love our social events and the coffee break for having not only scientific discussions, but also for the conversations that went beyond the scientific scope.

I am also grateful to Dr. Eero Rinne and his group, who hosted me for a month and a half at the Finnish Meteorological Institute (FMI) in Helsinki, where I learned a lot about sea ice and oceanography in polar oceans. Moreover, I thank Dr. Claudia Wekerle for introducing me to ocean modeling at the Alfred Wegener Institute (AWI) in Bremerhaven.

Finally, I would like to thank my wife Anna, my parents Marianne and Ulrich as well as my brother Henri, for always supporting me in good and complicated times. Especially in the last weeks before submitting the thesis, Anna constantly motivated and encouraged me to finish this work. She is the person I can always rely on. Last but not least, I would like to express my gratitude to my whole family and friends who are always there for me.

Scientific environment

This thesis was prepared at the Deutsches Geodätisches Forschungsinstitut of the Technical University of Munich (DGFI-TUM). To a large extent, the research was performed as part of the project *Variations in ocean currents, sea ice concentration, and sea surface temperature along the northeast coast of Greenland (NEG-OCEAN)* funded by the German Research Foundation (DFG) under grants BO1228/13-1 and DE2174/3-1. A cooperation with the Alfred Wegener Institute (AWI), Helmholtz Centre for Polar and Marine Research, supported the comparison and combination process by providing FE-SOM and by sharing valuable knowledge about ocean modeling in polar areas.

A research stay at the Finnish Meteorological Institute (FMI) in Helsinki supported by the TUM Graduate School (TUM-GS) and FMI, significantly supported the deeper understanding of sea ice dynamics as well as the challenges of ocean modeling in regions affected by sea ice. Furthermore, several presentations at international scientific conferences, such as at the European Geoscience Union (EGU) General Assembly or the ESA Living Planet Symposium, widened my public visibility.

A Appendices

A.1 Publications

This section contains the 4 publications, which are the framework of this work. With the exception of P-1.2, all publications are published under open access conditions. All publications are printed in their finalized version. The overall contribution and separated into different criteria for each publication are listed as percentages in the following table.

Furthermore, current section lists several co-authored publications, which were produced during the doctoral phase.

Crit. \ Pub.	P-1.1	P-1.2	P-2	P-3
Idea	95%	45%	80%	75%
Realization (Implementation)	100%	50%	90%	100%
Analysis and Discussion	75%	35%	75%	85%
Figure Compilation	100%	50%	100%	100%
Manuscript Writing	70%	20%	80%	80%
Overall Contribution	88%	40%	85%	88%

P-1.1 Monitoring the arctic seas: How satellite altimetry can be used to detect open water in sea-ice regions

Müller, F. L., Dettmering, D., Bosch, W., and Seitz, F. (2017). Monitoring the arctic seas: How satellite altimetry can be used to detect open water in sea-ice regions. *Remote Sensing*, 9(6), ISSN: 2072-4292, DOI: 10.3390/rs9060551

Copyright

The publication was published in *Remote Sensing*, which is an open-access MDPI journal. All published articles are distributed under the terms and conditions of the Creative Commons Attribution License (<http://creativecommons.org/licenses/by/4.0/>). The copyright remains with the author.

Summary

The Arctic seas are covered by a dynamic changing sea ice layer with significant influences on the ocean-ice-atmosphere interaction. In particular, the northern Nordic Seas are under the influence of seasonally changing sea ice cover with a maximum in March and a minimum in September. The sea ice area is characterized by a semi-closed sea ice surface, but also by ice floes and elongated as well as circular shaped open water areas (i.e. leads and polynyas). These irregularly distributed open water areas provide the only possibility to obtain information about the sea level during the sea ice season, since they allow a direct observation of the ice-free ocean surface within the sea ice area.

Satellite altimetry is able to monitor leads/polynyas and to provide quantitative information of the sea level in ocean regions affected by sea ice. In order to obtain reliable sea surface heights within the sea ice regions, it is necessary to assign altimeter echoes, also called waveforms, to sea ice or open water conditions. The different surface types have a direct influence on the waveform shape and backscattered power. Reflections by leads or small polynyas without any wave patterns result in a single-peak and narrow waveform shape in connection with a strong backscattered power. In contrast, sea ice or open ocean waveforms are characterized by a more diffuse scattering leading to weaker reflected power, several smaller peaks and a generally broader waveform shape.

In order to identify waveforms reflected by lead and polynyas an unsupervised classification approach was developed without using already classified training data or fix defined and satellite mission-dependent thresholds. For this purpose, a partitional clustering algorithm (i.e. K-medoids) is applied to search for similar waveform patterns among a subset of selected waveforms representing the majority of all possible scatter types and to sort them in a predefined number of clusters. In particular, the clustering is based on six pre-defined waveform features describing the shape and power of the individual waveforms of the subset. After clustering, the clusters are assigned to ocean, sea ice and

lead/polynya conditions by analyzing the mean feature values of each cluster with respect to physical background knowledge about the scattering behavior dependent on the surface conditions. The clustered waveforms depict the reference model for categorizing all remaining waveforms, which are not part of the subset. The remaining waveforms are labeled to the clusters by applying a K-Nearest Neighbor classifier, which searches for the closest distance between the reference model and the remaining waveforms.

The unsupervised classification was developed and tested with waveform data of Envisat and SARAL. The two missions differ in terms of their observation bandwidth, which leads to a slightly differing backscatter behavior regarding the waveform shape, but does not require adaptations of the unsupervised classification procedure.

The classification performance is evaluated by an internal and external validation. The internal validation is based on a 10-Fold cross-validation and provides information about the minimal error, which must be expected from the classification methodology itself. Therefore, parts of the clustered reference model are excluded and re-classified with the remaining reference data. This reveals an internal miss-classification rate of $2.30\% \pm 0.08$ for Envisat and $1.93\% \pm 0.05\%$ for SARAL. Furthermore, an external, automatic and quantitative validation based on image-processed and binarized SAR images from various radar imaging satellite missions shows an overall consistency rate of 70.7% for Envisat and 76.9% for SARAL. The radar image-based validation approach is described in Passaro et al. (2018b).

The unsupervised classification enables the detection of lead and polynya radar altimeter returns and enables studies of the sea level within sea ice regions. In particular, it allows the reliable computation of sea surface heights for a variety of applications. Furthermore, the developed method is applicable to all satellite altimetry missions and polar regions on Earth.

Contribution

As stated in P-1.1: Felix L. Müller developed the classification and validation methods, conducted the data analysis and wrote the majority of the paper. Denise Dettmering supervised the present study, contributed to the manuscript writing and helped with the discussions of the applied methods and results. Wolfgang Bosch initiated the study. Florian Seitz supervised the research. Both were involved in the writing process and discussed the methods presented in the manuscript as well. The overall contribution of Felix L. Müller is estimated to be **88%**.

Article

Monitoring the Arctic Seas: How Satellite Altimetry Can Be Used to Detect Open Water in Sea-Ice Regions

Felix L. Müller *, Denise Dettmering, Wolfgang Bosch and Florian Seitz

Deutsches Geodätisches Forschungsinstitut, Technische Universität München, Arcisstraße 21, 80333 Munich, Germany; denise.dettmering@tum.de (D.D.); wolfgang.bosch@tum.de (W.B.); florian.seitz@tum.de (F.S.)

* Correspondence: felix-lucian.mueller@tum.de; Tel.: +49-089-23031-1115

Academic Editors: Frédéric Frappart, Ole Andersen, Sergey Lebedev, Guillaume Ramillien, Deepak R. Mishra and Prasad S. Thenkabail

Received: 24 February 2017; Accepted: 29 May 2017; Published: 1 June 2017

Abstract: Open water areas surrounded by sea ice significantly influence the ocean-ice-atmosphere interaction and contribute to Arctic climate change. Satellite altimetry can detect these ice openings and enables one to estimate sea surface heights and further altimetry data derived products. This study introduces an innovative, unsupervised classification approach for detecting open water areas in the Greenland Sea based on high-frequency data from Envisat and SARAL. Altimetry radar echoes, also called waveforms, are analyzed regarding different surface conditions. Six waveform features are defined to cluster radar echoes into different groups indicating open water and sea ice waveforms. Therefore, the partitional clustering algorithm K-medoids and the memory-based classification method K-nearest neighbor are employed, yielding an internal misclassification error of about 2%. A quantitative comparison with several SAR images reveals a consistency rate of 76.9% for SARAL and 70.7% for Envisat. These numbers strongly depend on the quality of the SAR images and the time lag between the measurements of both techniques. For a few examples, a consistency rate of more than 90% and a true water detection rate of 94% can be demonstrated. The innovative classification procedure can be used to detect water areas with different spatial extents and can be applied to all available pulse-limited altimetry datasets.

Keywords: satellite altimetry; Envisat; SARAL; unsupervised classification; K-medoids; Greenland Sea; Fram Strait

1. Introduction

The Arctic Ocean, including its peripheral seas, e.g., the Greenland Sea, is considered one of the most important components of the Earth's climate system [1]. In particular, these areas show strong responses to global warming and may affect climate conditions globally, for example, by changing the oceanic thermohaline circulation. The north polar regions are crucial contributors to the global ocean current system by carrying cold and fresh water southwards. Most of the Arctic Ocean is covered by varying extents of sea ice with open water areas and floes with different spatial extents as well as fully closed ice surfaces. The seasonal fluctuations of ice covers significantly impacts the atmosphere-ocean interaction (e.g., ice-albedo). While a closed sea ice cover prevents the ocean from heat emission, openings in the ice lead to a warming of the first atmospheric layers.

The evolution of sea ice is strongly influenced by sea surface temperature, wind, waves and ocean currents [1]. During recent decades, increasing sea surface temperatures and an enhanced warm water inflow in the Arctic Ocean resulted in decreased sea ice extent and volume [2,3]. Additionally, the Greenland ice sheet experienced strong environmental changes due to an increasing mass loss enhancing melt water influx into the Arctic Ocean [4].

The monitoring of the changing north polar ocean conditions, especially in the Greenland Sea, allows investigating interconnections between land, ocean, and atmospheric processes as well as their climate forcing. Today, remote sensing systems provide a large set of different sensors for monitoring the polar regions. Radar satellite altimetry is able to provide quantitative information about sea surface heights, significant wave heights, and dynamic ocean topography [5,6]. However, in order to derive reliable altimetry products, a careful selection of measurements from open water areas is necessary. By analyzing the radar return signal of the altimeter, the so-called waveform, information about the reflecting surface can be derived. This allows the classification of waveforms in water- and sea ice-returns and the detection of open water areas in sea ice regions. For example, calm open water areas within the footprint cause a very single-peak shape. With an along-track resolution of less than a kilometer using high-frequency data, conventional satellite altimetry missions (such as Envisat and SARAL) are able to detect small open water areas that might be missed by imaging Synthetic Aperture Radar (SAR) satellite missions (Sentinel-1A/B, Radarsat-1/2, etc) in case a high-resolution acquisition mode is not available. Additionally, small water areas have insufficient backscatter properties to be mapped by passive microwave satellite missions (e.g., Special Sensor Microwave Imager (SSM/I) and SSM/I Sounder (SSM/IS)). However, altimeter radar echoes reflected from non-uniform scatterers, like sea ice regions, are challenging to interpret because the large surface footprint of several kilometers usually covers several ice types.

The first studies dealing with satellite altimetry in sea ice regions were published in 1980 by Dwyer and Godin [7] and in 1992 by Fetterer et al. [8]. After the launch of the ESA satellites ERS-1 and ERS-2, covering high latitudes in a repeat orbit, further studies were conducted by Laxon [5] and Laxon et al. [9]. They analyzed the potential of ERS-1 sea ice monitoring and the interannual variability of sea ice thickness by employing ERS-1 and ERS-2 altimetry data. Furthermore, Peacock [10] provides a first sea surface height determination in the Arctic ocean. In recent years, several sea ice applications have been explored e.g., the detection of openings in the ice. Connor et al. [11] applied a peakiness parameter, defined by Peacock [10] in order to detect small open water bodies in the sea ice cover using high-frequency data of Envisat. Zakharova et al. [12] continues with the development of a lead detection algorithm by using the Centre National d' Études Spatiales (CNES) and Indian Space Research Organisation (ISRO) satellite SARAL and maximum power threshold. Currently, all pulse-limited altimetry-based approaches for detecting water returns in sea ice regions use thresholds for different parameters. This has the disadvantage that the thresholds have to be set manually and individually for every altimetry mission. Furthermore, a deep knowledge about the different scatter characteristics in sea ice regions is required. Besides Zygmuntowska et al. [13] developed another approach using the waveforms shape for classifying airborne SAR altimeter echoes over the Arctic sea ice in a supervised way.

The present study proposes a new strategy to detect open water areas based on an unsupervised classification of high-frequency altimetry radar echoes. The approach is able to detect water domains with different spatial extents and can be easily applied without any deeper knowledge about surface-dependent backscatter characteristics. The method is applicable to all available pulse-limited altimeter data and is independent of mission-specific radar frequencies and characteristics. Furthermore, the results are compared to processed SAR images using the method described in [14] to obtain quantitative information about the classification performance.

The present paper is structured into three main parts. First, the study area and the applied datasets are introduced. Section 3 presents the method and processing procedure as well as the comparison process of the obtained results. Section 4 presents the classification results and provides evidence of the classification performance. At first, quantitative information considering the entire available validation dataset (Section 4.1) is derived before some visual comparisons between the SAR images and the altimetry overflights are provided. The paper finishes with a conclusion and an outlook to future research.

2. Study Area and Data Sets

This section provides an introduction to the study area and the different remote sensing datasets used for classification and validation.

2.1. Greenland Sea and Fram Strait

The study area ranges from 70.0°N to 81.5°N in latitude and from the north-east coast of Greenland to 28.0°E in longitude and covers the Greenland Sea and the Fram Strait (see Figures 1 and 2). The Greenland Sea belongs to the peripheral seas of the Arctic ocean. It connects the Fram Strait in the north, a narrow passage between north-east Greenland and Svalbard, with the Norwegian Sea as well as the Iceland Sea in the south. This area is affected by the East Greenland Current (EGC), which transports more than 90% of fragmented sea ice from the Arctic Ocean through the Fram Strait southwards [15]. Therefore, the EGC represents the main and most important freshwater outlet of the Arctic Ocean. According to Serreze and Barry [16] the Greenland Sea and the region of the Fram Strait is strongly influenced by rapid atmospheric and changing sea ice conditions as well as comparatively fast ocean currents with a mean velocity of 20–30 cm/s [17] and maxima up to 80 cm/s [18]. The sea ice state reaches from a nearly closed sea ice cover, showing straight lined and circular shaped open water bodies, leads and polynyas, up to individual ice floes ranging from a few meters to kilometers in diameter [16]. Applying open water detection to the Greenland Sea and the Fram Strait offers one the chance to sensitize the unsupervised classification method for a various number of different sea ice and ocean conditions.

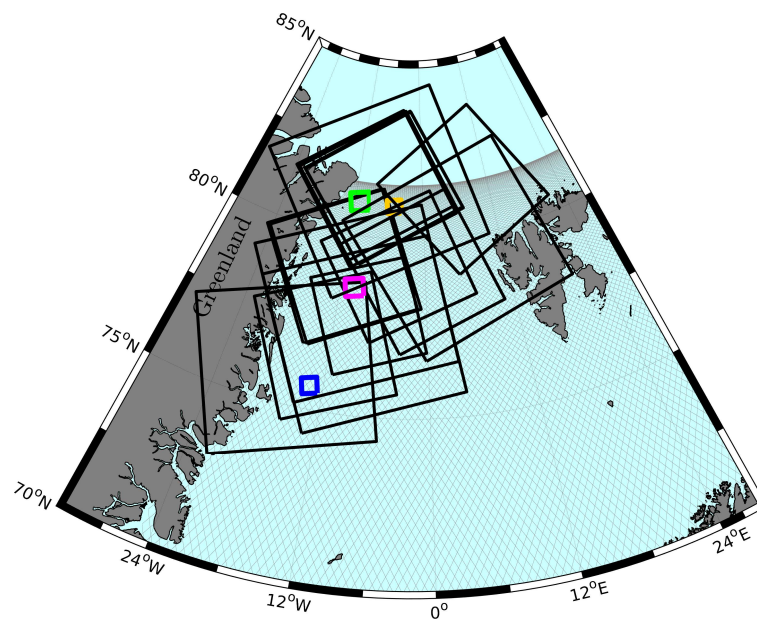


Figure 1. Black rectangles indicate locations of the SAR images from ALOS and Radarsat-2 used for comparison with Envisat classification results against the background of nominal sun-synchronous ground tracks of one Envisat cycle. The four subsets discussed in Section 4.2 are highlighted by different colors.

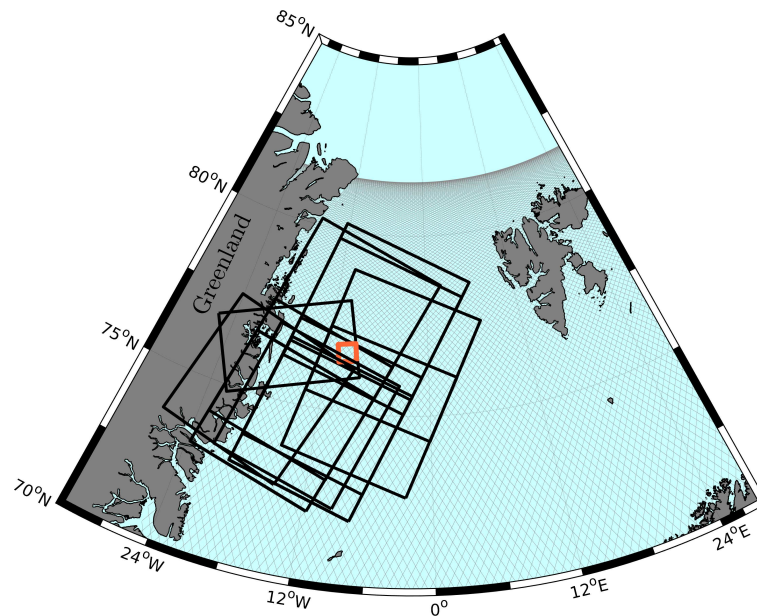


Figure 2. Black rectangles indicate locations of the SAR images from Sentinel-1A used for comparison with SARAL classification results against the background of nominal sun-synchronous ground tracks of one SARAL cycle. One subset discussed in Section 4.2 is highlighted in orange.

2.2. Radar Altimetry Data

In the present investigation, the high-frequency radar altimetry data of the ESA satellite Envisat and the CNES/ISRO altimetry satellite SARAL are used. Data of the missions Jason-1, Jason-2 and Jason-3 are disregarded due to their low orbit inclination (about 66°) not covering the Greenland Sea and Fram Strait.

Envisat and SARAL carry pulse-limited radar altimeters and are placed on the same 35 day repeat-orbit covering polar areas up to $\pm 81.5^\circ$ geographical latitude. Envisat was launched in March 2002 and orbits the Earth at an altitude of nearly 800 km. In October 2010, Envisat left the repeat-orbit and started to drift until in May 2012, the ESA mission was decommissioned after an unexpected signal loss. SARAL was placed in orbit in February 2013 and is still active even though in July 2016, the satellite started its drifting orbit phase without fix repeat period.

All computations and methodologies used in this study are based on official high-frequency Sensor Geophysical Data Record (SGDR) v2.1 dataset of Envisat's radar altimeter (RA-2) and the SGDR-T dataset of the AltiKa radar altimeter mounted on SARAL. In case of SARAL, data until July 2016 and in case of Envisat, data until the end of the mission are used. In this study, waveforms observed in the Greenland Sea and Fram Strait (see Section 2.1) are employed in the classification process. In order to calculate the altimeter backscatter values, different features stored in the SGDR dataset, for example, atmospheric attenuation and instrumental corrections (e.g., sigma naught calibration factor) are additionally used.

The two satellite missions differ mainly in the emitted radar bandwidth, the pulse repetition frequency and the footprint size of the illuminating area onto the surface. RA-2 emits *Ku*-band signals with a repetition frequency of 1800 pulses per second, covering an nominal elliptic area of approximately up to 10 km diameter [11] depending on the surface conditions. Before transmitting to earth, the waveforms are sampled to 18 Hz by the on-board processing. AltiKa works in the *Ka*-band, with a repetition frequency of 4 kHz, generates 40 Hz averaged waveforms and has half the antenna aperture of Envisat. This leads to a smaller footprint size up to 8 km diameter and an improved spatial resolution [19]. Beside instrumental influences, the waveform's shape is mainly affected by various surface characteristics. Detailed explanations referring to the representation of the varying waveform's shape can be found in Section 3.1.

2.3. Imaging Synthetic Aperture Radar (SAR) Data

A possible source for validating the classification results is the usage of imaging synthetic aperture radar (SAR) data. Beside the altimeter satellites, several multispectral and SAR imaging satellite missions regularly provide snapshots of periodically changing ocean conditions. In contrast to multispectral sensors, working mostly in the visible and infrared spectrum, SAR sensors are unaffected by cloudiness and lighting conditions, which makes it easier to identify appropriate scenes. However, SAR sensors are side-looking instruments, which can cause a shadowing of very flat and smooth surface structures (e.g., leads or polynyas) due to interjacent higher topography (e.g., ice floes, ridges). Additionally, the recorded backscatter values do not only depend on the surface characteristics (e.g., roughness) but also on the incidence angle of the reflected radar waves, which makes it more complex to provide information about different surface types. Furthermore, it has to be mentioned that most SAR satellites are placed on sun-synchronous orbits, which allows for a uniform capture of ice state but limits the minimum time lag between the acquisition dates of the SAR images and the altimetry measurements of Envisat and SARAL also using sun-synchronous orbits.

Aiming at a small time lag between SAR images and satellite altimetry, wide swath data are qualified best since these images cover a spatially extended area with medium pixel spacing. For this investigation, SAR images of the JAXA Advanced Land Observing Satellite (ALOS) [20], MDA's Radarsat-2 [21] and ESA's Sentinel-1A (S-1A) [22] are used. The Envisat classification results are compared with ALOS PALSAR Level 1.5 Wide Beam (WB) images offered by the Alaska Satellite Facility (ASF) DAAC and with Radarsat-2 (R-2) Scan SAR Mode data provided by ESA. The SARAL classification outcomes are compared with Level-1, S-1A extra wide swath mode data. S-1A images are made available through the ESA/Copernicus Sentinel Data Hub. Specifications, temporal availability in the target region, and information about the used imaging SAR products are listed in Table 1. To distinguish between open water pixels, appearing in near black, and sea ice pixels, appearing in bright gray, HH-polarized images are used. For more information regarding SAR polarization and the influence of different surface scattering see Dierking W. [23] and Jackson et al. [24].

Table 1. Synthetic Aperture Radar (SAR) image specifications [20–22] and altimeter satellites covering same time periods.

SAR Satellite	Band	Mode	Swath Width (km)	Pixel Size (m)	Period (mm/yyyy)	Altimeter Satellite
ALOS	L-Band	Wide Beam	250–350	100 × 100	June 2007–May 2008	Envisat
Radarsat-2	C-Band	Scan SAR Wide	500	50 × 50	June 2008–present	Envisat/SARAL
Sentinel-1A	C-Band	Extra Wide	400	40 × 40	October 2014–present	SARAL

In order to ensure similar sea ice conditions and allow for an unbiased comparison between SAR and altimetry, only images with a time lag less than about 3.5 h, with respect to the altimetry crossings, are used. The comparison is based on 16 grayscaled SAR images during the lifetime of Envisat and 19 images for SARAL. The SAR data are selected from different epochs considering a varying sea surface state with a focus on periods with various sea ice coverage. Figures 1 and 2 display the locations of all used SAR images. The scenes are mainly located in the Fram Strait and near the north-east coast of Greenland. Tables 2 and 3 list sensor and temporal information for all conducted comparison pairs. Two of the R-2 images are used for multiple satellite overflights. In the case of SARAL classification, it has to be mentioned that, due to sun-synchronous orbits and fixed revisit times of Sentinel-1A and SARAL, it is not possible to find suitable pairs for comparison that show good spatio-temporal coverage with a time gap smaller than 2 h 40 min during the study period.

Table 2. Acquisition date of the SAR images and time gap between altimetry observations and imaging data used for comparison with Envisat classification results.

SAR-Satellite	Acquisition Date	Time Gap hh-mm
ALOS	14 June 2007	02-30
ALOS	1 October 2007	02-57
ALOS	7 October 2007	01-55
ALOS	10 November 2007	03-07
ALOS	10 December 2007	02-50
ALOS	26 December 2007	02-13
ALOS	5 January 2008	02-40
ALOS	7 January 2008	01-46
ALOS	12 January 2008	02-49
ALOS	4 May 2008	01-25
R-2	4 November 2008	01-47
R-2	20 April 2009	02-09 00-29
R-2	21 April 2009	02-07
R-2	10 February 2010	03-04
R-2	14 March 2010	01-52 00-13 01-27
R-2	16 October 2010	02-04

Table 3. Sentinel-1A acquisition date of the SAR images and time gap between altimetry observations and imaging data used for comparison with SARAL classification results.

Acquisition Date	Time Gap hh-mm
23 October 2014	02-41
16 November 2014	03-34
14 November 2014	02-49
18 November 2014	02-42
3 December 2014	02-40
6 December 2014	02-58
27 December 2014	03-33
1 January 2015	02-59
15 January 2015	03-20
18 January 2015	03-27
16 March 2015	03-08
6 February 2015	03-29
6 February 2015	03-28
10 February 2015	03-22
22 February 2015	02-59
2 March 2015	02-44
9 March 2015	02-56
19 April 2015	02-53
15 May 2015	02-54

2.4. Sea Ice Data

Polar sea areas are affected by moving sea ice due to the influences of wind and ocean currents [16]. This results in a rapid change and high diversity of the sea surface conditions. To reach a realistic

comparison of altimetry results and SAR images, the compensation for sea ice motion within the time interval between the two observation sets is required. For this purpose, daily ice vector velocity fields are exploited within the validation process. Therefore, the “Polar Pathfinder Daily 25 km EASE-Grid Sea Ice Motion Vectors, Version 3” of the National Snow and Ice Data Center (NSIDC) are employed [25]. This dataset contains zonal and meridional sea ice velocity observations of active and passive sensors as well as in situ measurements interpolated to a 25 km spacing grid referring to an azimuthal equal area map projection. This dataset covers the entire altimetry era until the end of May 2015.

The sea ice velocity data are used to shift the SAR image, respectively, the image pixel coordinates, assuming an averaged ice motion (direction and velocity) over the time interval between the altimetry measurement and the SAR image. For this purpose, only homogeneous data represented by small standard deviations in direction and velocity inside a predefined box (± 35 km) around the altimetry track are selected to compute a mean displacement vector. Sea ice velocity vectors located close to the coastlines (within 25 km) are eliminated due to erroneous ice observations [25].

The comparison is performed only in areas affected by sea ice to suppress the influence of falsely detected SAR ice pixels caused by diffuse scattering behavior due to rough swell in the open ocean. Therefore, daily “Sea Ice Concentrations from Nimbus-7 SMMR and DMSP SSM/I-SSM/IS Passive Microwave Data, Version 1” of the NSIDC [26] with a spatial resolution of $25 \text{ km} \times 25 \text{ km}$ are interpolated to the altimetry high-frequency data. Observations outside the ice edge without sea ice are excluded from the comparison process.

3. Methods

This study is based on an unsupervised classification process of altimetry waveforms. Unsupervised classification algorithms group unassigned data into a predefined number of classes without any background information about the data and their sources using only “natural” and hidden intra-cluster similarities [27]. The classification is performed based on a set of features characterizing the input data. In contrast, supervised classification is based on a-priori information of a well known or labeled dataset to classify and assign the observations [28]. Examples for unsupervised classification methods are artificial neural networks (e.g., Self-Organizing Maps [29]) or partitional clustering algorithms (e.g., K-means and K-medoids [30,31]). In the present investigation, a partitional cluster algorithm, K-medoids, is used for separating a set of unlabeled waveform data into clusters indicating different waveform properties. Therefore, features have to be defined describing various waveform characteristics. Based on the clustering results, K-nearest-neighbor is applied to assign unclassified waveform data.

In this section, at first, features for describing the various waveform shapes and their characteristics are specified and explained. This is followed by the description of the methodical background of the clustering and classification process. The last part of Section 3 presents the validation approach for the classification procedure. The presented methods are applied independently to Envisat and SARAL.

3.1. Waveform Features

The shape of altimetry waveforms strongly depends on the surface characteristics within the altimeter footprint. Figure 3 shows Envisat/RA-2 and SARAL/AltiKa radar pulses reflected by ocean, leads, and sea ice. Major differences can be detected in the power magnitude and the number and shape of the signal peaks. Leads produce very narrow and peaky waveforms due to the specular scattering of calm and flat water. In contrast, radar pulses originating from ocean or sea ice surfaces are influenced by waves or interlaced and piled ice floes, respectively, leading to multi peaks and wider, noisier shapes.

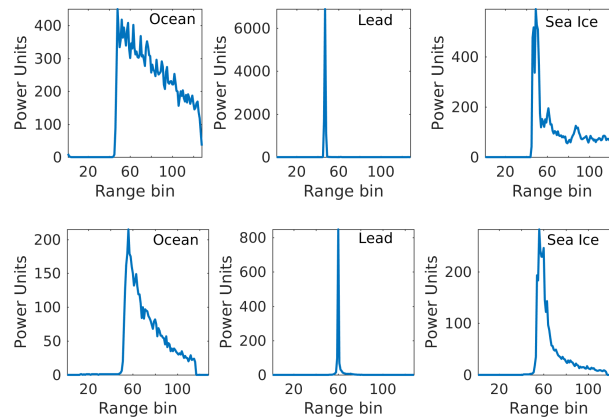


Figure 3. Waveform examples for Envisat (**top row**) and SARAL (**bottom row**) for three different surface scatterers: Ocean (**left**), Lead (**middle**), and Sea Ice (**right**).

In order to characterize a waveform and identify the main evocative surface scatterer, a number of waveform features are defined. The computed values constitute a waveform feature space that provides the input for the clustering and classification process. To increase the efficiency of the algorithm and to get a reliable open water detection, the selected features should fulfill the following conditions:

1. The features should characterize different waveform types.
2. The selected features should be stand alone and without linear dependence and major correlations among each other.
3. The feature space should be adaptable to any altimetry waveform.
4. All features should exhibit the same order of magnitude for equal weighting among each other.

In the present investigation, six features are defined to describe the waveforms mainly focusing on the reflected radar pulse shape (width) and the recorded power intensity. These features are applicable for each pulse-limited altimeter waveform, i.e., for Envisat as well as for SARAL.

- **Waveform maximum (Wm)**
The waveform height is described by the maximal power of the returning radar pulse σ_{max} . It provides information about the backscatter of calm or rough surface conditions. To compute σ_{max} for Envisat as well as SARAL, the maximum waveform power and mission specific rectifications are applied by using instrumental and atmospheric corrections from the provided datasets (see Section 2.2).
- **Trailing edge decline (Ted)**
The trailing edge decline is computed by fitting an exponential function, considering an exponential decay of AltiKa waveforms, from the waveform power maximum to the last bin. The estimated decay rate is used to characterize the decline of the trailing edge after the maximum.
- **Waveform noise (Wn)**
This feature quantifies the trailing edge scattering. It is computed as median absolute deviations of the trailing edge fitting (see Ted) residuals. This parameter is very small for single peak waveforms (leads) and moderate for oceans.
- **Waveform width (Ww)**
The number of bins where the power is equal to zero provides information about the waveform's width.
- **Leading edge slope (Les)**
The leading edge slope is obtained by subtracting the first bin position containing more than 30%

of the power maximum from the bin position of the maximum power. The difference provides relative information about the width and steepness of the leading edge independent of the absolute position of the leading edge, i.e., the range.

- **Trailing edge slope (Tes)**

In contrast to the leading edge slope, the trailing edge slope is obtained by subtracting the last bin position containing more than 30% of the maximum from the bin position of the maximum power. This difference provides similar information to Ted in the case of single-peak waveforms but supports the identification of strong specular peaks in front of an ocean-like trailing edge.

The selected features in the present investigation show a varying order of magnitudes, which results in an irregular weighting in the clustering algorithm. In order to comply with condition 4 (see above) a standardization has to be processed. Before conducting the unsupervised classification procedure, the features are reduced by subtracting their average and divided by their standard deviation (standard-score).

The features are calculated for RA-2 and AltiKa waveforms in the same way. In the case of SARAL, the maximum power is limited to 1250 counts. Power counts above this limit are not recorded due to too high backscatter values that cannot be resolved by the tracking window [12]. The waveforms are cut without a clear maximum peak in the radar echo, which makes it impossible to compute all features (e.g., leading edge slope) and to constitute the complete feature space. These waveforms, which are not flagged in the SGDR dataset, are skipped from the further classification process. Furthermore, all waveforms are neglected, for which no reliable computation of the defined features is possible (e.g., if trailing edge fitting is impossible with 95% confidence).

3.2. Clustering

Within the clustering process a representative subset of all waveforms from a single mission will be used to define waveform groups, so-called clusters, that will later be used to also classify all remaining observations. In a first step, this reference model has to be created. For this purpose, a set of several waveforms, containing a majority of all possible scatter types, has to be selected. To this end, waveform data covering an area in the central Greenland Sea within bounds of 15°W/10°E longitude and 68°N/80°N latitude are used. To cover as many sea ice types as possible, the epoch is selected at the beginning of the melting period in early summer from April to May [32]. For Envisat, Cycle 57 (2007, containing about 307,000 waveforms), and for SARAL, Cycle 12 (2014, ca. 670,000 waveforms) are selected.

To group the reference data, a K-medoids cluster algorithm is implemented that clusters unsupervised data into K clusters. K-medoids performs a distance minimization between the features and the most centrally located feature (medoids) based on the feature space itself. Thereby, K-medoids is more robust to outliers and noise in contrast to K-means, which tries iteratively to estimate an optimal partition of unlabeled data by minimizing the distances between the coordinates of a mean cluster center (centroids) and the features. However, in contrast to K-medoids, K-means integrates every value of the feature space into the arithmetic average [27].

At first, K-medoids randomly chooses K medoids of the feature space and computes the distances to every feature. In the next steps, the algorithm rearranges every single feature until there is no motion within the K clusters and the minimal distances to the medoids are found. However, the clustering result depends on the initial randomly chosen medoids. This is why the algorithm is repeated several times and the best solution is selected by analyzing the final sum of all distances within the clusters. This leads to high computational efforts by employing large input datasets, but it is considerable that the clustering has to be performed just once per altimetry mission. To reduce the computation times, the algorithm examines only a random sample of cluster members during each medoids updating step. The size of the sample is set by default to 0.1% of the total number of data points. The iteration terminates if the medoids are stabilized.

Partition clustering algorithms require an initialization of the number of clusters K . In the present investigation, K is chosen empirically after several test runs by evaluating the best segmentation results [31]. Indicators for defining an appropriate K are, for example, the analysis of the sum of all distances within the clusters and, additionally, a visual analysis of all clusters. In order to obtain a clear partitioning of waveforms, it is useful to set K larger than the desired number of the three surface types, the present investigation is looking for, namely, calm open water, ocean or sea ice conditions. Figure 4 shows the clustering for 30 classes based on derived waveform features of about 307,000 Envisat waveforms (the clustering results for SARAL waveforms can be found in the Supplementary section, Figure S1). The displacements between the points and the medoids are computed using Euclidean distances.

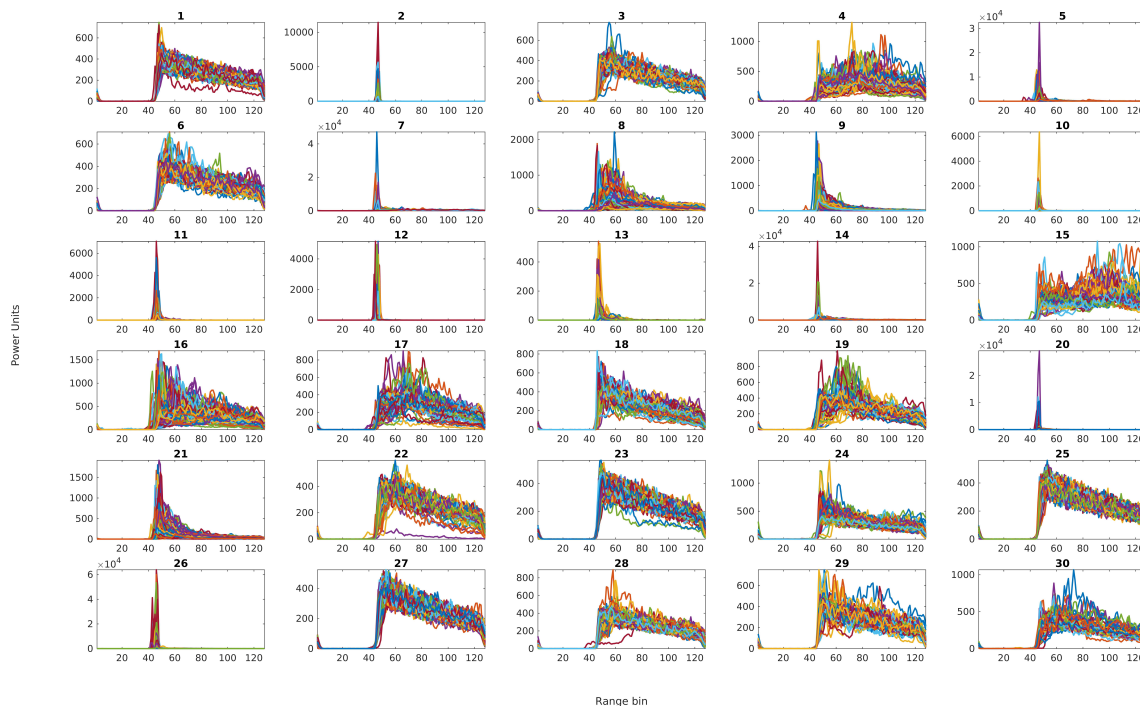


Figure 4. Envisat waveform clusters ($K = 30$) after K -medoids clustering showing segmented waveforms (every twenty fifth per cluster).

After running K -medoids, each cluster has to be assigned to one surface condition. The 30 clusters need to be manually condensed to three main classes indicating ocean, sea ice, and lead/polynya returns. This is done based on the feature statistic per cluster (see Figure 5) and knowledge on the physical backscattering behavior of different surfaces. It is well known that radar returns from dominant scatterers (i.e., a lead with a calm, mirror-like surface) cause single-peak waveforms with high power and narrow shape. Radar echoes nearly entirely reflected by sea-ice show a more diffuse scattering, weak power and no clear peaks. Using these relationships and transferring them to the cluster statistics enable a nearly unambiguous assignment. However, questionable clusters with ambiguous feature properties remain and are labeled as “undefined”.

Figure 5 indicates the cluster assignment by different colors. Lead and polynya returns (clusters 2, 10–12, 20, and 26) are characterized by a very narrow and peaky shape and high maximum power values. In contrast, ocean returns (clusters 1, 3, 6, 18, 22, 23, 25, 27–29) are wider and show a greater trailing edge decay. Waveforms belonging to the ice class (clusters 5, 7–9, 13, 14, 16, 21, 24, and 30) are between these two groups. They are defined by a smaller trailing edge decay and slope as well as bigger power values than ocean returns. However, there are clusters (4, 15, 17, and 19), that cannot clearly be assigned to one surface type. As an example, cluster 19 shows an ocean like behavior, but is characterized by an indistinct leading edge as well as a steeper ice-like trailing edge. Undefined

waveform classes show, apart from more noise in the cluster itself, no clear signature or trend to the underlying feature space or to the three main surface classes.

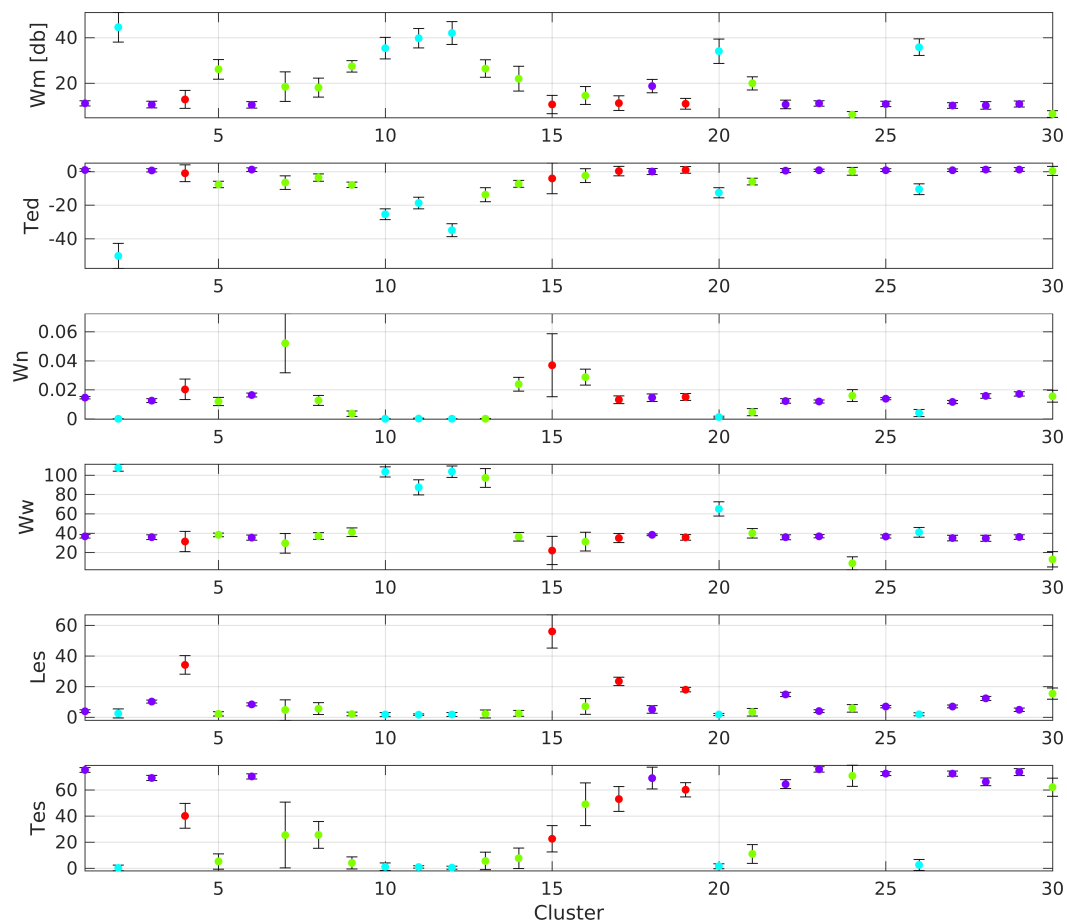


Figure 5. Means and standard deviations of waveform features (see Section 3.1) per cluster. Four classes are illustrated using different colors: “lead/polynya” (cyan), “ocean” (purple), “ice” (green), and “undefined” (red).

3.3. Classification

The waveform model created by the clustering (Section 3.2) can now be used to classify all waveforms. For this purpose the K-Nearest Neighbor (K-NN) classifier is employed. In general, K-NN belongs to the memory-based classifiers and does not require a stochastic model [28]. Basically, K-NN searches for the closest distance between a query point and a given input model. Similar to the K-medoids algorithm, the K-NN uses the euclidean distance. However, K has a completely different meaning than in the K-medoids algorithm. The K is now defined as the number of neighbors used for the classification. The cluster assignment of a specific waveform is done based on the majority of clusters of these K nearest neighbors. K must be set before the classification process starts.

In the present study, K is estimated by performing a 10-fold cross-validation. Therefore the reference model used for the clustering and already assigned to the clusters is divided into 10 randomly sorted, but equally sized subsets and validated against each other. This means, that every subset is used as a test sample and the remaining subsets as training sets. In order to find an appropriate K for K-NN, the cross-validation is performed based on different numbers of neighbors. Figure 6 shows the mean misclassification error as a percentage of the 10-fold cross-validation in the case of SARAL and Envisat. Similar errors can be expected for the classification of the remaining unlabeled waveforms. The minimum error defines the optimal number of neighbors. SARAL displays less variability and a

smaller misclassification rate than Envisat. The K-NN method seems to be more stable with clustered SARAL than with Envisat waveforms, which can be explained due to less variability in the AltiKa waveforms and a more robust waveform clustering. For SARAL a minimum error rate is obtained with $K = 20$ ($1.93 \pm 0.05\%$). In the case of Envisat, nearest-neighbor number $K = 44$ ($2.3 \pm 0.08\%$) is used, providing a good balance between low error and variance.

The misclassification rate in connection with the defined number of neighbors gives information about the K-NN prediction error based on the reference model and class labels. This parameter can be used to estimate the internal precision of the classification approach. In this study, a minimal error of about 2% has to be expected from the methodology itself.

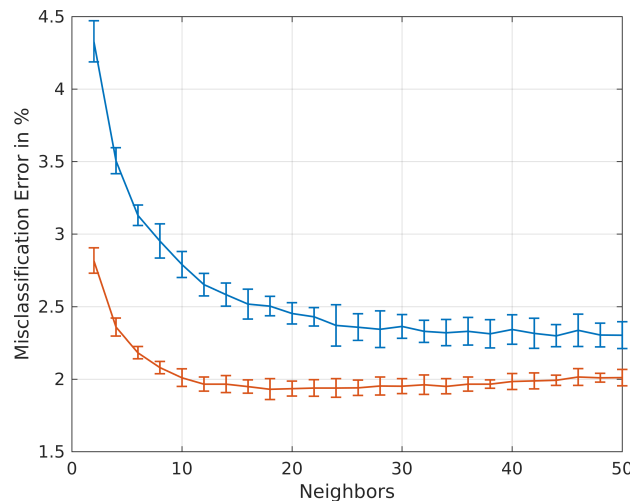


Figure 6. Misclassification error and its standard deviation for SARAL (red) and Envisat (blue) with varying number of K neighbors as computed by 10-fold cross-validation.

After defining an appropriate K , the remaining waveforms are applied to K-NN. In the end of the classification process every waveform is labeled by a certain cluster and, consequently, assigned to a specific surface type.

3.4. Validation Approach

In order to conduct an external validation for the waveform classification, a comparison with independent SAR images is performed. For this purpose, the defined waveform classes of ocean, lead/polynya, sea ice are assigned to water (ones) and non-water (zeros) observations. Undefined waveform classes are also labeled with zeros. In order to provide quantitative information about the classification performance, it is necessary to compare the results to an external dataset. For this purpose, imaging SAR data are used, as they regularly provide snapshots of different sea surface states in the study area.

Before performing an automatic comparison between SAR and the classification results, the SAR images are pre-processed by using the ESA toolbox SNAP, version 4.0.0 for Sentinel-1A as well as Radarsat-2 and the MapReady toolbox, version 3.1.22 for ALOS image data offered by ASF. Basically, the following standard routines are applied to the imaging SAR data:

1. Thermal noise removal (only S-1A)
2. Radiometric calibration
3. Speckle filter (only Radarsat-2)
4. Delay Doppler terrain correction
5. Reprojection to Lambert Azimuthal Equal Area map projection
6. Converting backscatter values to db
7. Datatype conversion in *uint8*

On the pre-processed SAR images, linear and circular shaped black and near black areas indicate openings inside the sea ice cover generated by a smooth surface and specular reflection of the radar waves. To automatically extract these areas, the SAR images have to be converted into binary pixel values by applying several image processing tools. The applied approach is described in detail by Passaro et al. [14]. Briefly summarized, the images undergo a noise and minimum filtering in order to emphasize dark pixel regions, followed by an adaptive thresholding that considers local illumination changes. Finally, a mathematic morphological closing operation is applied to the black and white coded images to link fragmented open water regions. To control the effect of the morphological closing operation a structure element (kernel) or convolution matrix is needed. Regarding linear and circular shapes of open water areas, an octagon with various size, considering the nominal pixel spacing of the SAR images, is employed. In the case of ALOS, the octagon size is six pixels around the center pixel, and in the case of Sentinel-1A and Radarsat-2, a kernel size of 12 pixels is used. Moreover, the image coordinates are shifted to compensate for sea ice-motion, for the acquisition time difference between altimetry and SAR (see Section 2.4). In a last step, the locations of the altimetry returns are interpolated to the SAR pixel locations by using nearest neighbor method.

4. Results and Discussion

In this study, 15,025 Envisat and 19,919 SARAL observations are investigated for which SAR image classification results are available for validation. 31.2% of the Envisat waveforms and 15.0% of the SARAL returns are assigned to water classes. Furthermore, 4.7% of Envisat and 14.2% of SARAL waveforms are set to undefined and defined as non-water returns. For a quantitative rating, 19 comparison pairs for SARAL and Envisat, respectively (see Section 2.3), are used. The results of this comparison are presented in the following section. Afterwards, examples are displayed to illustrate and discuss the functionality of the validation approach.

4.1. Automatic Comparison to SAR Images

As mentioned above, the automatic comparison process only relies on observations in areas with a semi-closed sea ice layer. This allows one to reduce false SAR classifications outside the ice edge due to an unreliable SAR image processing. Table 4 provides the numbers of measurements assigned to water and ice by the two observation techniques and, therefore, allows for an assessment of the altimetry classification performance. The absolute number of water and ice detections are listed column-wise for the altimetry classification results and row-wise for the SAR open water detection. The table shows that 1124 of the 15025 Envisat observations are identified as water by both, altimetry and SAR, whereas 837 locations are assigned to non-water by altimetry and to water by SAR. Assuming the SAR to be the ground truth validating the altimetry water detection, four dependencies are derived to rate the classification results. The total consistency rate, $P(CR)$ is computed by summing up the bold values and dividing them by the total number of comparison points. In addition, three conditional frequencies are derived: The true water detection rate ($P(Alt|SAR)$) is computed by dividing the “correct” altimetry water detections by the total number of SAR water observations, whereas the false water detection rate ($P(Alt|\overline{SAR})$) is defined as the relation between the water altimetry detections not confirmed by SAR and the total number of SAR ice detections. Moreover, the percentage of correctly classified water returns $P(SAR|Alt)$ represents the “correct” water altimetry detections in relation to the total number of open water detections by altimetry.

In the case of Envisat, a consistency rate of 70.7% is reached. In detail, nearly 60% of SAR water detections are truly classified by Envisat ($P(Alt|SAR) = 0.57$) in contrast to below 30% of SAR ice observations that are falsely assigned to water areas by Envisat ($P(Alt|\overline{SAR}) = 0.27$). However, only about a quarter of all Envisat open water detections are also classified by SAR ($P(SAR|Alt) = 0.24$).

The comparison between SARAL and Sentinel-1A water detection yields a higher consistency rate of 76.9% but a smaller true water detection rate of less than 30% ($P(Alt|SAR) = 0.28$). At the same

time, the false water detection rate $P(Alt|\overline{SAR})$ is very small and yields only 12.3%. Moreover, the correctly classified water return rate $P(SAR|Alt) = 33\%$ is better as for Envisat.

It has to be noticed that for the interpretation of these numbers it is important to consider that inconsistencies are not only due to altimetry classification but that the SAR open water detection as well as the sea ice-motion correction also contribute to the error budget. For example, most of the SARAL comparisons take place during the sea ice maximum between January and mid March, when the pack ice is very close and exhibits only small openings in the ice, which makes it challenging to be detected by the SAR image processing.

Analyzing the absolute water detection numbers of Envisat versus SAR images, it is remarkable that the number of open water points differs by 2732 between the SAR detection and the Envisat classification. The Envisat classification identifies significantly more open water areas than the SAR processing (factor of nearly 2.4). In the case of SARAL, a transposed situation can be found. This can be explained by different SAR sensor characteristics and an insufficient pixel resolution as well as an imprecise SAR image processing, including an unreliable sea ice-motion correction. Additionally, the altimeters are affected by off-nadir returns, which can cause an enhanced number of open water detections. In the case of Envisat, a larger footprint size than SARAL intensifies off-nadir effects.

Overall, it is important to understand, that the classification performance numbers of SARAL and Envisat are not directly comparable with each other. The underlying different instrumental, sensor, and spatio-temporal conditions differ too strongly to provide qualitative information that would allow for a comparative assessment of the two altimetry satellites. More details related to the impacts of SAR and altimetry processing on the quantitative comparison process can be found in Section 4.2.

Analyzing, for example, $P(CR)$ of Envisat and SARAL, the quantitative comparison confirms the reliability of the altimetry-based classification method and a good performance of their results. However, it has to be kept in mind that a data comparison of two totally different Earth observation techniques for open water detection in a very dynamic study area is not possible without a variety of uncertainties and inaccuracies. In order to provide a better impression of the difficulties of a quantitative comparison approach, the next section shows a couple of examples in a visual comparison.

Table 4. 2D contingency tables based on Envisat—ALOS/R-2 (top) and SARAL—S-1A (bottom) comparisons. The table shows the number of points classified as water/ice from altimetry (Alt) with the corresponding classification from SAR.

	Alt (Water)	Alt (Ice)	Σ
SAR (water)	1124	837	1961
SAR (ice)	3569	9495	13064
Σ	4693	10332	15025
	Alt (Water)	Alt (Ice)	Σ
SAR (water)	987	2600	3587
SAR (ice)	2007	14325	16332
Σ	2994	16925	19919

4.2. Visual Comparison

Using different SAR image subsets, this section will provide some visual comparisons between open water classification by altimetry and SAR images. The images were selected in order to indicate possible difficulties due to uncertainties in the SAR image or altimetry processing as well as sea ice motion correction. Figures 7 and 8 show five visual examples before (left) and after (right) image processing. The altimetry measurement locations are superimposed on the SAR image. Cyan colored altimetry observations identify open water classifications. These regions are plotted in white in the binary coded SAR images (right column). Figure 7a–f display Envisat–ALOS and Figure 7g,h Envisat—Radarsat-2 comparisons. Figure 8 shows a visual example of one SARAL—Sentinel-1A comparison. Metadata information, i.e., acquisition date and applied sea ice motion correction on each comparison is provided next to the images (visualized classification results without class assignment can be found in supplementary Fig. S2–S6). Moreover, Table 5 displays quantitative comparison results.

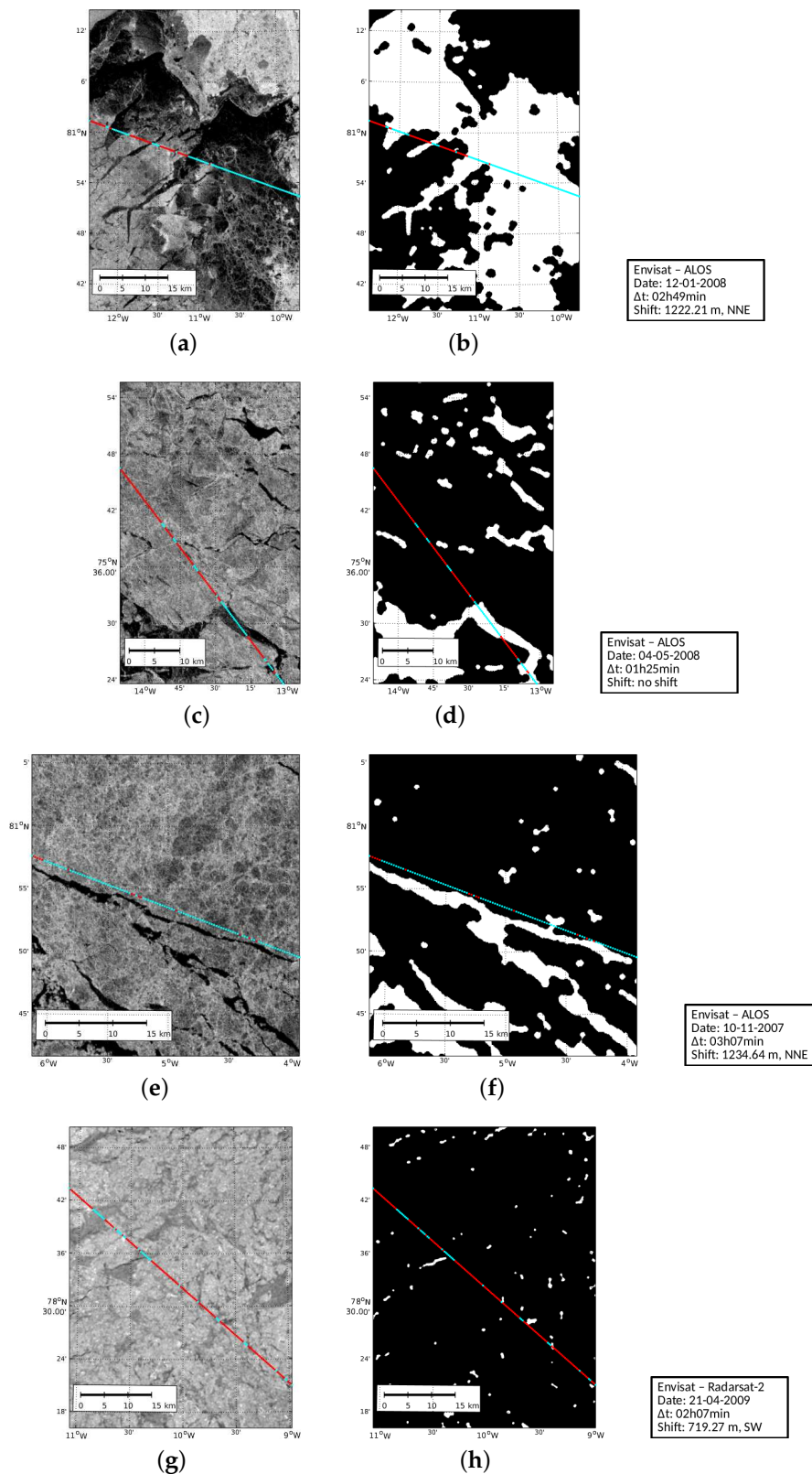


Figure 7. Examples of open water detection from Envisat against ALOS (a–f) and Radarsat-2 (g,h) before (left) and after SAR image processing (right) with open water indicated in white. Boxes provide additional image and processing information. Red: ice detection, cyan: open water detection. The geographical locations of the image subsets are displayed in Figure 1; from top to bottom in green, blue, yellow and magenta.

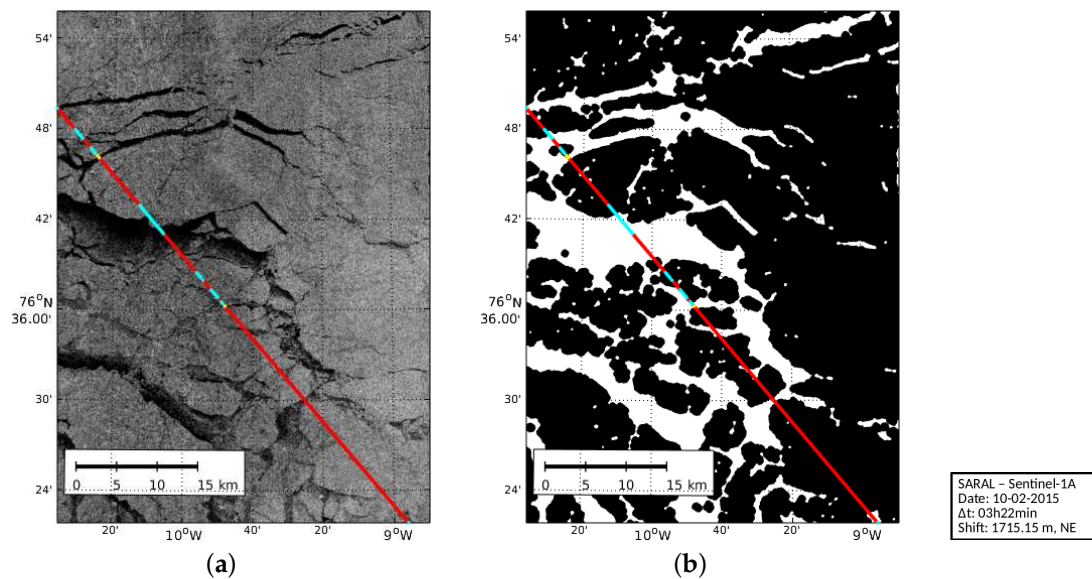


Figure 8. Example (orange highlighted in Figure 2) of open water detection from SARAL against Sentinel-1A before (left) and after SAR image processing (right) with open water indicated in white. Box provides additional image and processing information. Red: ice detection, cyan: open water detection, yellow: saturated AltiKa observations.

Table 5. Table providing percentage statistical information about conditional $P(X|Y)$ and consistency $P(CR)$ rates of visual examples discussed in Section 4.2. “SAR” and “Alt” indicate imaging SAR and altimetry. Ice detections are indexed by overline character marked shortcuts.

Subset	$P(CR)$	$P(Alt \overline{SAR})$	$P(SAR Alt)$	$P(Alt SAR)$
Figure 7b	90.63%	15.91%	91.86%	94.05%
Figure 7d	85.10%	16.04%	64.58%	88.57%
Figure 7f	12.61%	88.99%	2.02%	100.00%
Figure 7h	76.22%	22.36%	0.00%	0.00%
Figure 8b	72.07%	12.41%	40.68%	25.53%

The first example (Figure 7a) demonstrates very good accordance between altimetry and SAR classification. The L-band image displays different sea ice and open water conditions. From West to East, various sized open water areas ranging from 200 m up to 3.5 km are visible. A large region appearing in dark reaches from the image center at 11°W to the eastern edge. It indicates a mixture of differently sized ice floes interrupted by open water sections. Analyzing the colored altimetry observations, the open water detection is in good accordance with the grayscaled as well as with the binary coded SAR image (Figure 7b). The quantitative comparison yields a consistency rate $P(CR)$ of 90.63%. Moreover, the altimetry classification approach provides a true classification rate close to 100% ($P(Alt|SAR) = 0.94$). This comprises small leads as well as larger areas of open water.

An almost perfect accordance between altimetry classification and SAR images can also be observed in Figure 7c, detecting an expanded lead in the southern image part and some small leads in the central part of the image. However, comparing Figure 7c and d to the altimetry classification results at 75°36.00'N, it is clearly visible that SAR image processing is not always able to segment very narrow lead fragments. This might happen because of a poor spatial pixel resolution of the SAR sensor (100 m), an insufficient identification of the ice-water transition, or a too restrictive threshold level in the SAR image processing. This deficiency in the automatic SAR image processing results in reduced performance in the quantitative comparison with a total consistency rate of about 85% and a true water detection rate of 88.6%.

However, there are also problems related to the altimetry observation technique. The example displayed in Figure 7e,f is characterized by a very long (ca. 47 km) and in most parts narrow lead located parallel to the satellite track. The SAR image is shifted about 1.2 km in the northeastern direction, assuming a steady sea ice motion. Even if the altimeter track is still located northwards at the off-nadir position of the lead, almost all measurements are classified as open water. As a consequence, in the quantitative comparison, just 2% of all Envisat open water detections are confirmed by SAR classification although they can be visually connected with the dominant lead in the image center. The overall consistency rate yields only 12.6%—probably due to the fact that the altimetry classification approach is not able to separate off-nadir water returns from nadir water returns or the mean sea ice motion correction is not enough to consider the total sea ice drift.

Additional discrepancies between altimetry and SAR classification can occur in areas with new, very thin ice coverage. Figure 7g shows those areas, appearing light gray in C-band, only a little darker than the surrounding older ice. These areas are correctly set to ice by the SAR image processing (see Figure 7h) because of the small brightness differences between the thin and surrounding ice types. In contrast, the altimetry returns within these areas are falsely classified and interpreted as calm open water since they show a very narrow and single-peaked lead/polynya-like shape. One explanation for this mis-interpretation is the dominant scattering of all flat and specular surfaces. Connor et al. [11] found that strong reflective surfaces, for example, leads/polynyas, can also affect the waveform shape if covered by very thin ice. A distinction from open water is not possible based on the altimetry waveform's shape. Since the ice is very thin, the retracked ranges should represent the water level well enough, even if the classification is wrong.

Related to the comparison process itself, uncertainties in sea ice motion correction can reduce the quantitative consistency rate. Figure 8a,b are corrected by ice-motion considering a time difference of more than 3 h. Analyzing Figure 8b, it can be shown that only 25.53% of the SAR detected ice openings are well identified by the altimetry data. A visual image inspection suggests that the applied ice motion correction is too small to completely compensate for the effect of the time lag.

Further challenging issues using SARAL SGDR-T data are so-called saturated waveforms. Zakharova et al. [12] pointed out that leads or strongly reflecting surfaces can exceed the maximum permissible power count value of 1250. The waveforms are cut and feature no clear peak due to a saturated power tracking window. Figure 8 highlights saturated SARAL observations in yellow. They are mainly located near small and calm open water areas, producing very high backscatter returns. In the classification process, they are omitted because of an unknown maximum peak position. In general, saturated SARAL waveforms are mainly traceable within the sea ice edge, but can provide evidence about the location of further open water areas. However, just 0.14% (i.e., 288 waveforms) of the comparison data are affected by a saturated power tracking window.

The present section shows a number of challenging and unavoidable impacts on the validation of the waveform classification process. Considerable parts of the inconsistencies do not originate from the altimetry classification but from the SAR classification or the ice-motion correction. In order to adequately rate the quantitative comparison results, it is necessary to keep these effects in mind.

5. Conclusions and Outlook

The present paper introduces an unsupervised classification approach based on pulse-limited multi-mission altimetry data to detect open water areas in a largely sea ice covered region. The study demonstrates the successful application of the clustering of pulse-limited altimeter waveforms for the automatic identification of open ocean, sea ice, lead and polynya observations. The approach is based on known partition cluster strategies (i.e., K-medoids) and memory-based classification methods (i.e., K-nearest-neighbor). A 10-fold cross-validation for the assessment of the precision of the classification method is performed. It indicates an internal misclassification error of about 2% for Envisat and SARAL. The algorithm is applicable to every pulse-limited altimetry satellite mission without requiring any deeper knowledge about mission specific details. Moreover, it can be assumed

that the developed approach also works for SAR altimetry waveforms if the waveform feature space is adapted adequately. Additionally, the presented method can be adapted to a number of open water detection or waveform classification tasks, e.g., for the identification of lake returns [33] or in inundation areas.

In order to evaluate the classification results, a comparison with SAR images is performed. In contrast to previous studies, the present validation relies not only on visual and manually selected examples, but also on a larger set of images and an automated comparison procedure. The comparison procedure allows for a quantitative assessment of the classification performance by assigning the altimetry observations to open water and sea ice returns and checking them against processed SAR images that indicate sea ice and open water areas. We reach consistency rates of 70.7% for Envisat and 76.9% for SARAL. However, it has to be underlined that the quantitative comparison results of Envisat and SARAL are not directly comparable because of significant differences in the underlying sensor and instrument characteristics of the available SAR missions.

When interpreting the comparison results, different sources of inconsistencies have to be considered, e.g., effects from the altimetry data and their classification procedure and uncertainties in SAR image processing as well as in the ice-motion correction. The Fram Strait and the Greenland Sea are one of the most dynamic areas on Earth. Fast changing sea ice conditions due to short, periodic melting and refreezing as well as rapid climate change make it hard to provide a high reliability in the comparison as well as in the altimetry classification results. Local phenomena, such as melt ponds (i.e., open water pools on the sea ice surface) and their impacts on the open-water detection, have to be investigated. Over specific sea ice types, altimetry waveforms show ambiguities, which prevents a clear attribution to sea ice or open water returns. In particular, specular thin and flat ice produces very specular returns resembling open water returns. In contrast, big ice floes or landfast ice can imitate ocean-like returns due to similarities in ocean surface roughness and reflectivity.

Further improvements of the classification method are possible. In particular, saturated SARAL waveforms have to be included in the classification process. In addition, the application of more recent sea ice motion data in combination with Sentinel-1B data could lead to a better spatio-temporal ratio within the validation process.

A reliable classification is an indispensable requirement for a meaningful estimation and an efficient computation of sea surface heights in the Arctic by retracking only open water waveforms. In addition to Envisat and SARAL, more pulse-limited (e.g., ERS-1/2) as well as delay-doppler altimetry data (e.g., CryoSat-2, Sentinel-3A) may be employed in the classification process and, thus, contribute to the generation of a long-term sea level record for the Arctic ocean.

Supplementary Materials: The following folder and figures are available online at www.mdpi.com/2072-4292/9/6/551/s1, Figure S1 displays SARAL waveform clusters, Figures S2–S6 and folder S2 contain Figures 7 and 8 showing the classification results without class assignment.

Acknowledgments: The authors thank the following institutions and agencies for providing their data and software products under the terms of the GNU General Public License. ESA for operating and managing Envisat, Sentinel-1A and the SNAP Toolbox. CNES for providing SARAL data. JAXA/METI and ASF DAAC for making ALOS PALSAR L1.5 data and MapReady Toolbox available as well ESA for maintaining MDA Radarsat-2 data in framework of Third Party Mission program. This work was supported by the German Research Foundation (DFG) through grants, BO1228/13-1 and DE2174/3-1. The publication is funded by the Technical University of Munich (TUM) within the framework of the Open Access Publishing Program. We thank five anonymous reviewers for their valuable comments that helped to improve the manuscript.

Author Contributions: Felix L. Müller developed the classification and validation methods, conducted the data analysis and wrote the majority of the paper. Denise Dettmering supervised the present study, contributed to the manuscript writing and helped with the discussions of the applied methods and results. Wolfgang Bosch initiated the study. Florian Seitz supervised the research. Both were involved in the writing process and discussed the methods presented in the manuscript as well.

Conflicts of Interest: The authors declare no conflict of interest.

References

1. Comiso, J. *Polar Oceans from Space*; Atmospheric and Oceanographic Sciences Library, Springer: New York, NY, USA, 2010.
2. Stroeve, J.C.; Markus, T.; Boisvert, L.; Miller, J.; Barrett, A. Changes in Arctic melt season and implications for sea ice loss. *Geophys. Res. Lett.* **2014**, *41*, 1216–1225.
3. Polyakov, I.V.; Beszczynska, A.; Carmack, E.C.; Dmitrenko, I.A.; Fahrbach, E.; Frolov, I.E.; Gerdes, R.; Hansen, E.; Holfort, J.; Ivanov, V.V.; et al. One more step toward a warmer Arctic. *Geophys. Res. Lett.* **2005**, *32*, L17605.
4. Sasgen, I.; van den Broeke, M.; Bamber, J.L.; Rignot, E.; Sørensen, L.S.; Wouters, B.; Martinec, Z.; Velicogna, I.; Simonsen, S.B. Timing and origin of recent regional ice-mass loss in Greenland. *Earth Planet. Sci. Lett.* **2012**, *333–334*, 293–303.
5. Laxon, S.W. Sea-Ice Altimeter Processing Scheme at the EODC. *Int. J. Remote Sens.* **1994**, *15*, 915–924.
6. Rio, M.H.; Hernandez, F. A mean dynamic topography computed over the world ocean from altimetry, in situ measurements, and a geoid model. *J. Geophys. Res. Oceans* **2004**, *109*, doi:10.1029/2003JC002226.
7. Dwyer, R.; Godin, R. *Determining Sea-Ice Boundaries and Ice Roughness Using GEOS-3 Altimeter Data*; Technical Report; NASA Wallops Flight Center: Wallops Island, VA, USA, 1980.
8. Fetterer, F.M.; Drinkwater, M.R.; Jezek, K.C.; Laxon, S.W.C.; Onstott, R.G.; Ulander, L.M.H. Sea Ice Altimetry. In *Microwave Remote Sensing of Sea Ice*; American Geophysical Union: Washington, DC, USA, 2013; pp. 111–135.
9. Laxon, S.; Peacock, N.; Smith, D. High interannual variability of sea ice thickness in the Arctic region. *Nature* **2003**, *425*, 947–950.
10. Peacock, N.R. Sea surface height determination in the Arctic Ocean from ERS altimetry. *J. Geophys. Res.* **2004**, *109*, C07001.
11. Connor, L.N.; Laxon, S.W.; Ridout, A.L.; Krabill, W.B.; McAdoo, D.C. Comparison of Envisat radar and airborne laser altimeter measurements over Arctic sea ice. *Remote Sens. Environ.* **2009**, *113*, 563–570.
12. Zakharova, E.A.; Fleury, S.; Guerreiro, K.; Willmes, S.; Rémy, F.; Kouraev, A.V.; Heinemann, G. Sea Ice Leads Detection Using SARAL/AltiKa Altimeter. *Mar. Geod.* **2015**, *38*, 522–533.
13. Zygmuntowska, M.; Khvorostovsky, K.; Helm, V.; Sandven, S. Waveform classification of airborne synthetic aperture radar altimeter over Arctic sea ice. *Cryosphere* **2013**, *7*, 1315–1324.
14. Passaro, M.; Müller, F.L.; Dettmering, D. Lead Detection using Cryosat-2 Delay-Doppler Processing and Sentinel-1 SAR images. *Adv. Space Res.* **2017**, under review.
15. Rudels, B.; Friedrich, H.J.; Quadfasel, D. The Arctic Circumpolar Boundary Current. *Deep-Sea Res. Part II* **1999**, *46*, 1023–1062.
16. Serreze, M.; Barry, R. *The Arctic Climate System*; Cambridge Atmospheric and Space Science Series; Cambridge University Press: Cambridge, UK, 2014.
17. Bersch, M. On the circulation of the northeastern North Atlantic. *Deep-Sea Res. Part II* **1995**, *42*, 1583–1607.
18. Woodgate, R.A.; Fahrbach, E.; Rohardt, G. Structure and transports of the East Greenland Current at 75°N from moored current meters. *J. Geophys. Res. Oceans* **1999**, *104*, 18059–18072.
19. Verron, J.; Sengenès, P.; Lambin, J.; Noubel, J.; Steunou, N.; Guillot, A.; Picot, N.; Coutin-Faye, S.; Sharma, R.; Gairola, R.M.; et al. The SARAL/AltiKa Altimetry Satellite Mission. *Mar. Geod.* **2015**, *38*, 2–21.
20. Japan Aerospace Exploration Agency (JAXA). *ALOS Data Users Handbook, Revision C*; Japan Aerospace Exploration Agency: Chofu, Tokyo, Japan, 2008.
21. MDA. *RADARSAT-2 Product Description*; Report RN-SP-52-1238, Issue 1/13; MacDonald, Dettwiler and Associates Ltd.: Vancouver, BC, Canada, 2016.
22. Sentinel-1 Team. *Sentinel-1 User Handbook*; GMES-S1OP-EOPG-TN-13-0001, Issue Draft; European Space Agency: Paris, France, 2013.
23. Dierking W. Sea Ice Monitoring by Synthetic Aperture Radar. *Oceanography* **2013**, *26*, doi:10.5670/oceanog.2013.33.
24. Jackson, C.R.; Apel, J.R. *Synthetic Aperture Radar: Marine User's Manual*; US Department of Commerce, National Oceanic and Atmospheric Administration, National Environmental Satellite, Data, and Information Service, Office of Research and Applications: Washington, DC, USA, 2004; pp. 81–115.

25. Tschudi, M.; Fowler, C.; Maslanik, J.; Stewart, J.S. *Polar Pathfinder Daily 25 km EASE-Grid Sea Ice Motion Vectors, Version 3*; Subset: Greenland Sea, Date Accessed: 16.11.2016; National Snow and Ice Data Center: Boulder, CO, USA, 2016.
26. Cavalieri, D.; Parkinson, C.; Gloersen, P.; Zwally, J.H. *Sea Ice Concentrations from Nimbus-7 SMMR and DMSP SSM/I-SSMIS Passive Microwave Data, Version 1*; Subset: Greenland Sea, Date Accessed: 16.11.2016; NASA National Snow and Ice Data Center Distributed Active Archive Center: Boulder, CO, USA, 1996.
27. Xu, R.; Wunsch, D.C. *Clustering*; IEEE Press Series on Computational Intelligence; IEEE Press: Hoboken, NJ, USA; Wiley: Piscataway, NJ, USA, 2009.
28. Hastie, T.; Tibshirani, R.; Friedman, J. *The Elements of Statistical Learning*; Springer: New York, NY, USA, 2009; Volume 2, pp. 337–387.
29. Kohonen, T. *Self-Organizing Maps*; Springer Series in Information Sciences, Springer: Berlin/Heidelberg, Germany, 2012.
30. Celebi, M. *Partitional Clustering Algorithms*; EBL-Schweitzer, Springer International Publishing: Cham, Switzerland, 2014.
31. Kaufman, L.; Rousseeuw, P.J. *Finding Groups in Data: An Introduction to Cluster Analysis*; Wiley Series in Probability and Mathematical Statistics; Wiley: New York, NY, USA, 1990.
32. Kvingedal, B. Sea-Ice Extent and Variability in the Nordic Seas, 1967–2002. In *The Nordic Seas: An Integrated Perspective*; American Geophysical Union: Washington, DC, USA, 2013; pp. 39–49.
33. Göttl, F.; Dettmering, D.; Müller, F.L.; Schwatke, C. Lake Level Estimation Based on CryoSat-2 SAR Altimetry and Multi-Looked Waveform Classification. *Remote Sens.* **2016**, *8*, 885.



© 2017 by the authors. Licensee MDPI, Basel, Switzerland. This article is an open access article distributed under the terms and conditions of the Creative Commons Attribution (CC BY) license (<http://creativecommons.org/licenses/by/4.0/>).

P-1.2 Lead detection using cryosat-2 delay-doppler processing and sentinel-1 sar images

Passaro, M., Müller, F. L., and Dettmering, D. (2018b). Lead detection using cryosat-2 delay-doppler processing and sentinel-1 sar images. *Advances in Space Research*, 62(6):1610 – 1625, ISSN: 0273-1177, DOI: 10.1016/j.asr.2017.07.011

Copyright

The publication was published in *Advances in Space Research*, which is the official journal of the Committee on Space Research (COSPAR). It is distributed by Elsevier. The copyright license is transferred to Elsevier.

Summary

The work focuses on the lead detection using CryoSat-2 Synthetic Aperture Radar (SAR) altimetry waveforms and Sentinel-1A SAR images. The latter is primarily used to rate the lead classification performance of SAR altimetry. The mounted SAR altimeter is characterized by a smaller along-track footprint and an improved spatial resolution compared to conventional altimeters for example Envisat. CryoSat-2 was the first satellite altimetry mission exploiting the full Delay-Doppler (DD) signal of a surface target from different look angles. The received DD signals from one surface target are stored in a stack diagram. Summing up all radar echoes (waveforms) acquired at different look angles provides the multilook SAR waveform. The summation of all waveforms in the across-track (i.e. range) direction, however, results in the Range Integrated Power (RIP) waveform, which contains information about the backscattering properties of the illuminated surface and provides information about the reflection behavior of individual scatterers with respect to the changing look angle. If the satellite passes a very smooth surface like a small lake or lead, the RIP displays a very peaky shape, contrary to a sea ice surface resulting in a more diffuse scattering. This behavior is exploited to develop a threshold-based classification method based on the CryoSat-2 stack by computing the Pulse-Peakiness of the RIP waveforms called the stack peakiness. When a lead enters the altimeter's field of view, more power is reflected back to the altimeter receiver, resulting in higher stack peakiness values. The stack peakiness value exceeding a pre-defined threshold defines the lead return at the nadir position (i.e. zero look angle) and identifies the corresponding multilook waveform enabling a reliable sea surface height determination.

Beside the SAR altimetry based lead detection approach, the publication also focuses on the identification of lead areas by using SAR images of Sentinel-1A. In contrast to SAR altimeters, which observe the Earth surface in nadir direction, Sentinel-1A carries a side-looking imaging SAR instrument. The SAR images contain backscatter information of the surface, which are transformed to pixel values. Dark pixel areas indicate a strong

specular behavior, which, for example, refers to the presence of leads, in contrast to sea ice or open ocean areas, which appear brighter. The brightness differences are exploited to develop an automatic, quantitative lead detection approach based on several image processing tools. The method aims at a segmentation of the SAR pixels indicating small open water bodies within the sea ice domain and sea ice surfaces. Therefore, the SAR images are noise reduced, dark-pixel emphasized and converted to binary values by applying an adaptive thresholding algorithm considering different illumination condition within the images. After the segmentation into binary values, the pixels undergo a mathematical morphological operation to connect fragmented lead areas.

In order to compare the processed images with the stack peakiness-based classification of CryoSat-2, the image coordinates are shifted to account for the sea ice drift between the acquisition times of CryoSat-2 and Sentinel-1A. The comparison is done by interpolating the SAR pixel coordinates to the CryoSat-2 observation locations using a simple nearest-neighbor interpolation.

The CryoSat-2 stack peakiness-based lead detection is compared with other stack based parameters, which are already provided in the CryoSat-2 dataset. A visual comparison with external SAR images shows that the stack peakiness-based classification recognizes leads at the nadir more position more reliably, than a detection based on the stack standard deviation or the stack kurtosis. The quantitative comparison based on 12 CryoSat-2 ground tracks reveals that the classification based on the stack peakiness performs equally as a lead detection based on the stack standard deviation and stack kurtosis.

Contribution

Marcello Passaro developed the classification approach, conducted the altimetry data processing and wrote the majority of the paper. Felix L. Müller developed and performed the validation approach and contributed to the manuscript writing. Denise Dettmering supported the study with discussions of the applied methods and results. The overall contribution of Felix L. Müller is estimated to be **40%**.



Lead detection using Cryosat-2 delay-doppler processing and Sentinel-1 SAR images

Marcello Passaro^{*}, Felix L. Müller, Denise Dettmering

Deutsches Geodätisches Forschungsinstitut der Technischen Universität München, Arcisstraße 21, 80333 Munich, Germany

Received 15 November 2016; received in revised form 12 April 2017; accepted 7 July 2017
Available online 15 July 2017

Abstract

In the Arctic and Antarctic Ocean, where part of the sea surface is seasonally or continuously covered by sea ice, the sea level monitoring from satellite altimetry relies on the localisation of open water areas, especially on the detection of leads: long and narrow fractures in the sea ice, which dominate the radar echoes even if hundreds of meters away from nadir.

The Cryosat-2 altimetry mission is based on the Delay-Doppler processing, in which the averaged waveform is formed by summing up several looks acquired at different look angles and stacked together. This imaging technique and the resulting improved along-track resolution are here exploited to evaluate different lead identification schemes.

In particular, stack and power statistics of Cryosat-2 waveforms are used to classify leads on a subset of 12 tracks in which the altimetry-based classification is compared to a classification based on Sentinel-1A SAR images. For this scope, a dedicated SAR-image automated processing is proposed to avoid the manual classification.

Results show that the adoption of a single new stack parameter (the Stack Peakiness) can perform equally well as the use of multiple stack parameters currently available. Moreover, a multi-waveform analysis of the Stack Peakiness helps to isolate the point where narrow leads cross the tracks at nadir.

For all the tested strategies, the number of altimetry-detected leads that are unidentified by SAR is comparable to the number of detections from both sensors. This could be due to presence of narrow leads, not detected by SAR due to resolution limits, but still dominant in the radar altimeter return due to the high backscatter.

© 2017 COSPAR. Published by Elsevier Ltd. All rights reserved.

Keywords: Leads detection; Delay-Doppler altimetry; Cryosat-2 stack data; Sentinel-1; SAR image processing

1. Introduction

The measurement of sea level variability in the global ocean is considered among the most important climatic indices. It relies on in situ observations provided by a wide but unevenly distributed set of tide gauges and, since more than 20 years, on measurements collected by the radar altimeters on board of several satellite missions.

The coverage of satellite altimetry over the ocean cannot completely be defined as global, since a large part of the Arctic and Antarctic oceans is excluded. On one side this is due to the limited latitude extent of most of the altimetric missions due to their orbit configuration. On the other side the ocean in the northernmost latitudes is partially covered by sea ice, which reflects the radar signal before it hits the sea surface, preventing the possibility to measure sea level. The estimation in the sea-ice covered regions is limited to the leads, narrow cracks in the sea ice that can be several tens of kms long. Since these ocean patches are very smooth and do not have a developed wave field, the signal

^{*} Corresponding author.

E-mail address: marcello.passaro@tum.de (M. Passaro).

returned to the satellite is much stronger than the one reflected from the surrounding ice and can dominate the registered waveforms even if the lead is not located at nadir. In particular, [Armitage and Davidson \(2014\)](#) have shown that a lead can be the dominant return in the waveform up to about 1.5 km away from the sub-satellite point (nadir). Such off-nadir returns, if not properly spotted, result in erroneous estimations of the sea level.

Cryosat-2 (CS-2) offers ways for improving the sea level records in these regions. With its orbit configuration, it provides coverage up to 88° in latitude. Thanks to the Delay-Doppler processing of its echoes (when operating in the so-called “SAR mode” over sea ice, not to be confused with SAR imaging from Sentinel-1 used in this study), it stores the signal registered by the satellite looking at the same resolution cell on the ground from different look angles. In particular, the beam-limited along-track footprint size (305 m, [Scagliola, 2013](#)) should guarantee a more precise determination of the lead position. Nevertheless, due to the size of the pulse-limited across-track footprint (1.65 km), the distinction of a lead return at nadir from an off-nadir reflection is still challenging. Most of the leads have width of less than a km ([Lindsay and Rothrock, 1995](#); [Kwok et al., 2009](#)), while Cryosat-2 has a sampling interval of roughly 300 m (using the 20-Hz rate): in most of the cases, only one range measurement per lead will correspond to the distance at nadir. Being able to correctly identify the nadir echoes of these narrow, but numerous open water openings can increase the amount of sea level measurements and therefore improve the records.

Previous studies on past altimetry missions have used lead-detection algorithms that distinguish leads from sea ice based on the shape of the received signal: Empirical thresholds were assigned in order to classify the waveforms based on the “pulse peakiness” ([Peacock and Laxon, 2004](#)). [Laxon et al. \(2013\)](#), [Ricker et al. \(2014\)](#) and [Rinne and Similä \(2014\)](#) have classified CS-2 signals using a combination of different waveform parameters (including the pulse peakiness) available in the European Space Agency (ESA) Baseline C Product files or computable from the waveforms. Recently, [Wernecke and Kaleschke \(2015\)](#) argued that it is possible to obtain an efficient lead classification only based on the absolute value of the maximum waveform power.

Leads can be also determined using thermal infrared sensors ([Willmes and Heinemann, 2015](#)), microwave radiometers ([Röhrs and Kaleschke, 2012](#)) and SAR images ([Ivanova et al., 2016](#)). SAR images have the advantage of being independent from weather conditions, while providing a good resolution (40 m for Sentinel 1A). They can be therefore used for comparison with the altimetry-based lead classification, but the time difference between the acquisition of the two different data sources needs to be taken in consideration, since sea ice moves on average from 4 km/day in winter up to over 9 km/day in summer (as measured by buoys in [Rampal et al. \(2009\)](#)) and leads can quickly refreeze and close ([Weeks, 2010](#)).

The objective of this study is to provide a first assessment of the lead-classification methodologies based on the Delay-Doppler processing of Cryosat-2 echoes in comparison to SAR images from Sentinel-1A. Our classification, based on a new parameter computed using the Delay-Doppler processing of CS-2 (in particular from the full stack information) and on a multi-waveform analysis to isolate the nadir return, is compared with the methodologies derived from the recent literature. A SAR-image processing chain is proposed to provide a reference for validation and, for the first time, is used to provide an objective comparison that is not based on a visual recognition of lead-like features.

A description of the dataset and the area of study is provided in Section 2. Section 3 describes the methodology used to analyse the altimetry and SAR dataset and to classify the leads. In Section 4 the results of the comparison are presented and discussed. Section 5 draws the conclusions and the outlook for future research.

2. Dataset

2.1. Cryosat-2 LIB-S data

By exploiting the Doppler frequency and the coherence of consecutive pulses, Delay-Doppler altimeters are able to perform multi-looked acquisitions, i.e. to associate to a resolution cell a certain number of looks (variable depending on the processing settings) acquired at different look angles as the satellite moves over the imaged area ([Raney, 1998](#)).

Using processing techniques inherited from the SAR processing, such as Range compression and Range migration correction, all the returns corresponding to the resolution cell (a 20-Hz sampling of the illuminated surface, i.e. one measurement every 300 m roughly) are aligned in a 2D-stack ([Figs. 1a and 2a](#)). The Cryosat-2 multilooked radar waveforms, such as the one in [Fig. 1c and 2c](#), are obtained by the incoherent sum of all the echoes in the stack. By summing up the returns in the across-track (Range) dimension ([Fig. 1b and 2b](#)), the so-called Range Integrated Power (RIP) waveform, can be generated. It contains information concerning the backscattering properties of the illuminated surface, but it also reveals details of the distribution of the scatterers as the satellite spans different look angles passing over the nadir position ([Wingham et al., 2006](#)).

When the satellite moves over a very smooth surface, such as for small lakes or leads ([Fig. 1](#)), the signal will be specularly reflected back and the RIP will be peaky. On the opposite, when flying over areas containing scatterers with different orientation, such as for wavy seas or ice, the backscattered power will be more normally distributed ([Fig. 2](#)).

LIB products provide statistical parameters that describe the RIP behaviour, but do not provide the full stack, limiting therefore the possibilities of analysis. The ESA Grid Processing on Demand (G-POD) service

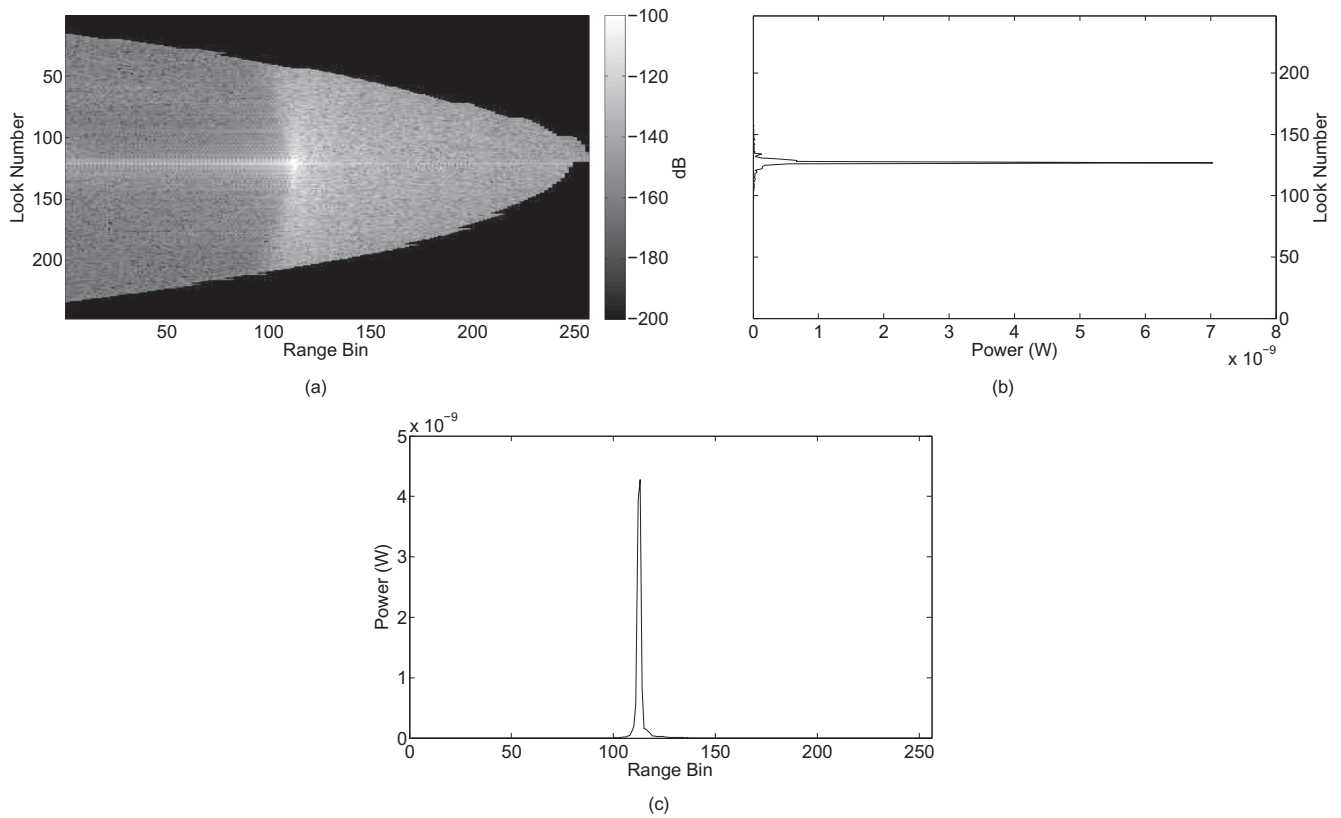


Fig. 1. Example of a stack (a), a RIP (b) and a multilooked waveform (c) acquired by Cryosat-2 over a lead.

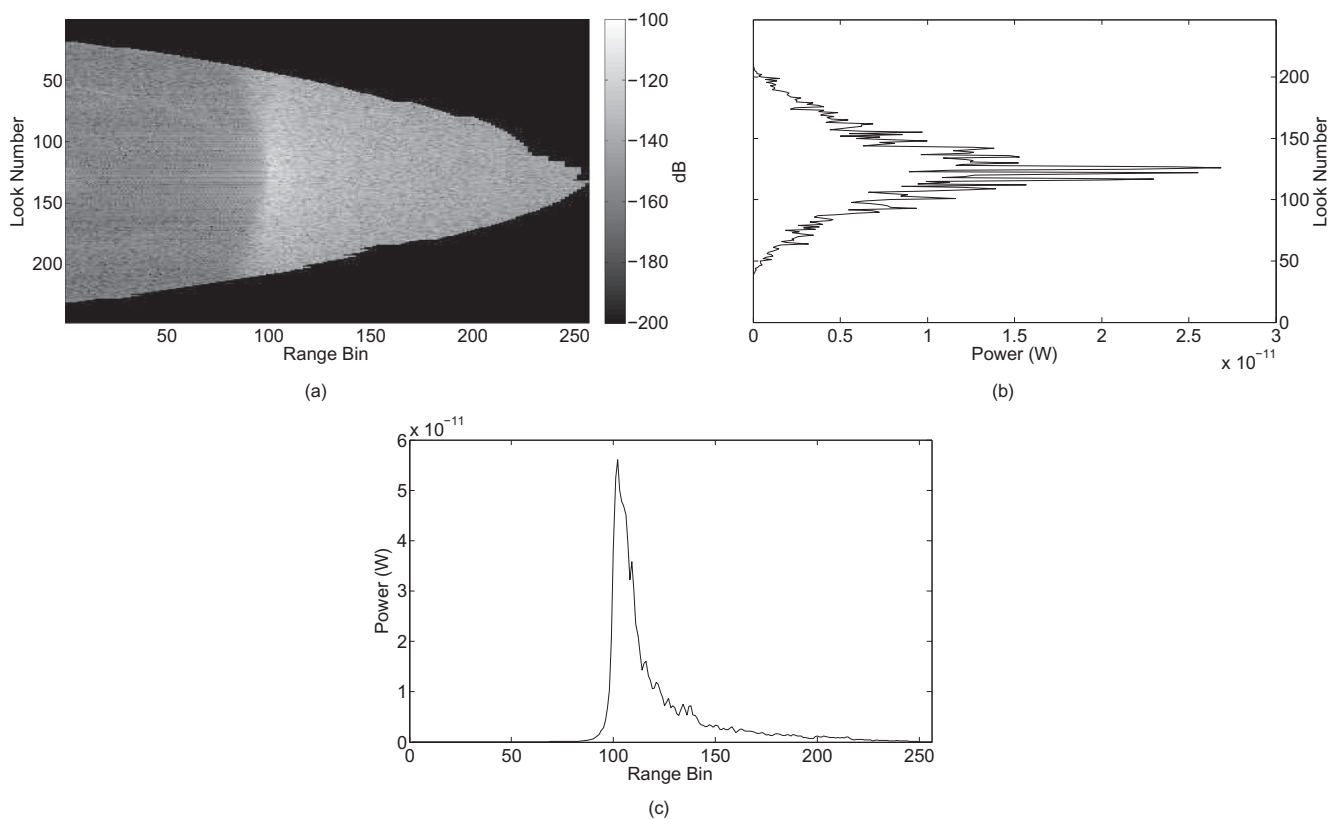


Fig. 2. Example of a stack (a), a RIP (b) and a multilooked waveform (c) acquired by Cryosat-2 over sea ice.

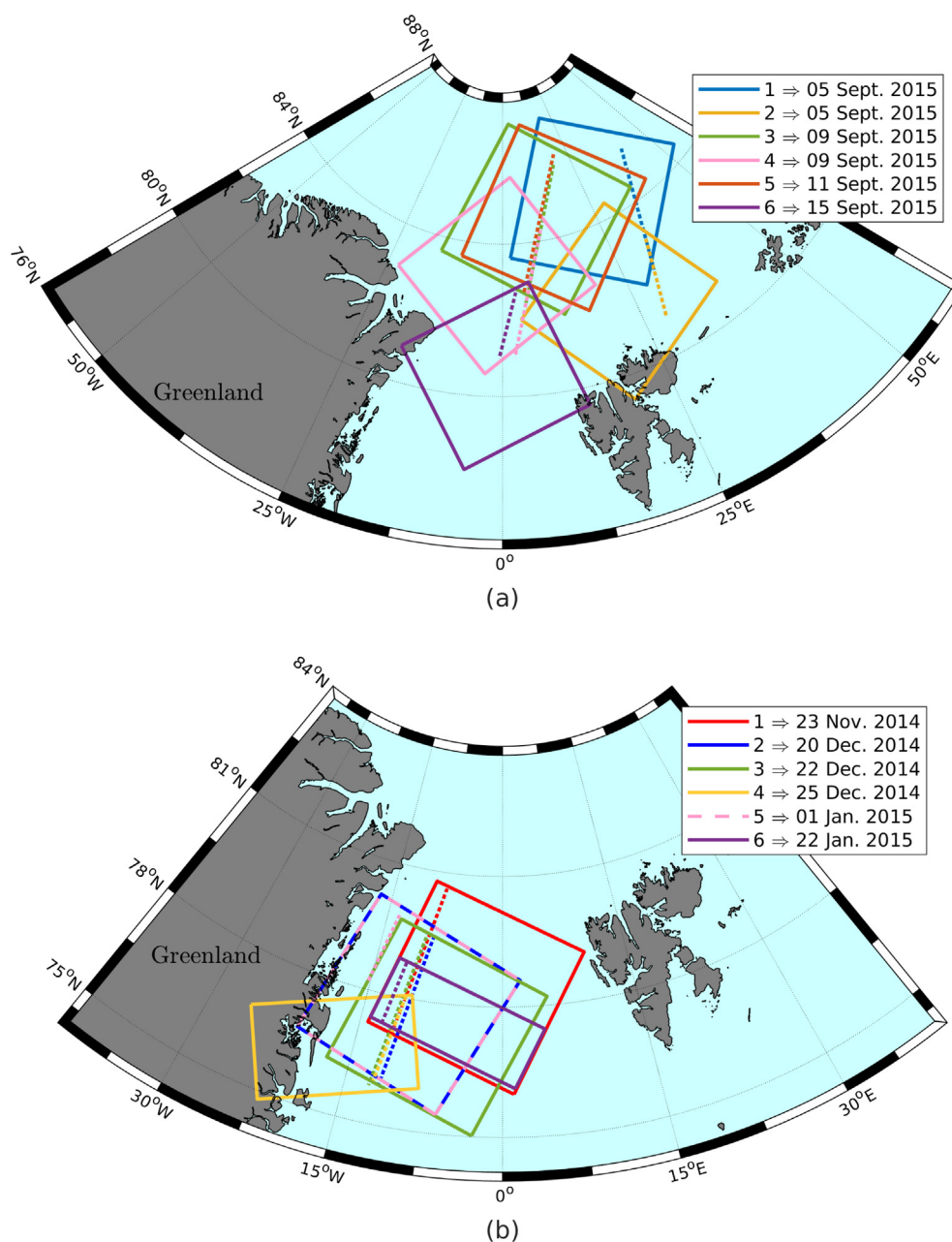


Fig. 3. Location and date of the SAR-images in the two control datasets. Dashed lines are the corresponding segments of CS2 tracks on which the classification is applied.

(see acknowledgements) is currently the only freely and easily available source to access these data. The ESA Baseline C version of this LIB stack (LIB-S) data set is used in this study (Scagliola and Fornari, 2015).

2.2. Sentinel-1A SAR images

One of the ways to verify the classification of altimetric echoes is the comparison with satellite SAR images. These have been used for lead detection, since very smooth water areas reflect electromagnetic waves like a mirror: consequently the slant incident radar waves reflect away from the spacecraft and flat water areas appear dark

(Dierking, 2013). Sentinel-1A SAR images are provided with two polarization modes HH and HV (where “H” indicates horizontal and “V” vertical). HH- and HV-polarization are particularly suitable for ice versus open water discrimination because of decreasing ocean clutter and smaller sensitivity to wind and wave scattering.

In the present investigation Level-1 dual-polarized SAR Sentinel-1A extra-wide-swath mode data at medium resolution (S1A-EW-GRDM-1SDH) are employed. The images are ground-range detected showing a 40-meter spatial resolution and a 400-km swath width, which allows a wide spatial coverage and a short revisit time. The images were pre-processed using the following standard

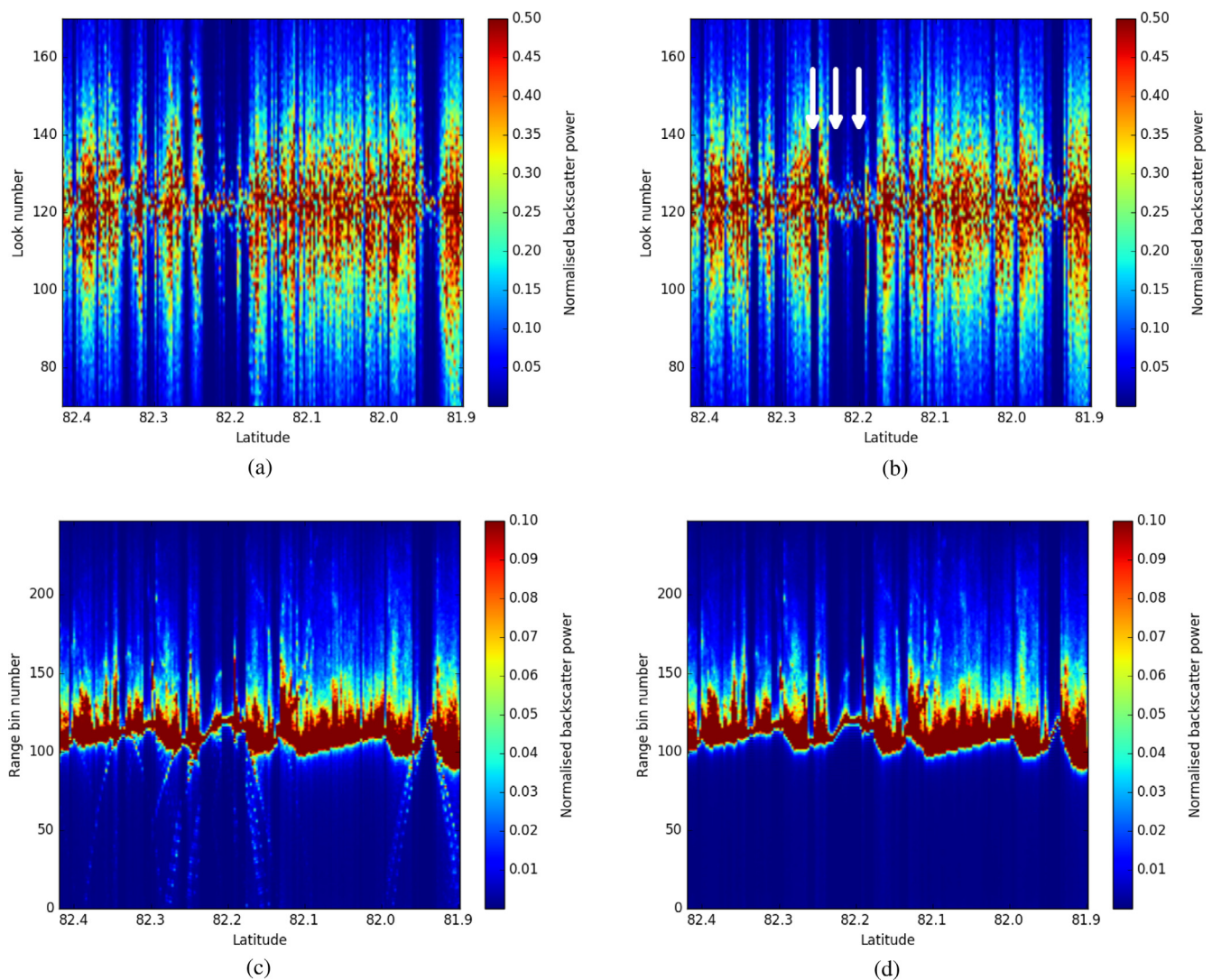


Fig. 4. Multilooked waveform (c and d) and RIP (a and b) radargrams from a CS-2 pass over sea ice acquired on the 5th September 2015 (see Fig. 3 for track location). All plots correspond to the same pass, but Hamming windowing has been applied in b and d. The arrows highlight residual sidelobe effects also despite the Hamming windowing. The normalised power has been saturated in order to visually show the sidelobe effect.

procedures: (1) Thermal noise removal, (2) Radiometric calibration, (3) Range Doppler terrain correction (Veci, 2016). The latter includes a coordinate transformation into an azimuthal equal area map projection to provide the same coordinate background as the sea ice motion vectors used to relate the images to the time of the altimetry overflight (see 2.3). In a last step, a type conversion to *uint8* is performed in order to get grayscale values and to reduce disk space.

In this study, two sets of control data of Sentinel-1A HH-polarised images are used (see Fig. 3): Set 1 comprises six images from September 2015 from the Arctic Ocean north of the Fram Strait. They are taken as a reference for comparison between the classification proposed in this study and the one described in Ricker et al. (2014). Set 2 includes six additional images taken between the north-east coast of Greenland and the Fram Strait. They are exploited as a further comparison using a different area

at various times of the year (November 2014 to January 2015).

All images were selected because of the time proximity with collocated Cryosat-2 tracks (never more than four hours of time difference) to reduce the influence of sea ice motion between the acquisition date of the imaging SAR and the altimetry record.

2.3. Sea ice velocities

Since sea ice can move significantly even in short time periods, it is desirable to take the ice velocity into account when comparing altimetry results with SAR images. For this purpose daily sea ice motion vectors provided by the National Snow and Ice Data Center (NSIDC) are used. At the time of writing, daily NSIDC ice motion vector fields are only available until 31 May 2015: therefore, the sea ice motion vectors are not applied to Set 1. The “Polar

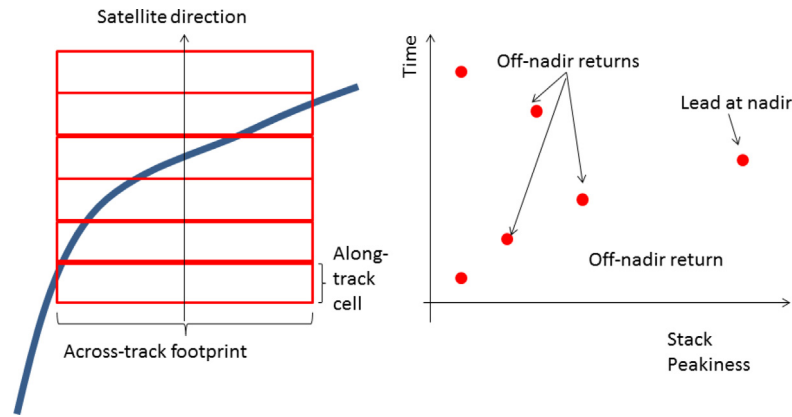


Fig. 5. Modelled lead (blue line) crossing over a CS-2 track (left) and expected SP behaviour (right). (For interpretation of the references to colour in this figure legend, the reader is referred to the web version of this article.)

Pathfinder Daily 25 km EASE-Grid Sea Ice Motion Vectors, Version 3” are based on data derived from different active and passive satellite sensors as well as in situ data. The data are provided at 25-km spatial resolution (Tschudi et al., 2016). The ice motion information is provided as zonal and meridional velocity grids.

Based on these data a mean velocity (magnitude and direction) is estimated by averaging all points in a ± 35 km rectangle box around each Cryosat-2 track. The SAR image, i.e., each of its pixel coordinates, is then shifted taking the acquisition time difference between SAR and CS-2 into account.

3. Methodology

3.1. Processing of Delay-Doppler altimetry data

3.1.1. Application of the Hamming window

When using LIB-S data in G-POD, it is possible to exploit different Delay-Doppler processing configurations. In order to apply the lead classification derived in this study, the Hamming-windowing step before the along-track Fast Fourier Transform is selected, which is currently the baseline of the distributed Cryosat-2 product (Bouzinac, 2012). Although this slightly lowers the along-track resolution and therefore creates some degree of dependence between consecutive echoes, it is needed in order to cut the energy coming from the sidelobes of the antenna.

Fig. 4 shows the so-called “radargrams” of a CS-2 track in a sea-ice covered region for the multilooked waveforms and for the RIP, without (a and c) and with (b and d) the Hamming window application. Each column corresponds to a 20-Hz RIP (a and b) or multilooked waveform (c and d). Before and after the peaky echoes typical of lead-like backscatter, high-power features are seen preceding the leading edge in the multilooked waveform radargram and in the non-zero look angles of the RIP radargram. In fact, the return coming from a sidelobe that sees a lead at nadir when the main lobe is side-looking has a shorter

range and therefore is registered before the leading edge corresponding to the resolution cell.

The sidelobe effects create false leading edges, influence the statistical analysis of the RIP and add backscattering of the same order of magnitude of the nadir return in the look angles closer to zero. These features mostly disappear after the application of the Hamming window, although residual signatures are visible, as highlighted by the arrows in Fig. 4b.

3.1.2. Definition of Stack Peakiness

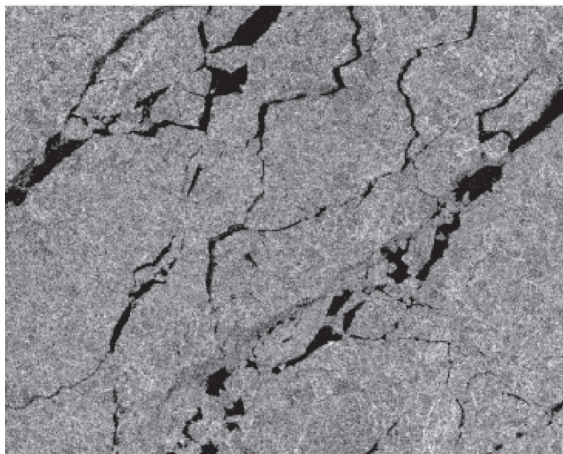
In order to characterise the RIP shape, the Stack Standard Deviation (SSD) and the Stack Kurtosis (SK) are already given in the ESA Baseline C product. These two indices, although useful to classify the kind of waveform, are not sufficient to isolate the nadir return of a group of waveforms influenced by a lead backscatter. The SSD is based on a gaussian fitting of the RIP, which is a poor approximation for peaky returns such as in Fig. 1b. The SK is highly influenced by remaining sidelobe effects in the looks that are close to the zero look, which can have a similar power. In order to compare the power at the zero look angle with the backscatter registered in the other looks, a new parameter called Stack Peakiness (SP) is defined in this study from the RIP normalised by its maximum value in the following way:

$$SP = \frac{1}{\overline{RIP}_{l,r}} \quad (1)$$

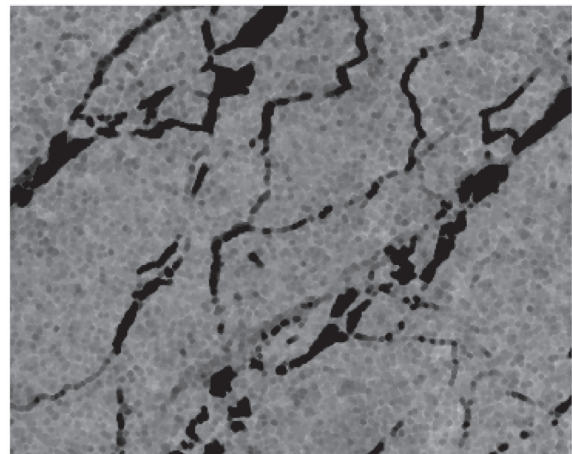
with

$$\overline{RIP}_{l,r} = \frac{\sum_{i=1}^N RIP(i)_{l,r}}{N} \quad (2)$$

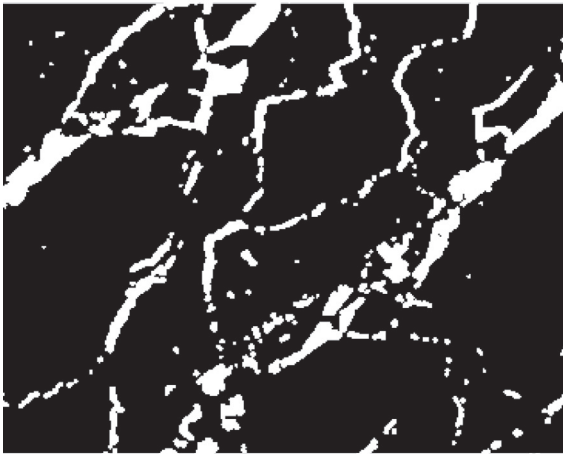
where N is the number of looks excluding the nadir look and $RIP(i)_{l,r}$ is the power from the look angle i , excluding the nadir look (i.e., at its right or left). A similar index of peakiness of the main return in comparison with the rest of echo was already defined in Ricker et al. (2014). Nevertheless this statistics was computed on the multilooked waveform, which is actually a time series of the received



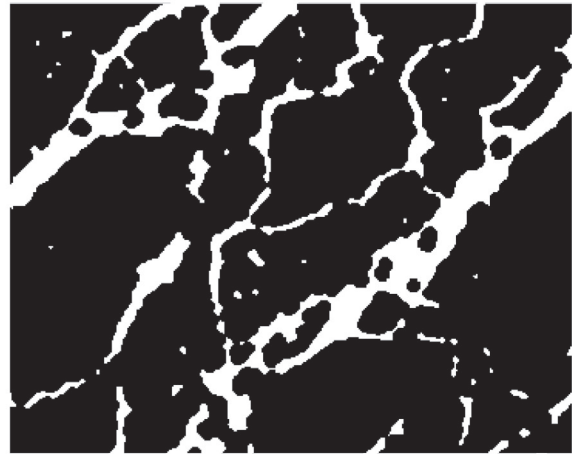
(a) Sentinel-1A image after SAR pre-processing



(b) Sentinel-1A image after median and minimum filtering



(c) Sentinel-1A image after segmentation



(d) Sentinel-1A image after morphological closing operation

0	0	1	1	1	0	0
0	1	1	1	1	1	0
1	1	1	1	1	1	1
1	1	1	1	1	1	1
1	1	1	1	1	1	1
0	1	1	1	1	1	0
0	0	1	1	1	0	0

(e) Octagon kernel for minimum filtering

Fig. 6. Sentinel-1A image subset of about 24×24 km: (a) the original grayscale SAR image after SAR pre-processing; (b) the same image after 5×5 median and minimum filtering; (c) the binary image after segmentation by adaptive thresholding; (d) final image after closing operation giving open water in white and sea ice areas in black. Plot (e) shows the octagon kernel with radius 3 around center pixel applied for the minimum filtering.

signal, while SP is able to compare the power reflected from the same resolution cell at different view angles.

The expected behaviour of SP in the case of a narrow lead crossing the CS-2 track is sketched in Fig. 5 and a verification with real data is provided in Section 4.1. When a lead enters the across-track pulse-limited footprint, the SP will be higher than a purely diffusive backscatter event, since the lead will scatter more energy back to the satellite. Nevertheless, the lead will still be slightly off-nadir in the across-track direction: Part of the incoming power will be

specularly reflected away. Off-nadir leads are usually characterised by lower levels of backscatter power compared to leads at nadir (Wernecke and Kaleschke, 2015). Consequently, a lead located off-nadir in the across-track direction will scatter less power back to the satellite, if compared with the same lead illuminated at nadir. The maximum SP, i.e. the time when the power at the zero look angle is strongest in comparison with the backscatter received at the other look angles, is therefore expected to correspond to the position in which the lead is at nadir.

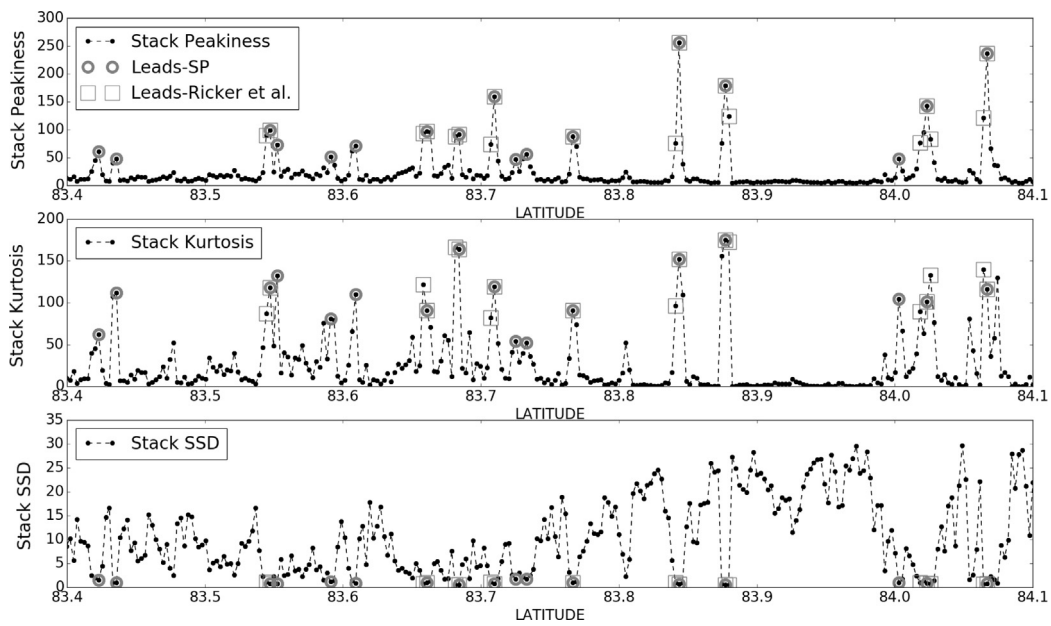


Fig. 7. SP behaviour along a CS-2 track acquired over sea ice (top plot). The figure shows the points that are recognized as leads by the SP-based classification described in this study (circles) and the results of the classification based on Ricker et al. (2014) (squares). The lower plots show Stack Kurtosis and Stack SSD for comparison.

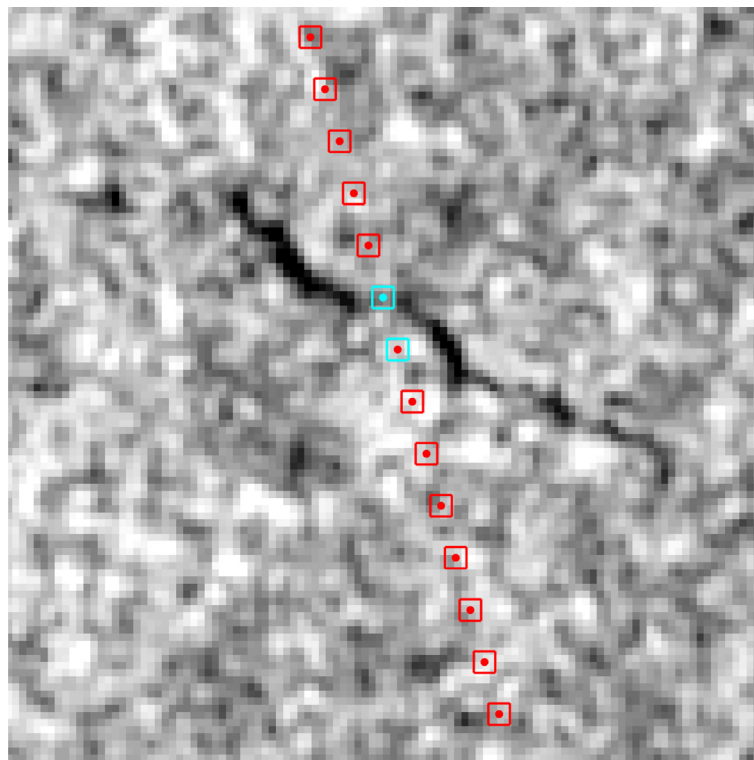


Fig. 8. 4.25 by 4.25 km zoom on a lead seen by Sentinel-1 image from 05/09/2015 at 12:46 (Image 1 of Set 1, see Fig. 3 for location), with Cryosat-2 crossing the area at 16:36. No ice motion correction is applied due to high variation in the ice flow direction. SP (dots) in comparison with classification results of Ricker (squares) showing in cyan lead detections.

3.2. Lead classification based on Cryosat-2

3.2.1. Use of Stack Peakiness

In this study, a local maxima of SP, such as the one in Fig. 5, is considered a potential lead waveform. The SP is almost constant over sea ice, but peaks in presence of a

lead, as shown in Section 4.1. Two additional criteria are used to identify the nadir leads:

- Median SP: The analysis of SP over all CS-2 tracks used for the validation with Set 1 and Set 2 (considering the whole length of each track over the Delay-Doppler geo-

graphical box) shows a median value of $SP_{median} = 8.67$ with a Median Absolute Deviation (MAD) of $SP_{MAD} = 8.72$. In order for a local maxima of SP to be classified as lead, the SP of the RIP before and after the local maxima has to be higher than $SP_{median} + SP_{MAD} \simeq 17$. This is done in order to avoid false detections, by utilising the fact that a lead that crosses the altimeter track influences the SP value also when not yet at nadir.

- **Minimum SP:** An empirical threshold $SP_{minlead} = 40$ is identified as the minimum SP of the RIP local maxima to be classified as lead. The threshold has been set by empirical observations of the locations of CS-2 points characterised by low SP values on the corresponding SAR images. This additional criteria is added in order to limit the recognition of leads that enter the field of view of the satellite, but never cross the nadir position. Their SP maxima is therefore expected to be lower than the SP maxima of nadir-crossing leads.

In the following sections, SP will be also used as acronym of the corresponding classification method.

3.2.2. Use of received power

Each Delay-Doppler waveform is characterised by a received power. The received power depends on the backscattering characteristic of the surface: flat surfaces such as the still water of small leads or melting ponds specularly scatter most of the incoming radar signal back in the same direction, while ice surfaces are characterised by diffuse scattering, which decreases the amount of power reflected back to the altimeter. In this study (Section 4.3) the adoption of an absolute threshold on received power to identify leads is verified and discussed. The applied threshold is 2.58×10^{-11} W, as proposed by [Wernecke and Kaleschke \(2015\)](#).

3.2.3. External lead classification

As previously mentioned, the classification proposed in [Ricker et al. \(2014\)](#) is used for comparison. The results of the classification were provided by the Alfred Wegener Institut (see Acknowledgements) for Set 1. The method consists on the use of thresholds set on three waveform-derived parameters (pulse peakiness, peakiness right of the power maximum, peakiness left of the power maximum), two RIP-derived parameters (SK and SSD) and a sea-ice concentration index. The peakiness right and left of the power maximum was directly computed from the waveform, while all the other parameters are provided in the raw data.

3.3. Lead classification based on Sentinel-1 SAR images

A set of image processing algorithms is applied to the Sentinel-1A scenes that should be used as a reference for the lead identification based on CS-2, aimed at extracting open water areas, i.e. black or near black surface areas,

by converting the SAR images into binary format. Leads or polynyas are represented by ones, while ice is coded with zeros. In order to replace the common visual classification an automated SAR image processing is proposed that enables quantitative comparisons with altimetry classification results. The following steps are applied to the SAR images (previously shifted considering the ice motion as described in Section 2.3):

- **Noise reduction:** To reduce noise in the image due to interfering scattering, a median filter is applied to the grayscaled image. For this purpose a window size of 5×5 pixels (equal to $200 \text{ m} \times 200 \text{ m}$ spatial scale) has been chosen to emphasize the transition between ice and water pixels and to minimize a false detection of open water pixels. The filter size is a compromise between noise reduction and compliance with the original image and was experimentally determined.
- **Dark pixel emphasizing:** After median filtering the grayscale image undergoes a minimum, non-linear filtering emphasizing dark pixel values. This is necessary to compensate uncertainties of the image shifting due to the ice motion (Section 2.3). To control the effect of the minimum filtering a convolution matrix or kernel is needed. Considering the linear and circular shape of openings in the ice, reliable results are reached by using an octagon kernel with a radius of 3 pixels around the center pixel. In [Fig. 6](#), a SAR image before (a) and after median and minimum filtering (b) as well as the used kernel (c) are shown.
- **Conversion to binary map:** To convert the filtered grayscale image into binary values, a segmentation based on thresholding is applied. For this purpose an adaptive threshold algorithm is employed to compensate spatial variations in contrast and illumination. We follow the approach of [Bradley and Roth \(2007\)](#) that divides the SAR image in foreground and background pixels. In a first step the integral image, a summation of pixel values from top left to bottom right, is computed. The next step computes the average of every pixel in a given neighborhood. The last processing step separates the SAR image in background and foreground by comparing the averaged pixel to the integral image.
- **Interconnection of lead fragments:** The spatial extent and the shape of a lead can vary very quickly from one meter to over 500 m due to persistent ice motion and refreezing ([Onstott and Shuchman, 2004](#)). In SAR images leads can show different pattern and pixel values. For example if the leads are refrozen or covered by frost flowers, the pixel values brighten up. Furthermore open water SAR signatures are sensitive to wind conditions. If there are calm conditions, leads appear small and disconnected and could be obscured by surrounding ice ([Onstott and Shuchman, 2004](#)). Additionally leads can be segmented due to limited resolution of the SAR image and inaccuracies of the thresholding. In order to reconnect these leads, a morphological closing operation

is applied to the binary images. The closing operator is a consecutive execution of a morphological dilatation followed by a morphological erosion. It enlarges pixel areas by mainly keeping the original boundary shape, thus it fills gaps and connects objects in a specific range. More details regarding the effect of closing operation on binary images can be found in [Gonzalez and Woods \(2008\)](#). As a closing operator, an octagonal kernel with radius of 12 pixels around the center pixel has been chosen based on empirical tests. [Fig. 6](#) visualizes the effect of the closing operation on the segmented binary image (from c to d). The thin adjacent lead fragments are connected by mainly preserving their natural linear spatial extent. As a downside, independent openings that are closely located can be linked, resulting in one widespread open water area.

For the statistical comparison between CS-2 and SAR lead classifications, the binary pixel values of the processed SAR image are interpolated to the altimetry track coordinates, using nearest-neighbor interpolation.

4. Results and discussion

4.1. Analysis of stack parameters

[Fig. 7](#) shows the evolution of the SP over a sea ice covered area in comparison with the Kurtosis and SSD stored in the ESA Baseline C product. Points that are identified as leads by the SP classification described in [Section 3.2.1](#) are highlighted by circles. For comparison, points that are identified as leads using the classification from [Ricker et al. \(2014\)](#) (Ricker from now on) are highlighted by squares.

The evolution of SP in the lead areas closely resembles the scheme of [Fig. 5](#): a peak, which corresponds to the strongest return from the zero look angle compared to the other looks, is easily identifiable, but the lead returns influence also the measurements nearby. The lead areas are also characterized by high Kurtosis and low SSD, but these two indices are often not able to univocally show a

local maximum or minimum: in some cases, the Kurtosis shows multiple peaks in the same sequence of points influenced by a lead, which may be attributed to high power in non-zero look angles due to residual sidelobe effects; the SSD, being based on a Gaussian fitting, is not able to distinguish subtle differences in the power distribution of the very peaky RIP waveforms in the lead areas.

Classifications that are based on these two stack parameters, such as Ricker, tend to classify as leads more points related to the same feature than the SP classification, which performs a sort of multi-waveform approach by looking for local maxima, rather than only considering thresholds on single measurements. In the case of narrow leads, a single-waveform approach can imply that off-nadir returns are being considered as leads. An example is found in [Fig. 8](#), in which the CS-2 track crosses a narrow lead: SP is able to detect the return in which the lead is at nadir, while Ricker classifies as lead also the neighbouring point, in which the lead is seen off-nadir.

4.2. Quantitative comparison with SAR images

The altimetry-based classification is rated considering the following parameters:

- Fraction of False Detections (FFD), i.e. the fraction of points along the CS-2 track that are identified as leads by the altimeter-based method, but identified as ice on the SAR image;
- Fraction of Correctly Classified Leads (FCCL), i.e. the fraction of leads on the SAR image (along the CS-2 track) that are also seen by the CS-2 classification. Note that this statistics concerns the number of leads, therefore two consecutive lead detections are considered as part of the same lead.

The coincidence between CS-2 and SAR lead detection is verified by simply interpolating the SAR binary image generated as in [Section 3.3](#) onto the altimetry track. An along-track tolerance of 400 m is applied in the comparison,

Table 1

Results of the CS-2-based lead classification with the methods described in the study, w.r.t. the SAR images classification. Col 1: name of the SAR images dataset; Col 2: classification method; Col 3: mean and standard deviation of the FFD (defined in [4.2](#)); Col 4: mean and standard deviation of the FCCL (defined in [4.2](#)); Col 5: ratio between FCCL and FFD, taken as final score of the method; Col 6: number of leads seen by each CS-2 lead classification method. For each classification method, the validation against SAR images without the morphological closing operation is identified by the suffix NC (No Closing).

Validation dataset	Lead detection	Mean(FFD) \pm std	Mean(FCCL) \pm std	FCCL/FFD	Tot lead
Set 1	Stack Peakiness	0.5444 \pm 0.1659	0.6465 \pm 0.2121	1.2	472
	Stack Peakiness NC	0.5795 \pm 0.1756	0.6065 \pm 0.2243	1.0	472
	Ricker et al. (2015)	0.4528 \pm 0.1594	0.5496 \pm 0.1982	1.2	279
	Ricker et al. (2015) NC	0.4982 \pm 0.1758	0.5427 \pm 0.2011	1.1	279
	Relative Power Threshold	0.2554 \pm 0.2199	0.4269 \pm 0.1985	1.7	144
	Relative Power Threshold NC	0.2971 \pm 0.2358	0.4276 \pm 0.2056	1.4	144
Set 2	Stack Peakiness	0.4472 \pm 0.2865	0.5007 \pm 0.2217	1.1	507
	Stack Peakiness NC	0.4869 \pm 0.2914	0.4392 \pm 0.2218	0.9	507
	Relative Power Threshold	0.2885 \pm 0.2178	0.4333 \pm 0.0728	1.5	188
	Relative Power Threshold NC	0.3349 \pm 0.2256	0.4397 \pm 0.0994	1.3	188

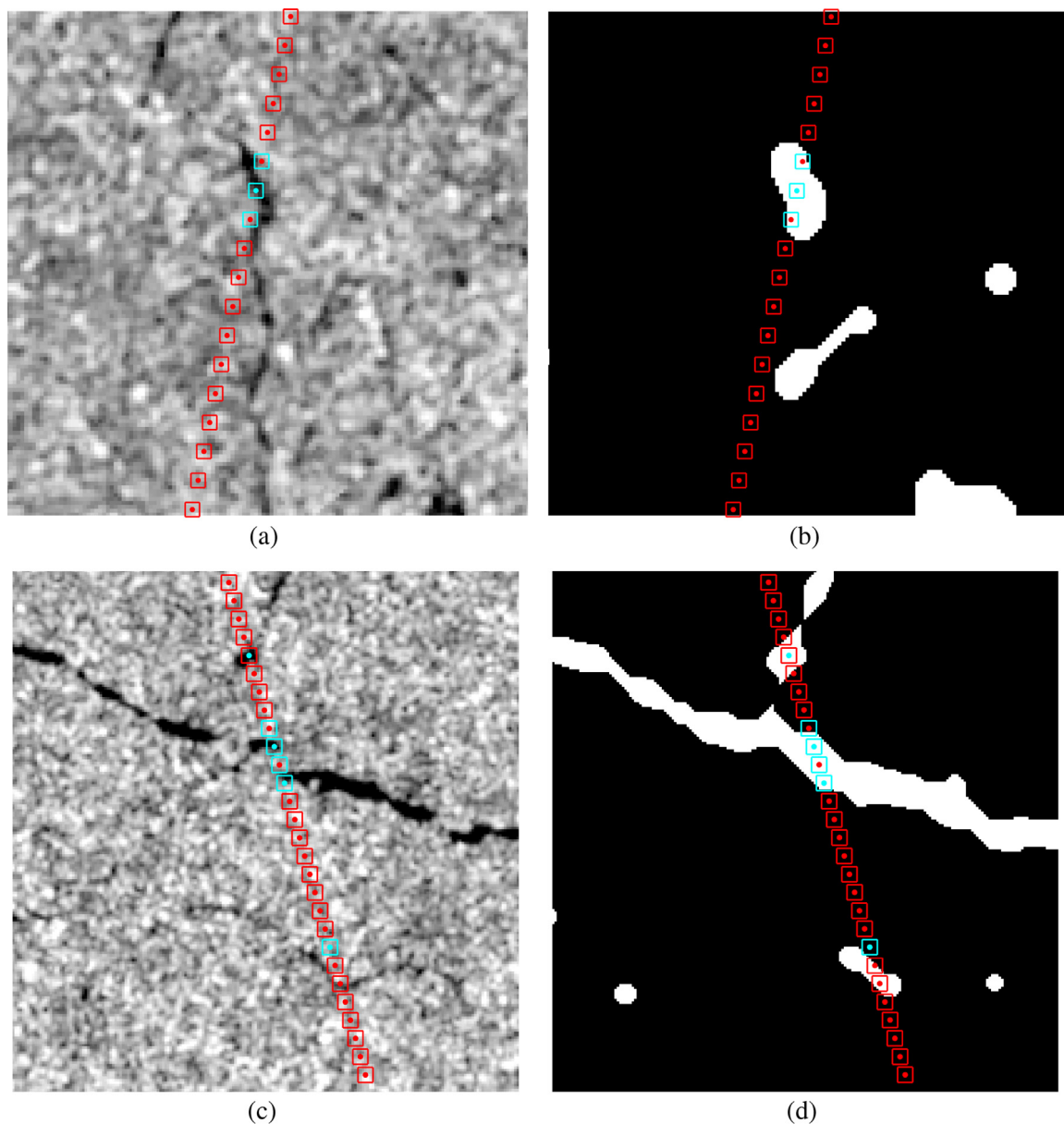


Fig. 9. Examples of lead detection from altimetry against SAR images before (a and c) and after the processing (b and d). a and b show a 5.35 by 5.18 km subset from Image 4 of Set 1, c and d illustrate a 8.11 by 8.34 km zoom from Image 1 of Set 1. Red: ice detection, cyan: lead detection. Squares: Ricker classification, dots: SP classification. (For interpretation of the references to colour in this figure legend, the reader is referred to the web version of this article.)

corresponding to the along-track resolution of CS-2 after the Hamming window application (Scagliola, 2013). The results are summarised in Table 1. The FCCL and the FFD are computed for each SAR image - CS-2 track couple and are shown taking their mean and standard deviation. The total number of leads detected by the SAR images is 232 for September 2015 (Set 1) and 275 for Set 2, while the table reports the total number of detections from the different altimetry-based methods. As a final score for each method, the ratio FCCL/FFD is adopted.

While the Relative Power Threshold and its results will be discussed in the next section, we firstly compare SP with Ricker. The two methods have the same score of 1.2 and

this result is also similar for SP in the control dataset, where the ice motion is applied. The only difference between the two methods is that SP finds 9% more of the leads recognised in the SAR images, but scores 9% worse in the FFD statistics. Essentially, the adoption of the SP index as a criteria is almost equivalent to the use of the 6 indices tuned in Ricker for the purpose of lead detection.

In both methods, the high standard deviation of FCCL and FFD attests the variability of the results depending on the different SAR scenes. We have not found a relationship with the seasonality, since the values are similar in both control data sets. The influence of seasonality cannot be excluded, but to assess it a larger amount of CS-2/SAR

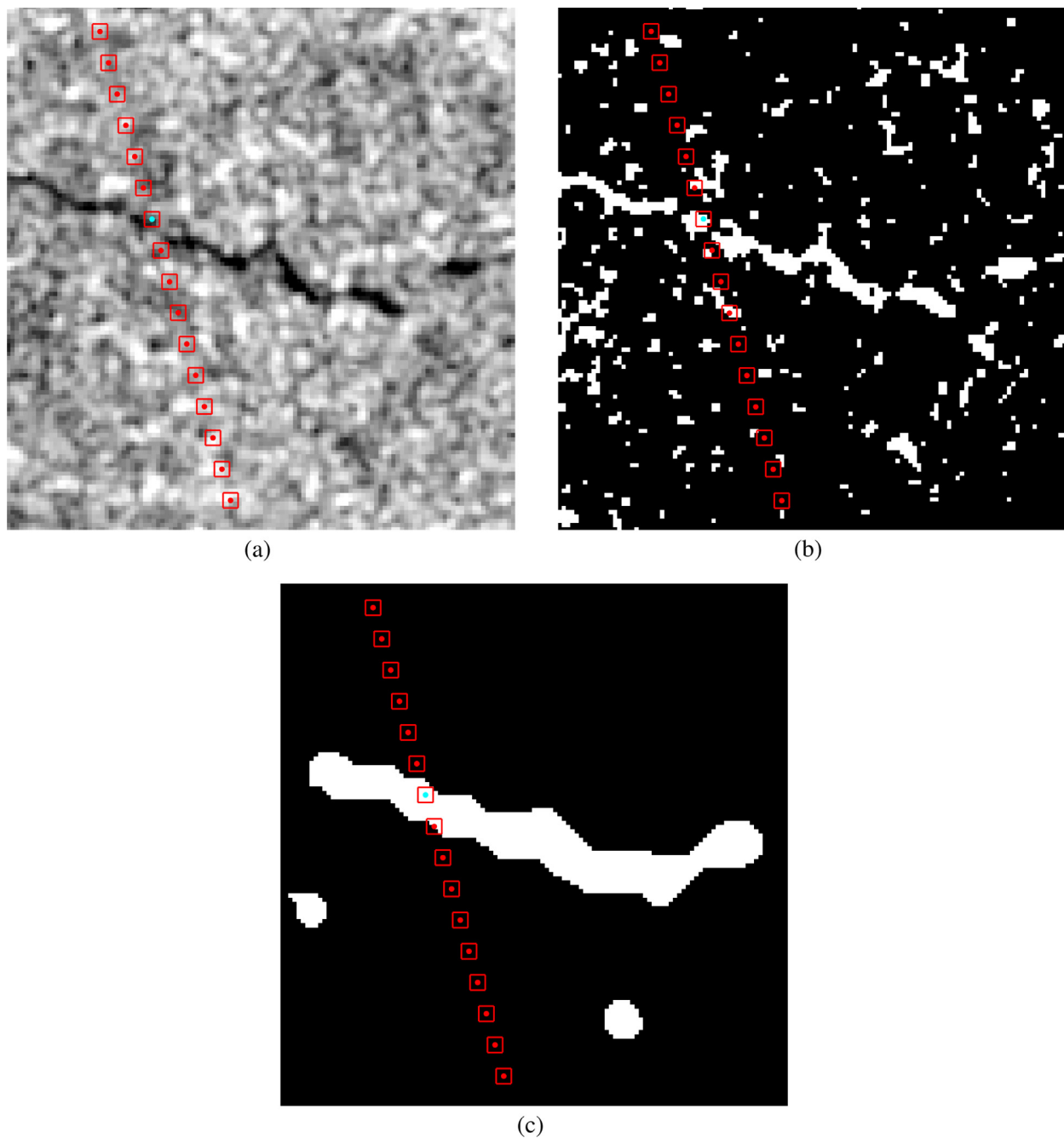


Fig. 10. Examples of lead detection from altimetry against SAR images (4.75 by 4.88 km extract from Image 1 from Set 1) before the processing (a), as a binary map without the filtering and closing (b) and after the full processing (c). Red: ice detection, cyan: lead detection. Squares: Ricker classification, dots: SP classification. (For interpretation of the references to colour in this figure legend, the reader is referred to the web version of this article.)

combinations are needed. This is not trivial, since an archive of these combinations does not exist and since the Stack data are not distributed in the ESA Baseline C CS-2 product and have to be acquired from an external source (G-POD).

Ricker was also validated against MODIS images by [Wernecke and Kaleschke \(2015\)](#). Their True Lead Rate (against MODIS taken as ground truth), essentially equivalent to the FCCL in this research, has a mean value of 60%, in line with our result considering the standard

deviation. Despite the different ground truth, the statistics is therefore robust, but the validation here presented can be easily replicable since the lead extraction from the ground truth does not rely on visual criteria such as in the previous studies.

We argue that the reason for which the score of Ricker and SP is equivalent lies in the filtering of the SAR images needed for noise reduction. [Fig. 9](#) shows two examples of the comparison between leads seen through SAR image processing and altimetry-based classification with SP and

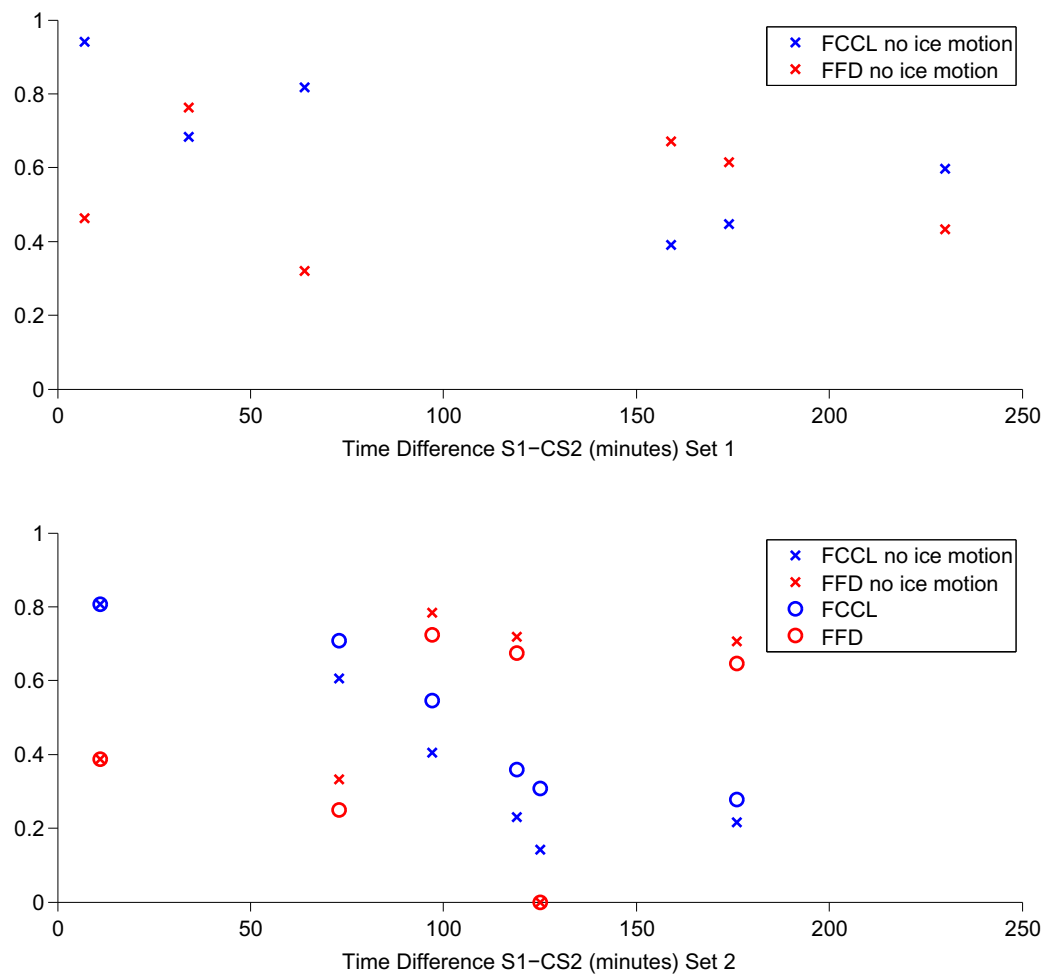


Fig. 11. FCCL (blue) and FFD (red) for each SAR image of Set 1 and Set 2 according to the time difference with the corresponding CS-2 track. In Set 1, the sea ice motion vectors are not applied, as in Table 1. In Set 2, statistics are shown with (circles) and without (crosses) the application of sea ice motion vectors. (For interpretation of the references to colour in this figure legend, the reader is referred to the web version of this article.)

Ricker. The figure shows that the filtering widens the borders of the lead, which has the effect of considering as a correct nadir detection the off-nadir CS-2 points that are classified as leads in Ricker. Nevertheless, the filtering is a necessary step to achieve an automatic and objective procedure for validation, as shown in Fig. 10: a binary map formed without the noise reduction described in Section 3.3 would result in several incorrect lead-like isolated features and as a consequence would strongly decrease the reliability of the comparison. Even with the filtering, the SAR processing is not always able to extract leads that are very thin, as for example in Fig. 9b. The binary map recognises the wider part of the lead that crosses the CS-2 track, but misses the elongated feature, due to the insufficient contrast between the ice edge and the thin lead.

A validation experiment was also undertaken to observe the effect of the closing operation. The results are listed for each altimetry classification method in Table 1. By comparing altimetry with SAR images without the closing, a general increase of the mean FFD by 3–4% is observed as well as a decrease of the FFCL, which result in a worse score.

The reason is observed in Fig. 10 c: the closing connects a lead that is seen fragmented in the original SAR image, which can be due to partial refreezing or noise. Without the closing, the lead identified by the altimeter would be interpolated on a black (ice) SAR binary pixel, resulting in an apparent false detection.

For the purpose of comparing the lead detection from satellite altimetry with the one applied on SAR images, the latter is considered as a ground truth. This assumption is only meant to provide a common ground for the comparison of different altimetry-based strategy, but it is an approximation of the reality: Despite the high resolution, Sentinel-1 is not able to distinguish leads that are narrower than 40 m, while such cracks in the ice could still be the dominant return in the altimetric waveforms. This difference is even more stringent after the application of the $200\text{ m} \times 200\text{ m}$ median filter for noise reduction in the SAR image. Moreover, the ability of both the automated SAR technique and the altimetry methods to distinguish between leads and melt ponds, which according to recent studies can occupy as much as 70% of the first-year ice area

in the melting period (Divine et al., 2016), remains hard to verify and further research is needed in this matter.

Finally, the impact of the time difference between S1 and CS-2 and of the application of the sea ice motion vectors in Set 2 is displayed in Fig. 11, considering the SP classification statistics. Regardless of the sea ice motion vectors, in both Sets the best results in terms of FCCL are obtained for S1-CS2 coupling close in time: in particular, only CS-2/SAR comparisons within 90 min show $FCCL > 0.4$ and the closest CS-2/SAR comparison has the best FCCL score. Moreover, in 4 out of 5 comparisons within 90 min, FCCL is higher than FFD, while the opposite happens in 6 out of 7 comparisons over 90 min, regardless of the sea ice motion vectors application. The latter has nevertheless a limited, but constant positive effect, reducing FFD and improving FCCL.

4.3. Received power as lead classifier

Using the distinction between true leads and false leads on the base of the comparison with SAR images, Fig. 12 shows, for every SAR image of the two datasets, the mean and standard deviation of the received waveform power from the points classified as leads by CS-2. The figure also shows as a dotted line the value of 2.58×10^{-11} , which has been proposed by Wernecke and Kaleschke (2015) as the threshold for the best representation of lead occurrence. This threshold is not entirely comparable with the values here presented, since it has been computed using the ESA Baseline B release of the CS-2 data, while at the time of writing this has been substituted with ESA Baseline C: small differences in the Delay-Doppler processing used to build the waveforms can lead to different power output associated to each echo.

Considering the results, the implementation of an absolute threshold to classify the leads does not look feasible. The proposed threshold, although it avoids false detections, does not find leads in three of the tracks from September 2015 and misses almost any lead in Set 2. The return power distribution of false leads and true leads is not constant: for example, the power distribution of false leads in images 1 and 2 from September 2015 is almost coincident with the power distribution of true leads in images 1 and 2 from Set 2. The power backscattered by a lead in fact does not depend only on the off-nadir or nadir view, but also on the presence of sea ice in the illuminated area, on possible refrozen areas of the lead and on its width. In general, the higher is the selected absolute power threshold, the higher is the confidence that the selected points are real leads, but the lower is the number of detections.

Nevertheless, the mean power of the true leads distribution is constantly higher than the one of the false leads distribution. We can use this information in a relative sense by computing the ratio between the power of the CS-2 returns classified as leads and the median of the power in the segment of the track considered (Power Ratio). As a tentative approach in this study, we considered the whole length of

the CS-2 segment downloaded for each corresponding Sentinel-1 image date. These vary between roughly 200 and 800 km. A histogram of the Power Ratio in the two datasets is shown in Fig. 13. Although they refer to different areas at different times, both datasets show that when the Power Ratio is below 10, the False Leads are predominant. Since the results are consistent, we keep the previously defined approach to define the Power Ratio. This relative threshold is therefore used as a “Relative Power Threshold” classification and the results are displayed in Table 1. Although the FCCL is lower than for the other methods, the false lead detections are also considerably less. This brings to an overall score $FCCL/FFD$ of 1.7 in Set 1 and 1.5 in Set 2. The Relative Power Threshold scores therefore best, but it is here derived *a posteriori* and further studies in different locations and at different times of the year are needed in order to understand whether the same threshold can be used systematically. Compared to the use of an absolute threshold, the performances of this method are not dependent on time and location of the track, but, as seen in Table 1, also the Relative Power

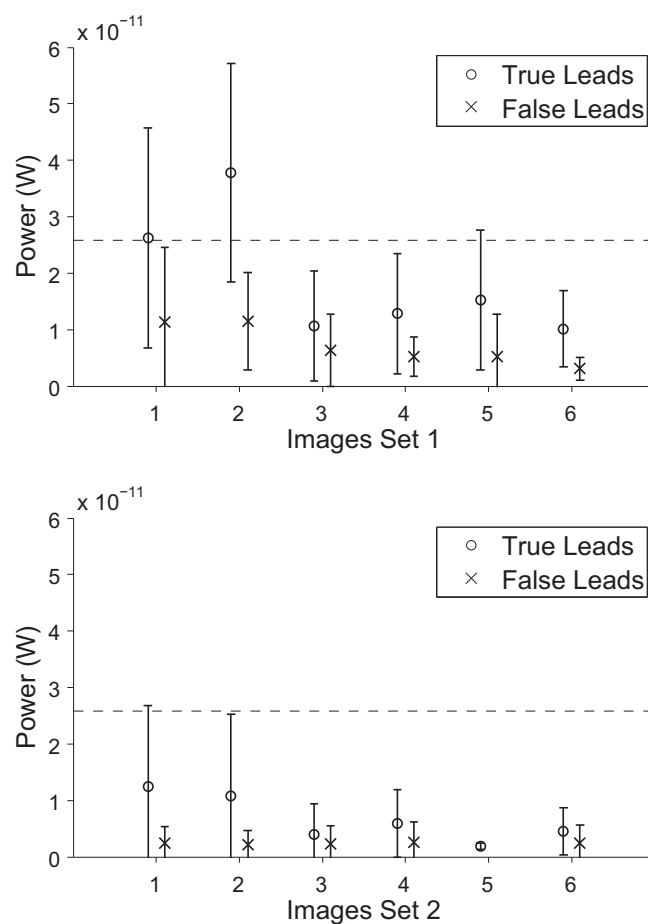


Fig. 12. Mean and standard deviation of the received power of True and False Leads in each image of the two control datasets. True and False Leads are the CS-2 waveforms classified as leads with the Stack Peakiness method and validated by means of comparison with the SAR images. The dashed horizontal line corresponds to the threshold proposed by Wernecke and Kaleschke (2015).

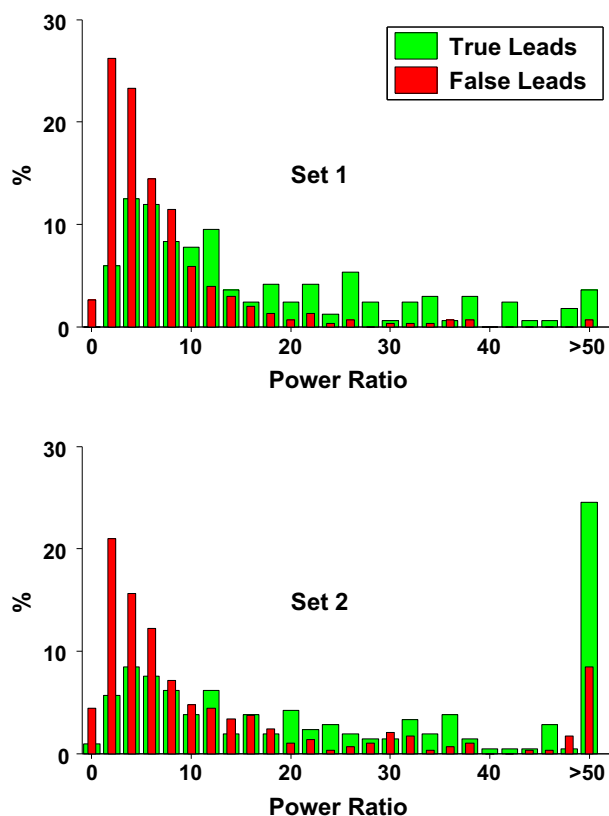


Fig. 13. Histogram of the received power of True and False Leads in both control datasets. True and False Leads are the CS-2 waveforms classified as leads with the Stack Peakiness method and validated by means of comparison with the SAR images.

Threshold brings as a drawback a significant reduction of the number of detected leads, in particular w.r.t. SP.

5. Conclusions

This study aimed at testing different Cryosat-based methods for lead classification taking the SAR images from Sentinel-1 as reference. SAR images have been processed in order to provide an automatic distinction between leads and ice.

A new parameter based on stack data, the Stack Peakiness, has been proposed. A visual analysis of the CS-2 tracks and SAR images has shown how SP can be used to isolate the nadir return from narrow leads crossing the track. The statistics show that in terms of correctly identified leads and false detections, the SP method has comparable results to the method proposed by Ricker et al. (2014), which combines six different waveform indices derivable from the CS-2 returns. The automated SAR processing is not able to highlight significant differences between SP and Ricker, due to the necessary filtering, nevertheless it constitutes a reliable, objective and easily replicable validation method.

In order to quantitatively understand whether SP avoids the off-nadir returns coming from the leads when

approaching the altimetry track, an easier and systematic access to CS-2 stack data is needed. In this case, further research could be planned to produce maps of sea surface height in the Arctic region using the identified leads and comparing the sea level variability with previous estimates.

Given the substantial differences of the power distribution of the leads observed in the datasets, the use of an absolute threshold on the return power to classify leads and avoid off-nadir returns, as proposed in previous studies, is not considered reliable. The best performances are nevertheless obtained by using the return power in a relative sense in comparison with the average power of the CS-2 returns in the area considered.

The percentage of false lead detections in comparison with the fraction of correctly classified leads is high for all the tested strategy. If the classification based on SAR images could be taken as the ground truth, this result would undermine the reliability of sea surface estimates in the Arctic Ocean, since it would imply that several reflections from the sea ice are considered for sea level measurements. Nevertheless, given that previous studies on-ground have shown that the width of a lead can be well below 1 km, it is likely that the altimeters spot leads whose width is below the SAR resolution. The time difference between CS-2 and SAR acquisitions plays also a key role and the comparability between the two sources clearly decreases after 60–90 min, despite the attempt of taking in consideration the sea ice velocity.

Although the SAR images do not represent the ground truth in terms of lead classification, given the resolution limits, they represent a well established comparison. The strength of this work is that the automatised validation can be easily reproduced in other areas, if an archive of CS-2 passes and Sentinel-1A images that are sufficiently close in time is provided. Indeed, further validation is needed in different sea-ice covered regions (multi-year and first year ice) and at different times of the year, since the presence of melt ponds and the refreezing of the leads could considerably alter the performances of any classification algorithm.

Future research should also address the exploitation of the SP for classification of the waveforms from the SAR-Interferometric mode of CS-2 (SARIn). In SARIn, the use of a second across-track antenna allows the localisation of different returns using the phase difference between the echoes reaching the two antennas. While the availability of SARIn in the sea ice region is limited to few patches (Armitage and Davidson, 2014) have shown that, combining the classification with an off-nadir ranging correction to characterise the off-nadir leads, the accuracy and the precision of sea ice freeboard measurements can be improved compared to the SAR mode.

Acknowledgements

The authors are thankful to Eero Rinne (Finnish Meteorological Institute, Helsinki) for providing a list of

available Sentinel-1 data and the corresponding Cryosat-2 passes in September 2015, and to Stephan Hendricks and Robert Ricker (Alfred Wegener Institute) for providing the corresponding lead classification. To all of them and to Andreas Wernecke (University of Hamburg) goes our gratitude for the useful discussions.

The authors would like to thank the International Space Science Institute (ISSI Bern) for its support to an international team focused on the current scientific issues in the observation of the sea level at polar latitudes, which fostered fruitful discussion for this paper.

The Cryosat-2 data were obtained using the ESA G-POD Service (<https://gpod.eo.esa.int/>). All Sentinel 1-A images are provided by ESA and downloaded at “Sentinels Scientific Data Hub”. The pre-processing was done by applying the “Sentinel Application Platform (SNAP)” in particular the Sentinel-1 toolbox (S1TBX), version 3.0.0 provided by ESA under the terms of the GNU General Public License. The Sea Ice velocity data were obtained using the Polar Pathfinder EASE-grids (<http://nsidc.org/data/nsidc-0116/versions/3>).

This work was partly supported by the German Research Foundation (DFG) through grants BO1228/13-1 and DE2174/3-1.

References

- Armitage, T.W., Davidson, M.W., 2014. Using the interferometric capabilities of the ESA Cryosat-2 mission to improve the accuracy of sea ice freeboard retrievals. *IEEE Trans. Geosci. Remote Sens.* 52, 529–536.
- Bouzinac, C., 2012. CryoSat Product Handbook. European Space Agency, https://earth.esa.int/documents/10174/125272/CryoSat_Product_Handbook.
- Bradley, D., Roth, G., 2007. Adaptive thresholding using the integral image. *J. Graph. GPU Game Tools* 12, 13–21.
- Dierking, W., 2013. Sea ice monitoring by synthetic aperture radar. *Oceanography* 26.
- Divine, D.V., Pedersen, C.A., Karlsen, T.I., Aas, H.F., Granskog, M.A., Hudson, S.R., Gerland, S., 2016. Photogrammetric retrieval and analysis of small scale sea ice topography during summer melt. *Cold. Reg. Sci. Technol.* 129, 77–84.
- Gonzalez, R.C., Woods, R.E., 2008. *Digital Image Processing*. third ed.. Prentice Hall, Upper Saddle River, New Jersey, USA.
- Ivanova, N., Rampal, P., Bouillon, S., 2016. Error assessment of satellite-derived lead fraction in the Arctic. *Cryosphere* 10, 585–595.
- Kwok, R., Cunningham, G., Wensnahan, M., Rigor, I., Zwally, H., Yi, D., 2009. Thinning and volume loss of the Arctic Ocean sea ice cover: 2003–2008. *J. Geophys. Res.: Oceans* 114.
- Laxon, S.W., Giles, K.A., Ridout, A.L., Wingham, D.J., Willatt, R., Cullen, R., Kwok, R., Schweiger, A., Zhang, J., Haas, C., et al., 2013. CryoSat-2 estimates of Arctic sea ice thickness and volume. *Geophys. Res. Lett.* 40, 732–737.
- Lindsay, R., Rothrock, D., 1995. Arctic sea ice leads from advanced very high resolution radiometer images. *J. Geophys. Res.: Oceans* 100, 4533–4544.
- Onstott, R.G., Shuchman, R.A., 2004. SAR measurement of sea ice. In: Jackson, Apel (Ed.), *Synthetic Aperture Radar: Marine User's Manual*, US Department of Commerce, National Oceanic and Atmospheric Administration, National Environmental Satellite, Data, and Information Service, Office of Research and Applications, pp. 81–115.
- Peacock, N.R., Laxon, S.W., 2004. Sea surface height determination in the Arctic Ocean from ERS altimetry. *J. Geophys. Res.: Oceans* 109.
- Rampal, P., Weiss, J., Marsan, D., 2009. Positive trend in the mean speed and deformation rate of Arctic sea ice, 1979–2007. *J. Geophys. Res.: Oceans* 114.
- Raney, R.K., 1998. The Delay/Doppler radar altimeter. *IEEE Trans. Geosci. Remote Sensing* 36, 1578–1588.
- Ricker, R., Hendricks, S., Helm, V., Skourup, H., Davidson, M., 2014. Sensitivity of CryoSat-2 Arctic sea-ice freeboard and thickness on radar-waveform interpretation. *Cryosphere* 8, 1607–1622.
- Rinne, E., Similä, M., 2014. Utilisation of CryoSat-2 SAR altimeter in operational ice charting. *Cryosphere* 10, 121–131.
- Röhrs, J., Kaleschke, L., 2012. An algorithm to detect sea ice leads by using AMSR-E passive microwave imagery. *Cryosphere* 6, 343–352.
- Scagliola, M., 2013. CryoSat footprints. Aresys technical note, SAR-CRY2-TEN-6331. Tech. rep., Aresys/ESA, Italy.
- Scagliola, M., Fornari, M., 2015. Main evolutions and expected quality improvements in BaselineC Level1b products. Aresys technical note, C2-TN-ARS-GS-5154. Tech. rep., Aresys/ESA, Italy.
- Tschudi, M., Fowler, C., Maslanik, J., Stewart, J., Meier, M., 2016. Polar Pathfinder daily 25 km EASE-grid sea ice motion vectors (Last Access: 08/08/2016), Boulder, Colorado USA. NASA National Snow and Ice Data Center Distributed Active Archive Center.
- Weeks, W., 2010. *On Sea Ice*. University of Alaska Press, Fairbanks, USA.
- Wernecke, A., Kaleschke, L., 2015. Lead detection in Arctic sea ice from CryoSat-2: quality assessment, lead area fraction and width distribution. *Cryosphere* 9, 1955–1968.
- Willmes, S., Heinemann, G., 2015. Pan-Arctic lead detection from MODIS thermal infrared imagery. *Ann. Glaciol.* 56, 29–37.
- Wingham, D., Francis, C., Baker, S., Bouzinac, C., Brockley, D., Cullen, R., de Chateau-Thierry, P., Laxon, S., Mallow, U., Mavrocordatos, C., et al., 2006. CryoSat: a mission to determine the fluctuations in Earth's land and marine ice fields. *Adv. Space Res.* 37, 841–871.
- Veci, L., 2016. SENTINEL-1 Toolbox SAR Basics Tutorial. Array Systems Computing Inc., <http://step.esa.int/main/>.

P-2 Dynamic ocean topography of the northern nordic seas: a comparison between satellite altimetry and ocean modeling

Müller, F. L., Wekerle, C., Dettmering, D., Passaro, M., Bosch, W., and Seitz, F. (2019b). Dynamic ocean topography of the northern nordic seas: a comparison between satellite altimetry and ocean modeling. *The Cryosphere*, 13(2):611–626, DOI: 10.5194/tc-13-611-2019

Copyright

The publication was published in The Cryosphere, which is an interactive open-access journal of the European Geosciences Union. It is distributed by Copernicus Publications. All accepted articles are published under the terms and conditions of the Creative Commons Attribution License (<http://creativecommons.org/licenses/by/4.0/>). The copyright remains with the author.

Summary

The northern Nordic Seas span the area between the Atlantic Ocean in the south, the Arctic Ocean in the north, the northeast coast of Greenland and the west Spitsbergen coast and depicts the most important pathway for water mass transformations between the Arctic and Atlantic Ocean. The region is directly affected by sea ice coverage and melting glaciers leading to an increased fresh water inflow. For more than 20 years, satellite altimetry observations are used in connection with a geoid model to monitor the dynamic ocean topography (DOT) and to provide information about the ocean surface circulation in the northern Nordic Seas. However, due to the challenging observation conditions, the altimeter observations are irregularly distributed showing data gaps in sea ice areas. Moreover, fixed orbit characteristics of the satellite mission limit an area-wide monitoring of the entire region.

Beside satellite altimeters, ocean models can provide a homogeneous representation sea surface height and ocean current information in various spatiotemporal resolutions. However, ocean models are limited by their mathematical and computational background as well as by introduced forcing data.

In this work, derived along-track DOT elevations from ALES+ retracked Envisat ranges and a high-resolution geoid (i.e. OGMOC) are used. The object of the publication is to compare altimetry-derived DOT elevations with modeled differential water heights (DWH) of the ocean model FESOM in order to assess similarities and discrepancies and to investigate the possibility for a combination by taking the advantages of both data sources. DWHs and DOT heights are very similar and refer to geopotential surfaces. The investigation period covers the years from 2003 - 2009, for which daily FESOM DWHs are provided. A comparison concerning the annual variation reveals a general

good agreement of the estimated phase and amplitude. Moreover, the annual oscillation is the most dominant signal in both datasets. However, a regional assessment of the annual signal shows up to 2-3 times stronger amplitudes of the altimetry-derived data, but still indicates good accordance of the phase. The differences in the amplitude are mainly addressed to a stronger smoothing of the model data, caused for example by a too strongly adjusted sea ice fraction and the neglecting of a global steric mass correction. Moreover, the model is based on coarse forcing model data and underrepresents the regional inflow of freshwater of the adjacent glaciers.

A reduction of both data sources by their means and the annual signal reveals high temporal as well as spatial correlations of more than 80%. The highest correlations appear in ice-free areas and in ocean regions with a clear ocean current signature. Smaller correlations are mainly in the sea ice area and close to the Greenland Shelf regions covered by sea ice, which can be addressed to high ocean sea ice dynamics leading to an enhanced error budget of the altimetry range observations. Remaining constant height differences are attributed to artificial effects caused by irregularities and an insufficient representation of the applied gravity model.

The publication states that even with an improvement of the detected differences, the principal discrepancies of the observation and model database will persist. However, it is plausible to combine both datasets, as there is a generally good agreement, showing no significant differences in order to exploit advantages for a combination.

Contribution

As stated in P-2: Felix L. Müller developed the comparison methods, conducted the data analysis and wrote the majority of the paper. Claudia Wekerle provided the FESOM data and contributed to the manuscript writing. Denise Dettmering supervised the present study, contributed to the manuscript writing and helped with discussions of the results. Marcello Passaro developed the retracking algorithm and helped with the application and discussion concerning the altimetry dataset. Wolfgang Bosch initiated the study. Florian Seitz supervised the research. The overall contribution of Felix L. Müller is estimated to be **85%**.



Dynamic ocean topography of the northern Nordic seas: a comparison between satellite altimetry and ocean modeling

Felix L. Müller¹, Claudia Wekerle², Denise Dettmering¹, Marcello Passaro¹, Wolfgang Bosch¹, and Florian Seitz¹

¹Deutsches Geodätisches Forschungsinstitut, Technische Universität München, Arcisstraße 21, 80333 Munich, Germany

²Climate Dynamics, Alfred Wegener Institute, Helmholtz Centre for Polar and Marine Research, Bussestraße 24, 27570 Bremerhaven, Germany

Correspondence: Felix L. Müller (felix-lucian.mueller@tum.de)

Received: 30 August 2018 – Discussion started: 22 October 2018

Revised: 28 January 2019 – Accepted: 1 February 2019 – Published: 20 February 2019

Abstract. The dynamic ocean topography (DOT) of the polar seas can be described by satellite altimetry sea surface height observations combined with geoid information as well as by ocean models. The altimetry observations are characterized by an irregular sampling and seasonal sea ice coverage complicating reliable DOT estimations. Models display various spatiotemporal resolutions but are limited to their computational and mathematical context and introduced forcing models. In the present paper, ALES+ retracked altimetry ranges and derived along-track DOT heights of ESA's Envisat and water heights of the Finite Element Sea Ice-Ocean Model (FESOM) are compared to investigate similarities and discrepancies. The goal of the present paper is to identify to what extent pattern and variability of the northern Nordic seas derived from measurements and model agree with each other, respectively. The study period covers the years 2003–2009. An assessment analysis regarding seasonal DOT variabilities shows good agreement and confirms the dominant impact of the annual signal in both datasets. A comparison based on estimated regional annual signal components shows 2–3 times stronger amplitudes of the observations but good agreement of the phase. Reducing both datasets by constant offsets and the annual signal reveals small regional residuals and highly correlated DOT time series (Pearson linear correlation coefficient of at least 0.67). The highest correlations can be found in areas that are ice-free and affected by ocean currents. However, differences are visible in sea-ice-covered shelf regions. Furthermore, remaining constant artificial elevations in the observational data can be attributed

to an insufficient representation of the used geoid. In general, the comparison results in good agreement between simulated and altimetry-based descriptions of the DOT in the northern Nordic seas.

1 Introduction

Observing the dynamic ocean topography (DOT) enables the investigation of important oceanic variables. Variations in the DOT are an indicator of changes in the ocean circulation, the major current pathways or water mass redistribution. Knowledge about Arctic water mass distribution and ocean transport variability is essential to understand and quantify changes in the global overturning circulation system (e.g., Johannessen et al., 2014; Morison et al., 2012). These relationships have led to studies and expeditions since the early 20th century, e.g., by Helland-Hansen and Nansen (1909) investigating northern polar circulation.

Nowadays, satellite altimetry, in connection with knowledge about the geoid, is one possibility to provide instantaneous DOT snapshots on a global scale. However, in polar regions, altimetry observations obey an irregular sampling in seasonally sea-ice-covered regions. Nevertheless, the launch of the European Space Agency's (ESA) Earth observation satellite ERS-1 in 1991 constituted the starting point of regular observed DOT information in the higher latitudes that now covers more than 25 years. This was followed by regularly improving radar altimetry as well as significant progress

in gravity field missions (e.g., GOCE and GRACE); remote sensing missions provided increasingly reliable DOT estimates. In addition to an expanded remote Earth observation mission constellation, advances in data processing (e.g., Laxon, 1994; Peacock and Laxon, 2004; Connor et al., 2009) also contributed to an increasing accuracy of DOT heights, mainly by improving radar echoes processing strategies (e.g., use of high-frequency data, enhanced retracking and radar echo classification algorithms).

Arctic DOT information for different periods and with different spatial resolutions has been estimated for example by Kwok and Morison (2011) based on laser altimetry or by Farrell et al. (2012) based on a combination of laser and radar altimetry. Moreover, Armitage et al. (2016) processed monthly altimetry-derived DOT outputs to combine them with GRACE ocean mass products. However, all these DOT results are based on grid processing with limited spatiotemporal resolutions, leading to unavoidable smoothing effects and leaving space for further DOT product improvements.

In addition to the observational database, model simulations have provided a variety of different climate variables in polar regions for more than 60 years (Koldunov et al., 2014). They are characterized by various spatiotemporal resolutions and simulation strategies. In spite of difficult observation conditions at high latitudes, models enable comprehensive analyses of interactions between the Arctic Ocean and atmospheric circulations. However, different models show significant discrepancies related to their fundamental outputs, e.g., sea-surface variability or ocean currents (Koldunov et al., 2014). Nevertheless, in contrast to satellite altimetry, models provide spatially homogeneous and temporally complete sea surface estimates. In order to get an impression of model accuracies, previous studies, for example Koldunov et al. (2014), performed an intercomparison of different ocean models, tide gauge observations and weekly averaged altimetry DOT data in the Arctic environment, limited, however, to gridded DOT data originating from sea-ice-free months. The authors conclude that models can catch and reproduce the most dominant low-frequency water level variabilities in the Arctic Ocean. Nevertheless, there is need for improvement in terms of seasonally independent analyses as well as an increased spatiotemporal resolution, which would, for example, enable a direct pointwise comparison.

Recent developments in numerical modeling focused on so-called unstructured mesh representations. According to Wang et al. (2014), unstructured ocean model grids with local refinements in the region of complex and highly dynamic circulation patterns (e.g., Fram Strait) allow for multi-resolution analyses of climate-relevant variables in specific areas of interest while keeping a coarse spatial representation for other regions (e.g., Wang et al., 2014; Zhang and Baptista, 2008). One of these models is the Finite Element Sea Ice-Ocean Model (FESOM, Wang et al., 2014). It includes, in addition to the ocean variables (sea surface height, temperature, ocean currents and salinity), a sea ice component

mapping the major ice drift pathways. Furthermore Wekerle et al. (2017) described a FESOM configuration that enables studies in the Fram Strait region and northern Nordic seas at a daily temporal resolution and a spatially refined 1 km mesh, resulting in an eddy-resolving ocean simulation in most of the study domain. Another sea ice ocean model setup with comparable resolution focusing on the same region is based on a Regional Ocean Modeling System (ROMS), which applies a grid size of 800 m around Svalbard (Hattermann et al., 2016). The model setup is regional and nested into a 4 km pan-Arctic setup. In terms of eddy dynamics, the ROMS and FESOM setups compare very well (personal communication, Tore Hattermann, January 2018). A slightly coarser model with up to 2 km resolution in the northern Nordic seas was described by Kawasaki and Hasumi (2016).

In the present study, along-track high-frequency DOT estimates of ESA's Envisat as well as water level outputs of FESOM are used for a direct comparison in order to analyze spatiotemporal correspondence and discrepancies. The overall motivation for this is the computation of a spatially homogeneous DOT without the need of gridding methods that smooth the altimetry spectral data content. Instead of such an interpolation, the unavoidable data gaps should be filled with model information from a combination of profiled altimetry data and gridded model data. A careful comparison of both datasets is a necessary prerequisite for such combination. The present investigation aims to explore the capacity for a combination and exploiting the advantages of both quantities. In particular, it is evaluated if the model outputs can bridge periods when altimetry fails (e.g., due to sea ice coverage). In the present study, the altimetry database consists of profiled 20 Hz DOT snapshots that were preprocessed using the classification presented by Müller et al. (2017). The comparison is conducted in the northern Nordic seas and the Fram Strait, covering the East Greenland and the West Spitsbergen currents. The present paper is structured into four main sections. First, the study area and the applied datasets and their preprocessing are introduced, followed by Sect. 3 describing the comparison methods and displaying the obtained results. The last two sections discuss the results and recapitulate the key aspects.

2 Study area and datasets

This section provides an overview of the study area, the used model and the observational database. In addition, more detailed information on the data preprocessing is given.

2.1 The northern Nordic seas and Fram Strait

The study area covers the northern Nordic seas and the Fram Strait, which connects the North Atlantic with the Arctic Ocean as depicted in Fig. 1. The study area is limited to 72 to 82° N and 30° W to 30° E. The bathymetry is complex in this

region: the deep Fram Strait (with depths up to 5 600 m at the Molloy Hole) lies between the wide northeastern Greenland continental shelf and the Svalbard archipelago, with the deep Greenland Sea to the south. Seamounts, ridges and steep slopes affect the ocean circulation.

The northern Nordic seas are characterized by contrasting water masses. Warm and salty waters of Atlantic origin are carried northward by the Norwegian Atlantic Current (e.g., Orvik and Niiler, 2002). After a bifurcation at the Barents Sea Opening, the remaining current that continues northward is termed the West Spitsbergen Current (WSC, e.g., Beszczynska-Möller et al., 2012; von Appen et al., 2016). A fraction of the Atlantic water carried by the WSC recirculates in the Fram Strait at around 79° N and continues to flow southward, forming the Return Atlantic Water (RAW), whereas the remaining part enters the Arctic Ocean via the Svalbard and Yermak branches (SB and YB). Along the Greenland continental shelf break, the East Greenland Current (EGC, e.g., de Steur et al., 2009) carries cold and fresh polar water as well as RAW southward.

Sea ice is exported via the Transpolar Drift out of the Arctic through the Fram Strait. As indicated in Fig. 1, the sea ice export occurs at the western side of the strait, which is thus ice-covered year-round. The eastern part of the Fram Strait is ice-free year-round due to the presence of warm Atlantic water. Around 10 % of the Arctic sea ice area is exported through the Fram Strait annually, an order of magnitude larger than the export through other Arctic gateways (Smedsrud et al., 2017).

2.2 Model basis: Finite Element Sea Ice-Ocean Model (FESOM)

In this study we use daily mean water level output from the Finite Element Sea Ice-Ocean Model (FESOM) version 1.4 (Wang et al., 2014; Danilov et al., 2015). FESOM is an ocean sea ice model which solves the hydrostatic primitive equations in the Boussinesq approximation. The sea ice component applies the elastic–viscous–plastic rheology (Hunke and Dukowicz, 2001) and thermodynamics following Parkinson and Washington (1979). The finite element method is used to discretize the governing equations, applying unstructured triangular meshes in the horizontal and z levels in the vertical. Water level heights (in the model labeled as sea surface height) η are computed from the following equation:

$$\partial_t \eta + \nabla \cdot \int_{z=-H}^{z=\eta} \mathbf{u} dz = 0, \quad (1)$$

where $\mathbf{u} \equiv (u, v)$ is the velocity vector and H is the water depth. Water elevations are relative to a geopotential surface and therefore comparable to an altimetry-derived dynamic ocean topography (Androsov et al., 2018). The upper limit in the integration is set to zero, which corresponds to a linear free-surface approximation. This implies that the ocean

volume does not change with time in the model. Thus, the model conserves volume but not mass. A correction for the global mean steric height change is not applied. To account for surface freshwater fluxes (precipitation, evaporation, river runoff, salinity changes due to sea ice melting and freezing), a virtual salt flux is introduced (see, e.g., Wang et al., 2014). The model does not take into account sea level pressure and ocean tide variations.

The global FESOM configuration used here was optimized for the Fram Strait, applying a mesh resolution of 1 km in the area 76–82.5° N, 20° W–20° E and a resolution of 4.5 km in the Nordic seas and Arctic Ocean (Wekerle et al., 2017). In the vertical, 47 z levels are used with a thickness of 10 m in the top 100 m and coarser vertical resolution with depth. The model bathymetry was taken from RTopo2 (Schaffer et al., 2016). For comparison, only the surface information is used (i.e., $z = 0$).

The model is forced by atmospheric reanalysis data COREv.2 (Large and Yeager, 2008) characterized by a daily temporal and 2° spatial resolution, and interannual monthly river runoff is taken from Dai et al. (2009). Sea surface salinity restored to the PHC 3.0 climatology (Steele et al., 2001) is applied with a restoring velocity of 50 m per 300 days. The simulation covers the time period 2000 until 2009, and daily model output was saved. A comparison with observational data (e.g., moorings) revealed that the model performed well in simulating the circulation structure, hydrography and eddy kinetic energy in the Fram Strait (Wekerle et al., 2017).

2.3 Observational basis: radar altimetry data

In the present study high-frequency radar altimetry data of the ESA satellite Envisat are used. The altimeter emits radar signals in the Ku band with a footprint (i.e., circular area on the ground illuminated by the radar) of approximately 10 km diameter (Connor et al., 2009). Envisat belongs to the pulse-limited altimetry missions and provides observations characterized by a spatial along-track resolution of circa 372 m (18 Hz). The mission was placed in orbit in 2002 and provided altimetry data until the end of March 2012. This study uses high-frequency waveform data that are extracted from the official Sensor Geophysical Data Records (SGDR) version 2.1 provided by ESA. Data measured during the nominal mission period (May 2002–October 2010) are organized into 35-day repeat cycles including a fixed relative orbit number (i.e., pass, from pole to pole) of 1002 passes per cycle (ESA, 2011). However, the first cycles of Envisat are affected by various instrumental issues and are not considered for the present study. Considering the temporal availability of FESOM and reliable observations of Envisat, SGDR data of a period covering 7 complete years (2003–2009) are used. Before using the Envisat altimetry observations, a classification is performed to eliminate sea-ice-contaminated measurements. Sea surface heights (SSHs) are calculated by applying the ALES+ retracking algorithm (Passaro et al., 2018)

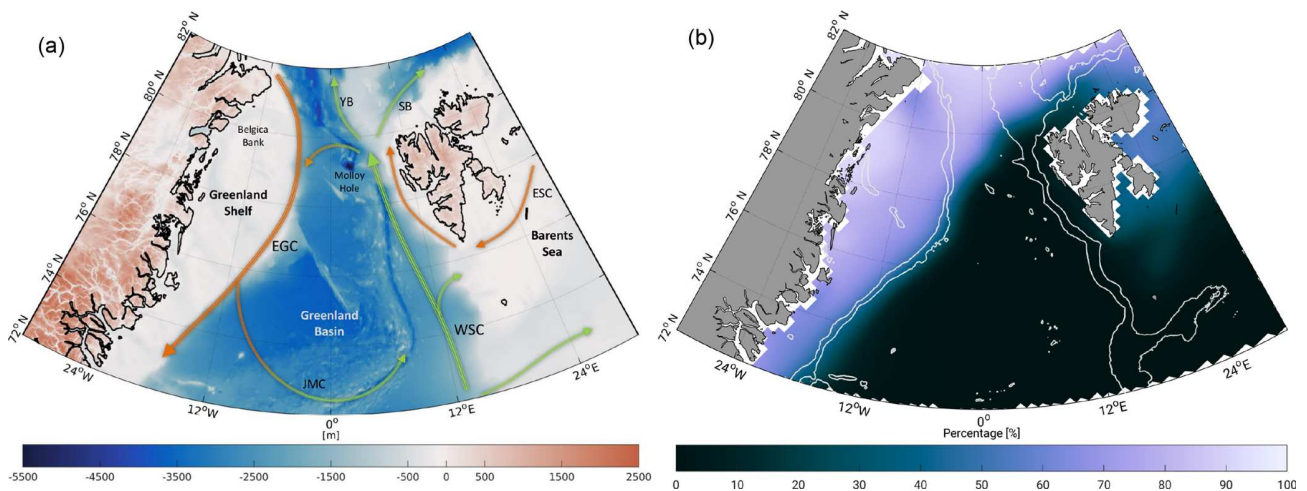


Figure 1. Overviews of the study area: **(a)** bathymetry of the northern Nordic seas and Fram Strait area based on RTopo2 topography model (Schaffer et al., 2016). Arrows display major current systems (East Greenland Current, EGC; West Spitsbergen Current, WSC; East Spitsbergen Current, ESC; Jan Mayen Current, JMC; Yermak Branch, YB; and Svalbard Branch, SB). Light green arrows indicate inflowing Atlantic water; orange represents fresh polar and returning Atlantic water. **(b)** Averaged sea ice concentration in percentage within 2003–2009 based on 25 km monthly National Snow and Ice Data Center (NSIDC, Fetterer et al., 2017) sea ice concentration grids. White lines display depth contours at -450 and -1500 m. White areas indicate missing or flagged data.

and geophysical corrections. Unrealistic or bad height measurements are excluded by performing an outlier detection based on sea level anomalies. Finally, a transformation to physical heights (dynamic ocean topography, DOT) is processed by subtracting geoid heights from SSH. The following subsections describe the individual preprocessing steps in more detail.

2.3.1 Sea ice and water discrimination

Most of the Arctic regions are affected by seasonal sea ice cover, which can prevent a reliable estimation of sea surface heights due to a direct impact on the reflected radar pulses. In order to overcome this difficulty and to allow for a SSH comparison with FESOM, a classification is performed to detect small open water gaps (e.g., leads, polynyas) within the sea-ice-covered area. For this purpose an unsupervised classification approach (i.e., without the use of any training data) based only on radar waveforms and derived parameters is applied. Several classification methods have been developed within the last years, which are all based on the analysis of the returned satellite radar echo (e.g., Laxon, 1994; Zakharova et al., 2015; Zyguntowska et al., 2013). Most of them impose thresholds on one or more parameters of the radar waveforms (e.g., maximum power or backscatter coefficient). In this study, an unsupervised classification approach is applied, which is independent of any training data. This method performed best in a recent study assessing the quality of different classification approaches with respect to very high resolution airborne imagery (Dettmering et al., 2018). Briefly summarized, the unsupervised classification approach, described by Müller et al. (2017), groups

an unassigned subset of altimetry radar waveforms into a predefined number of classes by applying a partitional cluster algorithm (i.e., k -medoids; see Celebi, 2015) in order to establish a reference waveform model to indicate different waveform and surface characteristics. In the following step, the generated waveform model acts as kind of assignment map for the remaining waveforms, which are allocated to the particular classes using a simple k -nearest-neighbor classifier. Further information and explanations can be found in Müller et al. (2017). The open water (leads, polynyas and open ocean) observations are used for all following processing steps. Measurements classified as ice are removed from the dataset. However, it has to be noted that some misclassifications, e.g., due to the presence of fast ice, can still remain in the observation dataset (Müller et al., 2017). During sea ice melt season, melt ponds and water bodies on top the sea ice layer can cause uncertainties in the computation of sea surface heights. The unsupervised classification is not fully tuned to discriminate carefully between radar waveforms originating from melt ponds or leads at the sea surface level. In the case of misclassification the estimated altimeter ranges can appear too short.

2.3.2 Sea surface height estimation

SSH is obtained by subtracting the measured range between satellite and water surface (including geophysical corrections) from the orbital altitude (i.e., ellipsoid height) of the satellite's center of mass. The range can be calculated by fitting a waveform model (e.g., Brown, 1977, or Hayne, 1980) to the individual radar returning signals. More information regarding retracking strategies can be found for example in

Vignudelli et al. (2011). Several retracking algorithms have been developed and optimized for special applications, surface conditions or study regions (e.g., open ocean, sea ice or inland water bodies). According to Serreze and Barry (2014) the northern Nordic seas are characterized by rapidly changing environmental conditions, making it difficult to use just one retracking algorithm. However, when combining heights derived with different retrackers, systematic offsets due to different retracker biases will be introduced (Bulczak et al., 2015). The usage of ALES+ overcomes this problem by adapting a subwaveform application of the classic open ocean functional form to different shapes of the radar signals, including the typical peaky signal shape of the returns from small leads and corrupted trailing edges typical of coastal waveforms. Passaro et al. (2018) have developed and tested the algorithm against standard open ocean and lead retrackers and showed improvements in precision and in terms of comparison with a local tide gauge. The algorithm was used to develop Arctic and Antarctic products in the framework of the ESA Sea Level Climate Change Initiative (Legeais et al., 2018).

After the retracking, the altimeter ranges are corrected for geophysical and atmospheric effects using external model data. Wind and wave effects are considered by using the sea state bias estimates of the ALES+ retracking approach. Furthermore a mean range bias correction, computed by a multi-mission crossover analysis (Bosch et al., 2014), is included to eliminate a known constant offset in the Envisat range measurements. One important correction is the ocean tide correction since the FESOM model does not include ocean tides. In this study, we use EOT11a (Savcenko et al., 2012; Savcenko and Bosch, 2012) to correct for tidal effects. Even if EOT11a is a global ocean tide model it performs reasonably well in the Arctic Ocean (Stammer et al., 2014). This study performs a validation by comparing different tide models to tide gauge data. For the Arctic Ocean, EOT11a shows rms values between 1.4 and 4.6 cm for the four major constituents, and it is the second best of the seven models in the test. Table 1 lists all corrections used within the present investigation.

To remove erroneous and unreliable sea surface height observations from the dataset, an outlier rejection is performed by applying a fixed threshold criterion. The SSH observations are compared to a long temporal mean sea surface (MSS), including more than 20 years of altimetry data, and sea level anomalies (SLAs) are built. The conversion is done by removing the DTU15MSS developed by Andersen and Knudsen (2009) from the along-track sea surface heights. Without being too restrictive within the sea ice zones with a higher noise level than in open ocean, a threshold of ± 2 m is introduced. This rejects 1.54 % of the high-frequency measurements of Envisat. After removing outliers the revised dataset is retransformed to sea surface heights by re-adding the MSS.

2.3.3 Dynamic ocean topography estimation

After obtaining sea surface heights the transition to physical heights is performed with respect to an underlying geoid model (i.e., the computation of DOT). In the present investigation the high-resolution Optimal Geoid Model for Modeling Ocean Circulation (OGMOC), developed up to a harmonic degree of 2190 and corresponding to a spatial resolution of nearly 9.13 km, is applied. This is one of the latest high-resolution global geoid models incorporating the most recent satellite gravimetry and satellite altimetry datasets. Moreover it is optimized for estimating ocean currents and it is assumed to provide the best possible solution for the current application. More details regarding to the constituents and processing strategy of the geoid can be found in Gruber and Willberg (2019) and Fecher and Gruber (2018). Briefly summarized, OGMOC is a combination of XGM2016 (Pail et al., 2018) and the EIGEN6-C4 model (Förste et al., 2004). XGM2016 is used up to degree 619. Between 619 and 719, XGM2016 and EIGEN6-C4 are combined applying a weighting function. Higher harmonic degrees (> 719) are retained unchanged from the EIGEN6-C4 model.

To minimize noise within the high-frequency altimetry database and to be more consistent with the spatial resolution of the geoid, the corrected along-track SSH observations get low-pass filtered by applying a moving average using a rectangle kernel adapted to the spatial resolution of the used geoid (9.13 km). Areas with sparse availability of along-track observations (e.g., leads, polynyas) less than the window size are not considered in the filtering process and remain unfiltered in the dataset. The DOT is derived by interpolating the geoid heights to the altimetry locations and subtracting them from the SSH observations.

3 Methods and results

The preprocessed ocean heights from altimetry and FESOM are compared with each other to identify similarities and discrepancies and to explore the possibility of a combination. Therefore, in the first step, both datasets are analyzed and examined regarding their temporal and spatial characteristics. The datasets are investigated in terms of constant offsets, seasonally occurring patterns (e.g., annual sea level variability) and residual sea level variations.

The FESOM data are provided on daily unstructured grids with local refinements in the central Greenland Sea and the Fram Strait. In contrast, the altimetry observations are sampled along-track and characterized by a high spatial resolution with irregular data gaps due to sea ice coverage. Figure 2 displays the inhomogeneously distributed FESOM nodes showing a maximum resolution of about 1 km. Moreover, three representative days of altimetry along-track data are shown with different behavior in observation availability depending on the season and the presence of sea ice. During

Table 1. Geophysical and empirical altimetry corrections applied in the study.

Corrections	Sources	References
Ionosphere	NOAA Ionosphere Climatology 2009 (NIC09)	Scharroo and Smith (2010)
Wet troposphere	ECMWF (2.5–2.0°) for Vienna Mapping Functions (VMF1)	Boehm et al. (2009)
Dry troposphere	ECMWF (2.5–2.0°) for Vienna Mapping Functions (VMF1)	Boehm et al. (2009)
Dynamic atmospheric correction	Inverse barometric pressure + (MOG2D)HF	Collected localization satellites (CLS)
Ocean tides	Global Empirical Ocean Tide model (EOT11a)	Savcenko et al. (2012)
Pole tides	From Envisat SGDR v2.1	Wahr (1985)
Solid Earth tides	From Envisat SGDR v2.1	Cartwright and Edden (1973)
Radial errors	Multi-mission Cross-Calibration (MMXO) version 15	Bosch et al. (2014)
Sea state bias	ALES+ sea state bias correction	Passaro et al. (2018)

the sea ice maximum in March (Kvingedal, 2013) most of the altimetry data close to the Greenland coast are missing due to a semi-closed sea ice cover. In contrast, in the summer season the tracks show fewer data gaps.

In order to allow a direct and pointwise comparison of both datasets, a resampling of at least one of them is necessary. Since the FESOM data exhibit a significantly higher spatial and a uniform temporal resolution, they will be interpolated using a nearest-neighbor algorithm with the times and locations of the altimetry observations. This prevents an unnecessary smoothing of the altimetry data.

3.1 Assessment of the annual cycle

It can be expected that the annual sea level variability is the dominant signal contained in both datasets (e.g., Bulczak et al., 2015). The present analysis performs a comparison of the annual and remaining temporal signal components within the investigation period by fitting harmonic functions to both datasets.

In the first step, daily height averages for the entire region are computed. Figure 3 shows the temporal evolution of the daily means within the investigation period for both datasets. An obvious offset of about 41 cm between the datasets caused by different underlying height references (geoid vs. bathymetry) is clearly visible. Furthermore, a linear trend or another long-term systematic behavior is not detectable, probably due to the short period of only 7 years. However, the altimetry-derived daily averaged DOT shows larger variations and a standard deviation of 9.0 cm. In contrast, the modeled data are characterized by a smoother behavior and a smaller standard deviation of 4.7 cm. These numbers include a clear seasonal cycle, which is also clearly visible in Fig. 3.

In order to examine both datasets concerning their annual period, the daily means are analyzed by a Fourier analysis (e.g., Stade, 2005). Therefore, both time series are centered at zero by reducing their constant offsets before the Fourier coefficients are obtained by applying a least-squares estimation (e.g., Thomson and Emery, 2014).

Figure 4a displays the amplitude spectrum of the interpolated FESOM and profiled altimetry daily means between

2003 and 2009. The modeled data are characterized by weaker amplitudes. The annual period constitutes the most dominant long-period signal. In the case of altimetry, the annual amplitude represents 6.9 cm and, in the case of FESOM, 3.9 cm of the sea level variability. Other frequencies can not be physically explained and thus are not further investigated in the present study. In particular, the semiannual signal is very small (1.5 cm) and shows no significant impact on both datasets. The remaining amplitudes are smaller than 1.5 cm in the case of altimetry (1.0 cm, FESOM).

However, an amplitude of almost 2 cm is detectable for a period of 3 days, which cannot be assigned to ocean or sea-ice-related dynamics. This is an artifact possibly caused by the irregular data sampling. In order to prove this hypothesis, the frequency analysis is also performed for the full FESOM grid. Figure 4b shows the amplitude spectrum and the estimated periods for the daily profiled FESOM DOT (red) and the original FESOM DOT (black). It can be clearly observed that the 3-day period is not confirmed by the original dataset. Moreover, higher discrepancies can be found in the short periodic domain, which can be attributed to more variability due to more input information. However, all other dominant periods are caught by both datasets. The obtained amplitudes show good agreement in all periods except for the annual signal. Here, the irregularly sampled profile data overestimate the amplitude by about 1 cm. This might be related to alias effects from remaining tidal influence due to the repeat cycle of Envisat (see Sect. 4 for more details).

As mentioned earlier the annual signal represents the most dominant signal in both datasets. By introducing the obtained annual Fourier coefficients to a harmonic fitting, the temporal evolution and the phasing can be shown (see Fig. 5). Aside from differences in the annual amplitudes, a phase shift of about 29 days is recognizable between the two signals. The maximum is reached at day of year (DOY) 230 (18 August) for altimetry and in the case of FESOM at DOY 259 (16 September).

However, it is obvious that one single harmonic function cannot represent the full complexity of the DOT variations in the northern Nordic seas. A detailed analysis of the annual signal considering different bathymetric features (e.g., shelf

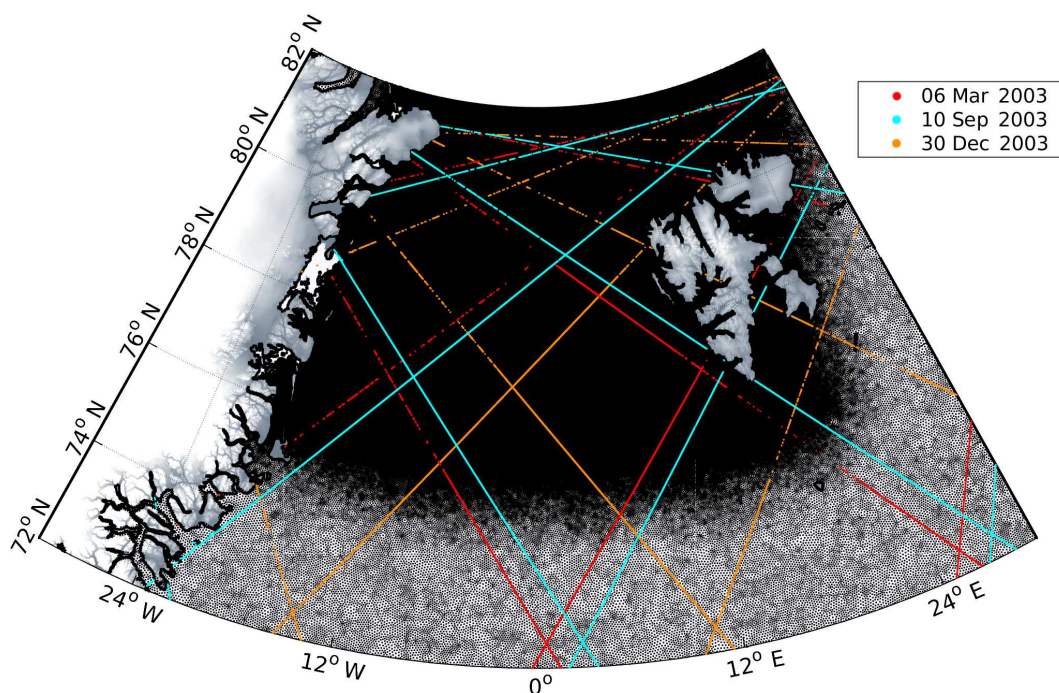


Figure 2. Locations of selected altimetry observations in wintertime and summertime. The small black dots indicate the unstructured FESOM grid nodes migrating at higher latitudes to a apparently closed black background.

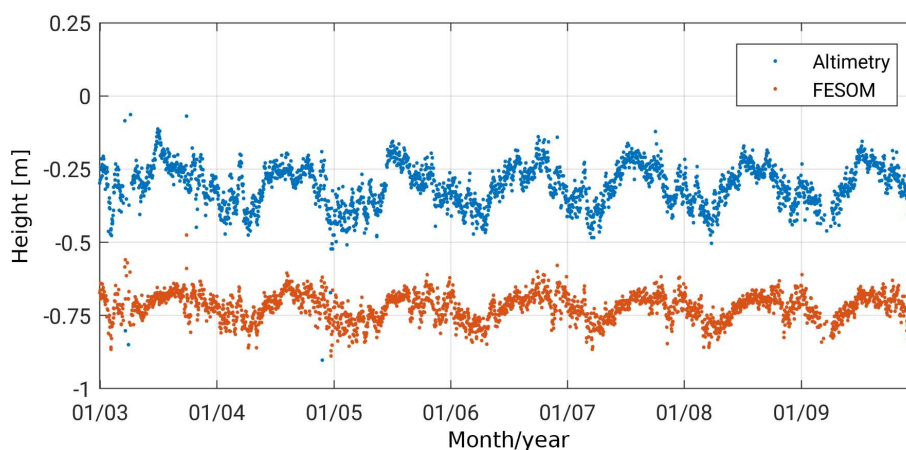


Figure 3. Temporal evolution of daily means of altimetry-derived DOT observations (blue) and FESOM SSH outputs (interpolated to the locations of altimetry measurements, red) within the investigation period and study area (see Sect. 2).

or deep sea areas) brings the opportunity to estimate region-dependent annual amplitudes and phases. This is presented in the following section.

3.2 Spatiotemporal pattern analysis

In order to analyze regionally dependent differences, the profiled altimetry data are monthly averaged and arranged into along-track bins of 7.5 km length. The bin structure follows the nominal 1 Hz ground track pattern of Envisat and reduces the high-frequency measurement noise. Enabling long-term

analyses, only satellite passes are admitted showing an availability of at least 64 repeat cycles, which corresponds to 96 % of the data in the evaluation period. Data gaps or missing bins are possible due to sea ice contamination or failing observations. For FESOM, daily data from the closest grid node are assigned to each bin. Thus, this dataset exhibits the same spatial resolution but a better temporal resolution, allowing for a more precise amplitude estimation.

Figure 6 displays for each bin the estimated annual DOT variations within 2003–2009. The amplitudes of both datasets show a similar pattern with smaller values along

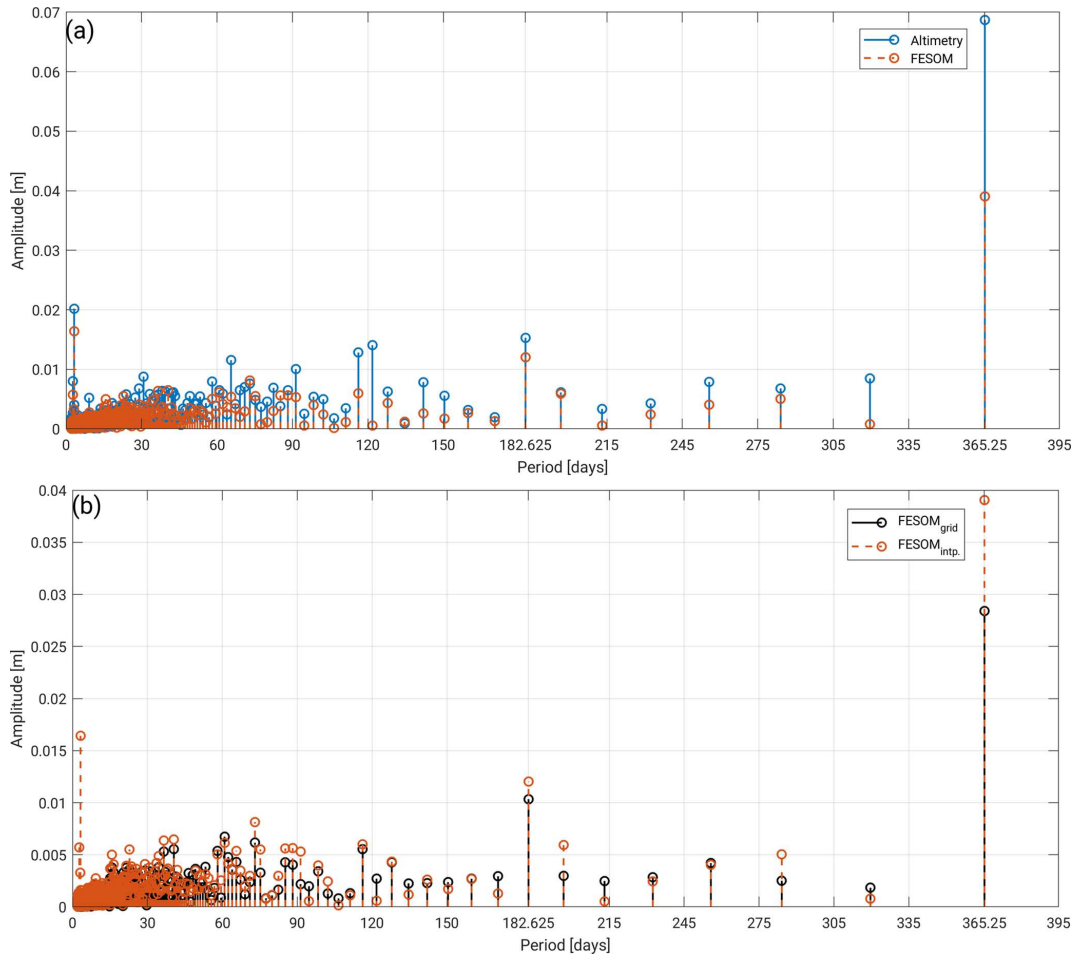


Figure 4. Fourier analysis amplitude spectrum of two altimetry locations interpolated with FESOM data (red) from (a) altimetry-derived DOT along-track observations (blue) and (b) original FESOM data (black) within the investigation area from 2003 to 2009 (see Sect. 2).

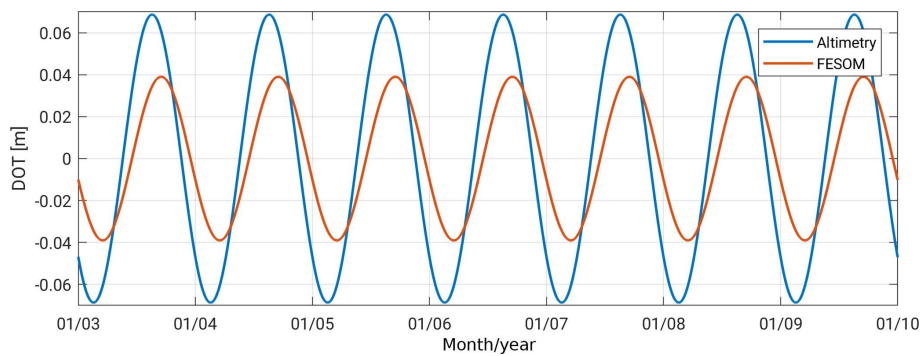


Figure 5. Annual cycles of DOT from along-track altimetry (blue) observations and FESOM (red) simulations within the investigation time and area (see Sect. 2).

the major current systems (EGC and WSC) and larger values along the Greenland and Svalbard coasts and in the area around the Molloy Hole. In general, the altimetry-derived amplitudes are larger than the model amplitudes. In the Greenland Basin, a 2–3 times stronger representation of the

annual amplitudes can be observed. Here, the mean altimetry amplitude reaches 6.3 cm. In the southern and eastern parts of the shelf regions, the altimetry amplitudes are smaller than the model amplitudes.

The maximum amplitudes in the Greenland Basin appear during August and September and show a mostly homogeneous distribution in both datasets. In ice-free regions both datasets show good agreement (also in comparison with results of Volkov and Pujol, 2012, and Mork and Øystein Skagseth, 2013). However, in ice-covered shelf regions, the central Fram Strait and close to calving glaciers, the derived amplitudes differ up to 8 cm. The altimetry estimated annual maximum on the Greenland Shelf occurs in November, which is confirmed by FESOM. Nevertheless, obvious phase differences between FESOM and altimetry can be found east of Spitsbergen, where the observed annual maximum occurs in the early spring months, in contrast to FESOM displaying a maximum in autumn. This could perhaps be caused by sea ice interference or strong ocean variabilities.

In order to account for different hydrological (e.g., glacier melt, water mass changes), atmospheric (e.g., winds, solar radiation) and oceanographic effects (e.g., ocean currents) in the study area, the region is subdivided into three main sub-areas: the deep basin region (Greenland Basin, < -450 m) and two shelf regions (Greenland Shelf, Barents Sea). Table 2 provides outlier-removed (3σ criterion) mean amplitudes and DOYs of the maximum amplitude for the three subregions, as well as their annual variabilities. FESOM shows similar amplitudes for all three areas, whereas altimetry exhibits smaller mean amplitudes for the Barents Sea than for the two other regions, where the mean amplitudes are about twice the amplitudes of FESOM. The phase shows good consistency between altimetry and FESOM on the Greenland Shelf but discrepancies of circa 34.25 days in the Greenland Basin and 19.5 days in the Barents Sea. A discussion of the differences is provided in Sect. 4.

3.3 Residual analysis

In order to analyze residual differences, both datasets are reduced by their regional estimated annual signal and constant offsets as given in Table 2. Figure 7 shows monthly averaged along-track residual DOT for altimetry and FESOM for the three study regions. In all areas, a high correlation between the datasets is visible. For the Greenland Basin and the Barents Sea, almost no systematic effects are detectable, whereas the altimetry time series for the Greenland Shelf exhibits multi-annual anomalies that are less pronounced in the FESOM time series, which only shows a small, insignificant behavior trends. However, the investigation period is too short to allow for a reliable interpretation of the underlying effects.

Figure 8 shows the geographical distribution of the mean residual signals and weighted average of standard deviation per bin. Both datasets display similar spatial patterns. However, obvious differences can be seen in some areas, e.g., the central Fram Strait and the transition areas between the deep basin and shelf regions. Comparing the variability of the residuals, the altimetry-derived DOT shows in general

higher values and an enhanced variations in the ice-covered shelf areas, contrary to FESOM displaying more variability in regions affected by ocean currents.

Figure 9 shows the differences between the averaged residual DOT of altimetry and FESOM (left) as well as their correlation per bin (right). The largest differences occur on the northern Greenland Shelf and in the Fram Strait, whereas fewer sea-ice-affected areas (e.g., Greenland Basin, Barents Sea), including the current and eddy regions (e.g., WSC), show good agreement. The correlations are mainly positive, with values above 0.5 % for 21 % of the bins. High positive correlations are displayed in the deep basin parts of the study area. Smaller positive correlations can be found in regions with strong bathymetric gradients and in northern areas of the major ocean currents (e.g., WSC, EGC).

Remarkable elevation differences occur between 80 and 82° N. These patterns are seen in the altimetry-derived DOT but not in the model and yield up to 0.4 m. They show a constant behavior within the entire investigation period, which cannot be attributed to seasonal ocean phenomena. Instead, these artifacts are due to geoid errors caused by residual ocean signals at polar latitudes (e.g., Kwok and Morison, 2015; Farrell et al., 2012). More discussion related to the geoid can be found in the next section.

4 Discussion

The comparison of the altimetry-derived and simulated DOT shows good agreement in terms of highly correlated regional time series and small residual heights. Predominately positive correlations between both datasets can be found in ice-free areas (e.g., Greenland Basin) and in regions affected by ocean currents. FESOM and altimetry display a very similar frequency behavior for the most dominant periodic DOT variability. In comparison with previous studies, the along-track altimetry DOT agrees concerning annual amplitudes and phases as obtained by Volkov and Pujol (2012) and Mork and Øystein Skagseth (2013).

However, the analysis also reveals some systematic discrepancies. These can be explained by three different error sources: they partly originate from modeling errors of FESOM, partly from measurement uncertainties of altimetry and partly from errors of the geoid used for computing the altimetry DOT. These points will be discussed in more detail in the following paragraphs.

FESOM is affected by synthetic smoothing due to the added numerical diffusion component stabilizing the model runs and preventing the simulated DOT from uncontrolled variabilities. Moreover, in the present investigation the FESOM run does not include the latest glacier runoff model, which causes further irregularities close to northeastern Greenland's coast. Another reason causing this smoothing effect can be found in the too strongly adjusted sea ice friction coefficient of the model, damping DOT variabilities in

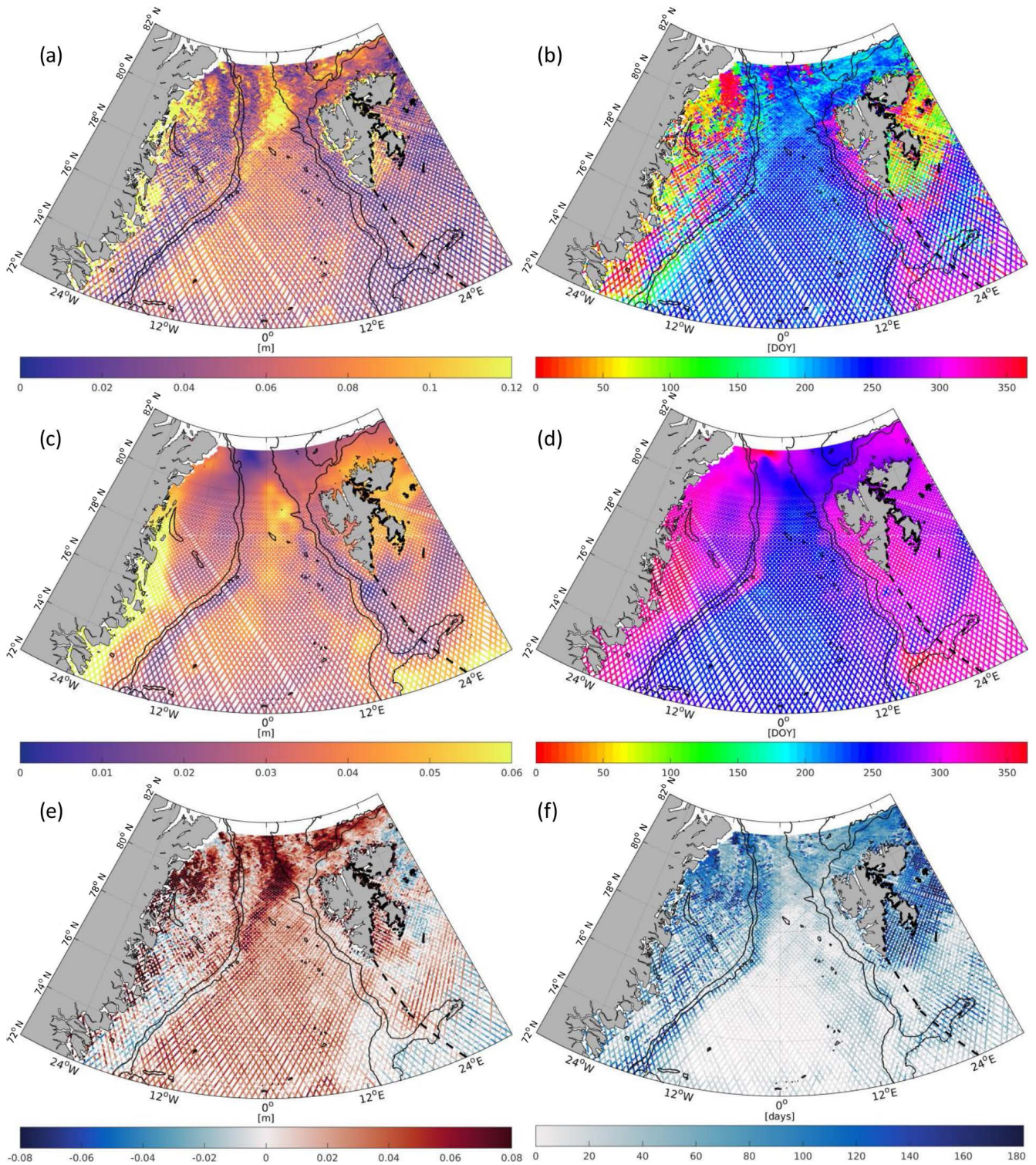


Figure 6. Mean annual amplitudes (**a**, **c**, **e**) and the day of year (DOY) of the annual maximum (**b**, **d**, **f**) per bin for altimetry (**a**, **b**) and FESOM (**c**, **d**) DOT heights. The bottom row (**e**, **f**) displays amplitude (in m) and phase differences (in days) of altimetry minus FESOM. RTopo2 bathymetric contours (black) indicate the shelf (-450 m) and the basin (-1500 m) regions. The dashed lines highlight the Barents Sea boundary (IHO, International Hydrographic Organization, 1953). Note the different scales of the amplitude color bars.

Table 2. Offset, averaged annual amplitude (Amp) and DOY/month of maximum amplitude with variability (Var) in three subregions.

Area	Source	Offset (Var) [m]	Amp (Var) [m]	DOY/Month (Var)
Greenland Basin	Altimetry	−0.301 (0.131)	0.063 (0.023)	232.75/Aug (33.61)
	FESOM	−0.744 (0.086)	0.030 (0.009)	267/Sep (29.24)
Greenland Shelf	Altimetry	+0.054 (0.099)	0.057 (0.038)	314.75/Nov (112.86)
	FESOM	−0.537 (0.054)	0.038 (0.013)	312.25/Nov (21.38)
Barents Sea	Altimetry	−0.180 (0.043)	0.040 (0.018)	284.25/Oct (102.42)
	FESOM	−0.667 (0.020)	0.038 (0.010)	303.75/Oct (13.04)

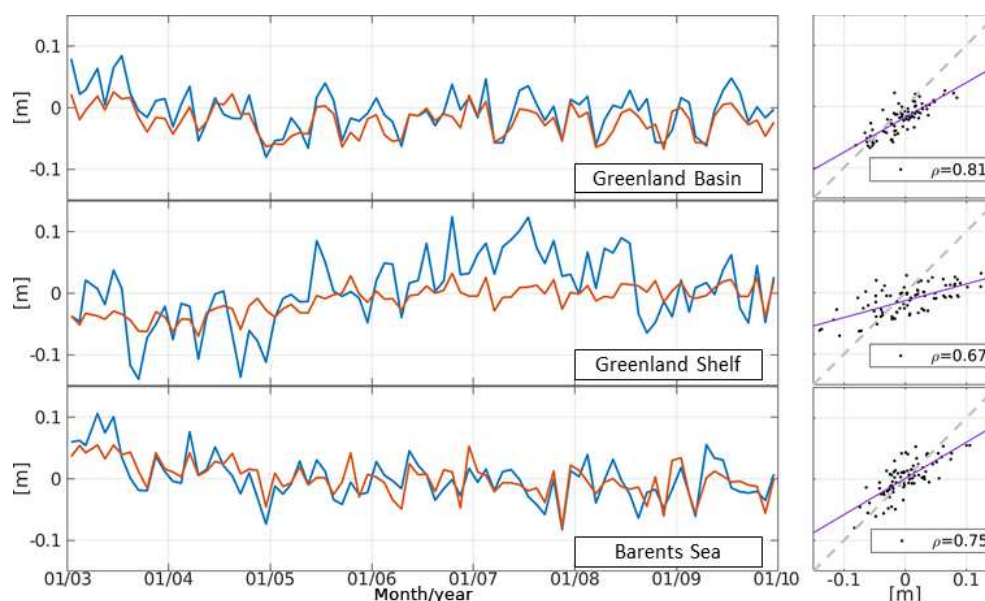


Figure 7. Monthly time series of averaged residual heights from altimetry (blue) and FESOM (red). Offsets and annual signals were removed for each region. Additionally, scatter plots and correlation (ρ) are displayed. Regression and bisectrix lines are shown by the purple and dashed gray lines, respectively.

sea-ice-affected regions. The model applies strictly the hydrostatic equations, which function as an assumption of the real sea state. Furthermore, it does not include tidal ocean signal and barometric effects and lacks a steric correction to ensure the global conservation of mass.

While the first two points are taken into account by correcting the altimetry observations, the latter point is currently not considered in the comparison. This should be acceptable since the impact on low-frequency regional sea level patterns is small (Griffies and Greatbatch, 2012). However, it will contribute to the constant and long-term differences visible in this study. In contrast, remaining differences in handling the atmospheric sea level pressure (i.e., caused by uncertainties of the used correction model) will show up in regional differences. They might be the reason for the observed temporal shifts of the maximum annual signal in the Greenland Basin. Even more important is the insufficiently realistic consideration of freshwater inflow (e.g., by glacier runoff) by FESOM. This can cause phase shifts as well as reduced annual am-

plitudes. Furthermore the coarse resolution of atmospheric forcing is an additional reason for a smoothed sea level representation and an underestimation of annual amplitudes.

For satellite altimetry, the polar oceans are a challenging region, especially when sea ice is present. In these areas, the returned radar echoes are comprised of signals from different surface reflectors such as different ice types and structures, melt ponds on ice and open water. The challenge is to extract valuable information about the sea level while disregarding all other reflectors. Even with the application of a dedicated waveform classification and special retracking, as performed here, DOT estimates in coastal and sea ice areas are significantly more noisy than in open ocean. Moreover, the applied range corrections can be biased by the Arctic Ocean conditions, leading to more unreliable range estimations in ice-covered shelf regions. Thus, in these regions, small-scale structures are not thoroughly reliable.

Due to its measurement geometry, satellite altimetry has a high along-track resolution, but data are scattered in time

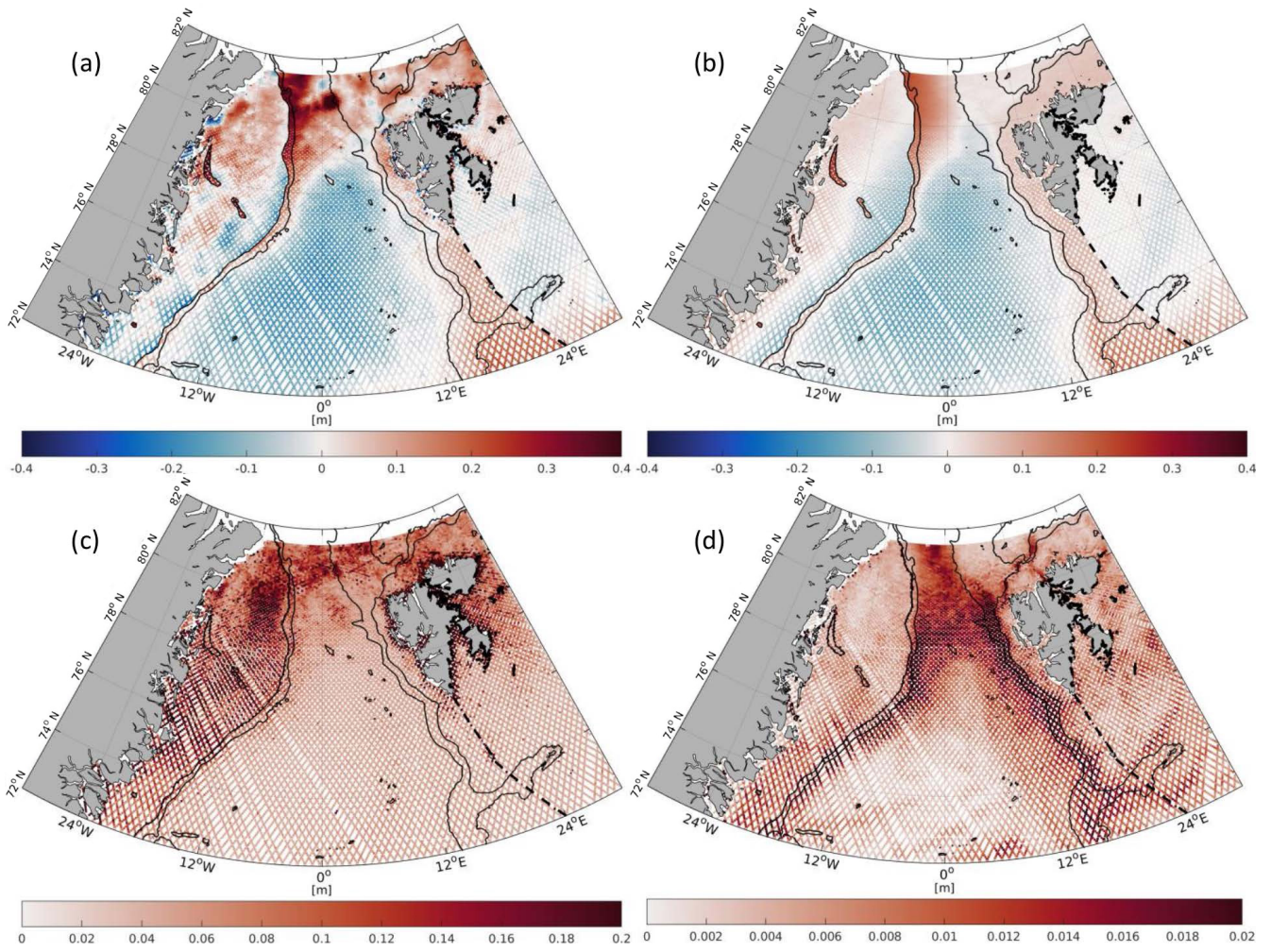


Figure 8. Weighted mean residual DOT (a, b) and weighted mean of standard deviation (c, f) for each bin from altimetry (a, c) and FESOM (b, d) within 2003–2009. Note the different scales of standard deviation color bars.

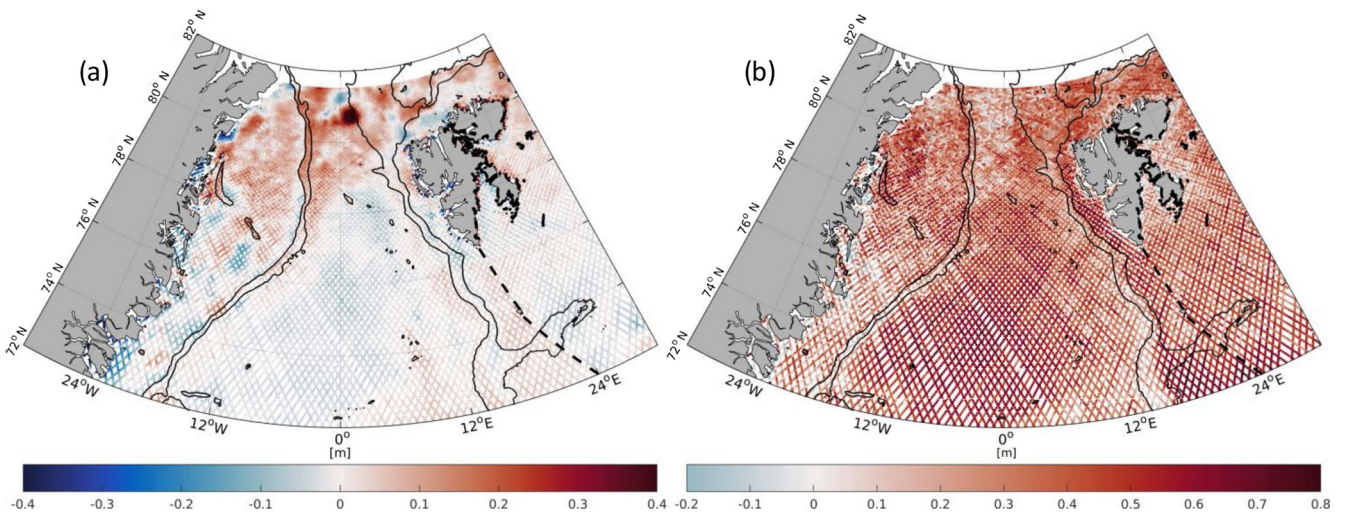


Figure 9. Differences (a) and correlations (b) between altimetry and FESOM binned along-track residual DOT within the investigation period.

and space. In addition, in polar regions, an irregular sampling due to missing data caused by sea ice coverage must be taken into account. This can significantly influence the estimation of annual sea level variability, as tests with simulated data with different sampling revealed (see Sect. 3.1).

However, an interpolation of the dataset as it is done in the majority of other studies (e.g., Kwok and Morison, 2015; Armitage et al., 2016; Farrell et al., 2012) could be avoided in order to conserve more high-frequency observations and spectral content.

This study is based on data from Envisat, whose repeat cycle is known to cause severe alias effects of 365 days for the tidal constituents K1 and P1 (see Volkov and Pujol, 2012, and Padman et al., 2018). Thus, errors in K1 and P1 in the applied ocean tide model may impact the estimated annual variation of the altimetry-based DOT. Passaro et al. (2015) showed that the effect can reach up to 1–3 cm. For this study, the EOT11a ocean tide model (Savcenko et al., 2012) is used. Even if that model is proven to be among the best models of the Arctic Ocean (see Stammer et al., 2014) the differences between FESOM and altimetry in the bin-wise estimated annual amplitudes could be partially attributed to this aliasing effect. However, the analysis presented in Sect. 3.1, which is based on averaged Envisat data, also shows a discrepancy of more than 1 cm between FESOM and altimetry amplitudes. Thus, the majority of this difference will be due to the smoothing effect of FESOM.

In addition to simulated and observational data irregularities, stationary artifacts caused by geoid inaccuracies can be clearly identified in the northern Fram Strait region. Following Kwok and Morison (2015) these synthetic looking elevations in the altimetry-derived DOT can be attributed to a combination of geoid residuals and oceanographic features, which are very challenging to separate from each other. A significant problem can be seen in the specific components of the geoid models. The higher spherical harmonics (degrees 720–2190), describing shorter wavelength patterns (10–30 km), are based on selective in situ and satellite altimetry gravity observations, which can be contaminated by sea ice or feature sparse availability. Within this study, one of the newest geoid models is used, which has been developed for ocean circulation studies and has been optimized to avoid striations and orange skin-like features. Nevertheless, it seems to contain the remaining artificial structures in the study area. According to Gruber and Willberg (2019), the higher spherical harmonics are covered by EIGEN6-C4 geoid model (Förste et al., 2004), which does not include current satellite altimetry data. However, mid spherical harmonic degrees, corresponding to a 30–100 km spatial wavelength, are represented by XGM2016 (Pail et al., 2018) including the latest altimetry marine gravity fields. Hence, a better representation of short wavelength patterns can only be reached by introducing the latest and updated altimetry data, supported by in situ measurements of the geoid compu-

tations. Similar effects are also visible when using alternative geoid models (Skourup et al., 2017).

5 Conclusions and outlook

In the present paper, high-frequency altimetry-derived DOT is compared with water elevations of FESOM in order to identify their similarities and discrepancies as well as their respective benefits. Both datasets are characterized by different limitations, which prevent a perfect representation of the dynamic topography in polar regions based on only one approach. The present investigation demonstrates that model simulations and observations are both needed to understand the complexity of ocean processes in the polar latitudes, especially in the Arctic Ocean.

The present paper shows basic agreement between a numerically simulated and an empirical estimated representation of the DOT in the northern Nordic seas in terms of annual variability and spatial behavior. However, inconsistencies due to the higher noise level of the observations, especially in sea ice areas, and the enhanced smoothing of the model are demonstrated. For example, an offset of about half a meter exists between the two datasets since the data of FESOM are not defined with respect to a standard reference frame (Androsov et al., 2018). Moreover, the annual sea level variability observed by the two datasets differs by a few centimeters. The residual heights show a similar pattern, high temporal correlations and only small differences, which are mainly related to sea ice coverage and geoid artifacts.

The results presented in this paper indicate that further improvements can be made to both datasets: the altimetry-derived DOT still needs a better or more restrictive handling of sea ice observations as well as a more reliable Arctic geoid. FESOM should be corrected for a global mean steric height change (Greatbatch, 1994) in order to ensure the conservation of mass and to make the observed altimetry heights directly comparable to the model heights. In addition, an improved handling of freshwater inflow is required to better account for mass changes due to glacier as well as river runoff.

However, even if these points will be improved, the principal limitations of observations (measurement noise and data gaps in regions with closed sea ice coverage) and models (absolute height level) will persist. Thus, it seems reasonable to exploit the advantages of both datasets through a combination of model and along-track observations. This will enable the derivation of a homogeneous DOT, equally sampled in time and space without the need of smoothing the altimetry measurements by gridding procedures. In such an approach, the absolute level as well as the annual variability of altimetry should be preserved, and the continuous spatial representation of the model should be used to bridge regions influenced by sea ice coverage and to get rid of unreliable high-latitude geoid artifacts. This will allow for an optimized determination of the Arctic DOT and the associated surface currents.

Concerning the current availability of altimetry-derived DOT estimations, it is possible to establish a combination of simulated and observation-based DOT representation covering more than 25 years, enabling climate-relevant conclusions.

Data availability. Envisat RA2 altimetry data access is available from ESA after fast registration submission (<https://doi.org/10.5270/EN1-85m0a7b>, ESA, 2018). The FESOM data can be requested from Alfred Wegener Institute. A final combined data product will be provided via PANGAEA (<https://www.pangaea.de/>, last access: 13 February 2019) once the project is completed.

Author contributions. FLM developed the comparison methods, conducted the data analysis and wrote the majority of the paper. CW provided the FESOM data and contributed to the manuscript writing. DD supervised the present study, contributed to the manuscript writing and helped with discussions of the results. MP developed the retracking algorithm and helped with the application and discussion concerning the altimetry dataset. WB initiated the study. FS supervised the research.

Competing interests. The authors declare that they have no conflict of interest.

Acknowledgements. The authors thank the ESA for operating Envisat and for supplying the SGDR v2.1 dataset. The authors thank the Chair of Astronomical and Physical Geodesy, Technical University of Munich (TUM), for providing the geoid model, OG-MOC. This work was mainly supported by the German Research Foundation (DFG) through grants BO1228/13-1, DE2174/3-1 and in part through grant OGreen79 as part of the Special Priority Program (SPP)-1889 "Regional Sea Level Change and Society" (SeaLevel). We thank Sine M. Hvidegaard and two further anonymous reviewers for their valuable comments that helped to improve the manuscript.

This work was supported by the German Research Foundation (DFG) and the Technical University of Munich (TUM) in the framework of the Open Access Publishing Program.

Edited by: David M. Holland

Reviewed by: Sine M. Hvidegaard and two anonymous referees

References

- Andersen, O. B. and Knudsen, P.: DNSC08 mean sea surface and mean dynamic topography models, *J. Geophys. Res.-Oceans*, 114, c11001, <https://doi.org/10.1029/2008JC005179>, 2009.
- Androsov, A., Nerger, L., Schnur, R., Schröter, J., Albertella, A., Rummel, R., Savcenko, R., Bosch, W., Skachko, S., and Danilov, S.: On the assimilation of absolute geodetic dynamic topography in a global ocean model: impact on the deep ocean state, *J. Geodesy*, 1–17, <https://doi.org/10.1007/s00190-018-1151-1>, 2018.
- Armitage, T. W. K., Bacon, S., Ridout, A. L., Thomas, S. F., Aksenov, Y., and Wingham, D. J.: Arctic sea surface height variability and change from satellite radar altimetry and GRACE, 2003–2014, *J. Geophys. Res.-Oceans*, 121, 4303–4322, <https://doi.org/10.1002/2015JC011579>, 2016.
- Beszczyńska-Möller, A., Fahrback, E., Schauer, U., and Hansen, E.: Variability in Atlantic water temperature and transport at the entrance to the Arctic Ocean, 1997–2010, *ICES J. Mar. Sci.*, 69, 852–863, <https://doi.org/10.1093/icesjms/fss056>, 2012.
- Boehm, J., Kouba, J., and Schuh, H.: Forecast Vienna Mapping Functions 1 for real-time analysis of space geodetic observations, *J. Geodesy*, 83, 397–401, <https://doi.org/10.1007/s00190-008-0216-y>, 2009.
- Bosch, W., Dettmering, D., and Schatke, C.: Multi-Mission Cross-Calibration of Satellite Altimeters: Constructing a Long-Term Data Record for Global and Regional Sea Level Change Studies, *Remote Sens.*, 6, 2255–2281, <https://doi.org/10.3390/rs6032255>, 2014.
- Brown, G.: The average impulse response of a rough surface and its applications, *IEEE T. Antenn. Propag.*, 25, 67–74, <https://doi.org/10.1109/TAP.1977.1141536>, 1977.
- Bulczak, A. I., Bacon, S., Naveira Garabato, A. C., Ridout, A., Sonnewald, M. J. P., and Laxon, S. W.: Seasonal variability of sea surface height in the coastal waters and deep basins of the Nordic Seas, *Geophys. Res. Lett.*, 42, 113–120, <https://doi.org/10.1002/2014GL061796>, 2015.
- Cartwright, D. E. and Edden, A. C.: Corrected Tables of Tidal Harmonics, *Geophys. J. Int.*, 33, 253–264, <https://doi.org/10.1111/j.1365-246X.1973.tb03420.x>, 1973.
- Celebi, M.: *Partitional Clustering Algorithms*, EBL-Schweitzer, Springer International Publishing, <https://doi.org/10.1007/978-3-319-09259-1>, 2015.
- Collected localization satellites (CLS): Dynamic atmospheric Corrections are produced by CLS Space Oceanography Division using the Mog2D model from Legos and distributed by Aviso+, with support from Cnes, AVISO+, available at: <http://www.aviso.altimetry.fr>, last access: 28 November 2016.
- Connor, L. N., Laxon, S. W., Ridout, A. L., Krabill, W. B., and McAdoo, D. C.: Comparison of Envisat radar and airborne laser altimeter measurements over Arctic sea ice, *Remote Sens. Environ.*, 113, 563–570, <https://doi.org/10.1016/j.rse.2008.10.015>, 2009.
- Dai, A., Qian, T., Trenberth, K. E., and Milliman, J. D.: Changes in Continental Freshwater Discharge from 1948 to 2004, *J. Climate*, 22, 2773–2792, <https://doi.org/10.1175/2008JCLI2592.1>, 2009.
- Danilov, S., Wang, Q., Timmermann, R., Iakovlev, N., Sidorenko, D., Kimmritz, M., Jung, T., and Schröter, J.: Finite-Element Sea Ice Model (FESIM), version 2, *Geosci. Model Dev.*, 8, 1747–1761, <https://doi.org/10.5194/gmd-8-1747-2015>, 2015.
- de Steur, L., Hansen, E., Gerdes, R., Karcher, M., Fahrback, E., and Holfort, J.: Freshwater fluxes in the East Greenland Current: A decade of observations, *Geophys. Res. Lett.*, 36, 23, <https://doi.org/10.1029/2009GL041278>, 2009.
- Dettmering, D., Wynne, A., Müller, F. L., Passaro, M., and Seitz, F.: Lead Detection in Polar Oceans – A Comparison of Different Classification Methods for Cryosat-2 SAR Data, *Remote Sens.*, 10, 1190, <https://doi.org/10.3390/rs10081190>, 2018.

- ESA: Envisat Altimetry Level 2 User Manual V 1.4, European Space Agency (ESA), October, 2011.
- ESA: RA-2 Sensor and Geophysical Data Record – SGDR, European Space Agency, <https://doi.org/10.5270/en1-85m0a7b>, 2018.
- Farrell, S. L., McAdoo, D. C., Laxon, S. W., Zwally, H. J., Yi, D., Ridout, A., and Giles, K.: Mean dynamic topography of the Arctic Ocean, *Geophys. Res. Lett.*, 39, 1, <https://doi.org/10.1029/2011GL050052>, 2012.
- Fecher, T. and Gruber, T.: Optimal Ocean Geoid as Reference Surface for Mean Ocean Circulation and Height Systems, in: EGU General Assembly Conference Abstracts, Vol. 20 of EGU General Assembly Conference Abstracts, p. 8691, 2018.
- Fetterer, F., K., Knowles, W., Meier, M., Savoie, and Windnagel, A. K.: Sea Ice Index, Version 3, north, Boulder, Colorado USA, NSIDC: National Snow and Ice Data Center, <https://doi.org/10.7265/N5K072F8>, 2017.
- Förste, C., Bruinsma, S., Abrikosov, O., Lemoine, J.-M., Marty, J. C., Flechtner, F., Balmino, G., Barthelmes, F., and Biancale, R.: EIGEN-6C4 The latest combined global gravity field model including GOCE data up to degree and order 2190 of GFZ Potsdam and GRGS Toulouse, GFZ Data Services, <https://doi.org/10.5880/icgem.2015.1>, 2004.
- Greatbatch, R. J.: A note on the representation of steric sea level in models that conserve volume rather than mass, *J. Geophys. Res.-Oceans*, 99, 12767–12771, <https://doi.org/10.1029/94JC00847>, 1994.
- Griffies, S. M. and Greatbatch, R. J.: Physical processes that impact the evolution of global mean sea level in ocean climate models, *Ocean Modell.*, 51, 37–72, <https://doi.org/10.1016/j.ocemod.2012.04.003>, 2012.
- Gruber, T. and Willberg, M.: Signal and Error Assessment of GOCE-based High Resolution Gravity Field Models, *J. Geodetic Sci.*, under review, 2019.
- Hattermann, T., Isachsen, P. E., von Appen, W.-J., Albrechtsen, J., and Sundfjord, A.: Eddy-driven recirculation of Atlantic Water in Fram Strait, *Geophys. Res. Lett.*, 43, 3406–3414, <https://doi.org/10.1002/2016GL068323>, 2016.
- Hayne, G.: Radar altimeter mean return waveforms from near-normal-incidence ocean surface scattering, *IEEE T. Antenn. Propag.*, 28, 687–692, <https://doi.org/10.1109/TAP.1980.1142398>, 1980.
- Helland-Hansen, B. and Nansen, F.: The Norwegian Sea - Its Physical Oceanography Based Upon the Norwegian Researches 1900–1904, Report on Norwegian Fishery and Marine Investigations, Fiskeridirektoratets havforskningssinstitutt, available at: <http://hdl.handle.net/11250/114874> (last access: 12 February 2019), 1909.
- Hunke, E. and Dukowicz, J.: The Elastic-Viscous-Plastic Sea Ice Dynamics Model in General Orthogonal Curvilinear Coordinates on a Sphere-Incorporation of Metric Term, *Mon. Weather Rev.*, 130, 1848–1865, 2001.
- IHO, International Hydrographic Organization: Limits of Oceans and Seas, PANGAEA, Bremerhaven, 1953.
- Johannessen, J. A., Raj, R. P., Nilsen, J. E. Ø., Pripp, T., Knudsen, P., Counillon, F., Stammer, D., Bertino, L., Andersen, O. B., Serra, N., and Koldunov, N.: Toward Improved Estimation of the Dynamic Topography and Ocean Circulation in the High Latitude and Arctic Ocean: The Importance of GOCE, *Surv. Geophys.*, 35, 661–679, <https://doi.org/10.1007/s10712-013-9270-y>, 2014.
- Kawasaki, T. and Hasumi, H.: The inflow of Atlantic water at the Fram Strait and its interannual variability, *J. Geophys. Res.-Oceans*, 121, 502–519, <https://doi.org/10.1002/2015JC011375>, 2016.
- Koldunov, N. V., Serra, N., Köhl, A., Stammer, D., Henry, O., Cazenave, A., Prandi, P., Knudsen, P., Andersen, O. B., Gao, Y., and Johannessen, J.: Multimodel simulations of Arctic Ocean sea surface height variability in the period 1970–2009, *J. Geophys. Res.-Oceans*, 119, 8936–8954, <https://doi.org/10.1002/2014JC010170>, 2014.
- Kvingedal, B.: Sea-Ice Extent and Variability in the Nordic Seas, 1967–2002, American Geophysical Union, 39–49, <https://doi.org/10.1029/158GM04>, 2013.
- Kwok, R. and Morison, J.: Dynamic topography of the ice-covered Arctic Ocean from ICESat, *Geophys. Res. Lett.*, 38, 2, <https://doi.org/10.1029/2010GL046063>, 2011.
- Kwok, R. and Morison, J.: Sea surface height and dynamic topography of the ice-covered oceans from CryoSat-2: 2011–2014, *J. Geophys. Res.-Oceans*, 121, 674–692, <https://doi.org/10.1002/2015JC011357>, 2015.
- Large, W. and Yeager, S.: The global climatology of an interannually varying air-sea flux data set, *Clim. Dynam.*, 33, 341–364, <https://doi.org/10.1007/s00382-008-0441-3>, 2008.
- Laxon, S. W.: Sea-Ice Altimeter Processing Scheme at the EODC, *I. J. Remote Sens.*, 15, 915–924, <https://doi.org/10.1080/01431169408954124>, 1994.
- Legeais, J.-F., Ablain, M., Zawadzki, L., Zuo, H., Johannessen, J. A., Scharffenberg, M. G., Fenoglio-Marc, L., Fernandes, M. J., Andersen, O. B., Rudenko, S., Cipollini, P., Quartly, G. D., Passaro, M., Cazenave, A., and Benveniste, J.: An improved and homogeneous altimeter sea level record from the ESA Climate Change Initiative, *Earth Syst. Sci. Data*, 10, 281–301, <https://doi.org/10.5194/essd-10-281-2018>, 2018.
- Morison, J., Kwok, R., Peralta Ferriz, C., Alkire, M., Rigor, I., Andersen, R., and Steele, M.: Changing Arctic Ocean freshwater pathways, *Nature*, 481, 66–70, 2012.
- Mork, K. A. and Øystein Skagseth: Annual Sea Surface Height Variability in the Nordic Seas, American Geophysical Union (AGU), 51–64, <https://doi.org/10.1029/158GM05>, 2013.
- Müller, F. L., Dettmering, D., Bosch, W., and Seitz, F.: Monitoring the Arctic Seas: How Satellite Altimetry Can Be Used to Detect Open Water in Sea-Ice Regions, *Remote Sens.*, 9, 551, <https://doi.org/10.3390/rs9060551>, 2017.
- Orvik, K. A. and Niiler, P.: Major pathways of Atlantic water in the northern North Atlantic and Nordic Seas toward Arctic, *Geophys. Res. Lett.*, 29, 1896, <https://doi.org/10.1029/2002GL015002>, 2002.
- Padman, L., Siegfried, M. R., and Fricker, H. A.: Ocean Tide Influences on the Antarctic and Greenland Ice Sheets, *Rev. Geophys.*, 56, 142–184, <https://doi.org/10.1002/2016RG000546>, 2018.
- Pail, R., Fecher, T., Barnes, D., Factor, J. F., Holmes, S. A., Gruber, T., and Zingerle, P.: Short note: the experimental geopotential model XGM2016, *J. Geodesy*, 92, 443–451, <https://doi.org/10.1007/s00190-017-1070-6>, 2018.
- Parkinson, C. and Washington, W.: A Large-Scale Numerical Model of Sea Ice, *J. Geophys. Res.*, 84, 311–337, <https://doi.org/10.1029/JC084iC01p00311>, 1979.
- Passaro, M., Cipollini, P., and Benveniste, J.: Annual sea level variability of the coastal ocean: The Baltic Sea-North Sea

- transition zone, *J. Geophys. Res.-Oceans*, 120, 3061–3078, <https://doi.org/10.1002/2014JC010510>, 2015.
- Passaro, M., Rose, S. K., Andersen, O. B., Boergens, E., Calafat, F. M., Dettmering, D., and Benveniste, J.: ALES+: Adapting a homogenous ocean retracker for satellite altimetry to sea ice leads, coastal and inland waters, *Remote Sens. Environ.*, 211, 456–471, <https://doi.org/10.1016/j.rse.2018.02.074>, 2018.
- Peacock, N. R. and Laxon, S. W.: Sea surface height determination in the Arctic Ocean from ERS altimetry, *J. Geophys. Res.*, 109, C07001, <https://doi.org/10.1029/2001JC001026>, 2004.
- Savcenko, R. and Bosch, W.: EOT11a – Empirical Ocean Tide Model From Multi-Mission Satellite Altimetry, Tech. Rep. 89, Deutsches Geodätisches Forschungsinstitut, Technische Universität München (DGFI-TUM), available at: <https://mediatum.ub.tum.de/doc/1304935/1304935.pdf> (last access: 12 February 2019), 2012.
- Savcenko, R., Bosch, W., Dettmering, D., and Seitz, F.: EOT11a – Global Empirical Ocean Tide model from multi-mission satellite altimetry, with links to model results, PANGAEA, <https://doi.org/10.1594/PANGAEA.834232>, 2012.
- Schaffer, J., Timmermann, R., Arndt, J. E., Kristensen, S. S., Mayer, C., Morlighem, M., and Steinhage, D.: A global, high-resolution data set of ice sheet topography, cavity geometry, and ocean bathymetry, *Earth Syst. Sci. Data*, 8, 543–557, <https://doi.org/10.5194/essd-8-543-2016>, 2016.
- Scharroo, R. and Smith, W. H. F.: A global positioning system-based climatology for the total electron content in the ionosphere, *J. Geophys. Res.-Space Phys.*, 115, a10318, <https://doi.org/10.1029/2009JA014719>, 2010.
- Serreze, M. and Barry, R.: *The Arctic Climate System*, Cambridge Atmospheric and Space Science Series, Cambridge University Press, available at: <https://books.google.de/books?id=DjH6AwAAQBAJ> (last access: 12 February 2019), 2014.
- Skourup, H., Farrell, S. L., Hendricks, S., Ricker, R., Armitage, T. W. K., Ridout, A., Andersen, O. B., Haas, C., and Baker, S.: An Assessment of State-of-the-Art Mean Sea Surface and Geoid Models of the Arctic Ocean: Implications for Sea Ice Freeboard Retrieval, *J. Geophys. Res.-Oceans*, 122, 8593–8613, <https://doi.org/10.1002/2017JC013176>, 2017.
- Smedsrud, L. H., Halvorsen, M. H., Stroeve, J. C., Zhang, R., and Kloster, K.: Fram Strait sea ice export variability and September Arctic sea ice extent over the last 80 years, *The Cryosphere*, 11, 65–79, <https://doi.org/10.5194/tc-11-65-2017>, 2017.
- Stade, E.: *Fourier Analysis*, John Wiley & Sons, Inc., Hoboken, New Jersey, <https://doi.org/10.1002/9781118165508>, 2005.
- Stammer, D., Ray, R. D., Andersen, O. B., Arbic, B. K., Bosch, W., Carrère, L., Cheng, Y., Chinn, D. S., Dushaw, B. D., Egbert, G. D., Erofeeva, S. Y., Fok, H. S., Green, J. A. M., Griffiths, S., King, M. A., Lapin, V., Lemoine, F. G., Luthcke, S. B., Lyard, F., Morison, J., Müller, M., Padman, L., Richman, J. G., Shriver, J. F., Shum, C. K., Taguchi, E., and Yi, Y.: Accuracy assessment of global barotropic ocean tide models, *Rev. Geophys.*, 52, 243–282, <https://doi.org/10.1002/2014RG000450>, 2014.
- Steele, M., Morley, R., and Ermold, W.: PHC: a global ocean hydrography with a high-quality Arctic Ocean, *J. Climate*, 14, 2079–2087, [https://doi.org/10.1175/1520-0442\(2001\)014<2079:PAGOHW>2.0.CO;2](https://doi.org/10.1175/1520-0442(2001)014<2079:PAGOHW>2.0.CO;2), 2001.
- Thomson, R. E. and Emery, W. J.: *Data Analysis Methods in Physical Oceanography*, Elsevier Science, 3 Edn., <https://doi.org/10.1016/b978-0-444-50756-3.x5000-x>, 2014.
- Vignudelli, S., Kostianoy, A. G., Cipollini, P., and Benveniste, J. (Eds.): *Coastal Altimetry*, Springer Berlin Heidelberg, <https://doi.org/10.1007/978-3-642-12796-0>, 2011.
- Volkov, D. L. and Pujol, M.: Quality assessment of a satellite altimetry data product in the Nordic, Barents, and Kara seas, *J. Geophys. Res.-Oceans*, 117, C3, <https://doi.org/10.1029/2011JC007557>, 2012.
- von Appen, W.-J., Schauer, U., Hattermann, T., and Beszczynska-Möller, A.: Seasonal Cycle of Mesoscale Instability of the West Spitsbergen Current, *J. Phys. Oceanogr.*, 46, 1231–1254, <https://doi.org/10.1175/JPO-D-15-0184.1>, 2016.
- Wahr, J. M.: Deformation induced by polar motion, *J. Geophys. Res.-Solid Earth*, 90, 9363–9368, <https://doi.org/10.1029/JB090iB11p09363>, 1985.
- Wang, Q., Danilov, S., Sidorenko, D., Timmermann, R., Wekerle, C., Wang, X., Jung, T., and Schröter, J.: The Finite Element Sea Ice-Ocean Model (FESOM) v.1.4: formulation of an ocean general circulation model, *Geosci. Model Dev.*, 7, 663–693, <https://doi.org/10.5194/gmd-7-663-2014>, 2014.
- Wekerle, C., Wang, Q., von Appen, W.-J., Danilov, S., Schourup-Kristensen, V., and Jung, T.: Eddy-Resolving Simulation of the Atlantic Water Circulation in the Fram Strait With Focus on the Seasonal Cycle, *J. Geophys. Res.-Oceans*, 122, 8385–8405, <https://doi.org/10.1002/2017JC012974>, 2017.
- Zakharova, E. A., Fleury, S., Guerreiro, K., Willmes, S., Rémy, F., Kouraev, A. V., and Heinemann, G.: Sea Ice Leads Detection Using SARAL/AltiKa Altimeter, *Mar. Geodesy*, 38, 522–533, <https://doi.org/10.1080/01490419.2015.1019655>, 2015.
- Zhang, Y. and Baptista, A.: SELFE: A semi-implicit Eulerian-Lagrangian finite-element model for cross-scale ocean circulation, *Ocean Modell.*, 21, 71–96, <https://doi.org/10.1016/j.ocemod.2007.11.005>, 2008.
- Zygmuntowska, M., Khvorostovsky, K., Helm, V., and Sandven, S.: Waveform classification of airborne synthetic aperture radar altimeter over Arctic sea ice, *The Cryosphere*, 7, 1315–1324, <https://doi.org/10.5194/tc-7-1315-2013>, 2013.

P-3 Geostrophic currents in the northern nordic seas from a combination of multi-mission satellite altimetry and ocean modeling

Müller, F. L., Dettmering, D., Wekerle, C., Schwatke, C., Passaro, M., Bosch, W., and Seitz, F. (2019a). Geostrophic currents in the northern nordic seas from a combination of multi-mission satellite altimetry and ocean modeling. *Earth System Science Data*, 11(4):1765–1781, DOI: 10.5194/essd-11-1765-2019

Copyright

The publication was published in Earth System Science Data, which is an interactive open-access journal, distributed by Copernicus Publications. All accepted articles are published under the terms and conditions of the Creative Commons Attribution License (<http://creativecommons.org/licenses/by/4.0/>). The copyright remains with the author.

Summary

The publication focuses on a novel combination methodology to combine altimetry-derived dynamic ocean topography (DOT) elevations with modeled water heights of an ocean model in order to provide a comprehensive description of the temporal evolution of geostrophic surface currents in a region, which is affected by sea ice and rapidly changing sea state leading to challenging observation conditions. The model data, provided by FESOM, is used to bridge data gaps of altimetry, caused for example by sea ice, to obtain a homogeneous representation of the DOT, which enables consistent and spatiotemporal highly resolved studies of the ocean surface circulation. The combination was performed in the northern Nordic Seas covering the observations period of the ESA missions, ERS-2 and Envisat between 1995 - 2012.

In particular, the methodology focuses on the combination of along-track altimetry-derived DOT observations and simulated differential water heights, which are very similar to the DOT. Central element of the combination of the total conceptually different datasets is the application of a Principal Component Analysis. After reducing both datasets by their mean and annual signal, the most dominant spatial patterns of the modeled water heights, as obtained from the PCA, are connected with the temporal variability of the altimetry-derived DOT in order to estimate combined principal components. In a next step, the principal components are multiplied by the corresponding spatial signals and summed up to complete the synthesis. In a last step, the reduced mean and annual signal from the observed database is readded to reference the combined dataset to the altimetry height level. The geostrophic components are obtained by applying the geostrophic equations to the combined DOT. The final combined dataset is provided on daily unstructured triangular meshes, displaying the spatial resolution equally to FESOM.

The final combination results are validated by external DOT products revealing a positive correlation of about 80%, but showing a temporal variability of the combined dataset. Furthermore, the combined geostrophic current components are compared to independent sea surface drifter observations, after reducing them by wind-driven current components. The comparison shows good agreement in spatial patterns, magnitude and current direction. In addition, a direct pointwise comparison by interpolating the combined velocity components onto the drifter locations and observation time reveals that 94% of the residuals are smaller than 0.15 m/s.

Since model information and altimetry observations are available, the methodology can be easily transferred to all polar regions on Earth. The combined dataset is made publicly available via PANGAEA following the link <https://doi.pangaea.de/10.1594/PANGAEA.900691> (Müller et al. (2019)).

Contribution

As stated in P-3: Felix L. Müller processed the combination and wrote most of the paper. Denise Dettmering supervised the present study, contributed to the manuscript writing and helped with discussions of the results. Claudia Wekerle provided the FESOM data and contributed to the manuscript writing. Christian Schwatke maintains the altimetry data base (OpenADB) at DGFITUM and supports with discussions. Marcello Passaro developed the retracking algorithm and helped with discussions concerning the altimetry dataset. Wolfgang Bosch initiated the study. Florian Seitz supervised the research. The overall contribution of Felix L. Müller is estimated to be **88%**.



Geostrophic currents in the northern Nordic Seas from a combination of multi-mission satellite altimetry and ocean modeling

Felix L. Müller¹, Denise Dettmering¹, Claudia Wekerle², Christian Schwatke¹, Marcello Passaro¹, Wolfgang Bosch¹, and Florian Seitz¹

¹Deutsches Geodätisches Forschungsinstitut, Technische Universität München, Arcisstraße 21, 80333 Munich, Germany

²Climate Dynamics, Alfred Wegener Institute, Helmholtz Centre for Polar and Marine Research, Bussestraße 24, 27570 Bremerhaven, Germany

Correspondence: Felix L. Müller (felix-lucian.mueller@tum.de)

Received: 14 June 2019 – Discussion started: 26 June 2019

Revised: 15 October 2019 – Accepted: 23 October 2019 – Published: 26 November 2019

Abstract. A deeper knowledge about geostrophic ocean surface currents in the northern Nordic Seas supports the understanding of ocean dynamics in an area affected by sea ice and rapidly changing environmental conditions. Monitoring these areas by satellite altimetry results in a fragmented and irregularly distributed data sampling and prevents the computation of homogeneous and highly resolved spatio-temporal datasets. In order to overcome this problem, an ocean model is used to fill in data when altimetry observations are missing.

The present study provides a novel dataset based on a combination of along-track satellite-altimetry-derived dynamic ocean topography (DOT) elevations and simulated differential water heights (DWHs) from the Finite Element Sea ice Ocean Model (FESOM) version 1.4. This innovative dataset differs from classical assimilation methods because it substitutes altimetry data with the model output when altimetry fails or is not available.

The combination approach is mainly based on a principal component analysis (PCA) after reducing both quantities by their constant and seasonal signals. In the main step, the most-dominant spatial patterns of the modeled differential water heights as provided by the PCA are linked with the temporal variability in the estimated DOT from altimetry by performing a principal component synthesis (PCS). After the combination, the annual signal obtained by altimetry and a constant offset are re-added in order to reference the final data product to the altimetry height level. Surface currents are computed by applying the geostrophic flow equations to the combined topography. The resulting final product is characterized by the spatial resolution of the ocean model around 1 km and the temporal variability in the altimetry along-track derived DOT heights.

The combined DOT is compared to an independent DOT product, resulting in a positive correlation of about 80 %, to provide more detailed information about short periodic and finer spatial structures. The derived geostrophic velocity components are evaluated by in situ surface drifter observations. Summarizing all drifter observations in equally sized bins and comparing the velocity components shows good agreement in spatial patterns, magnitude and flow direction. Mean differences of 0.004 m s^{-1} in the zonal and 0.02 m s^{-1} in the meridional component are observed. A direct pointwise comparison between the combined geostrophic velocity components interpolated onto the drifter locations indicates that about 94 % of all residuals are smaller than 0.15 m s^{-1} .

The dataset is able to provide surface circulation information within the sea ice area and can be used to support a deeper comprehension of ocean currents in the northern Nordic Seas affected by rapid environmental changes in the 1995–2012 time period. The data are available at <https://doi.org/10.1594/PANGAEA.900691> (Müller et al., 2019).

1 Introduction

Water mass flowing northward and southward through the Greenland Sea and Fram Strait represents the major pathways of the bidirectional water exchange between the Arctic Ocean and the global conveyor belt. Most of the water mass is transported via the northward-flowing West Spitsbergen Current (WSC) and the southward-flowing East Greenland Current (EGC). More than 60 % of the total water transport is based on geostrophic movements, caused for example by water density and sea level elevation variations (Rudels, 2012).

Geostrophic currents (GCs) can be directly derived from measurements of the dynamic ocean topography (DOT) with respect to the Earth's gravity field and rotation and the Coriolis force involved. In contrast to hydrographic pressure, temperature and salinity observations, collected by irregularly distributed in situ data (e.g., ARGO floats or ship-based measurements), satellite altimetry is the only possibility for obtaining spatially and temporally homogeneous information about the global geostrophic circulation. In situ sampling platforms can deliver high-resolution measurements, but in polar regions their availability is limited due to sparse spatial coverage and challenging environmental conditions. However, especially in sea ice areas, even geostrophic ocean currents derived by altimetry suffer from irregular sampling and data gaps. Furthermore, the generation of a dataset requires some sort of interpolation or gridding techniques, which cause smoothing effects and a coarser spatio-temporal resolution. Moreover, in open-ocean regions, beyond the sea ice edge, the spatial coverage of altimetry data is sparse due to the along-track acquisition geometry with constant and fixed orbit patterns. Hence, studies are limited to long-term means (e.g. Farrell et al., 2012) or to satellite altimetry missions dedicated to sea ice conditions (e.g., CryoSat-2; Kwok and Morison, 2015, and ICESat; Kwok and Morison, 2011). Nevertheless, monthly DOT estimates have been generated and published by Armitage et al. (2016) using DOT observations derived from long-term satellite altimetry. Furthermore, Armitage et al. (2017) presented a dataset based on a 12-year altimetry observation (from 2003 to 2014) of geostrophic currents at a monthly time frame on a $0.75^\circ \times 0.25^\circ$ longitude–latitude regular data grid up to a latitudinal limit of 81.5° N. The authors created a dataset which combines satellite-altimetry observations from ice-covered and open-ocean regions. Further publicly available geostrophic ocean current products based on observational data from satellite altimetry only and in combination with in situ buoys (e.g. Rio et al., 2014) are provided, for example, by the GlobCurrent project and by the Copernicus Marine Environment Monitoring Service (CMEMS). However, the latter's datasets are limited to open-ocean conditions.

Besides observation-based ocean circulation products, model simulations provide information about the ocean dynamics. In general, their resolution is much better than these of observations; however, they rely on the underlying mathematical or physical formulations, which naturally contain simplifications and suffer from deficiencies in process descriptions. Ocean models differ in spatio-temporal resolutions, forcing the model background and underlying mathematical formulations. Recent developments focus on so-called unstructured ocean models, allowing for locally highly refined spatial resolutions (Danilov, 2013), while keeping a coarser resolution in other regions of the Earth (e.g., Finite Element Sea ice Ocean Model in Wang et al., 2014, or Model for Prediction Across Scales, Ocean model – MPAS-Ocean – in Ringler et al., 2013). One of the unstructured models is the Finite Element Sea ice Ocean Model version 1.4 (FESOMv1.4) described by Wang et al. (2014). In the following text, FESOMv1.4 is abbreviated by FESOM.

For the northern Nordic Seas, an eddy-resolving configuration has been developed, enabling the simulation of small-scale eddies down to 1 km (Wekerle et al., 2017). Besides total ocean current velocities including wind-driven and geostrophic components, FESOM includes sea surface heights with respect to the bottom ocean topography, which can be also seen as an estimation of the dynamic ocean topography. Applying the gradient to these differential water elevations leads to the computation of simulated geostrophic currents. In contrast to observational based data, models show consistent spatio-temporal resolutions and enable investigations of ocean surface currents under the sea ice layer. However, they are limited to a fixed defined mathematical background and function as an assumption of the reality.

The current publication aims to present an innovative combined data product based on the advantages of both simulated and observed datasets. In contrast to other commonly used datasets or assimilation methods, the introduced product is mainly focused on the observational side by filling in modeled DOT elevations where altimetry data are missing or corrupted. Several investigations and consistency checks have been made by Müller et al. (2019), concluding with good agreement of simulated and observed DOT in terms of the most-dominant seasonal signals and spatial patterns aiming at a combination of the temporal variability provided by altimetry along-track derived DOT elevations with simulated spatio-temporally homogeneous DOT heights of the model. The combined dataset obtained is characterized by the spatially homogeneous resolution of the model and the temporal variability in altimetry-derived DOT elevations. This enables further studies of geostrophic surface currents in sea ice regions consistent in space and time and may help to deepen the knowledge about polar ocean current dynamics.

The dataset is based on a combination of multi-mission satellite-altimetry data from the ESA mission Envisat as

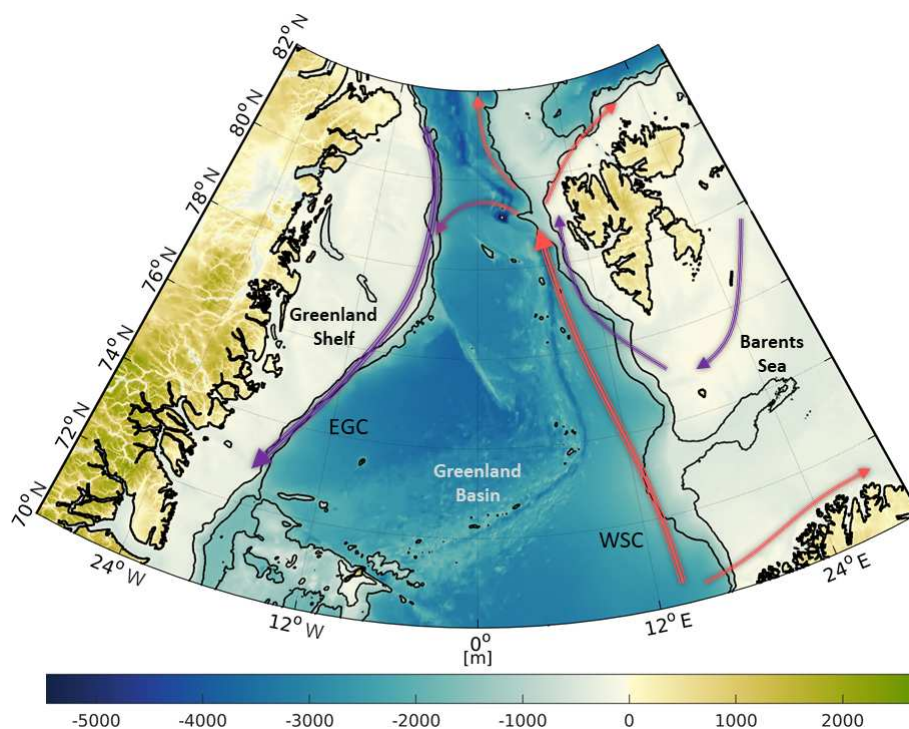


Figure 1. Bathymetry of the study area (northern Nordic Seas and Fram Strait) based on RTopo2 topography model (Schaffer et al., 2016). Major current systems (West Spitsbergen Current – WSC; East Greenland Current – EGC) are displayed by arrows in red (inflowing Atlantic water) and blue (returning polar water). Contour lines indicate depths of -450 and -1500 m.

well as ERS-2 and the eddy-resolving model, FESOM version 1.4 (Wang et al., 2014), covering a period of about 17 years. The combination approach is based on the commonly known principal component analysis (e.g. Jolliffe, 2002; Preisendorfer, 1988), which is successfully applied in historic sea level analyses and reconstruction investigations (e.g. Ray and Douglas, 2011; Church et al., 2004).

The study area covers the Fram Strait region, the Greenland Sea and parts of the Norwegian Sea as well as the Barents Sea (Fig. 1). The different regions are summarized by northern Nordic Seas. In geographical coordinates the investigation area is limited to 72 to 82° N and -30° W to 30° E.

The paper is structured in four sections. First, the datasets and combination method are introduced, followed by the results. Furthermore, the combination's reliability is evaluated by comparing the obtained datasets with in situ drifter velocities and independent satellite-derived DOT products. The study closes with a summary and concluding remarks of the most significant aspects.

2 Data

2.1 Observations: radar altimetry data

The observational part of the combination is provided by high-frequency along-track satellite-derived dynamic ocean topography data of the ESA satellites ERS-2 and Envisat.

The missions cover a period of about 17 years (May 1995–April 2012) up to a latitudinal limit of 81.5° N. The data pre-processing of ERS-2 and Envisat-observed ranges to derived DOT heights follows the descriptions of Müller et al. (2019). Altimetry ranges are retracked by ALES+ (Passaro et al., 2018), and open water and sea ice are discriminated by applying the method of Müller et al. (2017). The obtained sea surface heights are reduced to DOT estimates by subtracting the highly resolved Optimal Geoid Model for Modeling Ocean Circulation (OGMOC), developed up to a harmonic degree of 2190 (Gruber and Willberg, 2019). ALES+ has been chosen as an optimal retracking algorithm due to the ability for a consistent range estimation independent of the backscattering surface (open-ocean, lead and polynya). Coarse outliers are excluded from the dataset by filtering the sea surface heights on the basis of sea level anomalies (i.e., sea surface heights minus a mean sea surface) before transforming them into physical DOT heights. A time mean inter-mission offset is removed by taking the Envisat time series as a reference within a 6-month overlap period (January 2003–June 2003), considering only height observations from ice-free regions in the southern part of the investigation area. Before introducing the altimetry DOT elevations to the further processing steps, the ellipsoid referenced observation coordinates are transformed to consider the spherical Earth representation of the model.

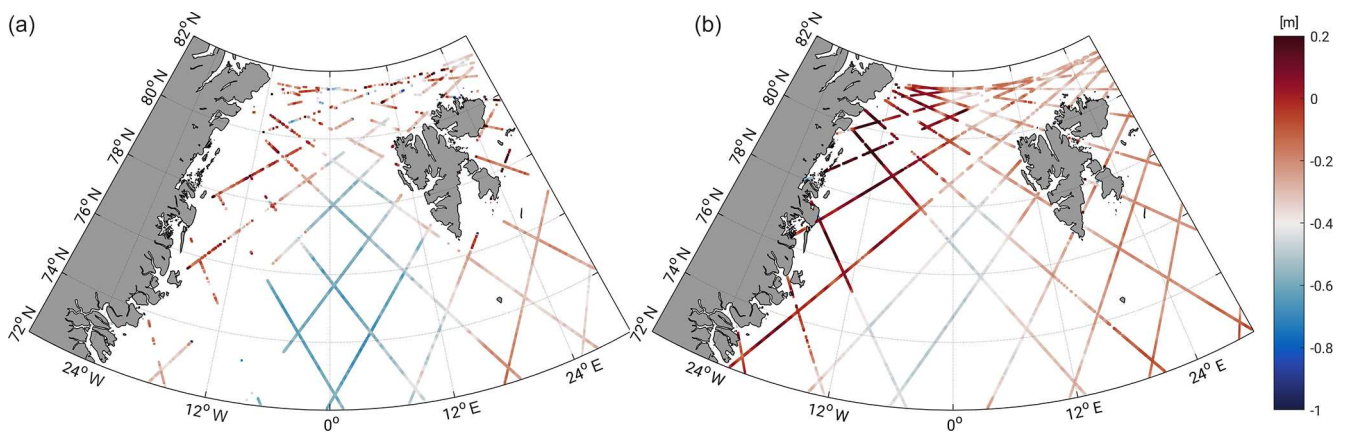


Figure 2. Exemplary pre-processed altimetry along-track DOT estimates for Envisat 3 d subcycle in March 2004 (a) and July 2006 (b), illustrating season-dependent data coverage.

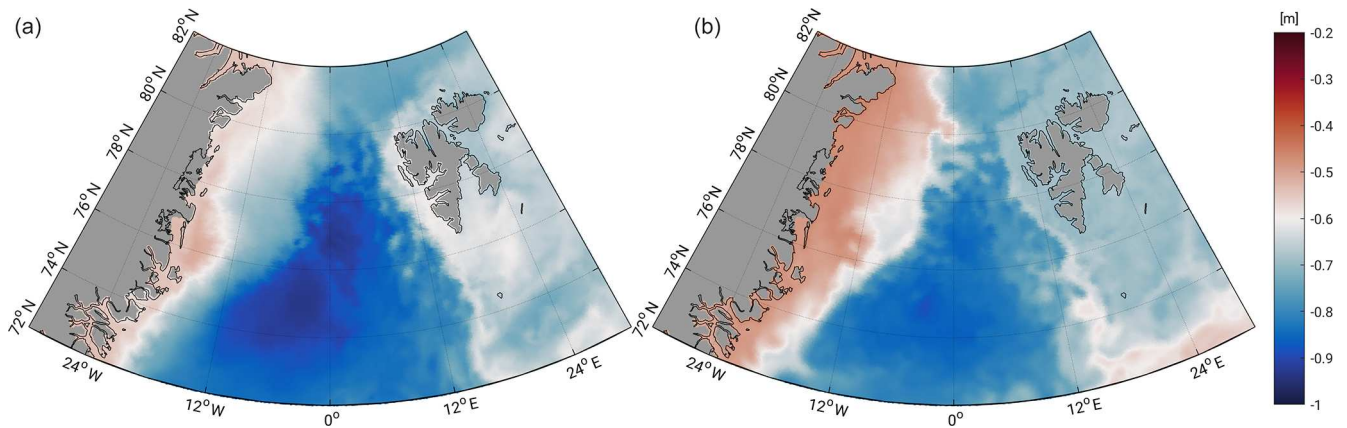


Figure 3. Exemplary differential water heights in March 2004 (a) and July 2006 (b) simulated by FESOM. Note the different scaling of color bars in comparison to Fig. 2.

Figure 2 shows, as an example, 3 d of altimetry data during the winter (March 2004) and summer (July 2006) season. In the winter, big data gaps can be noticed close to the eastern Greenland coast due to the presence of sea ice in contrast to summer, when most of the data are available.

2.2 Simulation: Finite Element Sea ice Ocean Model (FESOM)

The second part of the combination consists of simulated differential water heights (DWHs; e.g., Fig. 3) with respect to the ocean bottom topography (i.e., bathymetry). The bathymetry acts as geopotential surface, which enables a linkage to the altimetry-derived DOT heights (Androsov et al., 2018). FESOM is a global multi-resolution ocean circulation model with an included sea ice component resolving the major sea ice drift patterns. The model is based on the standard set of hydrostatic primitive equations in the Boussinesq approximation and is characterized by an unstructured triangular mesh with 47 vertical levels (Wang

et al., 2014). The horizontal resolution in the configuration used in this study reaches up to 1 km in the Fram Strait and northern Greenland Sea area and can be described as “eddy-resolving”. Furthermore, the geographical model coordinates are referenced to a spherical Earth representation with a radius of 6367.50 km. More details of the FESOM configuration can be found in Wekerle et al. (2017). The present study uses only daily DWHs of the surface level covering the period 2002–2009.

2.3 Comparative datasets

For validation a comparison with externally generated absolute dynamic topography (ADT) elevations, from ADT-derived geostrophic velocity components and to geostrophic ocean velocity that reduced in situ drifter observations, is performed. The ADT data including geostrophic velocity components (Pujol and Mertz, 2019), provided by CMEMS, are characterized by a daily and $1/4^\circ$ spatial resolution and are based on multi-mission altimetry data. The ADT grids are

created by adding temporally variable sea level anomalies to a mean dynamic topography and cover the complete time period of the developed datasets. However, no ADT and current data are available in sea ice areas, which limits the comparison to ice-free regions and seasons.

Further interpolated surface drifter trajectories from CMEMS (Rio and Etienne, 2018) with a 6 h interval are used. Following the pre-processing steps of the drifting buoys, described by Rio and Etienne (2018), all surface drifters are analyzed concerning their drogue status and local wind slippage corrections. Besides geostrophic velocities, drifter observations include ageostrophic movements (e.g., Ekman currents, Stokes drift, inertial oscillations, local wind effects, etc.). Hence, the drifter data must be corrected in order to enable a comparison with satellite-altimetry-derived and simulated derived geostrophic currents. Local wind corrections, also provided by CMEMS (Rio and Etienne, 2018), are directly subtracted from the drifter velocities, considering the drogue status. The Ekman current is taken from global grids providing velocities at 15 m depth (drogue on) and at the surface (drogue off) level. The computation of the Ekman fields follows the explanations and processing scheme of Rio and Hernandez (2003) and Rio et al. (2014). The 3-hourly available Ekman grids are downloaded from the GlobCurrent data repository and have a spatial resolution of $1/4^\circ$ and global coverage. However, grid nodes north of 78.875° N are not defined, which limits the comparison to central parts of the Greenland Sea and neglects the Fram Strait area. The Ekman velocities are interpolated to the drifter positions and subtracted from the drifting buoys velocity by taking the drogue status into account. The Stokes drift is provided globally (Raschle and Arduin, 2013, distributed by GlobCurrent) and applied only to undrogued surface drifter data in the same way as the Ekman fields (Rio et al., 2014). Following the suggestions of Andersson et al. (2011), the Ekman–Stokes-drift-reduced drifter velocities are low-pass filtered by a 25 h cutoff, two-point Butterworth filter to remove tidal and inertial oscillations. Furthermore, drifters showing observations with time gaps of more than 1 d are filtered separately (Andersson et al., 2011).

Most of the drifter buoy observations are collected in ice-free regions affected by currents (see Fig. A1). Analyzing the geostrophic amplitudes and phases, the major pathway and stream velocity of the West Spitsbergen Current is clearly identified, in contrast to the East Greenland Current, which is mostly covered by sea ice. Due to high variability, most of the drifter data can be found in the West Spitsbergen region and in the southern parts, where Atlantic water enters the Greenland Sea. Most of the drifting buoys are carried through the Fram Strait or enter the Barents Sea. Only a few drifter buoys turn around and follow the East Greenland Current. Furthermore, smaller eddies in the central Greenland Sea can be observed. In this study, nearly 70 000 in situ observations are available, of which 63 % are characterized by a drogue-on status. The number of drifter measurements

strongly increases between 2007 and 2012. However, hardly any data can be used between 2000 and 2006. Nevertheless, a validation of the ERS-2 data products is possible between 1995 and 2000.

3 Method

In order to generate a combined spatio-temporally consistent dataset based on irregular distributed altimetry observations, it is necessary to connect the along-track derived DOT estimates with a spatially consistent modeled DOT representation to fill the observation gaps. The following section describes briefly the combination of along-track DOT heights with the modeled water level, while keeping the spatial height reference of the altimetry observations.

The combination is mainly based on a principal component analysis (PCA) transferring the method of historic sea level reconstruction (e.g. Church et al., 2004; Ray and Douglas, 2011) to the present purpose. Altimetry observed along-track DOT heights represent the temporal DOT variability, whereas the spatial signal is provided by FESOM. Figure 4 highlights the interrelationship of the datasets and gives an overview over the main processing chain. The individual work steps are described chronologically. The output of the processing steps are combined geostrophic currents (cGCs) and dynamic ocean topography (cDOT) data representing the temporal variability in the altimetry measurements and the spatial homogeneity of the ocean model.

3.1 Data pre-processing

The input of the data production chain is along-track DOT elevations and daily simulated finite-element-formulated DWHs. In order to establish an equal combination basis, both datasets are treated equally. First, they are reduced by their time mean offsets and the most-dominant seasonal (i.e., annual) signal (Müller et al., 2019).

In a second step, the reduced FESOM grids are introduced to a PCA in order to decompose them in a linearly uncorrelated, temporal part (i.e. principal components) describing the temporal evolution and in empirical orthogonal functions (EOFs) identifying the most-dominant spatial structures of the time series. They are sorted in a decreasing order with respect to their contribution to the total signal variance. In order to reconstruct the original signal, the principal components and the corresponding EOFs have to be multiplied and summed up. The product of one combination pair is called a mode. This inverse process of PCA is also called principal component synthesis (PCS). PCS is not necessarily always used to reconstruct the full signal; however the approach can be also limited to a certain number of retaining modes, representing a significant percentage of the total signal. Mathematical and functional relations are explained in Jolliffe (2002). In order to determine the number of the most significant EOFs, the root-mean-square error (RMSE)

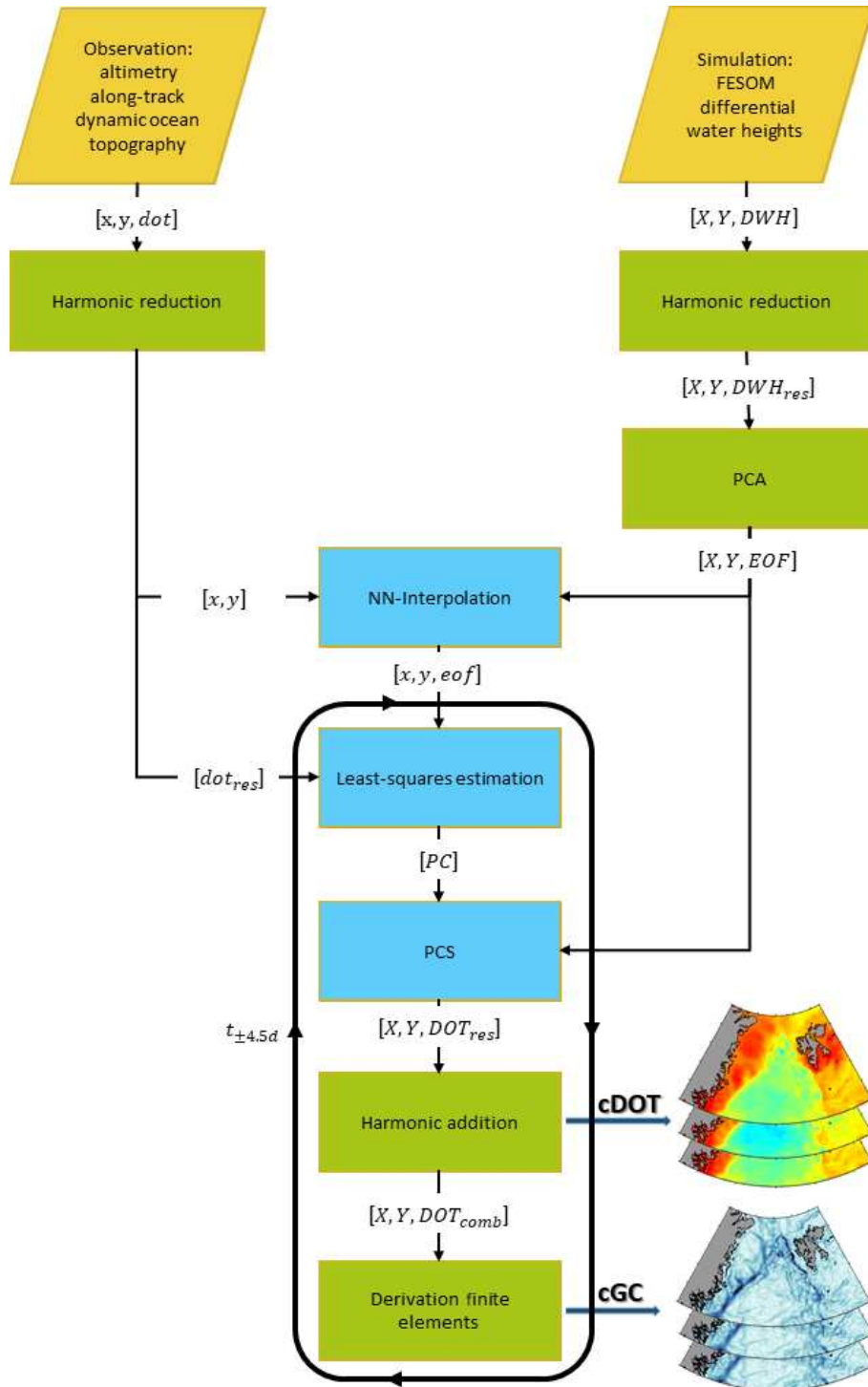


Figure 4. Main processing chain for the generation of combined ocean topography (cDOT) and geostrophic currents (cGCs) showing the main processing steps, i.e., the combination (in light blue) and auxiliary steps (in green). The necessary input data are highlighted in orange. Upper-case coordinates (X, Y) are grid coordinates, whereas lower-case coordinates (x, y) are on the satellites’ tracks. The same holds for the datasets: data labeled in capital letters are given as a grid, and lower-case letters represent along-track quantities. The “comb” index stands for combined products, and “res” is residual products, reduced by annual signal and constant offset. For dataset abbreviations, see the main text.

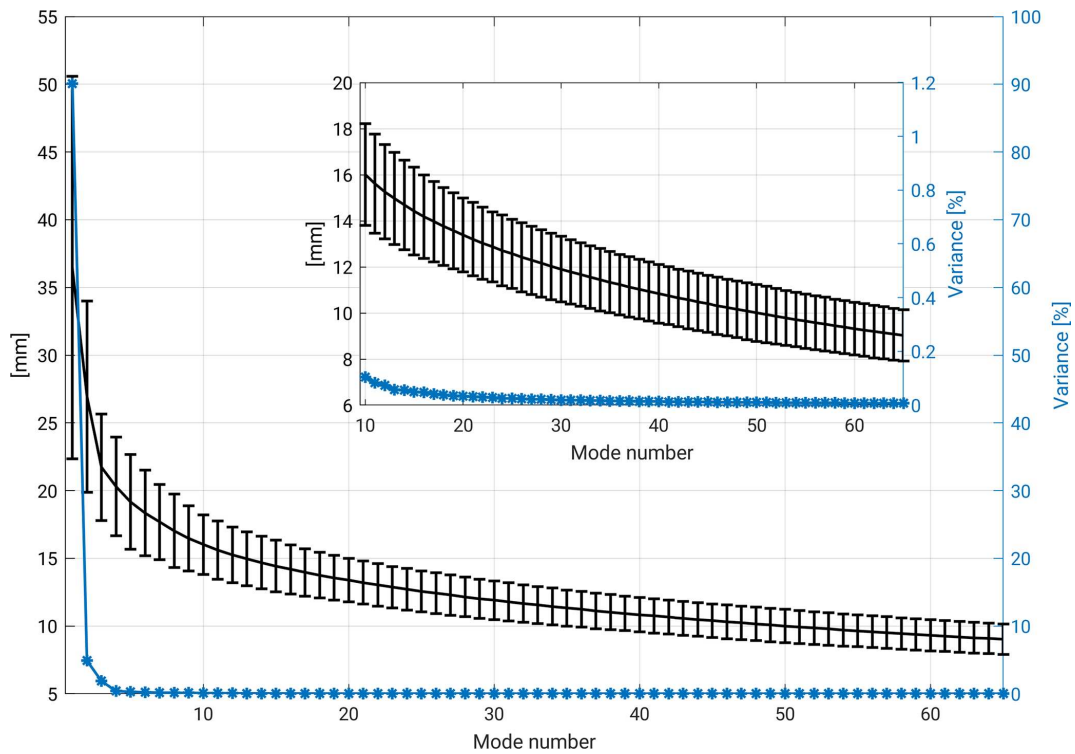


Figure 5. Percentage of variance (blue) and daily averaged root-mean-square error (black) including standard deviation of FESOM original data and reconstructed signal for 65 modes of principal component synthesis. For better overview, modes 10–65 are zoomed in.

is computed for comparing the original FESOM DWH and the reconstructed signal. The RMSE is computed by (Barnston, 1992)

$$\text{RMSE}(t) = \sqrt{\overline{(l_t - r_t)^2}}, \quad (1)$$

where l substitutes the original FESOM DWH and r the reconstructed grids of the day t , where the overbar is computed over all grid nodes. Figure 5 shows the evolution of the temporal amount of variance and the temporally averaged RMSE with respect to the individual number of modes. It is decided to use a RMSE threshold of 10 mm, corresponding to 50 modes and a summed variance of more than 99%. In the following processing steps, only the spatial signals (i.e., EOFs) of FESOM are used. In contrast, the principal components, describing the temporal evolution of the different modes, are neglected.

3.2 Combination

The combination step links the pre-processed along-track DOT heights with the most significant spatial pattern obtained from the PCA of the FESOM differential water heights. The processing is based on daily temporal resolution, including 9 d of radar altimetry data for each time step. The time steps are referred to the mean of a 9 d time span (i.e., $t_{\pm 4.5 \text{ d}}$). The combined DOT heights (cDOTs) can be

represented by a linear combination of n combined estimated principal components and the obtained EOF grids from FESOM. The functional relation of the PCS is described in Eq. (2):

$$\text{cDOT}_{\text{res}}(X, Y, t) = \sum_{i=1}^n \text{PC}_i(t) \cdot \text{EOF}_i(X, Y), \quad (2)$$

where n corresponds to the number of significant principal components and empirical orthogonal functions. PC_i substitutes the n unknown combined principal components and $\text{EOF}_i(X, Y)$ the n most-dominant spatial pattern on the FESOM grid (see Sect. 3.1).

The principal components (PC_i) are estimated by fitting the model EOFs to the altimetry-derived DOT elevations dot_{res} . Therefore, the EOF grids are interpolated to the observation coordinates based on nearest-neighbor interpolation (NN-Interpolation), resulting in along-track sampled empirical orthogonal functions ($\text{eof}_i(x, y)$). The solution for PC_i is then given by applying the least-squares method (e.g. Koch, 1999) to Eq. (3):

$$\text{dot}_{\text{res}}(x, y, t_{\pm 4.5 \text{ d}}) = \sum_{i=1}^n \text{PC}_i(t) \cdot \text{eof}_i(x, y), \quad (3)$$

where $\text{dot}_{\text{res}}(x, y, t_{\pm 4.5 \text{ d}})$ includes all altimetry-derived DOT heights within $\pm 4.5 \text{ d}$ and $\text{eof}_i(x, y)$ the corresponding

along-track interpolated modeled EOFs. The result are n time series of combined principal components.

Furthermore, Gaussian weighting, which considers uncertainties in the altimetry DOT heights due to the presence of sea ice, is introduced to the least-squares process. The individual weights are defined by using an external sea ice concentration from the National Snow and Ice Data Center (NSIDC; Fetterer et al., 2017) interpolated via nearest-neighbor interpolation to the observation coordinates considering an enhanced error budget of altimetry range estimations due to noisier observations within the sea ice area. In a last step, the estimated principal components are introduced to the PCS (Eq. 2) in order to construct a combined DOT solution ($\text{cDOT}_{\text{res}}(X, Y, t)$). The individual combination steps are outlined in Fig. 6 and are briefly summarized in chronological order as follows:

1. Separation of reduced FESOM DWH into most-dominant spatial patterns (EOF) and time series of principal components applying PCA. However, the principal components obtained are not used but neglected, since new principal components are estimated from altimetry-derived DOT and most-dominant spatial patterns (EOF) of FESOM in the further combination steps.
2. Nearest-neighbor interpolation of EOF to altimetry along-track observations (x, y) obtaining profiled eof.
3. Least-squares estimation of combined principal components (PC_i) by solving Eq. (3) based on altimetry DOT observations (dot_{res}) and interpolated eof.
4. Application of Eq. (2) to obtain the combined DOT (cDOT_{res}) dataset in the FESOM grid (X, Y) based on PC_i (step 3) and EOF (step 1). Furthermore, an outlier detection based on an accuracy determination of the combined principal components is performed to reject erroneous combination estimations.

3.3 Data generation

In order to reconstruct the full signal and to rescale the combined heights to the altimetry height reference, the previous subtracted altimetry time mean offset and annual signal are re-added (Sect. 3.1). In the next step, combined geostrophic currents (cGCs) are obtained by computing the zonal (u_g) and meridional (v_g) geostrophic velocity components at the surface, given by Eq. (4):

$$\begin{aligned} u_g &= -\frac{g}{f} \frac{\partial h}{\partial y}, \\ v_g &= \frac{g}{f} \frac{\partial h}{\partial x}, \end{aligned} \quad (4)$$

where g is the acceleration of gravity (9.832 m s^{-2}), $f = 2\Omega \sin \phi$ the Coriolis force, ϕ the latitude and Ω the Earth's

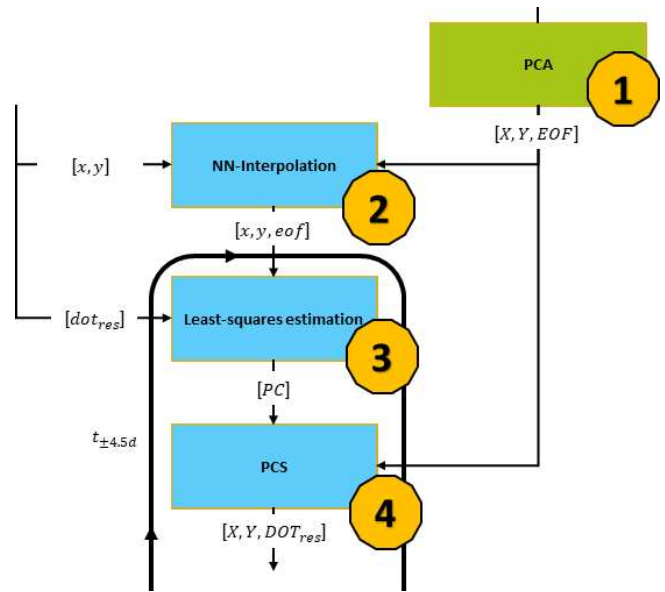


Figure 6. Subset of Fig. 4, outlining combination steps. Numbers indicate the chronological order of the individual processing steps.

rotation rate. ∂h denotes the horizontal gradient in x and y direction of cDOT height h . The derivatives $\frac{\partial h}{\partial y}$ and $\frac{\partial h}{\partial x}$ are solved based on the finite-element method (see Appendix B), which prevents further smoothing effects, since no re-gridding to a regular grid is necessary. Furthermore, the geostrophic absolute velocity (A_g), phase ϕ_g and eddy kinetic energy (EKE) can be computed by applying Eq. (5):

$$A_g = \sqrt{u_g^2 + v_g^2} \quad \phi_g = \arctan \frac{v_g}{u_g}, \quad (5)$$

$$\text{EKE} = \frac{1}{2} ((u_g(t) - \overline{u_g})^2 + (v_g(t) - \overline{v_g})^2),$$

where t substitutes the velocity at a certain time and the overbar indicates the mean velocity for a defined time period (e.g., quarterly).

4 Datasets

The combined DOT and geostrophic current velocity fields are based on DOT heights derived from satellite-altimetry and simulated differential water heights from FESOM (Müller et al., 2019). The dataset spans a time period from mid-May 1995 to early April 2012 and covers the investigation area of the northern Nordic Seas limited to $72\text{--}82^\circ \text{ N}$ and $-30^\circ \text{ W--}30^\circ \text{ E}$. The dataset is saved in NetCDF format. As a result of the combination process, the processed grids are stored in daily temporal and unstructured spatial resolution with local refinements up to 1 km. Missing days in the dataset due to longer periods of missing altimetry observations and unreliable combined principal components are possible. The data product is given in units of meters in the case of DOT and in meters per second for the geostrophic components.

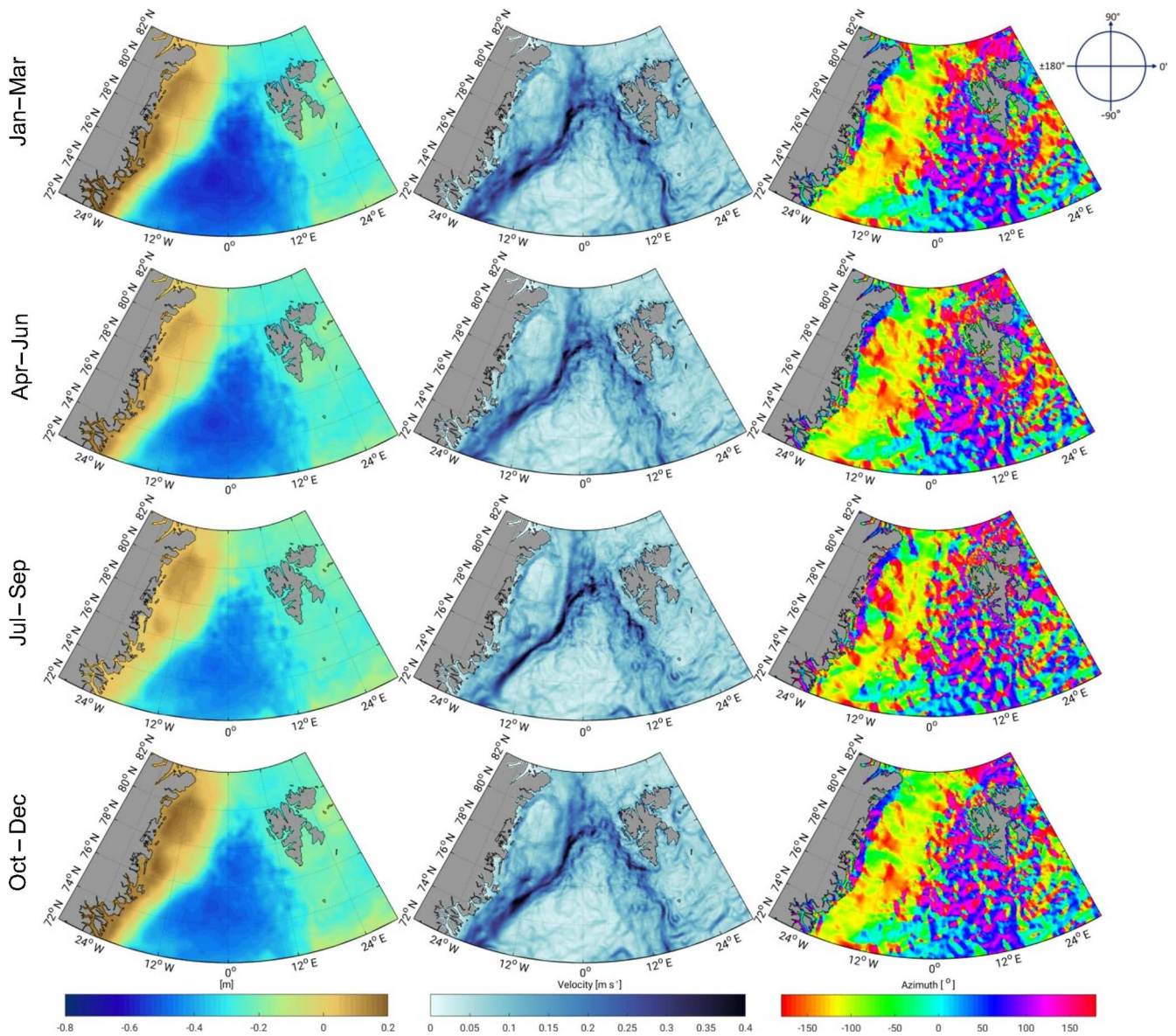


Figure 7. Three-monthly averaged combined DOT heights (left), absolute geostrophic velocities (middle) and flow direction (right) from 1995 to 2012.

Figure 7 illustrates quarterly averaged daily combined DOT heights and derived geostrophic components expressed in velocity and azimuth. All meshes show the same spatial resolution with local refinements in the central Greenland Sea and Fram Strait region (approx. 1 km) and suggest the finite-element structure of the input model. The 3-monthly averaged cDOT fields vary by circa 1 m across the northern Nordic Seas, with maximum variations in the winter months. Furthermore, the anti-phase relationship in the annual oscillation (Bulczak et al., 2015) between the deep basins and the shelf areas in winter and summer can be seen. The derived geostrophic components show a strong meander-

ing West Spitsbergen Current and a more clear flow structure in the East Greenland Current.

5 Comparison with external datasets

The produced datasets are compared to independent datasets providing daily sampled DOT heights and observations of surface drifter buoys. However, it must be noted that the comparison is challenging, since no dataset can be used as ground truth in the whole study area.

In order to follow a comparison with in situ observations, the combined geostrophic components are spatio-temporally interpolated to surface drifter locations. This enables the

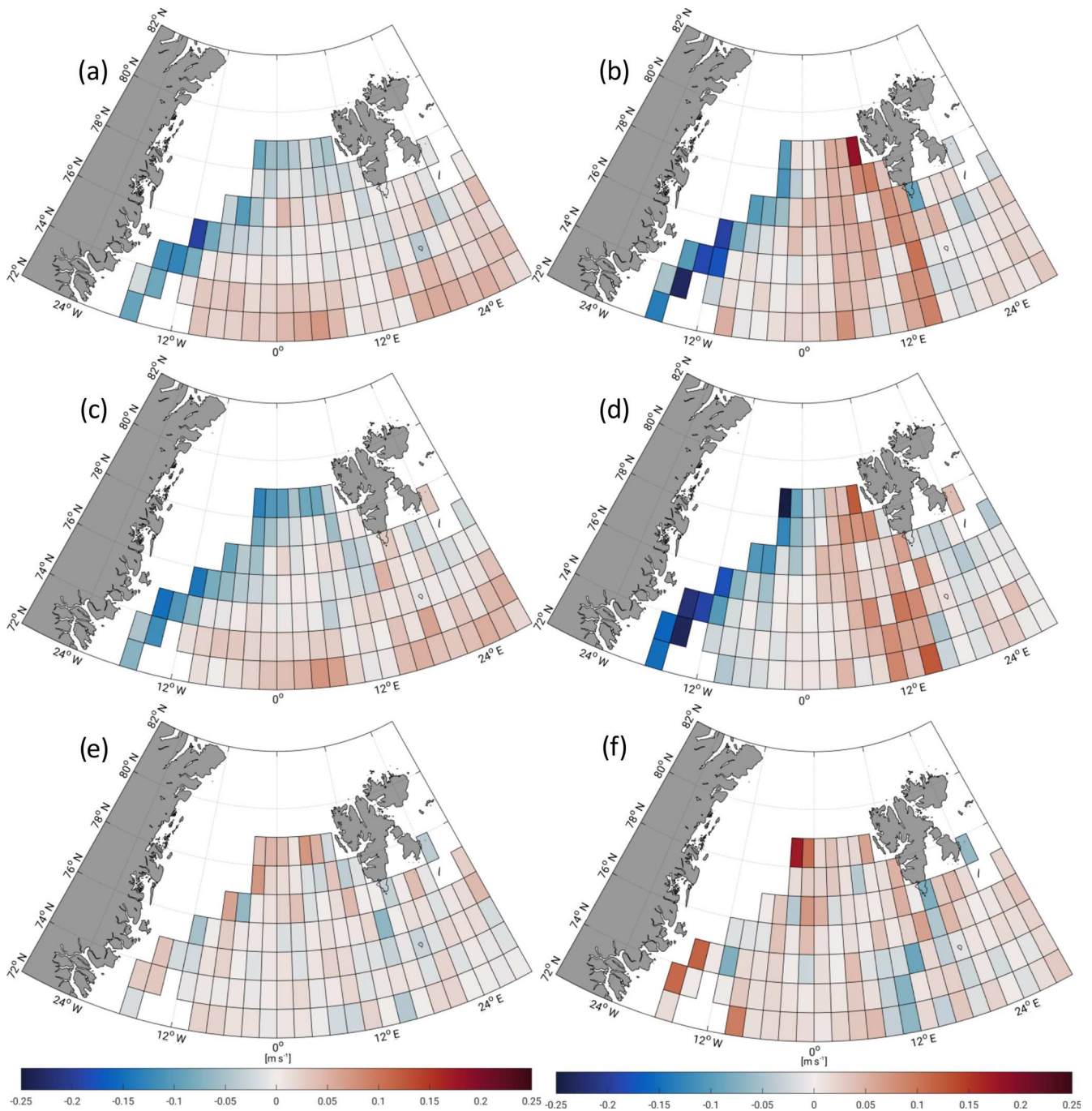


Figure 8. Temporally averaged geostrophic u (a, c, e) and v (b, d, f) components of drifter observations (a, b), combined dataset (c, d) and differences (e, f), respectively, binned in $2^\circ \times 1^\circ$ (longitude–latitude) boxes within the investigation time (1995–2012).

analyses of differences between geostrophic currents from observations and from the derived combined product. Therefore, the combination procedure is applied to the drifter epochs. This is done by interpolating the estimated combined principal components linearly to the drifter times followed by a PCS (Eq. 2) and a spatial nearest-neighbor interpolation to the drifter location. The results are combined DOT heights at

the drifter observation time and location. In order to compare with the geostrophic drifter measurements, the cDOT heights are transformed into geostrophic velocities (Sect. 3.3). Following Andersson et al. (2011), the drifter observations are grouped into $2^\circ \times 1^\circ$ longitude–latitude boxes. In order to perform statistically reliable analyses, only bins with at least two

different surface drifters and 50 observations are used (Andersson et al., 2011).

Figure 8 displays temporally averaged u and v components of the drifter observations (Fig. 8a, b) and the combined geostrophic currents (Fig. 8c, d). The differences (Fig. 8e, f) agree well with spatial patterns of the velocity components (i.e., drifter minus combination). The East Greenland and West Spitsbergen Current are resolved by both datasets in both velocity components. The drifter and the cGCs describe the same amplitude and flow direction in most of the bins. However, the v component shows bigger differences than the zonal component, caused mainly by a higher variability due to the primarily meridional flow direction of the currents in this area. Good agreement to the drifter data is shown by slight mean differences of $0.004 \text{ m s}^{-1} \pm 0.02 \text{ m s}^{-1}$ in the zonal (u) and $0.01 \text{ m s}^{-1} \pm 0.04 \text{ m s}^{-1}$ in the meridional (v) component.

When computing the RMSE between the measured geostrophic velocities and the combined velocities based on the individual trajectories for each drifter, a mean of $0.127 \text{ m s}^{-1} \pm 0.034 \text{ m s}^{-1}$ in the case of the u velocity and $0.132 \text{ m s}^{-1} \pm 0.039 \text{ m s}^{-1}$ for the v velocity are obtained. Moreover, the RMSE may reach 0.225 m s^{-1} for u and 0.232 m s^{-1} for v . Higher RMSE values can be found in regions with strong current activity (e.g., WSC).

Figure 9 shows the RMSE distribution of absolute velocity (Eq. 5) for the period 1995–2012 (blue curve). In addition, the same quantity derived based on the altimetry-only ADT currents is plotted in green. Both datasets are characterized by a very similar behavior. Nevertheless, the combination shows smaller residuals; 35 % of the combined residuals are smaller than 0.1 m s^{-1} in contrast to 27 % of the altimetry-only-derived geostrophic absolute velocity. In general, the results of both datasets are comparable to previous studies of the World Ocean and to Volkov and Pujol (2012), describing a maximal RMSE of around 0.2 m s^{-1} and a typical range of 0.07 to 0.15 m s^{-1} for the northern Nordic Seas in both components.

Figure 10 shows daily 3-monthly averaged EKE of the combined and ADT grids within the investigation period (1995–2012). The EKE results are computed by subtracting 3-month means from the daily datasets (Eq. 5). The ADT appears smoother and shows big data gaps in sea ice regions in comparison to the combined results. Furthermore, the combined eddy fields show finer eddy structures within the sea ice area and close to the Greenland coast. The cGCs are characterized by a higher spatial resolution and more variability in current regions.

The cDOT grids are evaluated against the daily and spatially averaged time series of ADT fields. Therefore, the cDOT fields are spatially interpolated to the ADT grids. Figure 11 shows that their mean reduced temporal evolution of both datasets. The comparison covers the full investigation period but is spatially limited to ice-free regions. The time series indicate a positive temporal correlation of nearly 80 %. Both

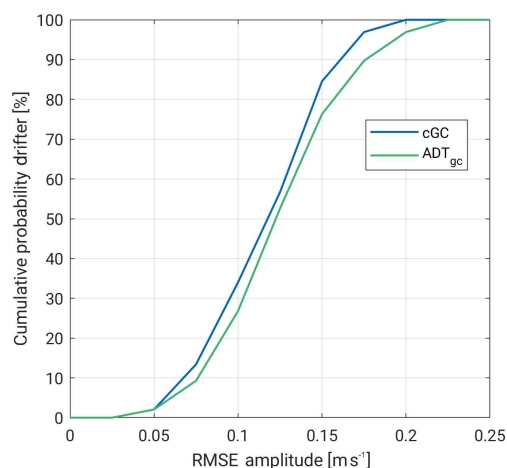


Figure 9. RMSE of geostrophic absolute velocity between drifter observations and of the trajectories interpolated combined and ADT datasets from 1995 to 2012.

datasets display high-frequency patterns. Compared to the stronger smoothed ADT grids with a standard deviation (SD) of $\pm 0.04 \text{ m}$, the cDOT heights are characterized by a higher variability ($\text{SD} = \pm 0.05 \text{ m}$) and display short periodic structures. Nevertheless, a slight offset between the time series between 1995 and 2003 of 2.5 and 2.0 cm between 2003 and 2012 can be observed, which might occur due to a different applied mean epoch of the ADT computation or an unconsidered bias in the retracking procedure of ERS-2 and Envisat.

6 Data availability

The final combined dataset can be downloaded from PANGAEA at <https://doi.org/10.1594/PANGAEA.900691> (Müller et al., 2019). Envisat (SGDR) and ERS-2 (REAPER-SGDR) altimetry data are available from ESA (Envisat: <https://doi.org/10.5270/EN1-85m0a7b> – ESA, 2018; ERS-2: <https://earth.esa.int/web/guest/-/radar-altimeter-reaper-sensor-geophysical-data-record-sgdr>, last access: 24 October 2019 – Brockley et al., 2017). The used FESOM data can be downloaded from PANGAEA at <https://doi.org/10.1594/PANGAEA.880569> or requested from Claudia Wekerle (AWI). The model code can be downloaded from <https://swrepo1.awi.de/projects/fesom> (last access: 24 October 2019) after registration. The in situ drifter observations and ADT grids with additional parameters are available via CMEMS (drifter data: http://resources.marine.copernicus.eu/?option=com_csw&view=details&product_id=INSITU_GLO_UV_L2_REP_OBSERVATIONS_013_044, last access: 13 January 2019 – Rio and Etienne, 2018; ADT: http://resources.marine.copernicus.eu/?option=com_csw&view=details&product_id=SEALEVEL_GLO_PHY_L4_REP_OBSERVATIONS_008_047, last access: 29 March 2019 – Pujol and Mertz, 2019). Data grids of

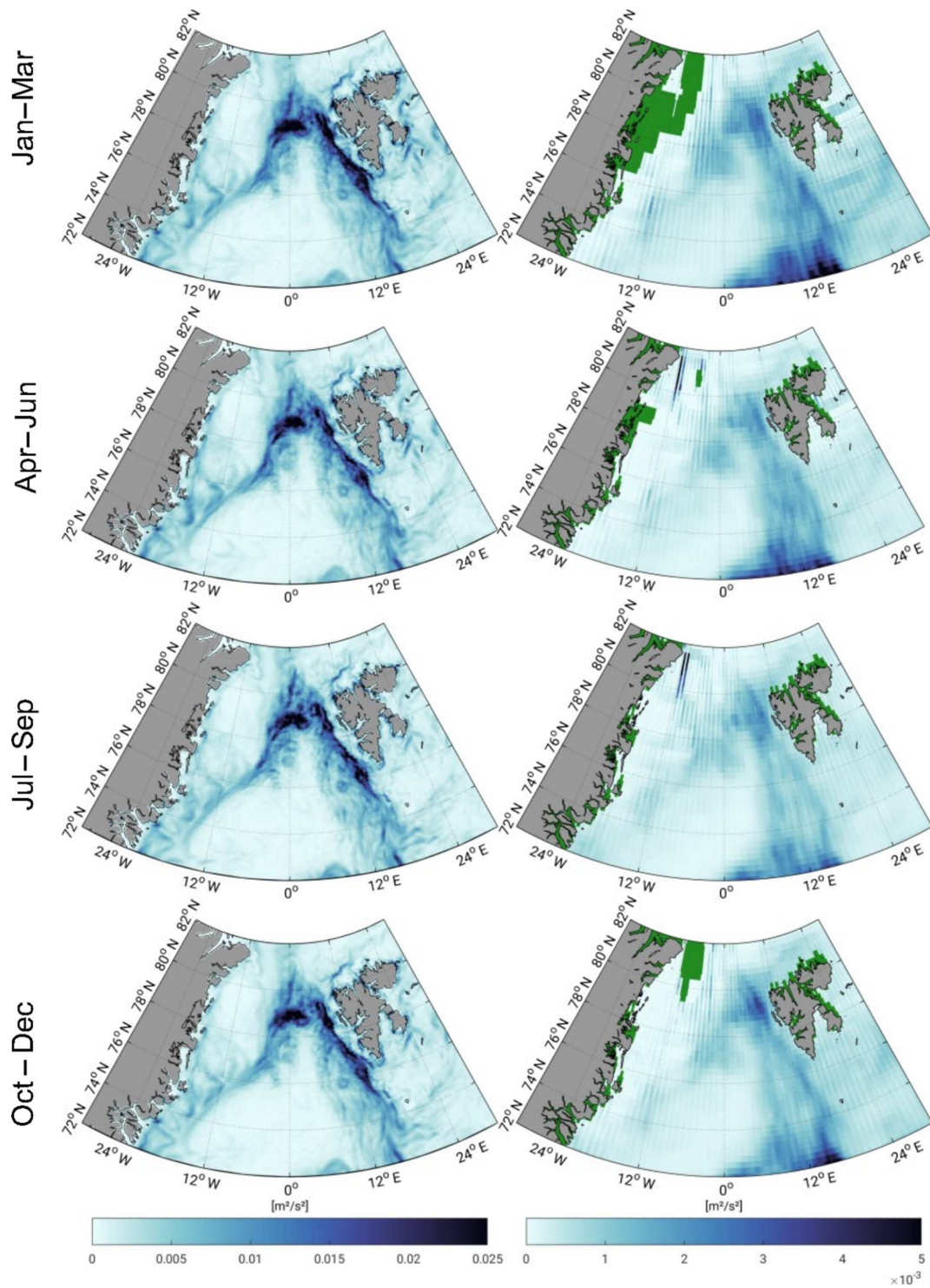


Figure 10. Three-monthly averaged geostrophic eddy kinetic energy within the FESOM period (1995–2012) for combined results (left) and ADT grids (right). Green areas indicate missing values.

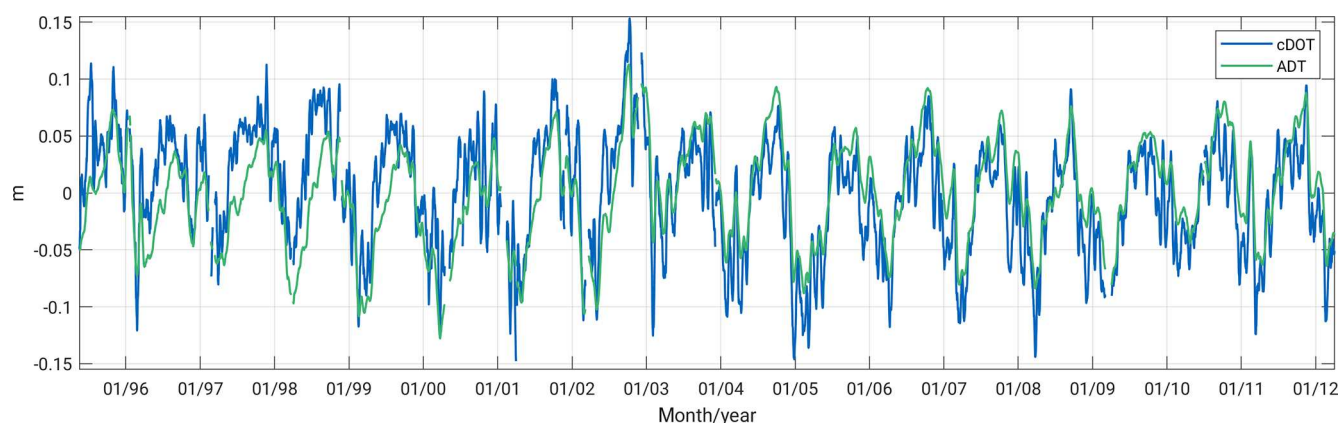


Figure 11. Zero-centered time series of daily and spatially averaged altimetry-only ADT grids and to the ADT grid nodes interpolated combined DOT (cDOT) limited to ice-free regions within 1995–2012 and the northern Nordic Seas.

the Ekman and Stokes drift are provided by GlobCurrent at <http://globcurrent.ifremer.fr/products-data/data-catalogue> (last access: 13 January 2019).

7 Summary and conclusions

The current paper presents an innovative dataset based on a combination of height observations from satellite altimetry with spatial information provided by an ocean model (FESOM). In case of altimetry data, an open-water classification procedure is applied in order to exploit along-track water height measurements within the sea ice area. Furthermore, height offsets between the open ocean and the sea ice area are removed by using one single retracking algorithm.

The combination approach takes advantage of the principal component analysis, especially the separation of the model data into its most significant spatial patterns and temporal components with respect to the total variability. The 50 most-dominant patterns (EOF) are used to combine them with ERS-2 and Envisat-observed along-track DOT heights in order to fill in observational gaps and to enable investigations based on a homogeneous DOT representation. In detail, the spatial information from FESOM and the temporal variability from altimetry are linked. The height level of the final product is given by altimetry by re-adding the previous estimated and subtracted annual signal and constant offset, since the model height reference is not clearly defined, whereas the obtained spatial resolution is defined by FESOM, which is characterized by local refinements in ocean current active areas smaller than 1 km. The combination is computed on a daily resolution and covers a time span of 17 years (1995–2012).

Geostrophic currents are provided by computing zonal and meridional slope gradients of the finite-element mesh. This allows comprehensive variability analyses of ocean currents not only in open-ocean areas but also within sea ice regions. A comparison with altimetry-only datasets shows that the

combination uses enhanced spatio-temporal resolution and displays short periodic structures and missing data gaps, especially in the regions covered by sea ice. Moreover, a positive correlation of nearly 80 % in open-ocean areas can be achieved.

A comparison with in situ surface drifter measurements, although limited to ice-free regions, indicates a similar and realistic representation of ocean current patterns and mesoscale eddies in the area of both datasets under investigation. Furthermore, good agreement in the comparison of binned surface drifter and derived combined geostrophic velocity components has been described.

A direct pointwise comparison for each drifter trajectory indicates a temporal RMSE of the differences between the drifter velocity components and the combination of about 0.13 m s^{-1} . In general, the RMSE values obtained range from 0.05 to 0.10 m s^{-1} in areas with low-flow activity and up to 0.22 m s^{-1} in regions with high current energy. Following Volkov and Pujol (2012), these velocities are comparable to previous estimates for the World Ocean.

The presented data product supports long-term studies of the dynamic ocean topography and the ocean current regime in polar regions affected by sea ice. Aiming at a more than 25-year extension of the dataset, more conventional altimetry (Saral and ERS-1) as well as delay-Doppler altimetry data (e.g., Sentinel-3A, Sentinel-3B and CryoSat-2) will be added to the combination process in the future.

Appendix A: Abbreviations and nomenclature of altimetric and FESOM height variables

- SSHs: sea surface heights are heights with respect to a reference ellipsoid.
- SLAs: sea level anomalies are heights with respect to a mean sea level.
- DOT: dynamic ocean topography describes heights with respect to a geopotential datum (i.e., geoid).
- ADT: absolute dynamic topography is identical to DOT (nomenclature used by AVISO).
- DWH: differential water height is simulated water height, with respect to a reference surface similar to the geoid but without considering secular changes (e.g., glacial isostatic adjustment – GIA, ocean bottom topography and self-gravitation). DWH and DOT are closely related.

Appendix B: Derivation of finite elements in FESOM

The FESOM configuration that was used is based on a finite-element formulation. Regarding the spatial discretization, the global ocean is discretized by using tetrahedral elements. These elements are constructed by first generating a surface triangular mesh (x, y) . In the vertical, z layers are used. The resulting vertical prisms are then cut into three tetrahedrons. In the finite-element method, variables are approximated as linear combinations of a finite set of basis functions $\{N_i\}$. Regarding the choice of these basis functions, FESOM uses a P1–P1 discretization, meaning that piecewise-linear basis functions are employed for both sea surface height η and horizontal velocity \mathbf{u} : $\eta = \sum_{i=1}^{N_{2-D}} \eta_i N_i$ and $\mathbf{u} = \sum_{i=1}^{N_{3-D}} u_i N_i$, where N_{2-D} and N_{3-D} denote the number of 2-D and 3-D nodes, respectively. The i th basis function N_i is equal to 1 at node i and linearly vanishes to 0 within elements containing this node.

Derivatives are computed by transformation into a reference element. In 2-D, we consider the reference element \hat{K} defined by nodes $\hat{a}_1 = (0, 0)$, $\hat{a}_2 = (1, 0)$ and $\hat{a}_3 = (0, 1)$. As local 2-D basis functions defined on \hat{K} , we choose the first-order polynomials $N_1(x, y) = 1 - x - y$, $N_2(x, y) = x$ and $N_3(x, y) = y$, with its Jacobian matrix $\mathbf{J}_N = \begin{pmatrix} -1 & -1 \\ 1 & 0 \\ 0 & 1 \end{pmatrix}$.

Any arbitrary element K in the physical domain defined by nodes a_1, a_2 and a_3 can be mapped onto the reference element \hat{K} by affine-linear transformation: $F: \hat{K} \rightarrow K$, $F(\hat{x}) = B\hat{x} + d$, with $B = (a_2 - a_1, a_3 - a_1)$ and $d = a_1$. When computing the gradient of a variable ϕ on the reference element \hat{K} , we obtain $\nabla_{\hat{x}}\phi(x) = \nabla_{\hat{x}}\phi(F(\hat{x})) = \nabla_x\phi(F(\hat{x}))\nabla_{\hat{x}}F(\hat{x}) = \nabla_x\phi(F(\hat{x}))B$. Thus, the gradient in the physical domain can be expressed as $\nabla_x\phi(F(\hat{x})) = \nabla_{\hat{x}}\phi(F(\hat{x}))B^{-1}$.

We now compute the gradient of η on element K by inserting $\phi = \sum_{i=1}^3 \eta_i N_i$ into the above equation: $\nabla_x\eta = \nabla_{\hat{x}}\sum_{i=1}^3 \eta_i N_i B^{-1} = (\eta_1, \eta_2, \eta_3)\mathbf{J}_N B^{-1}$.

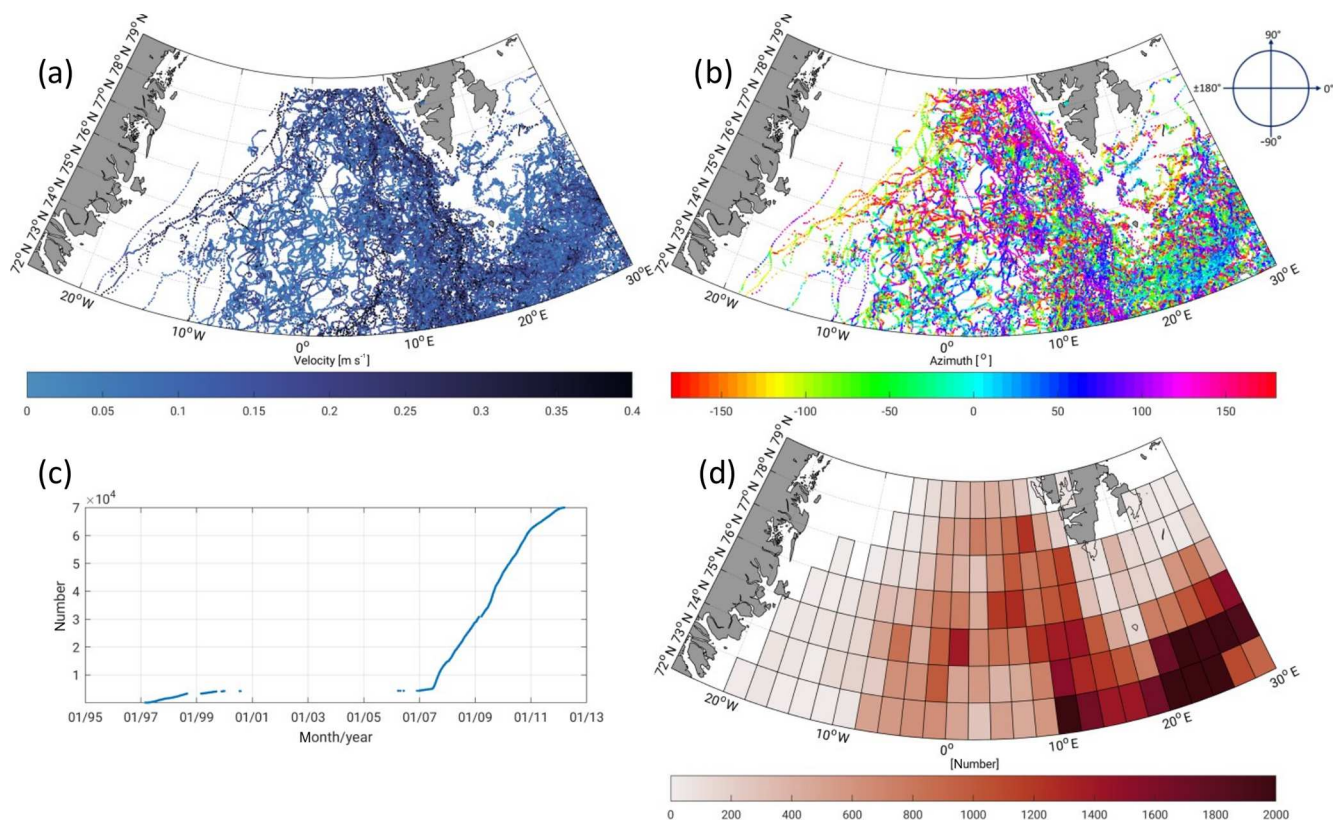


Figure A1. Amplitude (a), azimuth (b), and cumulative number (c) of geostrophic surface drifter velocities and number of records in $2^\circ \times 1^\circ$ boxes (d) within the 1995–2012 investigation time period. Approximately 63 % of the observations were obtained by an attached drogue.

Author contributions. FLM processed the combination and wrote most of the paper. DD supervised the present study, contributed to the paper writing and helped with discussions of the results. CW provided the FESOM data and contributed to the paper writing. CS maintains the altimetry database (OpenADB) at DGFI-TUM and supported the discussions. MP developed the re-tracking algorithm and helped with discussions concerning the altimetry dataset. WB initiated the study. FS supervised the research.

Competing interests. The authors declare that they have no conflict of interest.

Acknowledgements. The authors thank H el ene Etienne from Collecte Localisation Satellites (CLS) for supporting the study with valuable advice regarding the surface drifter data processing. The authors thank the Chair of Astronomical and Physical Geodesy, Technical University of Munich (TUM), for providing the geoid model, OGMOC. We also thank ESA for providing ERS-2 and Envisat altimetry data, CMEMS for maintaining the ADT grids as well as the surface drifter velocities and GlobCurrent for providing ageostrophic currents (i.e., Ekman and Stokes drift). The simulations were performed at the North-German Supercomputing Alliance (HLRN). This work was mainly supported by the German Research Foundation (DFG). The publication is funded by the German Research Foundation (DFG) and TUM in the framework of the Open Access Publishing Program.

We thank two anonymous reviewers for their valuable comments that helped to improve the paper.

Financial support. This research was mainly supported by the German Research Foundation (DFG) through grant nos. BO1228/13-1, DE2174/3-1 and TI296/7-2.

Review statement. This paper was edited by Giuseppe M. R. Manzella and reviewed by two anonymous referees.

References

- Andersson, M., Orvik, K. A., LaCasce, J. H., Koszalka, I., and Mauritzen, C.: Variability of the Norwegian Atlantic Current and associated eddy field from surface drifters, *J. Geophys. Res.-Oceans*, 116, C08032, <https://doi.org/10.1029/2011JC007078>, 2011.
- Androsov, A., Nerger, L., Schnur, R., Schr oter, J., Albertella, A., Rummel, R., Savcenko, R., Bosch, W., Skachko, S., and Danilov, S.: On the assimilation of absolute geodetic dynamic topography in a global ocean model: impact on the deep ocean state, *J. Geodesy*, 93, 141–157, <https://doi.org/10.1007/s00190-018-1151-1>, 2018.
- Armitage, T. W. K., Bacon, S., Ridout, A. L., Thomas, S. F., Aksenov, Y., and Wingham, D. J.: Arctic sea surface height variability and change from satellite radar altimetry and GRACE, 2003–2014, *J. Geophys. Res.-Oceans*, 121, 4303–4322, <https://doi.org/10.1002/2015JC011579>, 2016.
- Armitage, T. W. K., Bacon, S., Ridout, A. L., Petty, A. A., Wolbach, S., and Tsamados, M.: Arctic Ocean surface geostrophic circulation 2003–2014, *The Cryosphere*, 11, 1767–1780, <https://doi.org/10.5194/tc-11-1767-2017>, 2017.
- Barnston, A. G.: Correspondence among the Correlation, RMSE, and Heidke Forecast Verification Measures; Refinement of the Heidke Score, *Weather Forecast.*, 7, 699–709, doi10.1175/1520-0434(1992)007<0699:CATCRA>2.0.CO;2, 1992.
- Brockley, D. J., Baker, S., F em enias, P., Mart inez, B., Massmann, F., Otten, M., Paul, F., Picard, B., Prandi, P., Roca, M., Rudenko, S., Scharroo, R., and Visser, P.: REAPER: Reprocessing 12 Years of ERS-1 and ERS-2 Altimeters and Microwave Radiometer Data, *IEEE T. Geosci. Remote*, 55, 5506–5514, <https://doi.org/10.1109/TGRS.2017.2709343>, 2017.
- Bulczak, A. I., Bacon, S., Naveira Garabato, A. C., Ridout, A., Sonnewald, M. J. P., and Laxon, S. W.: Seasonal variability of sea surface height in the coastal waters and deep basins of the Nordic Seas, *Geophys. Res. Lett.*, 42, 113–120, <https://doi.org/10.1002/2014GL061796>, 2015.
- Church, J. A., White, N. J., Coleman, R., Lambeck, K., and Mitrovica, J. X.: Estimates of the Regional Distribution of Sea Level Rise over the 1950–2000 Period, *J. Climate*, 17, 2609–2625, [https://doi.org/10.1175/1520-0442\(2004\)017<2609:EOTRDO>2.0.CO;2](https://doi.org/10.1175/1520-0442(2004)017<2609:EOTRDO>2.0.CO;2), 2004.
- Danilov, S.: Ocean modeling on unstructured meshes, *Ocean Model.*, 69, 195–210, <https://doi.org/10.1016/j.ocemod.2013.05.005>, 2013.
- ESA: RA-2 Sensor and Geophysical Data Record – SGDR, <https://doi.org/10.5270/en1-85m0a7b>, 2018.
- Farrell, S. L., McAdoo, D. C., Laxon, S. W., Zwally, H. J., Yi, D., Ridout, A., and Giles, K.: Mean dynamic topography of the Arctic Ocean, *Geophys. Res. Lett.*, 39, L01601, <https://doi.org/10.1029/2011GL050052>, 2012.
- Fetterer, F. K., Knowles, W., Meier, M., Savoie, and Windnagel, A. K.: Sea Ice Index, Version 3, north, Boulder, Colorado USA. NSIDC: National Snow and Ice Data Center, <https://doi.org/10.7265/N5K072F8>, 2017.
- Gruber, T. and Willberg, M.: Signal and Error Assessment of GOCE-based High Resolution Gravity Field Models, *Journal of Geodetic Science*, accepted, 2019.
- Jolliffe, I. T.: *Principal Component Analysis*, vol. 2, Springer-Verlag New York, <https://doi.org/10.1007/b98835>, 2002.
- Koch, K.-R.: *Parameter Estimation and Hypothesis Testing in Linear Models*, Springer Berlin Heidelberg, <https://doi.org/10.1007/978-3-662-03976-2>, 1999.
- Kwok, R. and Morison, J.: Dynamic topography of the ice-covered Arctic Ocean from ICESat, *Geophys. Res. Lett.*, 38, L02501, <https://doi.org/10.1029/2010GL046063>, 2011.
- Kwok, R. and Morison, J.: Sea surface height and dynamic topography of the ice-covered oceans from CryoSat-2: 2011–2014, *J. Geophys. Res.-Oceans*, 121, 674–692, <https://doi.org/10.1002/2015JC011357>, 2015.
- M uller, F. L., Dettmering, D., Wekerle, C., Schwatke, C., Bosch, W., and Seitz, F.: Geostrophic Currents in the northern Nordic Seas – A Combined Dataset of Multi-Mission Satellite Altimetry and Ocean Modeling, Dataset, <https://doi.org/10.1594/PANGAEA.900691>, 2019.

- Müller, F. L., Wekerle, C., Dettmering, D., Passaro, M., Bosch, W., and Seitz, F.: Dynamic ocean topography of the northern Nordic seas: a comparison between satellite altimetry and ocean modeling, *The Cryosphere*, 13, 611–626, <https://doi.org/10.5194/tc-13-611-2019>, 2019.
- Müller, F. L., Dettmering, D., Bosch, W., and Seitz, F.: Monitoring the Arctic Seas: How Satellite Altimetry Can Be Used to Detect Open Water in Sea-Ice Regions, *Remote Sens.*, 9, 551, <https://doi.org/10.3390/rs9060551>, 2017.
- Passaro, M., Kildegaard, S. R., Andersen, O. B., Boergens, E., Calafat, F. M., Dettmering, D., and Benveniste, J.: ALES+: Adapting a homogenous ocean retracker for satellite altimetry to sea ice leads, coastal and inland waters, *Remote Sens. Environ.*, 211, 456–471, <https://doi.org/10.1016/j.rse.2018.02.074>, 2018.
- Preisendorfer, R. W.: *Principal component analysis in meteorology and oceanography*, Elsevier Science Pub. Co., Amsterdam, New York, 1988.
- Pujol, M. I. and Mertz, F.: *Product User Manual For Sea Level Sla Products, Global Ocean Gridded L4 Sea Surface Heights And Derived Variables Reprocessed (1993–Ongoing)*, 1.0, available at: http://resources.marine.copernicus.eu/?option=com_csw&view=details&product_id=SEALEVEL_GLO_PHY_L4_REP_OBSERVATIONS_008_047, last access: 29 March, 2019.
- Rascle, N. and Arduin, F.: A global wave parameter database for geophysical applications. Part 2: Model validation with improved source term parameterization, *Ocean Model.*, 70, 174–188, <https://doi.org/10.1016/j.ocemod.2012.12.001>, 2013.
- Ray, R. D. and Douglas, B. C.: Experiments in reconstructing twentieth-century sea levels, *Prog. Oceanogr.*, 91, 496–515, <https://doi.org/10.1016/j.pocean.2011.07.021>, 2011.
- Ringler, T., Petersen, M., Higdon, R. L., Jacobsen, D., Jones, P. W., and Maltrud, M.: A multi-resolution approach to global ocean modeling, *Ocean Model.*, 69, 211–232, <https://doi.org/10.1016/j.ocemod.2013.04.010>, 2013.
- Rio, M.-H. and Etienne, H.: Copernicus in situ TAC, Global ocean delayed mode currents from drifting buoys, *Product User Manual – PUM, Report (technical document (specification, manual))*, <https://doi.org/10.13155/41257>, 2018.
- Rio, M.-H. and Hernandez, F.: High-frequency response of wind-driven currents measured by drifting buoys and altimetry over the world ocean, *J. Geophys. Res.-Oceans*, 108, 3283, <https://doi.org/10.1029/2002JC001655>, 2003.
- Rio, M.-H., Mulet, S., and Picot, N.: Beyond GOCE for the ocean circulation estimate: Synergetic use of altimetry, gravimetry, and in situ data provides new insight into geostrophic and Ekman currents, *Geophys. Res. Lett.*, 41, 8918–8925, <https://doi.org/10.1002/2014GL061773>, 2014.
- Rudels, B.: Arctic Ocean circulation and variability – advection and external forcing encounter constraints and local processes, *Ocean Sci.*, 8, 261–286, <https://doi.org/10.5194/os-8-261-2012>, 2012.
- Schaffer, J., Timmermann, R., Arndt, J. E., Kristensen, S. S., Mayer, C., Morlighem, M., and Steinhage, D.: A global, high-resolution data set of ice sheet topography, cavity geometry, and ocean bathymetry, *Earth Syst. Sci. Data*, 8, 543–557, <https://doi.org/10.5194/essd-8-543-2016>, 2016.
- Volkov, D. L. and Pujol, M.: Quality assessment of a satellite altimetry data product in the Nordic, Barents, and Kara seas, *J. Geophys. Res.-Oceans*, 117, C03025, <https://doi.org/10.1029/2011JC007557>, 2012.
- Wang, Q., Danilov, S., Sidorenko, D., Timmermann, R., Wekerle, C., Wang, X., Jung, T., and Schröter, J.: The Finite Element Sea Ice-Ocean Model (FESOM) v.1.4: formulation of an ocean general circulation model, *Geosci. Model Dev.*, 7, 663–693, <https://doi.org/10.5194/gmd-7-663-2014>, 2014.
- Wekerle, C., Wang, Q., von Appen, W.-J., Danilov, S., Schourup-Kristensen, V., and Jung, T.: Eddy-Resolving Simulation of the Atlantic Water Circulation in the Fram Strait With Focus on the Seasonal Cycle, *J. Geophys. Res.-Oceans*, 122, 8385–8405, <https://doi.org/10.1002/2017JC012974>, 2017.

Co-authored publications

While working on the thesis project, three different co-authored publications were produced, in which the algorithms and datasets presented here are included. Please note that the last one is a review publication, presenting current work in the field of polar ocean satellite altimetry. The publications are freely accessible and used in the text as normal citations.

- CoP-1** Göttl, F., Dettmering, D., Müller, F. L., and Schwatke, C. (2016). Lake level estimation based on cryosat-2 sar altimetry and multi-looked waveform classification. *Remote Sensing*, 8(11), ISSN: 2072-4292, DOI: 10.3390/rs8110885
- CoP-2** Dettmering, D., Wynne, A., Müller, F. L., Passaro, M., and Seitz, F. (2018). Lead detection in polar oceans—a comparison of different classification methods for cryosat-2 sar data. *Remote Sensing*, 10(8), ISSN: 2072-4292, DOI: 10.3390/rs10081190
- CoP-3** Quartly, G. D., Rinne, E., Passaro, M., Andersen, O. B., Dinardo, S., Fleury, S., Guillot, A., Hendricks, S., Kurekin, A. A., Müller, F. L., Ricker, R., Skourup, H., and Tsamados, M. (2019). Retrieving sea level and freeboard in the arctic: A review of current radar altimetry methodologies and future perspectives. *Remote Sensing*, 11(7), ISSN: 2072-4292, DOI: 10.3390/rs11070881

A.2 Supplementary material

the current section contains supplementary material, cited in the text.

Name	Lifetime	Repeat time	Radar band	Operator	Remarks
ERS-2	1995-2011	35 days	K_u	ESA	-
Envisat	2002-2010	35 days	K_u	ESA	ERS-2 orbit
Envisat-EM	2010-2012	ca. 30 days	K_u	ESA	drifting orbit
SARAL	2013-2016	35 days	K_a	CNES/ISRO	ERS-2 orbit

Table A.1: Overview of the key parameters of the used satellite altimetry missions. Please note that all listed missions cover the northern Nordic Seas up to a latitudinal limit of 81.5°N.

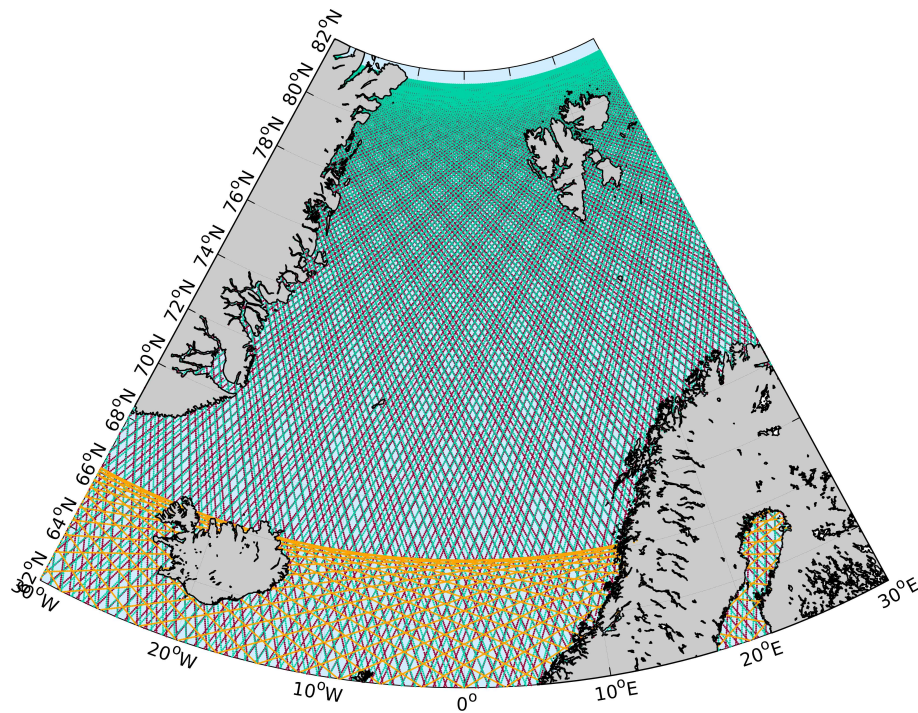


Figure A.1: Ground track patterns of ERS-2, Envisat and SARAL in dark red; the drifting orbit phase of Envisat-EM in green and Jason-1,2,3 in orange. The investigation area is defined by 72°N to 82°N and –30°W to 30°E (Figure 1.1)

A.2 Supplementary material

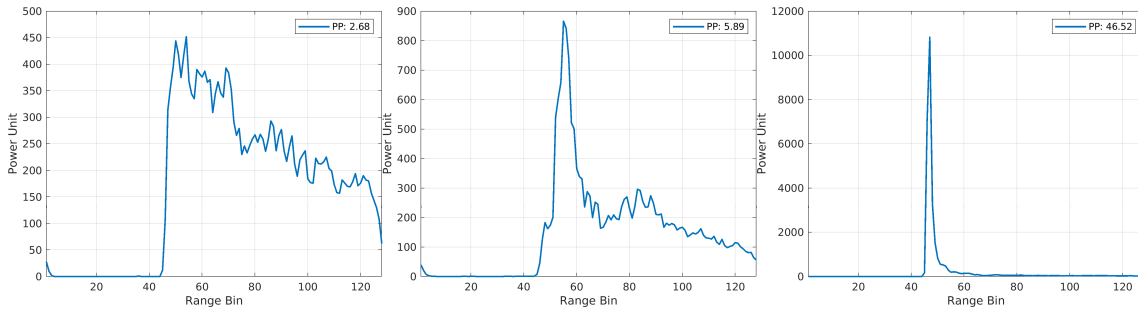


Figure A.2: Examples of Envisat waveforms for open ocean (left), sea ice (middle) and lead / polynya (right) conditions with Pulse-Peakiness (PP) values.

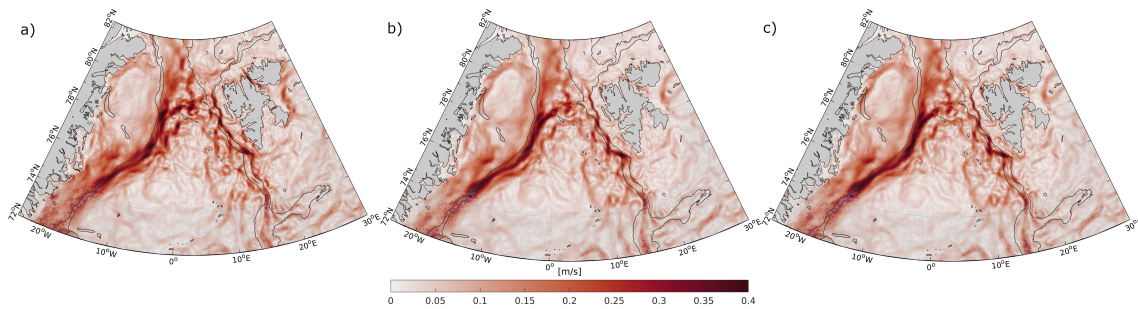


Figure A.3: Averaged geostrophic surface velocity for cool periods, 1996-1998 (a), 2008-2012 (c) and a warm period between 2002-2007 (b). Bathymetric contours indicate depths of -1500 m and -450 m, taken from RTopo2 (Schaffer et al. (2016)).

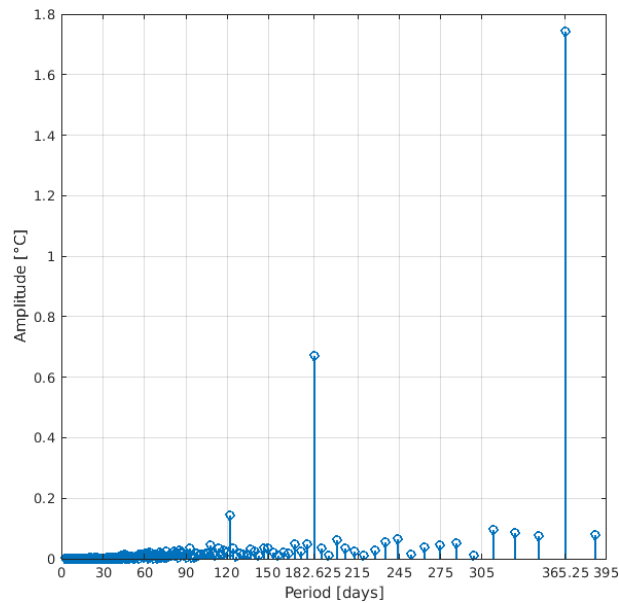


Figure A.4: Fourier analysis amplitude spectrum of the sea surface temperature within the WSC area between 1995-2012.